Technische Universität München

Physik-Department, Institut E21
Forschungs-Neutronenquelle Heinz Maier-Leibnitz (FRM II)

Vortex matter beyond SANS

Neutron studies of vortex structures covering a length scale of 0.01 to $10\,\mu\mathrm{m}$

Tommy Reimann M. Sc.

Vollständiger Abdruck der von der
Fakultät für Physik der Technischen Universität München
zur Erlangung des akademischen Grades eines

Doktors der Naturwissenschaften (Dr. rer. nat.)

genehmigten Dissertation.

Vorsitzender:		Prof. Dr. Michael Knap
Prüfer der Dissertation:	1.	Prof. Dr. Peter Böni
	2.	Prof. Dr. Winfried Petry
	3.	Prof. Dr. Michel Kenzelmann, Universität Basel (nur schriftliche Beurteilung)

Die Dissertation wurde am 21.09.2016 an der Technischen Universität München eingereicht und durch die Fakultät für Physik am 09.01.2017 angenommen.

Contents

List of Abbreviations

CCD	charge-coupled device
DFI	dark-field image
DPC	differential phase contrast image
FC	field cooling
FFT	fast Fourier transform
HFC	high field cooling
IMS	intermediate mixed state
IS	intermediate state
MCP	micro-channel plate
MS	Meissner state
nGI	neutron grating interferometry
NS	normal conducting state
NVS	neutron velocity selector
PPMS	physical properties measurement system
RRR	residual resistivity ratio
SANS	small-angle neutron scattering
SEM	scanning electron microscopy
SH	Shubnikov state
SDD	sample-to-detector distance
TI	transmission image
USANS	ultra-small-angle neutron scattering
VSANS	very-small-angle neutron scattering
ZFC	zero field cooling

List I. Abbreviations used in this thesis.

1. Vortex matter: A playground for condensed matter physicists

Superconductivity is one of the most fascinating and vivid research areas in condensed matter physics. For one thing, the strong interest in superconducting material arises since it abruptly loses any electrical resistance below a critical temperature [1] and is hence of high technological relevance. For instance, superconductors enable the non-dissipative transport of energy or the generation of high persistent currents required to produce strong magnetic fields [2]. In order to synthesize materials of high transition temperatures and of better technical applicability, most experimental and theoretical work on this subject has focused on the underlying mechanisms of superconductivity or on the processes which hamper lossless current transport. As a result of this research, superconductors are nowadays used for the generation of high magnetic fields [2], e.g. required for magnetic resonance imaging, they serve as material for radio-frequency cavities of high quality factor used in particle accelerators [3], replace conventional power lines for the inner-city transport of electric currents [4], or enable Maglev trains to reach velocities above $600\,\mathrm{km\,h^{-1}}$ [5].
However, owing to its unusual magnetic properties, the superconducting state is also of fundamental interest: Superconductors show ideal diamagnetic behavior for weak applied fields, called the Meissner effect [6]. For increasing field strength, superconductors can reveal fundamentally different behaviors. In type-I materials, to which most elemental superconductors belong to, superconductivity abruptly breaks down once the magnetic field energy exceeds the condensation energy and a first-order transition to the normal conducting state takes place. In contrast, in the majority of superconductors (denoted as type-II), the sample gradually becomes less diamagnetic above a first critical field while still preserving superconductivity. In this way, the superconducting state is stabilized for distinctly higher fields, which only enables its aforementioned technical applications. Intriguingly, the partial field penetration is realized by the nucleation of magnetic, particle-like *vortex lines* (commonly also denoted as *flux lines*) each carrying exactly one magnetic flux quantum [7]. This flux quantization reflects the macroscopic coherence and the quantum mechanical nature of the superconducting phase.
Once nucleated in the sample, the vortices in type-II superconductors are exposed to a variety of interactions [8]: (i) a repulsive (in few cases attractive) inter-vortex interaction promoting a vortex arrangement on a regular lattice, (ii) an interaction with the crystal lattice, transferring the crystallographic anisotropy to the

vortex configuration, (iii) thermal activation which provokes liquid-like behavior, (iv) an interaction with randomly distributed pinning centers which gives rise to amorphous or glassy configurations, and (v) topological restrictions arising from the sample geometry and its boundaries which induce an inhomogeneous spatial distribution of the vortices[1] [7]. This rich variety of interactions gives rise to surprisingly complex phase diagrams within the vortex state, including e.g. liquid, solid, glassy and amorphous phases. In order to describe this multitude, the term *vortex matter* has been coined that emphasizes the strong analogy to condensed matter formed by atoms [8].
However, unlike 'common' matter, whose density is primarily influenced by temperature and pressure, the density of vortex matter is affected by the applied field and the temperature, which can both be readily tuned. For this reason, vortex matter is a simple and ideally suited model system to study questions of rather general importance. For instance, vortex matter is frequently employed to study the characteristics and dynamics of melting transitions arising in its phase diagram [9], since the two-dimensional flux line structure eases an experimental observation and theoretical modeling of such processes. Vortex matter is furthermore predestined to investigate effects of random disorder on a regular crystalline arrangement, since disorder is easily generated by introducing a small amount of impurities to the material. In particular, the Bragg glass state [10], characterized by an algebraic decay of the translational correlation function of the lattice, has been firstly identified in the vortex state of (K,Ba)BiO_3 [11]. This discovery disproved long-standing speculations about the instability of this phase.

Domain structures in superconductors

Domain structures in the superconducting vortex lattice are a further example emphasizing the generic aspect of vortex matter [12]. Such domain structures arise if the inter-vortex interaction exhibits an attractive component, leading to a bundling of vortices which are surrounded by the Meissner phase [13]. A vortex attraction occurs in particular in the *intermediate mixed state* (IMS) of superconductors with a low Ginzburg-Landau parameter like vanadium [14] and niobium [15]. On these materials, the vortex attraction has been studied extensively in the 1970s [16]. Since a similar vortex attraction has been found in novel multi-band superconductors[2], the interest in superconducting domains has recently resurged.
A facet of vortex lattice domains, that has however not been addressed so far, is their resulting morphology which shows a variety of different patterns, including

1 While vortex-vortex and crystallographic interactions act only individually on the vortices, thermal activation, pinning and geometrical barriers act collectively on the vortex ensemble on a larger length scale.

2 The most prominent representative might be MgB_2. [17]

laminar, dendritic and bubble phases. Domain structures of strong similarity are frequently observed in various other physical systems on different time as well as length scales [18]. Some representatives of these systems are presented in Fig. 1.1 which exemplarily shows bubble (top row) and laminar (bottom row) patterns arising in Langmuir films, in confined ferrofluids, in solvent-cast films of block copolymers and in ferromagnetic films. The figure also introduces their respective equivalent found in the IMS of Nb. The superconducting domains are exceptional, because their domain patterns can be tuned and even interconverted by the applied magnetic field, which underlines the generic model character of vortex matter [19]. The similarity of the presented domain morphologies furthermore suggests that findings on the domain nucleation and on the corresponding pattern formation in superconductors could be generalized to other systems revealing phase separation. Nonetheless, a comprehensive theoretical understanding of the domain nucleation process in superconductors and how it is influenced by the vortex interactions listed above has not been given so far. Especially the strong influence of the sample geometry has been insufficiently examined due to a lack of adequate analytical methods.

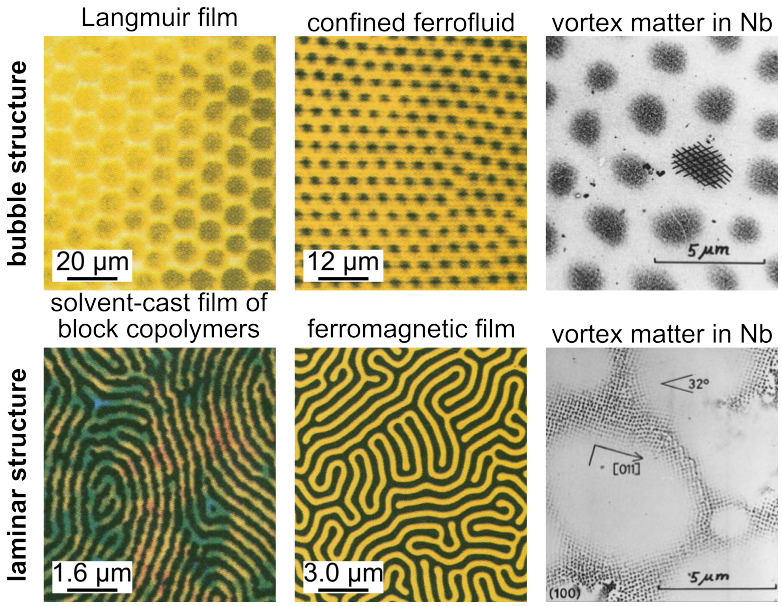

Figure 1.1.: Generic domain patterns. Comparison of different physical systems revealing phase separation which leads to similar tubular (top row) and laminar (bottom row) domain morphologies. Left and middle column taken from [18]. Reprinted with permission from AAAS. Right column taken from [13] with permission of Springer.

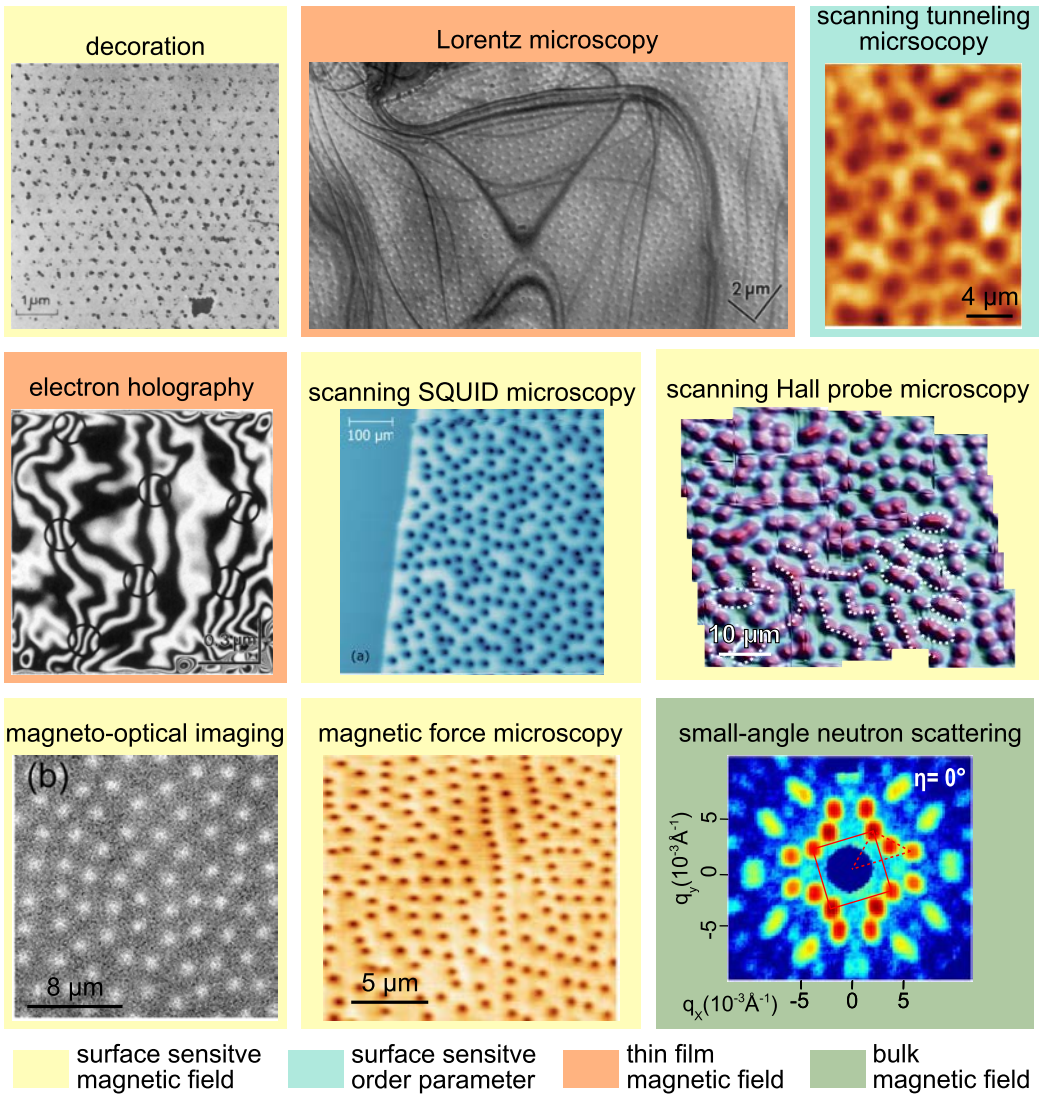

Figure 1.2.: Experimental methods probing vortex matter. Decoration (taken from [20] with permission from Elsevier), Lorentz microscopy (reprinted by permission from Macmillan Publishers Ltd: Nature [21], ©(1992)), scanning tunneling microscopy (Reprinted with permission from [22], ©(2014) by the American Physical Society), electron holography (Reprinted with permission from [23], ©(1994) by the American Physical Society), scanning SQUID microscopy [24], scanning Hall probe microscopy [25], magneto-optical imaging (Reprinted from [26] with the permission of AIP Publishing), magnetic force microscopy (Reprinted figure with permission from [27], ©(2012) by the American Physical Society), small-angle neutron scattering (Reprinted figure with permission from [28], ©(2012) by the American Physical Society)).

Experimental approaches probing vortex matter

The interest in superconducting vortex matter is also reflected in the high number of experimental methods available to examine its structure. An overview of these techniques is given in Fig. 1.2. Although this list is not intended to be exhaustive, most experimental results on the vortex structure are based on these approaches. The available methods can be grouped in (i) techniques probing the magnetic flux on the sample surface generated by the superconducting vortex (decoration, scanning SQUID, Hall probe or magnetic force microscopy, and magneto-optical imaging), (ii) approaches probing the superconducting order parameter (scanning tunneling microscopy), and (iii) techniques which are sensitive to the magnetic field distribution within thin samples (Lorentz microscopy and electron holography). While, by means of these methods, vortex structures can be imaged with an exceptional spatial as well as time resolution, none of the aforementioned techniques is capable of probing the vortex lattice within the bulk of the material. However, parasitic effects as branching [29], surface pinning or geometrical constraints [7] usually hamper an unambiguous determination of bulk behavior by means of surface observations. The vortex configuration detected at the sample surface does hence not necessarily reflect the situation within the material. All of the discussed approaches imply furthermore restrictions on the sample shape, since mostly flat samples (sometimes plane on the atomic scale) are required to distinctly focus on the specimens' surface. Thus, bulk behavior and effects arising from the sample geometry cannot be sufficiently studied by the available methods.
In contrast, neutrons can easily penetrate even thick bulk samples and due to their magnetic moment probe the magnetic field modulation within the vortex state independently of the underlying sample shape. The crystallographic structure of the vortex lattice, whose inter-vortex distance typically lies in the range of a few 100 nm, is usually probed by means of small-angle neutron scattering (SANS) [30] (see Fig. 1.2 on the bottom right). However, conventional SANS is incapable of probing superconducting domain structures arising on the micron length scale. Methods like ultra-small-angle [31] or very-small-angle neutron scattering [32](USANS & VSANS) extend the accessible size-range to the micronscale, but have not been used for the investigation of vortex domains so far. Neither of these integral scattering methods probing the reciprocal space of the vortex lattice can provide a spatial resolution and hence determine the real-space distribution of vortices within the sample.

Outline of this thesis

In this thesis, it will be shown how a combination of the radiographic techniques neutron grating interferometry (nGI) and diffractive imaging with the scattering methods USANS, VSANS and SANS can provide novel insight into the bulk behavior of vortex matter covering a length scale of 0.01 to 10 µm. By using the unique

contrast mechanism of nGI, which maps reciprocal space scattering signatures in real space, and the high angular resolution provided by USANS, the demonstrated approach allows to cover the formerly existing gap between the minimal spatial resolution obtained with neutron radiography and the maximal structure size probed by SANS. A listing of the used techniques and their probed size ranges is given in Fig. 1.3. Since the typical IMS domain size of a few micrometers lies within this resolution gap, the presented approach enables a first determination of the spatial distribution and morphology of vortex domains arising in the bulk of type-II superconductors. Moreover, this approach allows to (i) image the domain distribution within a sample during the nucleation of the IMS, (ii) study the morphology of the resulting domain structure and how it is affected by pinning and geometrical constraints, (iii) map the process of field penetration into the bulk of superconducting material and finally (iv) obtain detailed information about the vortex distribution and local distortion within a sample. It has to be emphasized that the demonstrated experimental approach is not restricted to superconductors, but can be applied to the variety of systems revealing a phase separation on the micrometer scale [18, 33].

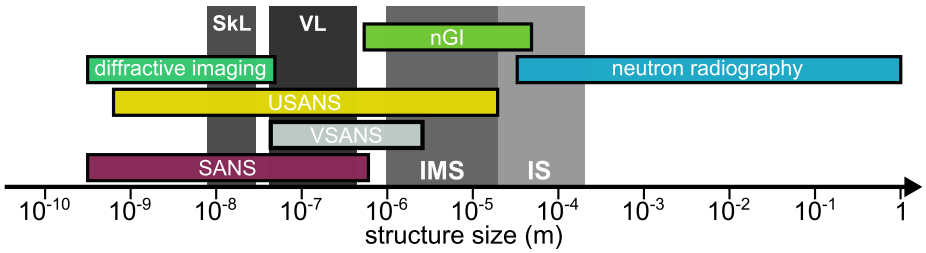

Figure 1.3.: Vortex matter beyond SANS. Comparison of neutron methods used in this thesis for the investigation of vortex matter. Marked are the length scales which can be probed by the respective method. Note that only neutron radiography can directly resolve the probed structures. SkL: skyrmion lattice, VL: vortex lattice, IMS: intermediate mixed state, IS: intermediate state.

The thesis is organized as follows: In Chap. 2, the theoretical fundamentals of vortex matter are reviewed. It will be focused on the domain structures arising in superconductors and on their generic properties. Furthermore, a brief summary is given, highlighting the similarities of superconducting vortices with skyrmion lines that arise in chiral magnets.
The theoretical basics of neutron scattering at large structures, which preferentially scatter neutrons in forward direction, are derived in Chap. 3. Considerations of this chapter result in relations allowing for the combined interpretation of SANS, USANS and nGI within a common theoretical framework.
Chap. 4 is concerned with the principle and capabilities of neutron grating interferometry (nGI). The information contained in the transmission, differential phase contrast, and dark-field image, obtained by means of nGI, will be derived

separately. In particular, the chapter focuses on the dark-field contrast modality and explains (i) how the contrast is linked to the samples' differential scattering cross-section and (ii) how quantitative information about the samples' microstructure, like texture directions and structure sizes, can be obtained by directional and quantitative dark-field imaging. The chapter closes with a discussion of complementary ultra-small-angle neutron scattering using a Bonse-Hart camera.
The details and characteristics of the experimental setups used for this thesis are given thereafter in Chap. 5. Again, particular attention is paid to neutron grating interferometry, since its implementation at the ANTARES beamline of the Heinz Maier-Leibnitz Zentrum (MLZ) was one of the main objectives of this work.
The last chapter of this thesis presents the experimental results demonstrating the capabilities of the combination of imaging and scattering methods. This chapter is divided in five self-contained sections highlighting different aspects of the presented study. In Sec. 6.1, the applicability of nGI to study superconducting domain structures is verified. For this purpose, the domain nucleation of the intermediate state (IS) in type-I superconducting lead is recorded. This example is used since the IS morphology is closely related to the slightly smaller IMS domain structure (compare Fig. 1.3), but has been studied more extensively. Hence, the IS is better suited to verify results obtained via nGI by literature. Thereafter, it will be focused on the IMS, particularly on (i) its nucleation in Nb samples of ultra-high purity but non-ellipsoidal cross-section, which enhances the influence of geometric effects on its domain distribution (Sec. 6.2), and on (ii) its formation and morphology variation in the presence of strong pinning (Sec. 6.3).
The usage of the IMS domain structure as contrast agent in order to image the field penetration into the bulk of a type-II superconductor showing significant pinning is demonstrated in Sec. 6.4. The obtained data are thereafter discussed in the framework of the critical state theory.
Finally, it will be demonstrated in Sec. 6.5 that diffractive neutron imaging based on a micro-channel plate (MCP) collimator could have a high impact for future investigation of vortex matter, since it allows a high resolution mapping of the spatial distribution and direction of vortices within a bulk material. This potential is demonstrated on the skyrmion lattice which is topologically similar to the vortex lattice in superconductors but possesses a slightly smaller spacing leading to an accordingly higher Bragg angle.

2. Theoretical principles of vortex matter in superconductors

In this chapter, the theoretical principles of vortex matter are reviewed to allow a comprehensive interpretation of the data presented in Chap. 6. At first, the general magnetic properties of superconducting materials are discussed within the framework of the Ginzburg-Landau theory (Sec. 2.1). This treatment directly leads to the subdivision of superconductors into type-I and type-II materials, whose differences are subsequently explained. Afterwards, in Sec. 2.2, the properties of the magnetic vortex lattice arising in type-II superconductors are considered, and its interplay with pinning forces and demagnetization effects is summarized. Sec. 2.3 treats the reasons for a domain nucleation in superconductors, followed by a review of its theoretical fundamentals. A discussion about the similarities between a vortex lattice of a type-II superconductor and the skyrmion lattice that occurs in some chiral magnetic materials, concludes this chapter.

2.1. Magnetic properties of superconductors

Superconducting materials are characterized by two phenomena which arise below a material specific critical temperature T_C: (i) the complete loss of the electrical resistance [1] and (ii) an expulsion of weak magnetic fields irrespective of the magnetic history of the sample, known as Meissner effect [6]. While the microscopic origin of superconductivity and its electrical properties can in most cases be explained in the context of the BCS theory [34], its macroscopic magnetic properties are interpreted by means of the Ginzburg-Landau-theory (GL-theory) [35][1], which will be discussed below. However, only a brief summary of the results of the theory is given. A more detailed derivation can be found e.g. in Ref. [37–39].
In the GL-theory, the superconducting state is described by a complex order parameter $\Psi_{GL}(\boldsymbol{r})$ which can vary spatially. The square of the order parameter describes the density of superconducting electrons. In order to examine the spatial behavior of $\Psi_{GL}(\boldsymbol{r})$ within the GL-model, the free energy of the superconducting state is expressed as a series expansion of the superconducting order parameter. The ground state of the system is found by minimizing this free energy, which

1 It has been shown that the GL-theory directly follows from the BCS theory at $T \approx T_C$ [36].

leads to the GL-differential equations [40]:

$$0 = \alpha\Psi_{\mathrm{GL}}(\boldsymbol{r}) + \beta\left|\Psi_{\mathrm{GL}}(\boldsymbol{r})\right|^2\Psi_{\mathrm{GL}}(\boldsymbol{r}) + \frac{1}{2m^*}\left(\mathrm{i}\hbar\nabla + 2e\boldsymbol{A}\right)^2\Psi_{\mathrm{GL}}(\boldsymbol{r}) \tag{2.1}$$

$$\boldsymbol{J} = -\frac{\mathrm{i}e\hbar}{m^*}\left[\Psi^*_{\mathrm{GL}}(\boldsymbol{r})\nabla\Psi_{\mathrm{GL}}(\boldsymbol{r}) - \Psi_{\mathrm{GL}}(\boldsymbol{r})\nabla\Psi^*_{\mathrm{GL}}(\boldsymbol{r})\right] - \frac{4e^2}{m^*}\boldsymbol{A}\left|\Psi_{\mathrm{GL}}(\boldsymbol{r})\right|^2 \ . \tag{2.2}$$

Here, α and β are approximated by introducing the positive constants a and b:

$$\alpha(T) \approx a(T - T_{\mathrm{C}}) \tag{2.3}$$

$$\beta \approx b \ , \tag{2.4}$$

while $\boldsymbol{J}$ is the superconducting current density, m^* the effective mass of the Cooper pairs, and $\boldsymbol{A}$ is the magnetic vector potential. The introduced temperature dependence of $\alpha(T)$ guarantees that the superconducting order parameter vanishes above T_{C}. The first GL-equation has the form of a Schroedinger equation with a nonlinear term which represents a repulsive potential of $\Psi_{\mathrm{GL}}(\boldsymbol{r})$ acting on itself [37]. Hence, the order parameter generally favors a homogeneous distribution in space.
For most applications, the set of GL-differential equations has to be solved numerically. However, simple considerations reveal that the GL-equations generally define two length scales which are characteristic for each superconductor: (i) the length scale on which a magnetic field is screened from the interior of the superconductor, denoted as magnetic penetration depth λ_{L}, and (ii) the length scale on which deviations in the order parameter are compensated, denominated as Ginzburg-Landau coherence length ξ_{GL}.

2.1.1. The magnetic penetration depth

Assuming that only a weak magnetic field is applied to the superconducting sample, the order parameter in Eq. 2.2 can be expressed by its homogeneous equilibrium value $\psi_0^2 = \frac{-\alpha}{\beta} = \frac{1}{2}n_{\mathrm{s}}$. Here, n_{s} is the density of superconducting electrons. By applying the curl operation on Eq. 2.2, it can be transformed to the London equation [41]:

$$\mu_0\nabla\times\boldsymbol{J} = -\nabla^2\boldsymbol{B} = -\frac{\mu_0 2e^2 n_{\mathrm{s}}}{m^*}\boldsymbol{B} = -\frac{1}{\lambda_{\mathrm{L}}^2}\boldsymbol{B} \ . \tag{2.5}$$

In the above equation, which is a partial differential equation for the magnetic induction, $\mu_0\boldsymbol{J}$ was replaced using Ampere's Law, and the magnetic constant μ_0 was introduced. Near the edge of a superconductor, the solution of Eq. 2.5 is an exponential decay of B from the surface to the interior of the sample, which is illustrated in Fig. 2.1 (a). The field degradation takes place on the characteristic

length scale λ_L:

$$\lambda_L = \sqrt{\frac{m^*}{2e^2 n_s \mu_0}} \propto (T_C - T)^{\frac{1}{2}} \ . \tag{2.6}$$

The origin of the field suppression are supercurrents $\boldsymbol{J}$ flowing near the surface of the sample and generating an opposite field within the sample (Fig. 2.1 (b)).

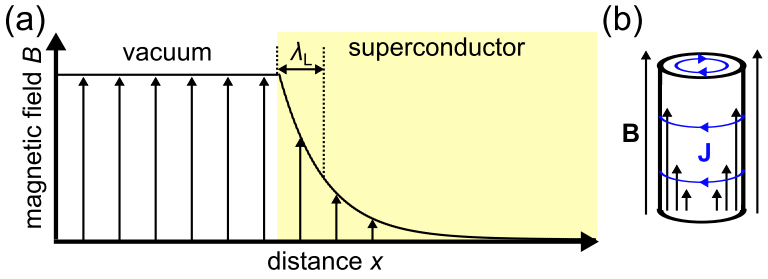

Figure 2.1.: The magnetic penetration depth: (a) Magnetic field profile at the edge of a thick superconductor. The magnetic field is exponentially extenuated with screening length λ_L. (b) Illustration of the Meissner effect in a superconducting cylinder in an axial magnetic field. The field is screened from the inside by circulating Meissner currents which flow in the plane perpendicular to the field.

2.1.2. The Ginzburg-Landau coherence length

In absence of a magnetic field, Eq. 2.1 yields in one dimension:

$$-\frac{\hbar^2}{2m^*}\frac{d^2\Psi_{GL}}{dx^2} + \alpha\Psi_{GL} + \beta\left|\Psi_{GL}\right|^2\Psi_{GL} = 0 \ . \tag{2.7}$$

If the order parameter is assumed to be real and is normalized to its equilibrium value ψ_0^2, the equation above reduces to [37]:

$$\xi_{GL}^2(T)\frac{d^2\psi}{dx^2} + \psi - \psi^3 = 0 \ , \tag{2.8}$$

in which the Ginzburg-Landau coherence length ξ_{GL} is given by:

$$\xi_{GL} = \frac{\hbar}{\sqrt{2m^*\left|\alpha\right|}} \propto (T_C - T)^{-\frac{1}{2}} \ . \tag{2.9}$$

Although the solution of Eq. 2.8 cannot be found analytically, the meaning of ξ_{GL} can easily be deduced, considering the extremal cases of $\psi \approx 0$ or $\psi = 1 - f \approx 1$. In both limits, Eq. 2.8 reduces to a linear ordinary differential equation, whose solution is an exponential decay. Hence, ξ_{GL} defines the length scale on which the

order parameter can vary in space.

2.1.3. The importance of the Ginzburg-Landau parameter κ: type-I, type-II/1 and type-II/2 superconductors

In the previous section, it has been discussed that the macroscopic behavior of a superconductor is characterized by the two length scales λ_L and ξ_{GL}. Although both quantities are temperature dependent, their ratio is in first-order approximation temperature independent near T_{C}. Hence, superconductors are routinely classified in terms of a material specific Ginzburg-Landau parameter κ:

$$\kappa = \frac{\lambda_{\mathrm{L}}(T)}{\xi_{\mathrm{GL}}(T)} \approx \text{const.} \tag{2.10}$$

The parameter κ can be interpreted by considering an interface which separates a superconducting, field free domain from a normal conducting region with the critical field B_{C}. The interface should have an area A_{NS}. The field can penetrate the superconducting region on a length λ_L. Hence, a volume $A_{\mathrm{NS}}\lambda_{\mathrm{L}}$ within the domain wall is penetrated by the magnetic field, saving a diamagnetic energy of [42]:

$$E_1 = -\frac{\lambda_{\mathrm{L}} A_{\mathrm{NS}}}{2\mu_0} B_{\mathrm{C}}^2 \ . \tag{2.11}$$

At the same time, the superconducting state is suppressed within a volume of approx. $A_{\mathrm{NS}}\xi_{\mathrm{GL}}$, leading to a lack of condensation energy of [42]:

$$E_2 = \frac{\xi_{\mathrm{GL}} A_{\mathrm{NS}}}{2\mu_0} B_{\mathrm{C}}^2 \ . \tag{2.12}$$

Thus, the surface tension of this interface γ_{NS} is given by:

$$\gamma_{\mathrm{NS}} = \frac{\Delta E}{A_{\mathrm{NS}}} = \frac{B_{\mathrm{C}}^2}{2\mu_0} (\xi_{\mathrm{GL}} - \lambda_{\mathrm{L}}) = \frac{B_{\mathrm{C}}^2}{2\mu_0} \delta \ , \tag{2.13}$$

in which δ is defined as the wall-energy parameter [38].
Obviously, the sign of the surface tension can change, depending on the ratio κ. However, the above considerations are only approximate solutions, as the magnetic penetration volume and the volume of suppressed superconductivity was only roughly estimated by means of λ_{L} and ξ_{GL}. A more advanced numerical evaluation of γ_{NS} including the GL-equations showed that for $\kappa \leq \frac{1}{\sqrt{2}}$, the surface tension is positive and the system will avoid the formation of such interfaces. In this case, the superconductor is denoted as *type-I* [35]. In contrast, for $\kappa \geq \frac{1}{\sqrt{2}}$, the surface tension is negative and the superconductor is unstable to the generation of multiple interfaces. These superconductors are denoted as *type-II*.

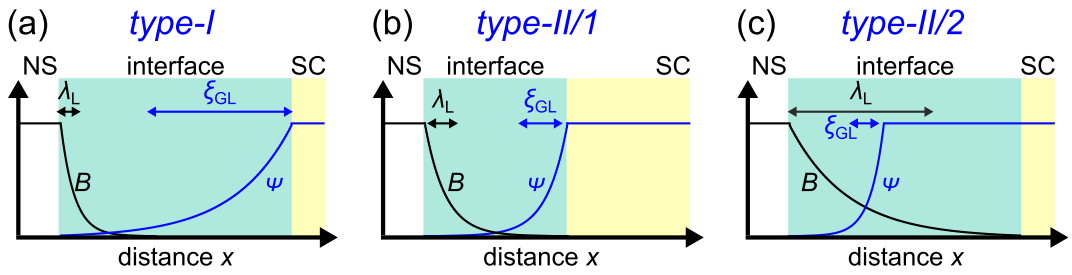

Figure 2.2.: Illustration of an interface between a normal conducting region (NS) and a superconducting domain (SC) for (a): small (type-I), (b): for intermediate (type-II/1), and (c) for large κ (type-II/2). Drawn is the magnetic field profile (black) as well as the superconducting order parameter (blue) near an NS-SC interface.

The next section discusses that type-I and type-II superconductors considerably differ in their magnetic properties. However, even within the type-II family, distinct variations exist in the magnetic behavior of superconductors having $\lambda_L \approx \xi_{GL}$. Hence, type-II material is additionally subclassified according to [7]:

$$\kappa \begin{cases} < 1 & \text{type-II/1} \\ \gg 1 & \text{type-II/2} \end{cases} \tag{2.14}$$

A summarizing illustration of the differences between type-I, type-II/1 and type-II/2 superconductivity near a normal conducting to superconducting boundary is shown in Fig. 2.2.

2.1.4. Magnetic properties of type-I, type-II/1 and type-II/2 superconductors

In the following section, the magnetic behavior of the different types of superconductors is addressed, considering the example of a long superconducting cylinder in a longitudinal magnetic field. In this case, demagnetization effects can be neglected. A type-I superconductor will completely expel the field from its interior until the critical value $B_C(T)$ is reached. The situation corresponds to a diamagnetic susceptibility of $\frac{dM}{dB} = \chi = -1$ and the superconducting phase is denoted as Meissner phase (MS). Above B_C, superconductivity breaks down via a first-order phase transition and the sample becomes normal conducting. The corresponding magnetic phase diagram is shown in Fig. 2.3 (a) [7].
The situation changes when the superconductor is of type-II. For low fields, the sample is still in the MS. However, it has been shown in Sec. 2.1.3 that the superconducting state becomes unstable for the generation of normal conducting / superconducting interfaces above the lower critical field B_{C1}. The consequence of this instability is the transition to the Shubnikov phase (SH) [43]. It is characterized by the emergence of magnetic vortices as has firstly been proposed by

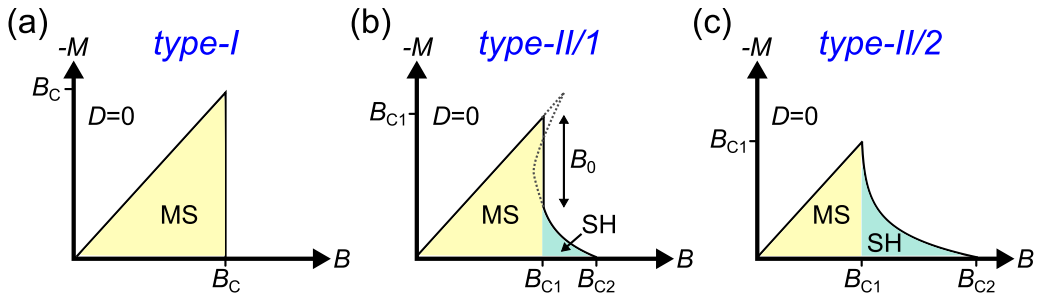

Figure 2.3.: Schematic magnetic phase diagrams for type-I, type-II/1 and type-II/2 superconductors which are not influenced by demagnetization effects. In type-I superconductors, only a Meissner state (MS) exists up to the field B_{C}, while type-II material additionally exhibit the Shubnikov phase (SH) between B_{C1} and B_{C2}.

.

Abrikosov [44]. Each vortex line carries a magnetic flux quantum $\Phi_0 = \frac{\hbar}{2e}$ and, hence, the magnetization $-M$ of the sample is decreased. However, the sample remains superconducting. An example decoration image of the typically formed vortex lattice is shown in Fig. 1.2. The structure of a vortex line will be examined in Sec. 2.2.1.
For superconductors with high κ (type-II/2), the transition at

$$B_{\mathrm{C1}} \approx \frac{\Phi_0}{4\pi\lambda_{\mathrm{L}}^2}\left(\ln\kappa + 0.5\right) \tag{2.15}$$

is of second order and the negative magnetization sharply drops down as a large number of vortices can instantaneously enter the sample above the first critical field [37]. When the distance of the vortices reaches the coherence length ξ_{GL} at

$$B_{\mathrm{C2}} = \frac{\Phi_0}{2\pi\xi_{\mathrm{GL}}^2}\ , \tag{2.16}$$

the superconducting state is no longer energetically favorable and the sample becomes normal conducting via a second order phase transition (see Fig. 2.3 (c)). The situation is slightly different in type-II/1 materials [7]. It has been shown numerically that the theoretical magnetization curve of such superconductors has an S-shape near B_{C1} as indicated in Fig. 2.3 (b) [45]. This peculiar shape is not observed in an experiment. However, it links to an instability that is caused by an unusual attractive interaction between the vortices. The origin of the attractive vortex-vortex interaction is discussed in Sec. 2.2.2. The behavior of the experimental magnetization is however found by a Maxwell-construction as shown in the phase diagram. Consequentially, as soon as B_{C1} is reached, many vortices penetrate the sample leading to a first-order drop in the magnetization of B_0.

2.2. Properties of vortex matter

In this section, the structure of a vortex line is reviewed (Sec. 2.2.1) and the interactions acting on the vortices are briefly considered. This discussion includes vortex-vortex interactions (Sec. 2.2.2), pinning forces (Sec. 2.2.3) as well as surface and geometrical barriers (Sec. 2.2.4), whose interplay is responsible for a multitude of vortex states found in type-II superconductors.

2.2.1. The structure of an isolated vortex line

In Sec. 2.1.3, it has been discussed that a type-II superconductor gains energy by emerging multiple NS-SC interfaces. The basic unit in which the system can split above B_{C1} is a single magnetic vortex carrying a flux of Φ_0. A smaller structure cannot be screened by the supercurrent while fulfilling its quantization condition. The structure of such a single vortex line is illustrated in Fig. 2.4 (a). Its core consists of a normal conducting region, in which the magnetic flux passes the sample, surrounded by screening currents. In case of $\kappa \gg 1$, the order parameter vanishes towards the center of the core as [7]:

$$|\Psi_{\mathrm{GL}}(r)|^2 \approx \left(1 + 2\frac{\xi_{GL}^2}{r^2}\right)^{-1} , \tag{2.17}$$

whereas the magnetic field outside the normal core of radius ξ_{GL} is given by [7] [37]:

$$B(r) \approx \frac{\Phi_0}{2\pi\lambda_{\mathrm{L}}^2} K_0\left(\frac{r}{\lambda_L}\right) . \tag{2.18}$$

K_0 is the modified Bessel function of zeroth order. The characteristics of Ψ_{GL} and $B(r)$ near a vortex core are drawn in Fig. 2.4 (b) for the case $\kappa = 10$.
The structure of the vortex cores slightly differs in type-II/1 superconductors. The reason is that the finite normal conducting core of radius ξ_{GL} can no longer be neglected as it is done in the derivation of Eqs. 2.17 and 2.18 for high kappa [7]. Refined numerical simulations of a vortex structure in type-II/1 material can be found in Refs. [45] and [46]. For our study, the differences are not relevant.

2.2.2. The interaction of vortex lines

The interaction force per unit length of two vortices A and B within a superconductor is given by [47]:

$$\boldsymbol{F}_{\mathbf{L}}^{\mathbf{A}} = \boldsymbol{J}^{\mathbf{B}} \times \boldsymbol{\Phi_0} . \tag{2.19}$$

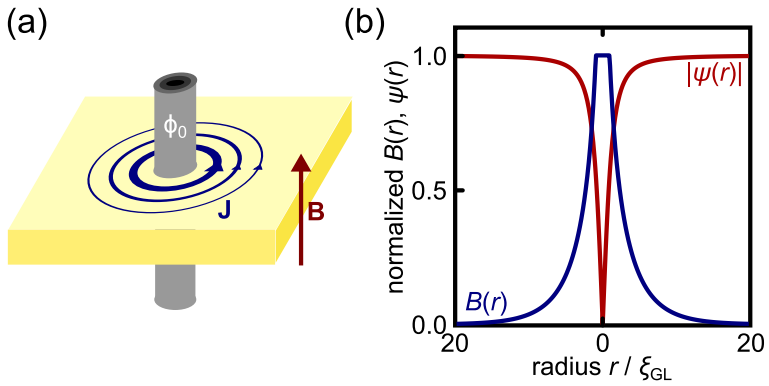

Figure 2.4.: The structure of a magnetic vortex. (a) Illustration of a magnetic vortex in a superconductor. The vortex carries exactly one flux quantum Φ_0 and is surrounded by supercurrents $\boldsymbol{J}$ which screen the remaining superconductor from the magnetic flux. (b) Calculated structure of a vortex with $\kappa = 10$ according to Eqs. 2.17 and 2.18. The order parameter is zero at the vortex center, while the magnetic field is approximately constant on a radius ξ_{GL}. Away from the center, ψ increases on the length scale ξ_{GL}, whereas B decreases on a distance λ_{L}.

This means, the interaction arises due to the Lorentz force between the magnetic flux within vortex A and the screening currents of vortex B. The situation is illustrated in Fig. 2.5 (a). As seen in the sketch of the triangle of forces, this interaction is purely repulsive for parallel vortices. Hence, the flux lines normally align in a configuration where the inter-vortex-distance is maximal which leads to the well known solution of a hexagonal vortex lattice [7, 44].

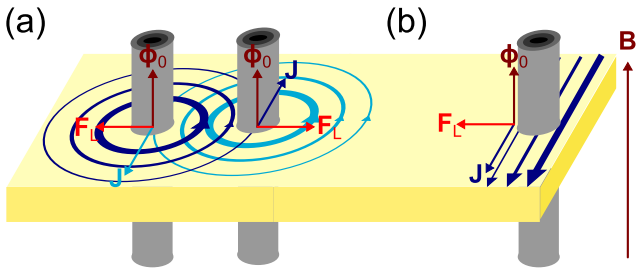

Figure 2.5.: Illustration of vortex interaction caused by the Lorentz force: (a) The repulsive interaction between two vortices arises, as the Lorentz force pushes one vortex in the direction perpendicular to its magnetic flux Φ_0 and to the screening current of the second vortex. (b) If a vortex has entered the sample from the edge, it is instantaneously driven to its center by the Lorentz forces acting between the magnetic flux and the Meissner screening current of the sample.

However, these considerations are only valid under the assumption that only the magnetic fields of the vortices overlap, but not their cores. Although this is certainly true in type-II/2 superconductors, in low κ materials (type-II/1), this

approximation is no longer valid. In contrast, the order parameter alters on the same length scale as the magnetic induction and the core regions of neighboring vortices overlap. For $B \ll B_{C2}$, the generalized interaction potential of two straight flux lines separated by r has been derived as [48]:

$$V(r) = \frac{\Phi_0^2}{2\pi\lambda_L^2\mu_0}\left[K_0\left(\frac{r}{\lambda_L}\right) - K_0\left(\frac{r}{\xi_{GL}}\right)\right] . \tag{2.20}$$

Therefore, by including the contributions of the vortex core, one achieves an additional attractive part in the inter-vortex interaction. Its physical explanation is that if the order parameter is suppressed on a length scale comparable to λ_L, vortices will gain energy by overlapping their core regions since then, the overall depression of Ψ_{GL} takes place in a smaller volume and condensation energy is gained.
The attractive interaction discussed above explains the jump of the magnetization found in type-II/1 superconductors at B_{C1} (Fig. 2.3 (b)) [49]: The formation of two separated vortex lines requires more energy than the formation of a pair. Thus, as soon as the first vortices enter the material, energy is released if the vortices bundle and new ones can be formed. Consequentially, one detects a higher B_{C1} upon increasing field than during field reduction [50] in type-II/1 materials, because the final flux expulsion at B_{C1} requires to break the vortex-vortex bond while flux penetration does not.
At last, the vortices not only interact with each other, but with all other external and internal currents in the sample. Hence, vortices formed on the sample surface are driven to the interior of the object by the Meissner currents which screen the sample. This process is illustrated in Fig. 2.5 (b). Additionally, an applied current will also accelerate the vortex lines perpendicular to the current direction in accordance to Eq. 2.19. This flux motion dissipates energy [51] and, hence, has to be prevented by vortex pinning in order to maintain the perfect conductance of the material.

2.2.3. The pinning of vortices

Pinning arises, if the free motion of a vortex line is hampered and a specific position within the sample is energetically more favorable than the others. If, for instance, one of the material parameters as e.g. B_C, T_C, λ_L or ξ_{GL} differ from its surrounding, this will lead to a gradient in the vortex energy landscape which corresponds to a pinning force density F_P. Possible pinning centers are impurities within the material [52], indentations on the sample surface [53], and crystallographic defects as grain boundaries or dislocations [54]. However, pinning can be softened at high temperature, as the thermal energy allows to overcome

the pinning potential [55]. Furthermore, any current density J_C higher than:

$$J_C = \frac{F_P}{B} \tag{2.21}$$

will unpin the vortex, since the Lorentz force (Eq. 2.19) exceeds the pinning force at this value.
Flux pinning is one of the mostly studied phenomena in superconductors, since it has dramatic consequences on its magnetic as well as electric properties and is thus of high technical relevance [2]. Prominent is the emergence of a strong hysteresis in an $M(B)$ measurement due to an inhomogeneous distribution of magnetic flux within the sample. In the following section, this will be explained within the framework of the critical state theory [40, 56].

The critical state

By introducing $\boldsymbol{J} = \nabla \times \boldsymbol{H}$ in Eq. 2.19, the Lorentz force density on a vortex line can be expressed in its vectorial form:

$$\boldsymbol{F} = (\nabla \times \boldsymbol{H}) \times \boldsymbol{B} \ . \tag{2.22}$$

Without loss of generality, the case that the field is applied along the x-direction and the current is flowing along y can be considered. Under these assumptions, one obtains [47]:

$$F = \frac{B}{\mu_0}\frac{\partial B}{\partial x} \ . \tag{2.23}$$

Hence, the Lorentz force acting on the vortex lattice depends on the gradient of B. The critical state theory assumes that this gradient adjusts everywhere in the sample, so that the current density is either J_C or zero. This approach is justified, because if the gradient could increase further, the Lorentz force acting on the vortices would exceed the pinning forces and the vortex lattice would be shifted to reduce this gradient. A simple but realistic qualitative discussion on hysteretic effects caused by pinning is possible within the Bean critical state model [56]. This theory supposes that the critical current density is constant all over the sample and independent of B and T.
In the following, the distribution of magnetic flux within a superconductor revealing strong pinning is compared to a pinning free sample. Moreover, within the framework of the critical state theory, it will be discussed how the flux distribution causes the magnetic hysteresis observed in hard superconductors. A typical hysteresis loop as expected in a type-II superconductor revealing significant pinning is illustrated in Fig. 2.6 (a). Corresponding experimental example data can be found e.g. in [57] or in Sec. 6.3. In the presence of strong pinning (blue curve), the

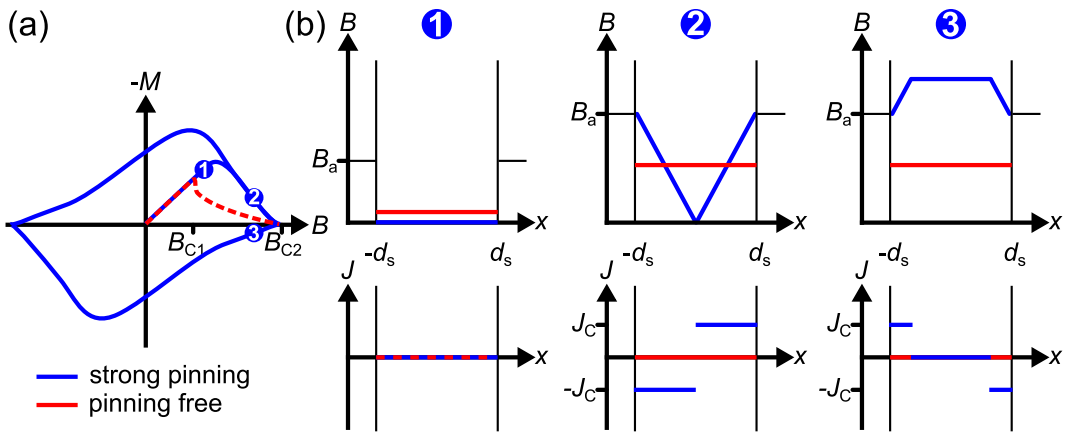

Figure 2.6.: Magnetic hysteresis of a slab in the Bean model. The field is applied parallel to the largest surfaces of the sample. (a) Magnetic hysteresis loop of a type-II superconductor for strong (blue) and negligible (red) pinning. For strong pinning, the magnetization is irreversible with a paramagnetic characteristic in the decreasing branch of the hysteresis loop. (b) Cross sections of the magnetic field profile and the current profile of the sample for the positions marked in (a). For explanations see below.

penetration of flux at B_{C1} is delayed compared to the case of a pinning free sample (red curve), and the hysteresis loop is rounded. Additionally, in the decreasing branch of the hysteresis loop, a paramagnetic signal arises. The magnetization is thus strongly irreversible and remanent.

The hysteresis can be explained within the Bean model by an examination of the flux distribution at different fields shown in Fig. 2.6 (b). In this illustration, profiles of the magnetic induction (top row) and of the magnetic current density (bottom row) within the sample are exemplarily shown for the points marked in the hysteresis loop (a). To exclude demagnetization effects in this discussion, a slab shaped sample of thickness $2d_s$ in x-direction is assumed and the field is applied parallel to the largest surface.

At point 1, the pinning free sample would already be in the Shubnikov phase. Hence, the induction inside this sample is finite due to the homogeneously distributed vortex lattice. In contrast, the macroscopic screening currents are zero, except in a small layer on the samples surface, which is not visible on the scale ($\gg \lambda_L$) of the figure. These screening currents are also present in the sample revealing pinning. However, they are not high enough to unpin vortices formed at the surface. Hence, in the presence of pinning, the induction and the flux within the sample are zero.

At point 2, the induction increased in the case of a pinning free sample, as the vortex lattice parameter is reduced and more flux enters. Still, macroscopic currents flow near the surface only. In the sample revealing pinning, the field had penetrated as well, but a constant field gradient has been formed according to the Bean model. The associated current density amounts the critical value all over the sample. The drawn situation corresponds to the field B_P at which the flux

front firstly reached the center of the sample. This situation is denominated as the 'Bean critical state' [37].
If the field is increased further above B_{C2}, the induction within the sample corresponds to B_a in both cases. A subsequent decrease of the fields will, however, result in the profiles shown for point 3. In the case of a pinning free sample, the induction is just reversibly reduced below B_a by the onset of diamagnetism. In contrast, in the center of the sample that reveals strong pinning, the induction remains approximately B_{C2}, because vortices can only be removed on the distance where the gradient between B_a and B_{C2} corresponds to the critical value. As in a paramagnet, the induction inside the sample is strongly enhanced compared to the applied one.
The assumption of the Bean model that J_C does not depend on the field and the position within the sample, is only a rough approximation. Different models have thus been developed to treat a more realistic $J_C(B,T,x)$[1]. However, the qualitative aspects about the field penetration process in the presence of pinning corresponds well to the actual situation.

Several remarks on the collective nature of pinning

At the end of this section, it has to be remarked that the critical current (Eq. 2.21) is not simply given by the summation of all individual pinning forces acting on each vortex of the vortex lattice. If the lattice would be considered as rigid, randomly distributed pinning forces acting on it would indeed add up to zero [37]. Nevertheless, as the vortex lattice is an elastic object, it can locally be bent to align in a configuration which reduces the total energy. However, this involves an increase of elastic energy of the lattice [7]. The final configuration of the vortex lattice is hence given by the minimization of both energy contributions. The influence of different pinning centers onto the vortices of the superconductor is therefore a collective phenomenon [58]. Consequentially, the total pinning potential depends also on the vortex-vortex interactions within the vortex lattice.

2.2.4. Surface and geometrical barriers

In Sec. 2.2.3, hysteretic behavior caused by pinning has been discussed. However, even in pinning free samples, magnetic hystereses can be observed as e.g. reported in Ref. [59]. Such irreversibilities occur, if the flux penetration into the sample is hampered by a surface or edge barrier while flux expulsion is not. Brandt [7] identified at least seven different mechanisms causing such a barrier, albeit some of which additionally require the sample to reveal significant pinning [60–62]. Hereafter, the focus will lie on the geometrical barrier introduced by Zeldov [63]

1 A comprehensive listing of various other models is given in Ref. [40].

and Indenbom [64], as its contribution is pronounced for the sample geometries investigated. In contrast, surface barriers as e.g. the Bean-Livingston-Barrier [65] require a surface smoothness of the order of the penetration depth, which is not achieved for the samples used in this thesis.
The origin of the surface barrier is illustrated in Fig. 2.7 (a), where a superconducting sample with rectangular cross-section in a weak applied magnetic field is shown. Magnetic flux is still expelled from the inside of the object, but the screening currents partially enhance the field on its surface. The maximum of this enhancement is found at the corners of the rectangular sample. This is why the first penetration of a vortex line will take place at these positions, as indicated in Fig. 2.7 (a). If the field is increased further, the penetrating vortex line will be bound to the surface as long as it has not completely penetrated the sample. This peculiar process of flux entrance goes along with an elongation of the flux line within the sample. As the core of the vortex is normal conducting, this stretched penetration requires more condensation energy than just the line energy of one straight flux line of length d. Hence, the first flux penetration requires a higher energy and is therefore delayed as in the case of pinning. Once a flux line has entirely entered the sample, it is instantaneously pushed to its center by the Lorentz forces (Fig. 2.7 (b)). A field free region between the center and the edge develops [64].
The described geometrical barrier does not exist in decreasing fields, when flux is repulsed from the interior of the sample. Hence, also the magnetic induction and the magnetization of the sample will dramatically differ for increasing and decreasing applied fields. As this magnetic hysteresis is not caused by pinning, the term *topological hysteresis* has been introduced [66]. It can be unambiguously distinguished from a hysteresis caused by pinning, as it must vanish at zero field.
The situation slightly differs in ellipsoidal samples. It has been shown that no geometrical barrier occurs in this case. As sketched in Fig. 2.7 (c), the flux lines penetrate the sample tangentially and no line elongation arises. However, in contrast to rectangular samples, these vortex lines are not driven to the center of the sample, but distribute homogeneously. The reason is that the Lorentz forces acting on the vortices are compensated by the increase in line energy, which is required to push the vortex into thicker regions of the sample [67].

Simulations of field penetration

The geometrical and pinning contributions driving the flux distribution in a superconductor, were discussed separately in the previous sections to give an overview of the various mechanisms determining the final magnetic state. An exact treatment of the interplay of these processes requires numerical simulations going beyond the scope of this thesis. Nonetheless, the discussed principles and main features caused by pinning and sample geometry, are all well confirmed by first principle calculations.

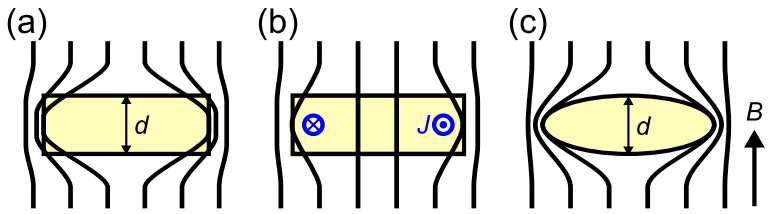

Figure 2.7.: Origin of the topological hysteresis. (a) and (b) show the process of flux penetration into a superconductor of rectangular cross-section. The field enhancement due to the samples demagnetization field is highest at the corners of the slab, which therefore corresponds to the positions of first flux penetration. As the vortex line has to be elongated to completely penetrate the sample, the critical field B_{C1} is enhanced. As soon as the vortex line has overcome this barrier, it is instantaneously driven to the center of the sample by the screening currents J (b). The surface barrier does not exist for field exit. In samples with an ellipsoidal cross-section (c), no surface barrier exists, as the field can tangentially penetrate the sample and no initial elongation is required.

Fig. 2.8 presents results of continuum electrodynamics computations by Brandt (Ref. [68, 69]) which show the field distribution in a superconductor. In (a), the magnetic field lines during field penetration (top left and bottom) as well as during field decrease (top right) are shown for a clean, strip shaped sample in the absence of pinning. These simulations confirm the strong bending of the flux lines near the corners of the sample and the connected geometrical barrier. Furthermore, they clearly reveal the flux enhancement in the center of the sample, which provokes a flux free region between the center and the edge. In contrast, the situation for a sample revealing strong pinning is visualized in (b) using the example of a thick disc in different applied fields. Shown are the field lines[1] for the initial penetration of a magnetic field into the sample. Clearly, in contrast to the pinning free case, the free motion of flux lines to the center of the disc is hampered by pinning. Furthermore, a flux gradient develops during the field penetration in accordance to the critical state theory. However, as the applied model directly takes the sample shape into account, the flux lines and the flux penetration front are bent. The latter one is the contour where the current density drops from $\pm J_C$ to zero. It is indicated as bold line in (b). The presented simulations show that even in complex objects, the field penetration can be qualitatively well understood by the simple principles sketched in this section. Due to the lack of adequate simulation results, discussions about the measured field distribution in this thesis will be based on the given qualitative arguments.

1 Exactly, the contour lines of the vector potential rA are plotted non-equidistantly. However, their direction corresponds to the direction of B.

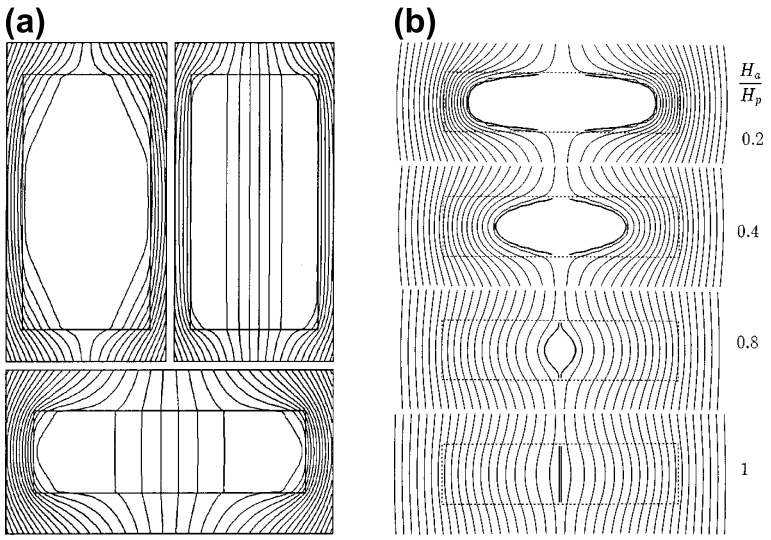

Figure 2.8.: (a) Field lines of the induction $\boldsymbol{B}\,(x,y)$ in strips with aspect ratio of 2 (top) and 0.3 (bottom) in the case of negligible pinning. The simulations show the situation in increasing field shortly before the field of first flux entry is reached (top left) and in decreasing field at $H = H_{\mathrm{C1}}/2$ (top right). Furthermore, for the smaller sample (bottom) a situation in increasing fields is shown, just above the field of first flux penetration. Reprinted from [68] with the permission of AIP Publishing. (b) Magnetic field lines during flux penetration into a thick disc with aspect ratio of 0.25 that reveals significant pinning. Reprinted figure with permission from [69] Copyright (2016) by the American Physical Society

2.2.5. The influence of demagnetization effects on the phase diagram

The effect of the sample geometry has so far only been treated as the origin of irreversibilities within the magnetic properties of a superconductor. Its phase diagram was supposed to be unaffected by the sample shape. However, this is an oversimplification of the real situation. In the following part, the effects of the sample geometry on the magnetic properties of type-I and type-II superconductors are examined. To get an illustration, consider the spherical superconducting sample in a homogeneous applied magnetic field $\boldsymbol{H}$ sketched in Fig. 2.9. In its superconducting state, the sample expels the field by the aforementioned superconducting screening currents $\boldsymbol{J}$ which generate a magnetization $\boldsymbol{M}$ inside the sample equal to $\boldsymbol{M} = -\boldsymbol{H}$. The magnetic flux density $\boldsymbol{B} = \mu_0(\boldsymbol{H} + \boldsymbol{M})$ consequentially vanishes inside the superconductor. However, these screening currents running along the latitudes of the sphere create a magnetic dipolar field outside the sample [40]. Hence, the magnetic field in the exterior of the sphere is given by the superposition of this demagnetization field with the applied one. The field that is created in this way is sketched in Fig. 2.9. Obviously, the field close to the sample surface is strongly enhanced in the equatorial plane. It amounts

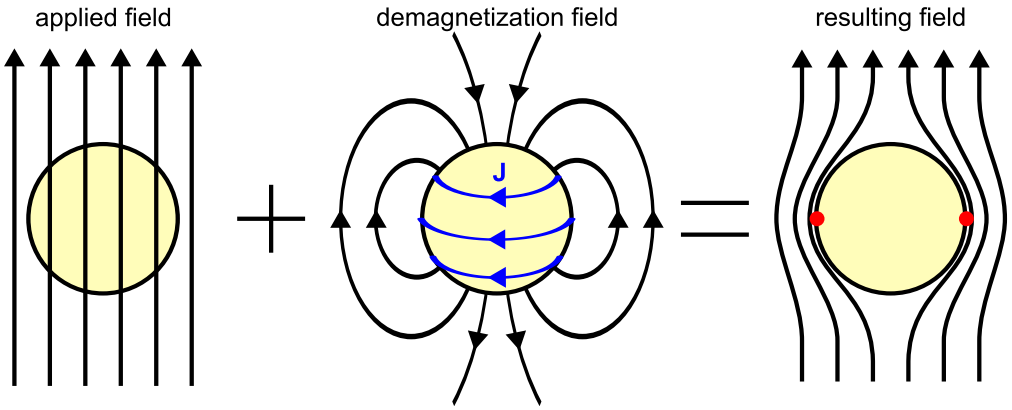

Figure 2.9.: Illustration of demagnetization effects on a superconducting sphere in an applied magnetic field. The field is screened from the inside of the sphere by superconducting screening currents. However, these currents create a dipolar field outside the sample, which is superposed to the applied one, and enhances the field on the surface of the superconductor.

[38, 70]:

$$\boldsymbol{B}_{\text{surface}} = \frac{3}{2}\boldsymbol{B} = (1-D)^{-1}\boldsymbol{B} \ . \tag{2.24}$$

The quantity D is referred to as the demagnetization coefficient, which numbers the maximal amplification of the external field caused by the sample. D is tabulated for different sample geometries [71–73]. However, the demagnetizing field within the sample is only homogeneous for elliptical shapes [72].
The illustrated behavior implies dramatic consequences on the magnetic phase diagram of a superconductor (Fig. 2.3): An applied field will partially exceed the critical values B_{C} or B_{C1} on the surface of the sample already at $(1-D)B_{\text{C}}$ and $(1-D)B_{\text{C1}}$, respectively. Hence, above these fields, the sample can no longer maintain a homogeneous Meissner state. The consequential variations of the phase diagrams of type-I, type-II/1 and type-II/2 superconductors are shown in Fig. 2.10 (a-c):
In type-I materials, the Meissner phase is already disturbed at $(1-D)B_{\text{C}}$, and a transition to the intermediate state (IS) takes place, which evolves into the normal conducting state at the critical field B_{C}. The IS is characterized by a coexistence of Meissner phase and normal conducting state in form of a magnetic domain structure.
The situation is similar in type-II/1 superconductors, where the intermediate mixed state emerges in fields $(1-D)B_{\text{C1}} < B < (1-D)B_{\text{C1}} + DB_0$. An explanation of these IMS phase boundaries is given in Ap. A.1. Similar to the IS, the IMS is characterized by a domain structure of Meissner and Shubnikov phases. The morphology and the theoretical fundamentals of the IS and IMS are extensively discussed in Sec. 2.3.

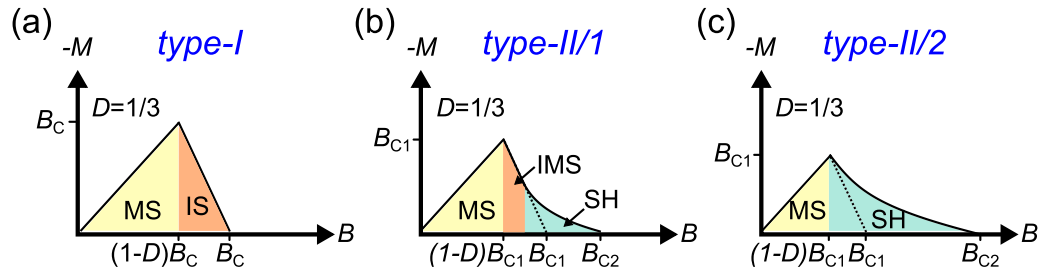

Figure 2.10.: Schematic magnetic phase diagrams for type-I, type-II/1 and type-II/2 superconductors if they are influenced by demagnetization effects. In contrast to the phase diagram shown in Fig. 2.3, the Meissner phase is already suppressed at $(1-D)B_C$ (type-I) and $(1-D)B_{C1}$ (type-II/1), respectively. Furthermore, in type-I materials, the MS-NS transition is accompanied by the emergence of an intermediate state (IS) while in type-II/1 superconductors an intermediate mixed state nucleates.

Finally, the impact of demagnetization is less pronounced in type-II/2 materials. Here, the transition from the Meissner to the Shubnikov phase is shifted to $(1-D)B_{C1}$, but only the slope of M for $B \geq (1-D)B_{C1}$ is decreased.

2.3. Domain nucleation in superconductors

It has been discussed in Sec. 2.2.5 that in samples having a non-zero demagnetization coefficient, the Meissner state (MS) is partially suppressed already in fields below the critical values B_C or B_{C1}. The reason for this behavior is the inhomogeneous field distribution at the sample surface. How the remaining Meissner phase is distributed within the sample is addressed in the following section. At first, it will be reasoned that a dispersion of the Meissner state in form of a domain structure is indeed the equilibrium configuration of the superconductor in the IS and IMS. Thereafter, the main theories on the IS domain structure will briefly be reviewed: The laminar model of Landau [74] (Sec. 2.3.2) and the hexagonal model of Goren and Tinkham [75] (Sec. 2.3.3). Afterwards, in Sec. 2.3.5, these models will be generalized to the case of the IMS. The goal will be to define the expected domain morphology and to set the limits for its typical length scales. In Sec. 2.3.6, the evolution of the IMS morphology and its interference by pinning is discussed based on molecular-dynamics simulations of the magnetic vortices. Finally, in Sec. 2.3.7, the IS and IMS nucleation is shortly discussed as a manifestation of a modulated phase which is caused by competing interactions.

2.3.1. Reasons for the domain nucleation in superconductors

At first glance, it seems reasonable to assume that the MS suppression will take place near the edges where the enhancement of the applied field is strongest. For a type-I superconductor, this situation is illustrated in Fig. 2.11 (a). However,

in the configuration shown, the outer field is still strongly distorted. The total energy of the system can further be reduced by a regular distribution of the normal conducting regions all over the sample, because this decreases the energy associated with the field distortion. Such a configuration is shown in Fig. 2.11 (b). As a similar fraction of the sample stays in the Meissner phase, the consumed condensation energy is equal in both cases (a) and (b). However, the spatial phase distribution of (b) requires the creation of multiple MS-NS interfaces whose energy has been estimated in Sec. 2.1.3. Hence, the emergence of a domain structure in the intermediate state is the consequence of an energy minimization between condensation, interface and field energy in samples with $D > 0$.

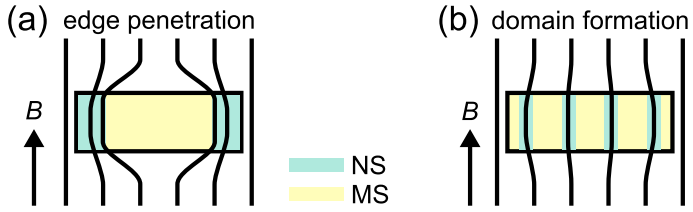

Figure 2.11.: Energy minimization via domain nucleation in superconductors with a non-zero demagnetization coefficient D. In the figure, the distribution of normal conducting regions within the sample is shown for a field slightly higher as $(1-D)B_{\mathrm{C}}$. The volume fraction of the normal conducting state (NS) is similar in (a) and (b). However, the formation of a domain structure (b) strongly reduces the disturbance of the applied field and lowers the total energy.

2.3.2. The Landau model

The IS domain structure has firstly been treated by Landau [38, 74]. He assumed an infinitely expanded plate of thickness t (larger than the magnetic penetration depth λ_{L}) in an applied magnetic field. The domain structure was supposed to consist of straight laminar regions of normal conducting phase embedded within the Meissner phase. An illustration of the domain structure in the Landau model is given in Fig. 2.12.
In the Landau model, the parameter describing the IS is the periodicity length a of the structure. It is given as the sum of the width of the normal conducting lamellae a_{n} and of the lamellae in the Meissner phase a_{s}:

$$a = a_{\mathrm{n}} + a_{\mathrm{s}} \ . \tag{2.25}$$

Since it is assumed that the field within the NS domains is B_{C}, the ratio of normal conducting regions at a specific applied field must amount to:

$$\frac{a_{\mathrm{n}}}{a} = \frac{B}{B_{\mathrm{C}}} \ . \tag{2.26}$$

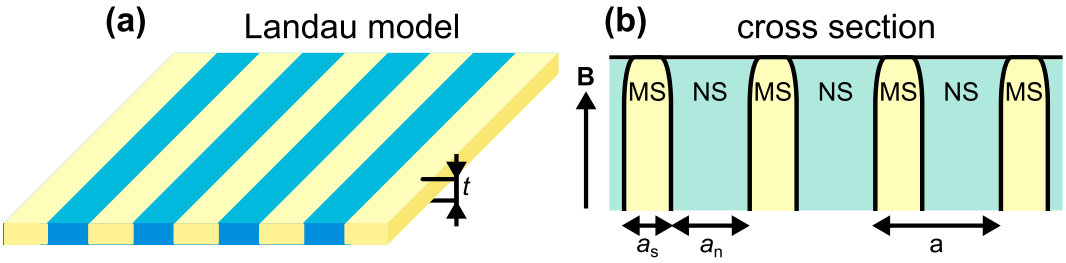

Figure 2.12.: Illustration of the Landau model. (a) The Landau model assumes a flat superconducting plate of thickness t in a perpendicular applied magnetic field $\boldsymbol{B}$. (b) The structure of the IS is given by an arrangement of NS and MS laminar domains of width a_n and a_s repeating on the distance a. It has been shown that a fanning of the NS domains near the surface further reduces the total energy of the IS.

The actual domain configuration is found by minimizing three energy contributions: (i) the interfacial energy between NS and MS domains, which prefers few large domains, (ii) the energy of the distorted magnetic field outside the sample, which favors many small domains, and (iii) the energy contribution arising due to a fanning of the NS domains near the surface that further advances smaller domains. Landau's derivation yields for the periodicity a [74]:

$$a = \left[\frac{\delta t}{f_\mathrm{L}\left(\frac{B}{B_C}\right)} \right] \ , \tag{2.27}$$

in which δ is the wall-energy parameter introduced in Sec. 2.1.3 and f_L is a numerical function tabulated in Ref. [76].
The Laudau model was later modified by assuming that the normal domains branch into several threads near the surface [29]. In this way, the outer field can be homogenized further, while the field within the NS domains is not strongly disturbed. It has been predicted that branching near the surface should occur for $t \geq 800\delta$ [38, 77].

2.3.3. The Goren-Tinkham model

A second model was introduced by Goren and Tinkham [75] in order to explain the observation of tubular magnetic domains within the IS [78]. Their model assumes a triangular arrangement of hexagonal normal conducting spots (diameter a_n) surrounded by Meissner phase. It is illustrated in Fig. 2.13 (a). The hexagonal spot structure is introduced as to guarantee close packing of the domains for high fields.
Again, the preferred repetition length a is found by minimizing the three energy contributions discussed in Sec. 2.3.2 with respect to a. However, this time, the

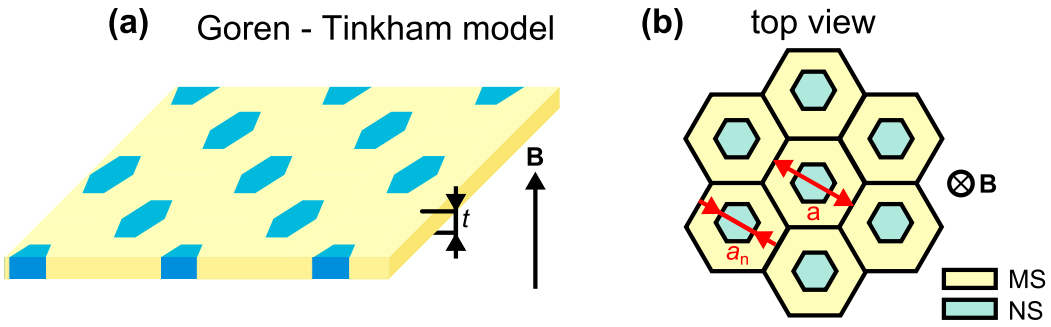

Figure 2.13.: Illustration of the Goren-Tinkham model. (a) This model assumes a flat superconducting plate of thickness t in a perpendicular applied magnetic field $\boldsymbol{B}$. (b) The structure of the IS is a triangular array of hexagonal normal conducting spots. Here, a_n is the diameter of the spots, while a is the repetition length of the pattern.

normal conducting ratio is given by:

$$\frac{a_\mathrm{n}}{a} = \sqrt{\frac{B}{B_\mathrm{C}}} \,, \tag{2.28}$$

since it is defined by an area $\propto a_\mathrm{n}^2$ and not by a distance as in the Landau model. Finally, minimizing the free energy results in:

$$a = \sqrt{\frac{2\delta t}{\frac{B}{B_\mathrm{C}}\left(1-\frac{B}{B_\mathrm{C}}\right)\left(1-\sqrt{\frac{B}{B_\mathrm{C}}}\right)}} \,. \tag{2.29}$$

2.3.4. Comparison of the models

The models of Landau and Goren-Tinkham clearly differ in their domain patterns. However, comparing the repetition lengths of the models, only small deviations exist. This is shown in Fig. 2.14, where the repetition length a of the domain structure (a) and the size of the normal conducting domains (b) is plotted against the reduced field B/B_C. For this graph, typical experimental parameters found for lead were used ($t = 1\,\mathrm{mm}$, $\delta = 55\,\mathrm{nm}$ [79]).
Clearly, the domain structure is coarser within the Landau model, but the differences vanish as the field approaches B_C, at which a diverges. At low inductions, though, a is distinctly smaller in the tubular Goren-Tinkham model. This suggests that a tubular domain structure as proposed by Goren and Tinkham is, at least in small fields, energetically preferred, since its field distortion is considerably smaller. Indeed, such a behavior has recently been predicted [80] and observed [19]. Nonetheless, it has already been mentioned in Ref. [75] that the energy difference between the two domain structures is marginal and not sufficient to unambiguously determine an equilibrium configuration. Hence, the domain structure is drastically influenced by small additional interactions as geometrical barriers (see Sec. 2.2.4)

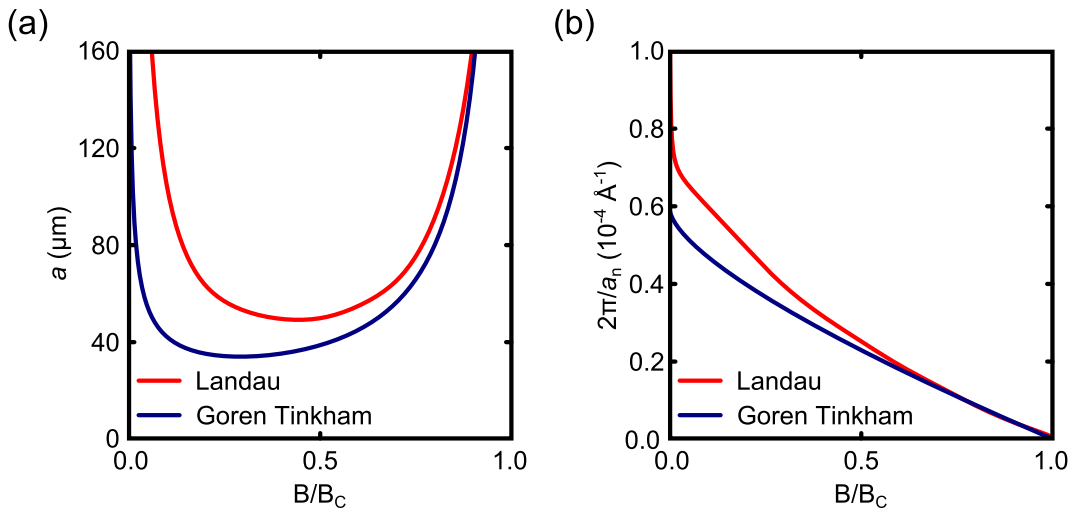

Figure 2.14.: Comparison of the domain repetition length and domain size according to the Landau and the Goren-Tinkham model. (a) Domain repetition length a as function of the normalized field B/B_C. (b) Inverse of the domain size as function of the reduced field. This reciprocal space representation corresponds to the information which can be gained by a neutron scattering experiment.

and pinning forces (see Sec. 2.2.3), which makes a modeling of the IS and IMS structures a difficult task. Additionally, this fact promotes complex phase diagrams of superconducting domain structures [80, 81]. An extensive discussion of this topic can be found in [82].
The consequences of the small energy difference between the Landau and the Goren-Tinkham models on the IS structure have been demonstrated e.g. in Ref. [19] by means of magneto-optical imaging on lead samples of different shapes. It has been found that the geometrical barriers in disc-shaped samples provoke a tubular (Goren-Tinkham) domain structure when the field is increased from the Meissner state, whereas a laminar (Landau) morphology is stabilized when the field is decreased from the normal conducting state. Corresponding data are depicted in Fig. 2.15.

2.3.5. Modification of the models for the IMS

The models introduced in Secs. 2.3.2 and 2.3.3 seem inapplicable to the intermediate mixed state as the wall-energy parameter is negative for type-II superconductors (Sec. 2.1.3). However, although δ was originally introduced to describe an NS-MS interface, a redefinition which allows the application of the two models on the IMS structure is possible [83, 84].

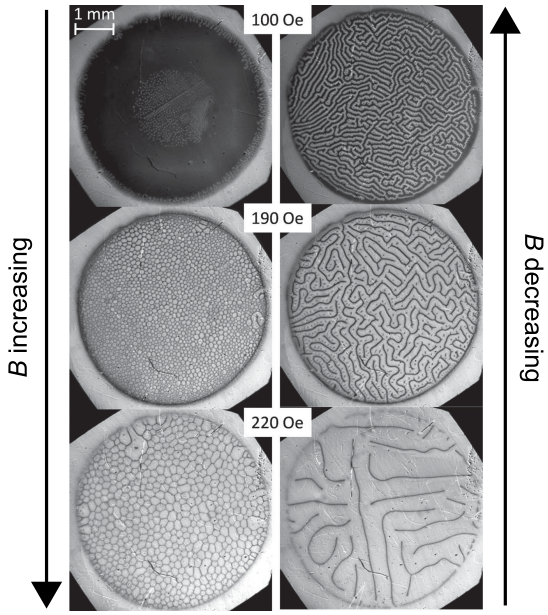

Figure 2.15.: Structure of the intermediate state in a disc-shaped Pb single crystal at 5 K. The left column shows magneto-optical images of the IS structure for increasing fields, while the situation for decreasing fields is depicted in the right column. Black regions correspond to the superconducting phase, whereas the sample is normal conducting in the bright regions. Reprinted figure with permission from [19] ©(2007) by the American Physical Society.

The wall-energy parameter

The wall-energy parameter which is associated to the surface tension γ via Eq. 2.13, can be defined as analogous to the calculation of the cleavage energy in a solid [85]. For this, consider the hexagonal vortex lattice illustrated in Fig. 2.16. If this two-dimensional lattice is split along a specific direction, one must expend the energy that is necessary to break all the vortex-vortex bonds along the cleavage. The surface tension of the generated interfaces is hence given by:

$$\gamma = \frac{1}{2}\frac{\text{Nr. of broken bonds} \times \text{energy per unit length of the bonds}}{\text{length of the interface}} \,. \quad (2.30)$$

The factor one half derives from the fact that a cut produces two interfaces. Moreover, this discussion only considers next nearest neighbor interactions. Using this redefinition of the surface tension, the wall-energy parameter can be defined as in Eq. 2.13 and be used with the models of Landau and Goren-Tinkham.
However, as the vortex lattice is strongly anisotropic, the interfacial energy will in general depend on the direction of the cleavage. Decoration images of the IMS confirm this assumption, as the domain boundaries form along specific directions within the lattice [7, 83].

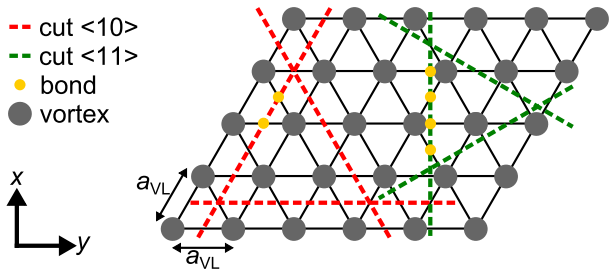

Figure 2.16.: Cutting through a vortex lattice. The sketched shows the top view on a hexagonal vortex lattice of lattice parameter a_{VL} as well as the cuts of lowest ($\langle 10\rangle$) and highest ($\langle 11\rangle$) interfacial energy. If the lattice would be split along the plotted lines, 2 ($\langle 10\rangle$) and $\frac{4}{\sqrt{3}}$ ($\langle 11\rangle$) bonds (yellow points) have to be broken per length a.

In order to estimate the effect of anisotropy on the surface tension, the cuts along the $\langle 10\rangle$ and $\langle 11\rangle$ directions, which are marked in Fig. 2.16, are considered. Using Eq. 2.30, their interfacial energy is determined to [84]:

$$\gamma_{\langle 10\rangle} = \frac{1}{2}\frac{2U_{\mathrm{bond}}}{a} = \frac{U_{\mathrm{bond}}}{a} \tag{2.31}$$

and

$$\gamma_{\langle 11\rangle} = \frac{1}{2}\frac{4U_{\mathrm{bond}}}{\sqrt{3}a} = \frac{2}{\sqrt{3}}\frac{U_{\mathrm{bond}}}{a} \approx 1.2\gamma_{\langle 10\rangle} \ , \tag{2.32}$$

respectively. U_{bond} is the energy per unit length of a single bond which can be estimated using the interaction potential given in Eq. 2.20. The cuts along $\langle 11\rangle$ and $\langle 10\rangle$ are distinguished, since the interfacial energy along them is maximal and minimal, respectively. The reason is, that if the vortex lattice is cut along an inclined angle to the $\langle 10\rangle$ direction, the resulting surface is vincinal and composed of $\{11\}$ planes with steps whose number increases with increasing inclination until a $\{10\}$ plane is reached. Hence, the surface tension increases with the inclination angle until a maximum is reached at 30° and the interfacial energy is reduced again. As this process repeats with 6-fold symmetry, the surface tension within a hexagonal vortex lattice must lie between the limiting values $\gamma_{\langle 11\rangle}$ and $\gamma_{\langle 10\rangle}$.
In a rough approximation, the wall-energy parameter can hence be supposed to be isotropic. It can be defined in a similar way as in Eq. 2.13:

$$\delta = \frac{2\mu_0\gamma_{\langle 10\rangle}}{B_0^2} \approx \frac{2\mu_0 U_{\mathrm{bond}}}{B_0^2 a_{\mathrm{VL}}} \ . \tag{2.33}$$

The magnetic field within the domains

For the IS structure, the induction within the normal conducting domains has been assumed to be B_{C}. In contrast, the field within the IMS domains corresponds

to the value B_0 which is connected to the vortex lattice parameter via:

$$a_{\mathrm{VL}} = \sqrt{\frac{2\Phi_0}{\sqrt{3}B_0}} \ . \tag{2.34}$$

Consequentially, the ratio $\frac{B}{B_C}$ in Eqs. 2.27 and 2.29 must be replaced by $\frac{B}{B_0}$ in order to obtain a sufficient description of the IMS structure.

Expansion for $D \neq 1$

The original models of Landau and Goren-Tinkham assume a slab shaped sample which is infinitely expanded perpendicular to the applied field ($D = 1$). This corresponds to a complete suppression of the Meissner state. In order to account for the IMS boundaries (see Ap. A.1) under realistic conditions ($D \neq 1$), the models can be generalized by replacing:

$$\frac{B}{B_0} \rightarrow \frac{B - (1-D)B_{\mathrm{C1}}}{DB_0} \tag{2.35}$$

in Eq. 2.27 and 2.29. This change considers the unsuppressed Meissner phase and guarantees a linear growth of the domain size ratio within the IMS, while it still includes the limit B/B_0 for $D = 1$. However, this simple expansion will only be valid as long as the influence of the sample edge can be neglected. Deviations might thus be expected for $D \ll 1$.

2.3.6. IMS formation as a self organization process of particles interacting through competing range interactions

Recently, the IMS structure has again gained a high interest, as similar complex vortex structures have been observed in superconducting MgB_2 [17]. As in type-II/1 superconductors, the deviations from the ideal hexagonal vortex lattice in MgB_2 have been attributed to the superposition of a short range repulsive and a long range attractive interaction. Although the physical reasons for the vortex attraction are different in MgB_2 and linked to two energy bands involved in the superconductivity, its observation has motivated a multitude of studies treating the alignment of partially attracting vortices [81, 86–90]. In all these studies, the evolution of the vortex structure was investigated by molecular-dynamics simulations.

In principle, such simulations start with a random arrangement of N vortices in a squared box where periodic boundary conditions are applied. In the following simulation loops, the forces acting on each individual vortex are calculated and translated into the vortex acceleration as well as into its velocity. The vortex lattice is then rearranged according to the velocities, and the reached vortex configuration is used as initial arrangement for another simulation loop. The

equation of motion of a vortex i is supposed to be [88]:

$$\eta \boldsymbol{v}_\mathrm{i} = \boldsymbol{F}_\mathrm{i} = \sum_{\mathrm{j}\neq\mathrm{i}} \boldsymbol{F}_\mathrm{ij} + \boldsymbol{F}_\mathrm{i}^\mathrm{p} + \boldsymbol{F}_\mathrm{i}^\mathrm{T} + \boldsymbol{f}_\mathrm{d} \ , \tag{2.36}$$

in which η is the Bardeen-Stephen friction coefficient [51], $\boldsymbol{F}_\mathrm{ij}$ is the interaction of the vortices i and j, $\boldsymbol{F}_\mathrm{i}^\mathrm{p}$ is the pinning force acting on the vortex, $\boldsymbol{F}_\mathrm{i}^\mathrm{T}$ is a temperature dependent thermal stochastic force, and $\boldsymbol{f}_\mathrm{d}$ is a potentially applied driving force. Usually, a vortex-vortex interaction as in Eq. 2.20 is assumed [86, 88, 90], but different types like hyperbolic repulsive and exponential attractive potentials have been used as well [81, 89, 91]. However, it has been stated in Ref. [81] that the results are in qualitative agreement for both types of interaction potentials. The stochastic force introduces random thermal fluctuations to the system, which drive the vortex arrangement out of metastable configurations.
Molecular-dynamics simulations can neither account for any demagnetizing effects, nor do they include the specific shape of the sample. Using this approach, the most stable vortex configuration in the absence of pinning is hence a single droplet [87]. Consequently, when predicting the IMS structure, molecular-dynamics simulations will fail in estimating the domain size and its repetition length. The multiple and non-local vortex interactions which should be treated within the Ginzburg-Landau theory are moreover oversimplified by the used point-like interaction potential.
Molecular-dynamics simulations are nonetheless very helpful in estimating the effects of pinning and thermal activation on the domain structure. Furthermore, the nucleation of the domains out of a regular or random vortex arrangement into a bundled configuration can solely be investigated by means of this method, since it allows to study the time evolution of the vortex formation [81]. For such processes, it can be assumed that the demagnetization effects are weak, since small shifts of the vortex positions do not distort the macroscopic field much outside of the sample. Hence, results of molecular dynamics simulations provide at least a hint to the microscopic behavior of the vortices which underlie the IMS domains.
Different works focused on the field and temperature dependence of the vortex alignment within the IMS [81, 90]. They have shown that for low inductions, the vortices will bundle in small bubbles, which are aligning in an ordered or random structure depending on the used interaction potential [81, 90]. In intermediate fields, the bubbles coalesce to elongated, more striped domains. Finally, for high applied fields, the vortices arrange in the hexagonal lattice configuration. A B-T-phase diagram deduced from molecular-dynamics simulations is shown in Fig. 2.17. Notice that a similar sequence of domain structures is expected within the IS [80].
The effect of pinning onto the vortex configuration has been explicitly treated in Ref. [87], [89] and [90]. They all reason that pinning strongly influences the domain structure: For few pinning centers, the surface of the vortex clusters and stripes gets fuzzier, and the domain shape becomes more irregular. Furthermore,

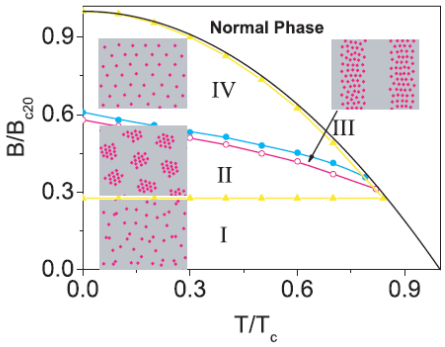

Figure 2.17.: Phase diagram of vortex matter as a function of field and temperature, deduced by molecular-dynamics simulations in the presence of pinning. Different vortex phases could be identified. A disordered phase (I), a hexagonally ordered superlattice (II), a superlattice of vortex stripes (III), and the usual hexagonal vortex lattice (IV). Reprinted figure with permission from [81]. Copyright (2016) by the American Physical Society.

a reduction of the cluster size has been deduced in Ref. [90], but has not been stated elsewhere. In the case of an increasing number of pinning sites, the domain structure finally breaks down, since the pinning prevents a bundling of the vortices [87, 89]. This behavior is shown in Fig. 2.18, in which the simulated equilibrium configuration of bubble and stripe domains is shown for an increasing amount of pinning centers. As seen from these calculations, pinning strongly affects the domain shape, and a high density of pinning centers can even prevent a nucleation of an IMS domain structure.

2.3.7. Concluding remark: IS and IMS nucleation as a pattern formation problem

The considerations of this section on domain nucleation in the IS and IMS seem very unique to superconductors at first glance. However, they can be put into a wider and more general framework as manifestation of modulated phases caused by competing interactions [18]. From this viewpoint, domain nucleation is always caused by a competition of interactions that favors a homogeneous ground state with nonlocal interactions that prefer spatial variation. While the surface tension and the energy associated with the field distortion, are the source of competition in superconductors, diverse interactions can cause similar behavior in other systems (best known might be the interplay of domain wall and stray field energy in ferromagnets [92]). A comprehensive listing can be found in Ref. [18].
As a main consequence of competing interactions, the free energy of the systems exhibits a minimum for a finite repetition length, independent of the particular type of interactions. The periodicity of the pattern is generally controlled by

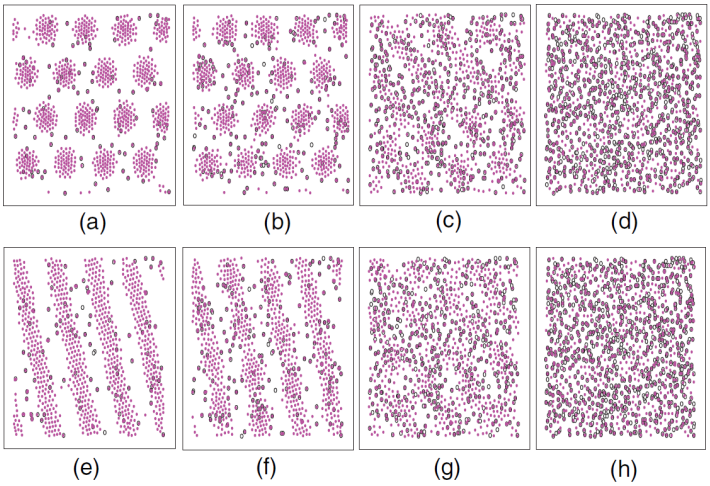

Figure 2.18.: Effects of pinning on the IMS structure, deduced from molecular-dynamics simulations. In the top row, a position in the phase diagram (2.17) of a tubular equilibrium configuration was studied, while the simulations in the bottom row applied parameters leading to a laminar phase. The density of pinning centers (black open circles) increases from left to right. The vortices are shown as magenta, solid circles. In both cases, pinning strongly smears the ordered vortex superstructure and finally leads to a disappearance of the IMS domains. Reprinted figure with permission from [89]. Copyright (2016) by the American Physical Society.

the ratio of competing interactions. However, it turned out that the developed domain pattern can mostly be classified as generic bubble, laminar, or dendritic structures (see Ref. [18] and references within). All these morphologies have been reported for the IS and IMS structure. However, as extensively discussed in this chapter, domains in superconductors stand out due to the fact that the competing interactions can be tuned in strength. This can either be achieved by a variation of the field and temperature (Sec. 2.1.3 and 2.3.5), a modification of the sample shape (Sec. 2.2.4), a variation of material parameters (Sec. 2.1), or by the introduction of disorder (Sec. 2.2.3). A detailed investigation of the IS and IMS structure therefore allows to address several question of general significance: (i) the evolution of the patterns during the domain nucleation, (ii) the metamorphose of the different domain morphologies, (iii) the influence of fixed boundary conditions on the domain nucleation, and (iv) the reaction of the systems to arbitrary types of disorder.

2.4. Similarities of the vortex lattice to the skyrmion lattice in MnSi

A skyrmion lattice is a non-trivial magnetic structure which has firstly been identified in the itinerant helimagnet MnSi [93]. This novel type of magnetic ordering has recently received strong interest, since it has been established in various systems, e.g. in different other members of the B20 crystal structure family [94, 95], in centrosymmetric ferromagnets with uniaxial anisotropy [96], or on surfaces of ferromagnetic monolayers [97]. For this thesis, skyrmions in chiral magnets are of interest, since they show a topological similarity to the vortex lines found in type-II superconductors that will be discussed below.

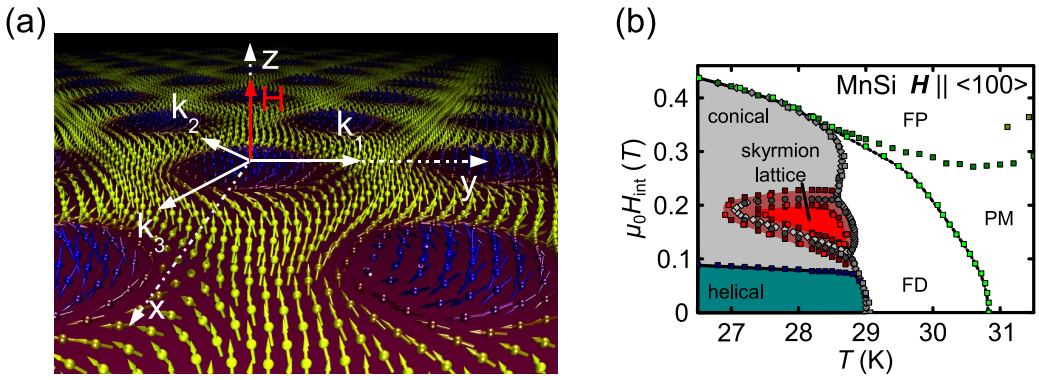

Figure 2.19.: The skyrmion lattice in MnSi. (a) Real space depiction of the spin crystal in a plane perpendicular to the magnetic field H. Taken from [98], with permission from S. Mühlbauer. (b) Magnetic phase diagram of MnSi. Below the critical temperature T_C, magnetic ordering arises. In zero field, a helical ground state is formed. In increasing applied fields, it successively transforms into a conical and finally into a ferromagnetic state (FP). Near the transition temperature, the A-phase is formed that is characterized by emergence of a skyrmion lattice. Data with courtesy of A. Bauer.

A graphical representation of the skyrmion lattice in MnSi is shown in Fig. 2.19 (a): Skyrmions can be considered as whirls in the local magnetization of the material, which are translationally invariant along the applied field. The structure of the skyrmion lattice can be described as a superposition of three helical spin modulations under 120°, aligned perpendicular to the magnetic field [99]. This spin alignment is accompanied by a topological winding number of $\Phi_w = -1$, which means that a skyrmion cannot be continuously transformed into a more trivial ferromagnetic or helical spin structure and is hence topologically protected [93]. Due to this stability, skyrmions possess particle-like properties similar to the

vortices in superconductors[1]. Like the flux line lattice, the skyrmion lattice is a two dimensional structure which can arise in various different symmetries [101], and is affected by pinning interactions as well as demagnetizing effects. Moreover, both lattices introduce a periodic modulation to the local magnetization of the sample. When using scattering methods that probe the local magnetic scattering length density contrast, similar results are obtained for the skyrmion and the vortex lattice.

The formation of a skyrmion lattice is caused by a competition of different interactions which is further examined on the example of MnSi: The magnetic structure of MnSi is determined by three hierarchical energy scales: (i) a strong ferromagnetic exchange, (ii) an intermediate Dzyaloshinskii-Moriya (DM) interaction, and (iii) a weak crystalline field interaction [93]. These interactions induce a complex magnetic phase diagram which is shown in Fig. 2.19 (b): As the ferromagnetic exchange and the DM interaction favor parallel and perpendicular alignment of neighboring spins, respectively, the ground state is given by a helical alignment of the magnetic moments. It is denominated as the helical state. However, due to the considerably stronger ferromagnetic exchange, these helices have a wavelength of $\lambda_{\mathrm{h}} = 18\,\mathrm{nm}$, which is much larger than the atomic lattice parameter. Finally, the crystal field interaction initially pins the direction of propagation of the helices to the $\langle 111 \rangle$-directions.

In an applied field, the directional degeneration of the helical modulation is firstly removed, as it is unpinned from the $\langle 111 \rangle$-axis. In the conical state above H_{C1}, the helices begin to align in direction of the applied field, forming a conical spin alignment until a ferromagnetic phase is stabilized in fields above H_{C2}.

Finally, the skyrmion lattice is formed in a small phase pocket close to the transition temperature of 29.5 K in fields between 100 and 200 mT, named the A-phase. In this region, the normally metastable skyrmion structure [102] is stabilized, since thermal fluctuations suppress its energy below that of the conical state [93]. Hence, the A-phase is a distinct thermodynamic phase which is separated from the conical state by a first-order phase transition.

1 Indeed, a systematic manipulation of single skyrmions has been demonstrated recently, which provides the possibility to use skyrmions as bits for data storage [100].

3. Theoretical fundamentals of neutron imaging and scattering

The formulas which are necessary to interpret neutron data obtained at superconducting domain structures will be derived in this chapter. Since the micrometer length scale of the domains strongly exceeds the neutron wavelength of a few angstrom, scattering takes place primarily under small angles. This imposes special requirements on the instrumental design, which will be discussed in Chap. 4, but also changes the theoretical treatment of the scattering process. Therefore, starting from the fundamental interactions of neutrons and matter (Sec. 3.1), the differential and total scattering cross-sections are introduced and extended to describe forward scattering (Sec. 3.2). Finally, the differential scattering cross-section is linked to a real space correlation function of the scattering length density and a geometrical explanation is given for both (Sec. 3.2.6). Only the derived relations allow for a quantitative description of (ultra-) small-angle neutron scattering data and neutron grating interferometry results in a common theoretical framework and hence enable their combined interpretation presented in this thesis. At the end of this chapter, the differential scattering cross-section of the superconducting vortex lattice is derived.

3.1. The interaction of neutrons and matter

The wave properties of the neutron (mass $m = 1.675 \times 10^{-27}\,\mathrm{kg}$ [103]) and its interaction with matter are described by the stationary Schroedinger Equation:

$$E\Psi(\boldsymbol{k},\boldsymbol{r}) = \left[-\frac{\hbar^2}{2m}\nabla^2 + V(\boldsymbol{r})\right]\Psi(\boldsymbol{k},\boldsymbol{r}) \tag{3.1}$$

which is a scalar wave equation for the wave function Ψ of the particle with energy E. As neutrons are neutral particles, their interaction with matter is not an electrostatic Coulomb interaction with the electron shell or the positively charged cores. Instead, neutrons essentially interact with the nuclei via the strong nuclear force or via magnetic interactions within the material. The first interaction is well described by the point-like Fermi pseudo-potentials at positions $\boldsymbol{r}_\mathrm{i}$:

$$V_\mathrm{nuc}(\boldsymbol{r}) = \frac{2\pi\hbar^2}{m}\sum_{\mathrm{i}=1}^{N} b_\mathrm{i}\delta(\boldsymbol{r}_\mathrm{i}) \tag{3.2}$$

in which b_i is the scattering length of the nuclei at position $\boldsymbol{r}_\mathbf{i}$ [104]. This approximation is valid as the wavelength λ of the considered thermal and cold neutrons is much larger than the interaction range of the strong nuclear force.
The magnetic interaction between the magnetic dipole moment $\boldsymbol{\mu}$ of the neutron and an internal or external magnetic field $\boldsymbol{B}$ is expressed by the Zeeman interaction:

$$V_\mathrm{mag}(\boldsymbol{r}) = -\boldsymbol{\mu} \cdot \boldsymbol{B}\,(\boldsymbol{r}) \ . \tag{3.3}$$

The nuclear and magnetic interactions lead to absorption, refraction and scattering of a neutron beam within a sample, which will be discussed below. Other interactions like spin-orbit interactions and gravitational forces occur as well, but can be neglected in most cases, due to their weak interaction potential.

3.1.1. Neutron absorption and refraction

In free space ($V = 0$), the solution of the Schroedinger Eq. 3.1 is a plane wave $\Psi \propto \exp(\mathrm{i}kx)$ with wavevector:

$$k^2 = \frac{2mE}{\hbar^2} \ . \tag{3.4}$$

However, the wavevector is modified under the influence of an interaction potential:

$$K(\boldsymbol{r})^2 = \frac{2m\left[E - V\,(\boldsymbol{r})\right]}{\hbar^2} \ . \tag{3.5}$$

Hence, in analogy to classical optics, an index of refraction n can be defined as [104]:

$$n(\boldsymbol{r}) = \frac{K(\boldsymbol{r})}{k} = \sqrt{\left[1 - \frac{V\,(\boldsymbol{r})}{E}\right]} \ . \tag{3.6}$$

This index of refraction describes the change of the neutron wave function within a material and is used to quantify neutron refraction and absorption.
To find an expression for the neutrons' index of refraction within a sample, the interaction potential has to be averaged over a macroscopic ensemble of nuclei with density N. For the Fermi pseudo-potential (Eq. 3.2), this results in:

$$\overline{V}_\mathrm{nuc} = \frac{2\pi\hbar^2}{m}\bar{b}N \ , \tag{3.7}$$

while an averaging of the magnetic interaction yields [104]:

$$\overline{V}_{\mathrm{mag}} = \pm \mu B \ , \tag{3.8}$$

because the neutron spin of $\frac{1}{2}$ allows only two possibilities for its orientation to the magnetic field: parallel and anti-parallel.
Finally, the scattering length defined in Eq. 3.2 is not a real, but a complex number. The index of refraction is therefore composed of the nuclear δ_{nuc} and magnetic real part δ_{mag} which are responsible for refraction, and an imaginary part β describing neutron attenuation:

$$n \approx 1 - \frac{1}{2}\frac{V}{E} = 1 - \delta_{\mathrm{nuc}} + \delta_{\mathrm{mag}} + \mathrm{i}\beta \tag{3.9}$$

$$= 1 - \frac{b_{\mathrm{c}} N \lambda^2}{2\pi} \pm \frac{m\lambda^2}{h^2}\mu B + \mathrm{i}\frac{\left(\sigma_{\mathrm{abs}} + \sigma_{\mathrm{inc}}\right) N\lambda}{4\pi} \ . \tag{3.10}$$

Here, $b_{\mathrm{c}} = \overline{b}$ is the coherent scattering length, while σ_{abs} and σ_{inc} are the absorption and the incoherent scattering cross-section per atom, respectively [104].
By means of the definitions derived above, the modulation of an initial neutron wave function Ψ_{i} within a sample of thickness t can be described entirely. In the absence of a magnetic field, the final state Ψ_{f} is given by:

$$\Psi_f = \exp\left(-\mathrm{i}k\delta_{\mathrm{nuc}}t\right) \exp\left(-k\beta t\right) \Psi_i \ . \tag{3.11}$$

Hence, the neutron phase is shifted by:

$$\Delta\Phi = -\lambda N b_{\mathrm{c}} t \ , \tag{3.12}$$

while the intensity is reduced according to the Lambert-Beer law, leading to a neutron transmission T:

$$T = \frac{I_{\mathrm{f}}}{I_{\mathrm{i}}} = \left|\frac{\Psi_{\mathrm{f}}}{\Psi_{\mathrm{i}}}\right|^2 = \exp\left[-\left(\sigma_{\mathrm{abs}} + \sigma_{\mathrm{inc}}\right) N t\right] \ . \tag{3.13}$$

The modulation of the neutron wave function within a sample is sketched in Fig. 3.1.

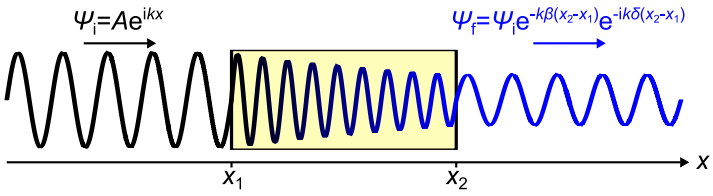

Figure 3.1.: Illustration showing the modulation of the neutron wave function within a sample (yellow). The final wave function is phase shifted and degraded according to Eqs. 3.12 and 3.13.

3.2. Description of the scattering process

Besides refraction and absorption, a neutron beam can be scattered off the sample. In the following part, it will be explained how structural information about the interior of the sample can be deduced from the angular distribution of the scattered intensity. The scattering process is sketched in Fig. 3.2: A neutron with wavevector $\boldsymbol{k_i}$ and wave function Ψ_i is scattered at an arbitrary structure defined by a non-zero interaction potential $V(\boldsymbol{r}) \neq 0$.

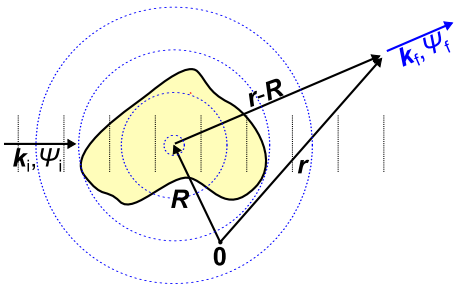

Figure 3.2.: Illustration of the scattering process. An incoming neutron Ψ_i is scattered by the potential at position $\boldsymbol{R}$. In first-order approximation, the outgoing wave Ψ_f is a superposition of the initial plane wave with a spherical wave, emanated from $\boldsymbol{R}$.

Again, the final state of the neutron Ψ_f is described by the stationary Schroedinger equation 3.1, and the incoming neutron can be described as plane wave $\Psi_\mathrm{i} \propto \exp(\boldsymbol{k_i} \cdot \boldsymbol{r})$. The solution of the scattered wave function is given by the Lippmann-Schwinger equation [105]:

$$\Psi_\mathrm{f}(\boldsymbol{k_f},\boldsymbol{r}) = \Psi_\mathrm{i}(\boldsymbol{k_i},\boldsymbol{r}) - \frac{m}{2\pi\hbar^2}\int \frac{\exp(\mathrm{i}k_\mathrm{f}|\boldsymbol{r}-\boldsymbol{R}|)}{|\boldsymbol{r}-\boldsymbol{R}|} V(\boldsymbol{R})\Psi_\mathrm{f}(\boldsymbol{k_f},\boldsymbol{R})\,d\boldsymbol{R}\ . \quad (3.14)$$

This equation can be solved iteratively by a successive inserting of $\Psi_\mathrm{f}(\boldsymbol{k_f},\boldsymbol{r})$ into the right hand side of Eq. 3.14. However, in most cases, this expansion can be interrupted after the first integral term, which leads to the Born approximation

for Ψ_f. For $|\boldsymbol{r}| >> |\boldsymbol{R}|$, this approximation yields:

$$\Psi_\mathrm{f}\left(\boldsymbol{k_f},\boldsymbol{r}\right) = \exp\left(\mathrm{i}\boldsymbol{k_i}\cdot\boldsymbol{r}\right) + \frac{\exp\left(\mathrm{i}\boldsymbol{k_f}\cdot\boldsymbol{r}\right)}{r} f(\boldsymbol{q}) \ . \tag{3.15}$$

Most scattering experiments can be evaluated within the Born approximation, even though it does not account for multiple scattering.
The introduced scattering amplitude $f(\boldsymbol{q})$ depends on the momentum transfer $\boldsymbol{q} = \boldsymbol{k_f} - \boldsymbol{k_i}$ of the neutron and is derived as the Fourier transform of the interaction potential:

$$f(\boldsymbol{q}) = -\frac{m}{2\pi\hbar^2}\int V\left(\boldsymbol{R}\right)\exp\left(-\mathrm{i}\boldsymbol{q}\cdot\boldsymbol{R}\right)d\boldsymbol{R} \ . \tag{3.16}$$

The scattered wave is approximately given as the superposition of the incident plane wave and a spherical wave, weighted by $f(\boldsymbol{q})$.

3.2.1. The differential and total scattering cross-section

A neutron scatting experiment, as e.g. small-angle neutron scattering, measures the differential scattering cross-section $d\sigma/d\Omega$ of the sample, which is defined by [106]:

$$d\sigma = \frac{\text{Number of neutrons deflected into } d\Omega}{\text{Number of incoming neutrons per unit area}} = |f(\boldsymbol{q})|^2\, d\Omega \ . \tag{3.17}$$

The measured differential cross-section of a neutron scattering experiment is hence related to the Fourier transform of the interaction potential. The total scattering cross-section is obtained by integration over all solid angles:

$$\sigma_\mathrm{tot} = \int \frac{d\sigma}{d\Omega} d\Omega \ . \tag{3.18}$$

Coherent and incoherent scattering cross-section

For pure nuclear scattering at N nuclei, the differential cross-section (Eq. 3.17) results from the Fermi pseudo-potential (Eq. 3.2):

$$\frac{d\sigma(\boldsymbol{q})}{d\Omega} = |f(\boldsymbol{q})|^2 = \sum_{\mathrm{i}=1}^{N}\sum_{\mathrm{j}=1}^{N} b_\mathrm{i} b_\mathrm{j} \exp\left[\mathrm{i}\boldsymbol{q}\cdot\left(\boldsymbol{r_i} - \boldsymbol{r_j}\right)\right] \ . \tag{3.19}$$

Any regular arrangement of the nuclei will result in a regular (coherent) scattering pattern. However, in a realistic situation, the scattering lengths can randomly differ, which disturbs this regularity. The deviations in b can either be caused by different spin configurations or different isotopes located at $\boldsymbol{r_i}$. In this case, the above potential can be split into the coherent part and its irregular deviations by

a fragmentation of b_i into its mean value $\overline{b} = b_\mathrm{c}$ and its fluctuation Δb_i. Therefore, the differential scattering cross-section is derived as:

$$\frac{d\sigma(\boldsymbol{q})}{d\Omega} = \overline{b} \sum_{\mathrm{i,j}=1}^{N} \langle \exp\left[\mathrm{i}\boldsymbol{q} \cdot (\boldsymbol{r_\mathrm{i}} - \boldsymbol{r_\mathrm{j}})\right] \rangle + \sum_{\mathrm{i,j}=1}^{N} (\Delta b_\mathrm{i})^2 = \left[\frac{d\sigma(\boldsymbol{q})}{d\Omega}\right]_\mathrm{coh} + \left[\frac{d\sigma(\boldsymbol{q})}{d\Omega}\right]_\mathrm{inc} , \quad (3.20)$$

where $\langle ... \rangle$ represents the averaging over the ensemble [107]. Hence, the measured differential scattering cross-section splits into a coherent part, producing a scattering pattern and an incoherent contribution which provides a constant background signal in all solid angles.

3.2.2. The scattering length density and its autocorrelation function

This thesis covers structures, whose sizes lie in the range of some 0.01 to 10 µm. The definition of the differential scattering cross-section via a discrete set of Fermi pseudo-potentials (Eq. 3.2) is therefore no longer reasonable. Instead, the scattering length density ρ is introduced which is the total scattering length per unit volume. Its spatial variation is expressed as scattering length density distribution $\rho(\boldsymbol{r})$. By using this definition, the differential scattering cross-section can be rearranged to:

$$\frac{d\sigma(\boldsymbol{q})}{d\Omega} = \left| \int_\mathrm{V} \rho(\boldsymbol{R}) \exp\left(-\mathrm{i}\boldsymbol{q} \cdot \boldsymbol{R}\right) d\boldsymbol{R} \right|^2 \quad (3.21)$$

$$= \int_\mathrm{V} \int_\mathrm{V} \rho(\boldsymbol{R})^* \rho(\boldsymbol{R_2}) \exp\left[-\mathrm{i}\boldsymbol{q} \cdot (\boldsymbol{R_2} - \boldsymbol{R})\right] d\boldsymbol{R} d\boldsymbol{R_2} \quad (3.22)$$

$$= \int_\mathrm{V} \left[\int_\mathrm{V} \rho(\boldsymbol{R})^* \rho(\boldsymbol{R} + \boldsymbol{r}) d\boldsymbol{R} \right] \exp\left(-\mathrm{i}\boldsymbol{q} \cdot \boldsymbol{r}\right) d\boldsymbol{r} \ . \quad (3.23)$$

The * denotes complex conjugation, as the definition implicitly includes the possibility that ρ is a complex number. Furthermore, the relation $\boldsymbol{R_2} - \boldsymbol{R} = \boldsymbol{r}$ has been used in Eq. 3.23. The term in square brackets is the autocorrelation function of the scattering length density distribution, often denoted as Patterson function.

3.2.3. The autocorrelation function of the scattering contrast

Only isolated particles were considered so far. However, in most cases, the investigated structures are not surrounded by vacuum, but by a second phase or a solvent having a different scattering length density. For a given scattering length density distribution, the scattering length contrast $\Delta\rho$ is thus defined as:

$$\Delta\rho(\boldsymbol{r}) = \rho(\boldsymbol{r}) - \overline{\rho} \ , \quad (3.24)$$

in which $\overline{\rho}$ is the mean value of $\rho\,(\boldsymbol{r})$. If this definition is inserted into Eq. 3.23, the differential cross-section as function of the scattering contrast is derived:

$$\frac{d\sigma(\boldsymbol{q})}{d\Omega} = \int\limits_{\mathrm{V}} \left[\int\limits_{\mathrm{V}} \Delta\rho(\boldsymbol{R})\Delta\rho(\boldsymbol{R}+\boldsymbol{r}) d\boldsymbol{R} \right] \exp\left(-\mathrm{i}\boldsymbol{q}\cdot\boldsymbol{r}\right) d\boldsymbol{r} \tag{3.25}$$

$$= \int\limits_{V} \gamma\left(\boldsymbol{r}\right) \exp\left(-\mathrm{i}\boldsymbol{q}\cdot\boldsymbol{r}\right) d\boldsymbol{r}\ . \tag{3.26}$$

Here, the inner integral can be identified as the autocorrelation function of the scattering length density contrast:

$$\gamma\left(\boldsymbol{r}\right) = \int\limits_{V} \Delta\rho(\boldsymbol{R})\Delta\rho(\boldsymbol{R}+\boldsymbol{r}) d\boldsymbol{R}\ . \tag{3.27}$$

From the perspective of the scattering length density contrast, the measured intensity at the detector is simply the Fourier transformation of its correlation function. Its geometrical interpretation is given in Sec. 3.2.6.

3.2.4. Quantities measured by scattering off large objects

In this section, the relations introduced above will be developed to the quantities which are measured by means of the neutron techniques (ultra-)small-angle scattering and grating interferometry which all analyze scattering in forward direction. Accordingly, the small-angle-approximation $\sin\vartheta \approx \tan\vartheta \approx \vartheta$ is used in what follows.
Without loss of generality, the neutron beam can be directed along the z-axis, which leads to $q_z = 0$ in this approximation. The differential cross-section might henceforth be rearranged to:

$$\frac{d\sigma(q_{\mathrm{x}},q_{\mathrm{y}},0)}{d\Omega} = \int\limits_{\mathrm{V}} \gamma\left(\boldsymbol{r}\right) \exp\left[-\mathrm{i}\left(q_{\mathrm{x}}x + q_{\mathrm{y}}y\right)\right] d\boldsymbol{r} \tag{3.28}$$

$$= \int\limits_{\mathrm{x,y}} G\left(x,y\right) \exp\left[-\mathrm{i}\left(q_{\mathrm{x}}x + q_{\mathrm{y}}y\right)\right] dxdy\ . \tag{3.29}$$

The introduced $G(x,y)$:

$$G(x,y) = \int\limits_{-\infty}^{\infty} \gamma\left(x,y,z\right) dz \tag{3.30}$$

is the projection of the autocorrelation function in beam direction. Its inverse is given by:

$$G(x,y) = \frac{1}{4\pi^2} \int\limits_{q_\mathrm{x},q_\mathrm{y}} \frac{d\sigma(q_\mathrm{x},q_\mathrm{y},0)}{d\Omega} \exp\left[\mathrm{i}\left(q_\mathrm{x}x + q_\mathrm{y}y\right)\right] dq_\mathrm{x} dq_\mathrm{y} \ . \tag{3.31}$$

By means of these definitions, the total scattering cross-section of Eq. 3.18 can be rearranged to:

$$\sigma_\mathrm{tot} = \int \frac{d\sigma(q_\mathrm{x},q_\mathrm{y},0)}{d\Omega} d\Omega = \frac{\lambda^2}{4\pi^2} \int\limits_{q_\mathrm{x},q_\mathrm{y}} \frac{d\sigma(q_\mathrm{x},q_\mathrm{y},0)}{d\Omega} dq_\mathrm{x} dq_\mathrm{y} = \lambda^2 G(0,0) \ . \tag{3.32}$$

At the first equality, $d\Omega = \frac{\lambda^2}{4\pi^2} dq_\mathrm{x} dq_\mathrm{y}$ was introduced.
An integration of Eq. 3.28 in y-direction results in the slit-smeared differential scattering cross-section $\left(\frac{d\sigma}{d\Omega}\right)_\mathrm{slit}$, which is given by:

$$\left(\frac{d\sigma(q_\mathrm{x})}{d\Omega}\right)_\mathrm{slit} = \int\limits_{-\infty}^{\infty} \frac{d\sigma(q_\mathrm{x},q_\mathrm{y})}{d\Omega} dq_\mathrm{y} \tag{3.33}$$

$$= 2\pi \int\limits_{-\infty}^{\infty} G(x,0) \exp\left(-iq_\mathrm{x}x\right) dx \ . \tag{3.34}$$

Its back transform results in the correlation function $G(x)$ and is given as:

$$G(x) = G(x,0) = \frac{1}{4\pi^2} \int\limits_{-\infty}^{\infty} \int\limits_{-\infty}^{\infty} \frac{d\sigma(q_x,q_y,0)}{d\Omega} dq_y \exp\left(iq_x x\right) dq_x \tag{3.35}$$

$$= \frac{1}{4\pi^2} \int\limits_{-\infty}^{\infty} \left(\frac{d\sigma(q_x)}{d\Omega}\right)_\mathrm{slit} \exp\left(iq_x x\right) dq_x \ . \tag{3.36}$$

In Chap. 4, it will be shown that the differential scattering cross-section (Eq. 3.28), the slit-smeared differential scattering cross-section (Eq. 3.33), and the correlation function (Eq. 3.31) are the quantities measured by small-angle neutron scattering (SANS), ultra-small-angle neutron scattering (USANS) and neutron grating interferometry (nGI), respectively. Therefore, the derived relations mutually link the results of these methods via different integrations and Fourier transformations, which are illustrated in the circle of SANS methods shown in Fig. 3.3 (a). The validity of these relations will be proven in Chap. 6.

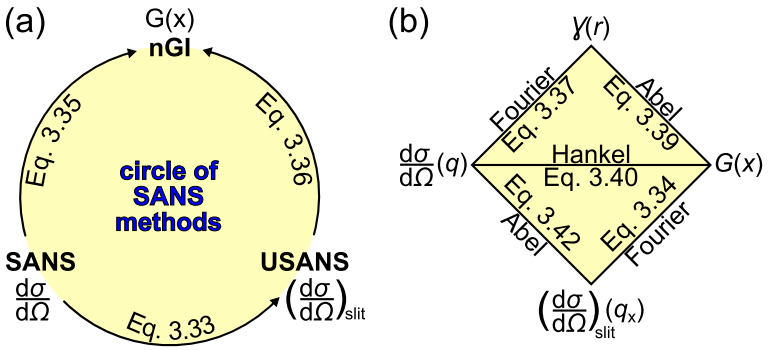

Figure 3.3.: Correlation of the different SANS methods. (a) Illustration showing how the quantities measured by SANS, USANS and nGI are mutually connected in the general case. (b) The relations of γ, $G(x)$,$d\sigma/d\Omega$ and $(d\sigma/d\Omega)_{\mathrm{slit}}$ for an isotropic scatterer.

3.2.5. Approximation of an isotropic scattering length density distribution

In the case of an isotropic scattering length density distribution, $\gamma(\boldsymbol{r})$ only depends on the modulus of $\boldsymbol{r}$. The radial symmetry is transferred to the differential scattering cross-section (Eq. 3.28), and reduces the three-dimensional integration to a one-dimensional [108]:

$$\frac{d\sigma(q)}{d\Omega} = 4\pi \int_0^\infty \frac{\sin(qr)}{qr}\gamma(r)r^2 dr \ . \tag{3.37}$$

The sinc function in the equation above results from the orientational averaging of the exponential function in Eq. 3.28. The inverse transformation is given by [108]:

$$\gamma(r) = \frac{1}{2\pi^2}\int_0^\infty \frac{\sin(qr)}{qr}\frac{d\sigma(q)}{d\Omega}q^2 dq \ . \tag{3.38}$$

The correlation function G (Eq. 3.30) can be expressed as an Abel transformation of γ :

$$G(x) = \int_{-\infty}^{\infty} \gamma(x,0,z)\,dz = 2\int_0^\infty \gamma(x,0,z)\,dz = 2\int_x^\infty \frac{\gamma(r)r}{\sqrt{r^2-x^2}}dr \ . \tag{3.39}$$

To establish a connection between $\frac{d\sigma(q)}{d\Omega}$ and $G(x)$, the Fourier-Hankel-Abel cycle can be used. It states that the two-dimensional Fourier transform of an Abel transform is the zeroth order Hankel transform. Hence, $G(x)$ and $\frac{d\sigma}{d\Omega}(q)$ are related

via [108]:

$$G(x) = \frac{1}{2\pi} \int_0^\infty J_0(qx) \frac{d\sigma(q)}{d\Omega} q dq \tag{3.40}$$

$$\frac{d\sigma(q)}{d\Omega} = 2\pi \int_0^\infty J_0(qx) G(x) x dx \ , \tag{3.41}$$

in which J_0 is the zeroth-order Bessel function of the first kind.
At last, the slit-smeared differential scattering cross-section is derived in terms of $\frac{d\sigma(q)}{d\Omega}$:

$$\left(\frac{d\sigma(q_\mathrm{x})}{d\Omega}\right)_\mathrm{slit} = 2 \int_0^\infty \frac{d\sigma}{d\Omega}\left(\sqrt{q_\mathrm{x}^2 + q_\mathrm{y}^2}\right) dq_\mathrm{y} = 2 \int_{q_\mathrm{x}}^\infty \frac{q}{\sqrt{q^2 - q_\mathrm{x}^2}} \frac{d\sigma(q)}{d\Omega} dq \tag{3.42}$$

which results again as an Abel transform of $\frac{d\sigma(q)}{d\Omega}$.
In summary, for an isotropic scatterer, the real space correlation functions γ and $G(x)$ are mutually connected by an Abel transformation, while they are linked to the differential scattering cross-sections by a Fourier transformation (see Fig. 3.3 (b)).

3.2.6. Interpretation of γ, $G(z)$, and $d\sigma/d\Omega$ using the example of diluted spheres

In this section, a geometrical interpretation of the correlation functions introduced in Sec. 3.2.4 is given for the case of diluted hard spheres. Although this particular example is one of the simplest, it illustrates the physical meaning of the correlation functions and their interpretation in general. For sake of simplicity, the scattering length contrast between particles and solvent is set to one.
For strongly diluted particles, most of the sample will consist of the solvent. Hence, the scattering length contrast of Eq. 3.24 can be approximated by:

$$\Delta\rho(r) = \begin{cases} 1 & r < R \\ 0 & \text{otherwise} \end{cases} \tag{3.43}$$

In this case, γ is derived as [109]:

$$\gamma(r) = \frac{4}{3}\pi R^3 \begin{cases} 1 - \frac{3}{4}\frac{r}{R} + \frac{1}{16}\left(\frac{r}{R}\right)^3 & r < 2R \\ 0 & \text{otherwise} \end{cases} \tag{3.44}$$

in which R is the radius of the spheres.
Clearly, $\gamma(0)$ corresponds to the volume of the particles. For $r > 0$, $\gamma(r)$ matches the volume of intersection of two spheres whose centers are separated by the distance r. As soon as the inter-particle distance reaches the diameter of the sphere, the correlation function equals zero. The intersection volume is schematically sketched in Fig. 3.4.

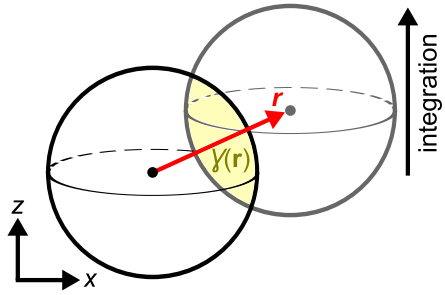

Figure 3.4.: Interpretation of the real space correlation function for diluted spheres. $\gamma(r)$ corresponds to the yellow volume shared by two spheres separated by r. In contrast, the correlation function $G(z)$ is the integration of this volume along the z-direction (marked as black arrow). Both correlation functions drop to zero at the diameter of the spheres $2R$.

The correlation function $G(x)$ is derived from Eq. 3.39. Spherical particles are one of the few examples in which a solution can be obtained analytically [110]:

$$G(x) = 2\pi R^4 \Re \left(\left[1 - \left(\frac{x}{2R} \right)^2 \right]^{\frac{1}{2}} \left[1 + \frac{1}{2} \left(\frac{x}{2R} \right)^2 \right] + 2 \left(\frac{x}{2R} \right)^2 \left(1 - \frac{x}{4R} \right)^2 \ln \left\{ \frac{\frac{x}{2R}}{1 + \left[1 - \left(\frac{x}{2R} \right)^2 \right]^{\frac{1}{2}}} \right\} \right) . \tag{3.45}$$

The restriction to the real part of the equation above ensures that $G(x)$ equals zero for $x > 2R$, as the function becomes thoroughly imaginary for larger x. $G(x)$ is the integration of the intersection volume, defined by γ, along a direction perpendicular to the neutron beam. Hence, similar to the correlation function γ, $G(x)$ drops to zero at $2R$ (see Fig. 3.4). Both correlation functions are plotted as function of the distance x in Fig. 3.5.
The differential scattering cross-section follows by inserting Eq. 3.44 into Eq. 3.37 to:

$$\frac{d\sigma(q)}{d\Omega} = 16\pi^2 \left[\frac{\sin(qR) - qR\cos(qR)}{q^3} \right]^2 . \tag{3.46}$$

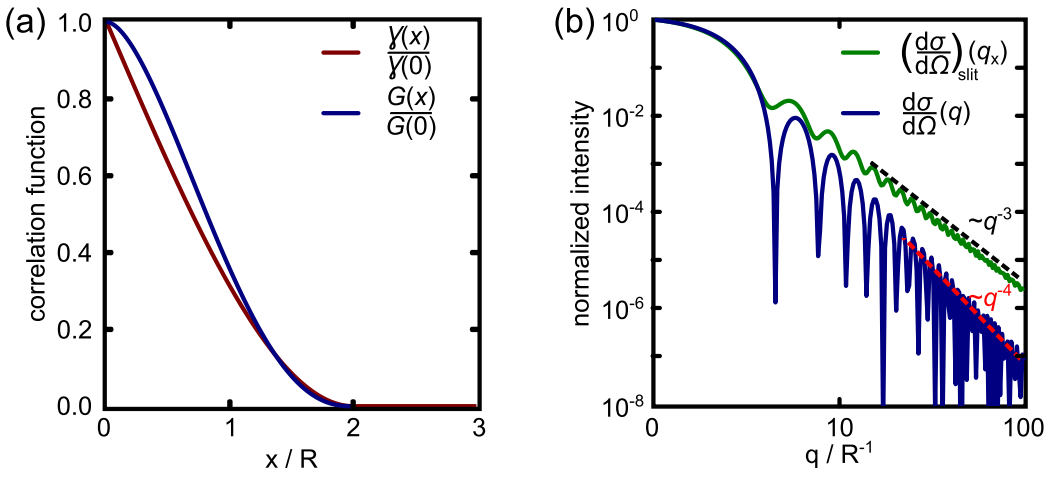

Figure 3.5.: Real space correlation and reciprocal space scattering functions of diluted spheres. (a) Normalized correlation functions $\gamma(x)$ and $G(x)$. While γ amounts the shared volume of two spheres separated by x, the correlation function $G(x)$ is the projection of $\gamma(r)$ along the z-axis. Hence, both functions drop to zero at $r = 2R$. (b) Differential scattering cross-section and slit-smeared differential scattering cross-section of the spheres as function of the wavevector transfer q. Both curves follow a Porod law for large q [111]. However, for $\left(\frac{d\sigma}{d\Omega}\right)_{\text{slit}}$, the Porod exponent is reduced by one, due to the one-dimensional integration along q_{y}.

This differential scattering cross-section is plotted in Fig. 3.5 (b). It is a quickly decreasing, oscillating function. In the low q-limit, the function behaves as $-q^2$, while the function follows a Porod law $\frac{d\sigma}{d\Omega} \propto q^{-\alpha_{\text{P}}}$ with $\alpha_{\text{P}} = 4$ in the high-q limit [111]. This is a characteristic of three dimensional structures having a smooth surface. The slit-smeared intensity of the diluted spheres according to Eq. 3.42, is additionally shown in Fig. 3.5. Its values were numerically calculated. Due to the one-dimensional integration along the q_y-direction, the morphology of the curve changed slightly in comparison to the differential scattering cross-section. General features of a slit-smeared curve can be observed: (i) The curve became smoother, (ii) the position of the maxima shifted to smaller q, and (iii) the Porod exponent α_{P} is reduced by one.

Finally, the macroscopic scattering cross-section $\Sigma = \frac{\sigma_{tot}}{V}$ can be calculated based on Eq. 3.32. In the case of a diluted two phase system, this equation has been reduced to [112]:

$$\Sigma = (\Delta\rho)^2 \lambda^2 \phi_v \frac{G(0)}{\gamma(0)} \ , \tag{3.47}$$

in which ϕ_v is the volume fraction of the particles in solution to the total volume of the sample.

By introducing Eqs. 3.44 and 3.45, the total scattering cross-section of diluted

spheres is finally calculated to:

$$\Sigma = \frac{3}{2} R(\Delta\rho)^2 \lambda^2 \phi_v \ . \tag{3.48}$$

3.3. Coherent scattering off the superconducting vortex lattice

It has been extensively discussed in Sec. 2.4 that the vortex lattice is characterized by a spatial variation of the local induction within the sample. Since the magnetic moment of the neutron interacts with the corresponding internal field distribution, this gives rise to neutron scattering.
The scattering amplitude of a vortex lattice, which is aligned parallel to the neutron beam, can be calculated by introducing the magnetic potential of Eq. 3.3 into Eq. 3.16:

$$f(\boldsymbol{q}) = -\frac{m}{2\pi\hbar^2} \boldsymbol{\mu} \cdot \int \boldsymbol{B}(\boldsymbol{R}) \exp(-\mathrm{i}\boldsymbol{q} \cdot \boldsymbol{R})\, d\boldsymbol{R} \tag{3.49}$$

$$= \frac{\gamma_\mathrm{n}}{4\Phi_0} \int B(\boldsymbol{R}) \exp(-\mathrm{i}\boldsymbol{q} \cdot \boldsymbol{R})\, d\boldsymbol{R} \ . \tag{3.50}$$

Here, the magnetic moment μ of the neutron was replaced by:

$$\mu = \gamma_\mathrm{n} \frac{e\hbar}{2m} \ , \tag{3.51}$$

in which γ_n is the gyromagnetic ratio of the neutron and e the elementary charge. The differential scattering cross-section is consequentially given by:

$$\frac{d\sigma}{d\Omega}(\boldsymbol{q}) = |f(q)|^2 = \frac{\gamma_\mathrm{n}^2}{16\Phi_0^2} \left| \int B(\boldsymbol{R}) \exp(-\mathrm{i}\boldsymbol{q} \cdot \boldsymbol{R})\, d\boldsymbol{R} \right|^2 \ . \tag{3.52}$$

The magnetic field within the lattice is periodic in two dimensions, and can therefore be expressed as a sum of individual contributions $\tilde{B}$:

$$B(\boldsymbol{R}) = \sum_{R_\mathrm{j}} \tilde{B}(\boldsymbol{R} - \boldsymbol{R}_\mathbf{j}) \ , \tag{3.53}$$

where the summation is performed over all lattice translation vectors $\boldsymbol{R}_\mathrm{j}$. By inserting the sum, Eq. 3.52 can be rearranged to:

$$\frac{d\sigma}{d\Omega}(\boldsymbol{q}) = \frac{\gamma_\mathrm{n}^2}{16\Phi_0^2}\left|\int \tilde{B}(\boldsymbol{R})\exp(-\mathrm{i}\boldsymbol{q}\cdot\boldsymbol{R})\,d\boldsymbol{R}\right|^2\left|\sum_{R_\mathrm{j}}\exp(-\mathrm{i}\boldsymbol{q}\cdot\boldsymbol{R}_j)\right|^2 \tag{3.54}$$

$$= \frac{\gamma_\mathrm{n}^2}{16\Phi_0^2}\left|\tilde{B}(\boldsymbol{q})\right|^2 S(\boldsymbol{q})\ . \tag{3.55}$$

Hence, as for a classic crystal, the differential scattering cross-section splits into a form factor $\tilde{B}(\boldsymbol{q})$, given as the Fourier transform of the local magnetic field within a vortex, and a structure factor $S(\boldsymbol{q})$ describing the periodicity of the two-dimensional lattice.
The form factor of the magnetic field profile has been calculated within different approximations of the vortex core structure. Examples are given in Ref. [113] or [114]. As a common result, the form factor decreases with λ_L^{-2}, which complicates the application of neutron scattering for the investigation of vortex matter in high κ superconductors.
As in crystallography, the structure factor in Eq. 3.55 can be expressed by two-dimensional delta functions $S(\boldsymbol{q}) \propto \sum_{\boldsymbol{G}}\delta(\boldsymbol{q}-\boldsymbol{G})$, if one assumes a perfectly ordered lattice. Hence, diffraction spots will only occur, if the momentum transfer $\boldsymbol{q}$ corresponds to a reciprocal scattering vector $\boldsymbol{G}$ of the vortex lattice. In the case of a hexagonal flux line arrangement, the spacing of the reciprocal lattice is given by:

$$g_\mathrm{VL} = \frac{2\pi}{d_\mathrm{VL}} = \frac{4\pi}{\sqrt{3}a_\mathrm{VL}} = \sqrt{\frac{8\pi^2 B}{\sqrt{3}\Phi_0}}\ , \tag{3.56}$$

whereas the symmetry of the reciprocal lattice corresponds to the symmetry of the flux line lattice rotated 90° around the beam axis. Since the vortex lines are translationally invariant along the direction parallel to the field lines, the reciprocal lattice is furthermore a point lattice in the plane that is perpendicular to the magnetic induction.
The scattering geometry and the reciprocal lattice are depicted in the Ewald construction of Fig. 3.6 (a): Obviously, for $\boldsymbol{B}$ perfectly parallel to the neutron beam, the scattering condition is only fulfilled for forward scattering as no other reciprocal lattice point than (0,0) intersects the Ewald sphere. Consequentially, an experimental determination of the vortex alignment requires a slight rotation of the vortex lattice around the angle φ_R, denoted as *rocking scan* (See Fig. 3.6 (b)). In this way, further vortex lattice planes fulfill the Bragg condition as the corresponding reciprocal lattice points pass through the Ewald shell. The total integrated intensity due to scattering at one specific reciprocal lattice point $\boldsymbol{G}$ is obtained by integrating Eq. 3.55 over all possible angles φ_R and subsequently

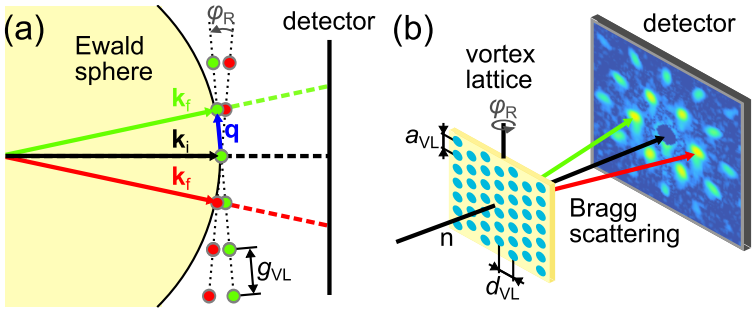

Figure 3.6.: Scattering at a vortex lattice. (a) Ewald construction for neutrons scattered at a vortex lattice. In order to fulfill the scattering condition, the vortex lattice has to be rotated by the angle φ_R, until a reciprocal lattice vector intersects the Ewald sphere. The corresponding cases for scattering at a (10) and (-10) plane are shown green and red, respectively. Consider that typically $k_\mathrm{i}/g_\mathrm{VL} \approx 1 \times 10^2$. Hence, the Ewald sphere near $(0,0)$ is approximately a plane. (b) To obtain the entire structural information, the sample (yellow) has to be successively rotated around φ_R and the corresponding scattering patterns have to be added together. The produced scattering pattern has the same symmetry as the vortex lattice (blue), but is rotated $90°$ around the neutron beam axis.

normalizing to the incident neutron flux. It has been derived to [16]:

$$I(\boldsymbol{G}) = \left(\frac{\gamma}{4\Phi_0}\right)^2 \frac{2\pi\lambda^2}{|\boldsymbol{G}|} \left|\tilde{B}\left(\boldsymbol{G}\right)\right|^2 V \eta_\mathrm{IMS} \ , \tag{3.57}$$

in which V is the sample volume and η_IMS is the volume fraction of vortex lattice domains. The last quantity is used to describe the intensity variation within the IMS as well, since in this phase the vortex form factor is constant but the volume fraction changes. In the usual case, η_IMS equals one.

4. Neutron methods investigating the micrometer range

The goal of this chapter is to provide an extensive overview of neutron grating interferometry and ultra-small-angle neutron scattering, both capable of probing vortex matter on the micrometer range. Therefore, based on the theoretical considerations of Chap. 3, it will be shown which information can be obtained by these two methods and how the data acquisition and evaluation are performed. The main focus will lie on the radiographic nGI method, as its implementation for investigations of vortex matter is one of the main objectives of this thesis. Hence, its contrast mechanism, which allows to study the distribution of micrometer structures in a sample, is explained. Furthermore, it will be discussed, how and to which extent structural information, like the size and the anisotropy of a microstructure, are gained by means of nGI. The chapter will close with a brief discussion of the USANS method based on a Bonse-Hart camera. Technical and experimental details of the nGI and USANS setups are however not reviewed until Chap. 5.

4.1. Neutron radiography

Neutron radiography is a non-destructive imaging method which provides information about the interior of a sample with high spatial resolution. In contrast to x-rays, neutrons are particularly sensitive to several light elements such as hydrogen or lithium, while heavier elements such as aluminum or lead can still be penetrated. Hence, neutron imaging is routinely applied whenever x-rays fail to generate sufficient imaging contrast or lack of penetration. Typical applications can be found in e.g. material science [115], cultural heritage research [116], geology [117], and engineering [118].
Standard neutron absorption radiography is neither sensitive to magnetic structures nor allows an investigation on the micrometer scale. However, since nGI is implemented into a neutron radiography instrument and its resolution is governed by the beamline, a prior general discussion on radiography allows a comprehensible introduction into grating interferometry.
A neutron imaging beamline is based on the principle of a pinhole camera [119]. Its basic setup is sketched in Fig. 4.1: The neutron source (e.g. the moderator of a nuclear reactor or a spallation source) is in line with an aperture pinhole, the sample, and a position sensitive detector with a high spatial resolution. In this

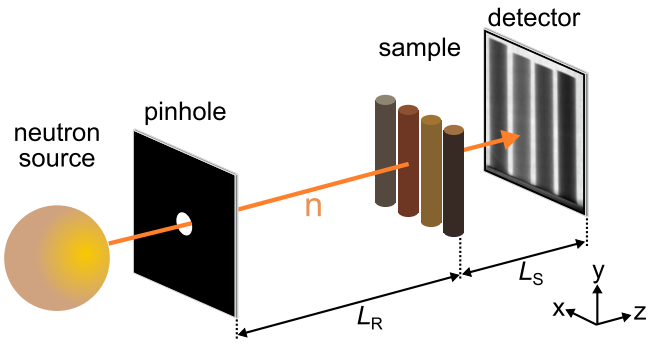

Figure 4.1.: Illustration of a neutron imaging beamline. The neutron source is in line with an aperture pinhole, the sample and a positional sensitive neutron imaging detector.

configuration, the attenuation of the neutron beam within an object generates an imaging contrast.
Different kinds of neutron imaging detectors exist, however in most cases a combination of a scintillator screen and a scientific CCD or CMOS camera is used. The spatial resolution of the obtained neutron images is limited to a few 10 µm by the divergence of the beam hitting the sample [119], the blurring within the neutron-to-light conversation process [120], and the optical resolution of the imaging recording system. The divergence of the beam projects a single point within the object plane into a sphere of radius d_R on the image plane (see Figure 4.2). By introducing the pinhole diameter D_R, the distance of the sample to the pinhole L_R and the sample-to-detector distance L_S, d_R can be expressed as:

$$d_R = \frac{D_R}{L_R} L_S. \tag{4.1}$$

Hence, the geometrical resolution can be increased by reducing the sample-to-detector distance L_S or the "L/D"-ratio L_R/D_R[1].
Strictly speaking, the final imaging resolution is a convolution of the three aforementioned contributions. However, in the presented study, the resolution is mostly limited by the geometrical resolution of the beamline, and contributions of the detector can be neglected. The reason is the bulky sample environment required for the vortex matter investigations, which highly increases the sample-to-detector distance and consequently reduces the geometrical resolution.

1 The subscript R was introduced to distinguish the "L/D"-ratio used to describe the geometrical resolution of the beamline from a similar term used in neutron grating interferometry (Sec. 4.2).

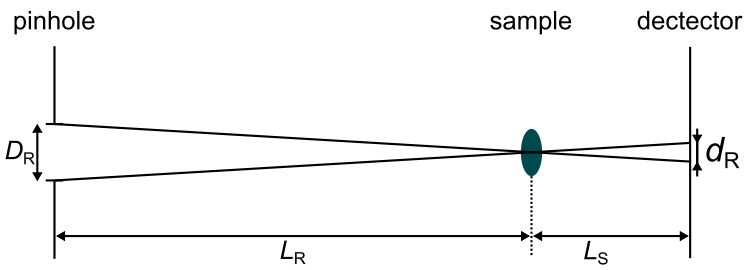

Figure 4.2.: Geometrical resolution of a pinhole camera. A point in the object plane is projected on a circle of radius d_R in the imaging plane.

4.2. Principle of neutron grating interferometry

Neutron grating interferometry (nGI) is an advanced neutron imaging technique which allows the simultaneous recording of the neutron transmission image (TI), the neutron differential phase contrast image (DPC), and the dark-field image (DFI) [121]. It is based on two neutron absorption gratings and one neutron phase grating implemented into a neutron imaging beamline [122]. A schematic depiction of its main components is shown in Fig. 4.3.

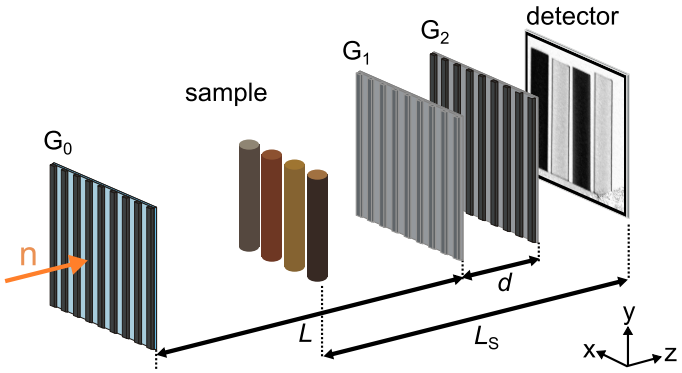

Figure 4.3.: Illustration of an nGI setup. The setup consists of the source grating G_0, the phase grating G_1, the analyzer grating G_2, and a neutron imaging detector. Optionally, a neutron velocity selector can be introduced between G_0 and G_1. The sample may either be placed between G_0 and G_1 or G_1 and G_2.

In principle, a neutron grating interferometer is a realization of a Talbot-Lau interferometer for neutrons [123]. The absorption grating G_0 (periodicity $p_0 \sim$ mm), which is located right behind the neutron pinhole, generates an array of coherent but mutually incoherent line sources. At a distance L ($\sim$ m) downstream, the phase grating G_1 ($p_1 \sim$ µm) imprints a periodic phase modulation of $\Delta\Phi \approx \pi$ onto the neutron wave front. Thereby, G_1 acts as the beam splitter of the interferometer,

which mainly splits the beam into the first orders whereas the zeroth order is suppressed. The introduced periodic phase modulation of the neutron wave front generates a complex intensity modulation of the neutron beam behind the grating. This pattern, often called 'Talbot carpet', is shown in Fig. 4.4.

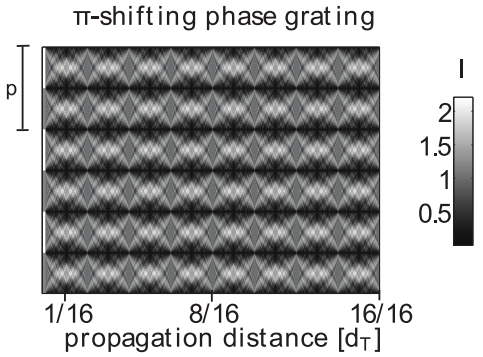

Figure 4.4.: Calculation of the Talbot carpet taken from Ref. [124]. Shown is the distribution of the intensity I as function of the propagation distance. The initial phase modulation is transferred into an intensity modulation which is maximal at the fractional Talbot distances d_n (Eq. 4.2) having an odd n. At the Talbot distance d_T, the phase modulation is recovered (Talbot self-imaging effect).

The original pure phase modulation is recovered at the Talbot distance d_T, whereas the intensity modulation is maximal at the fractional Talbot distances d_n with an odd n, but vanishes at even n [125]:

$$d_\mathrm{n} = \frac{n}{16} d_\mathrm{T} = n \frac{p_1^2}{8\lambda} \ . \tag{4.2}$$

The interference pattern generated by this Talbot effect, has approximately half the periodicity of the phase grating. It is hence not directly accessibly by an imaging detector as its pitch is well below the detector resolution. Therefore, the analyzer grating G_2 ($p_2 \approx p_1/2$) is introduced at a distance $d \sim$ cm from G_1, right in front of the detector [126]. As the periodicities of the interference pattern and G_2 match, the transmitted intensity I is minimized if the grating lines cover the interference maxima and vice versa. A translation x_g of one of the gratings G_i (i = 1,2,3) perpendicular to the beam and to the grating lines will thus result in an intensity oscillation in each detector pixel (j,l) as illustrated in Fig. 4.5.
The intensity oscillation can be approximated by:

$$I(x_\mathrm{g},j,l) = a_0(j,l) + a_1(j,l) \cos\left(\frac{2\pi x_\mathrm{g}}{p_\mathrm{i}} - \varphi(j,l) \right) \ , \tag{4.3}$$

in which a_0, a_1 and φ are the offset, amplitude and phase of the oscillation,

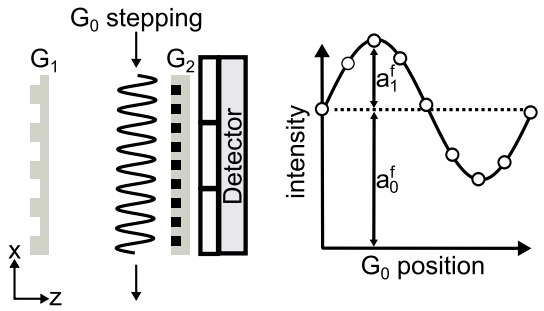

Figure 4.5.: Illustration of an nGI stepping scan. An x-translation of G_0 perpendicular to the neutron beam will result in a translation of the interference pattern and hence in an intensity oscillation in each detector pixel. By taking neutron images at different positions of G_0, the parameters a_0, a_1 and φ can be extracted.

respectively [122].
An nGI scan measures the change of $I(x_g,j,l)$ due to the influence of the sample onto the interference pattern. Therefore, neutron images are taken with (s) and without (f) a sample introduced to the interferometer for different positions x_g of the grating G_0. A typical data set is shown in Fig. 4.6 consisting of 8 samples (a) and 8 open beam images (b), respectively. Additionally, a dark image (d) has to be recorded with the same exposure time. This dark image is taken with closed camera shutter to amount the dark current and offset in each detector pixel of the CCD chip.
In order to calculate the TI, DPC, and DFI, the recorded sample and open beam images taken at different G_0-positions x_g are filtered for gamma spots [127] and subtracted by the dark image in order to correct for the dark-current of the CCD chip. Thereafter, a_0, a_1 and φ can be extracted for each detector pixel. This evaluation can be conducted pixel-wise by a least squares fitting of $I(x_g,j,l)$ to Eq. 4.3. Alternatively, a Fast Fourier Transformation (FFT) of the oscillation [128] can be conducted, in which a_0 and a_1 are the zeroth and first order Fourier coefficient, and φ is the first order phase. A fast routine for the least squares approach was given in Ref. [129], in which the chi-square minimization is reduced to a matrix operation acting on the whole image. The results of this thesis were evaluated using this algorithm. However, the differences in the a_0, a_1 and φ for the three data evaluation procedures are marginal.

4.2.1. The transmission image

As illustrated in Fig. 4.7 (a), neutron absorption leads to an attenuation of the whole interference pattern and therefore to a reduction of the mean value of $I(x_g,j,l)$, which is a_0. Hence, the neutron transmission image is calculated

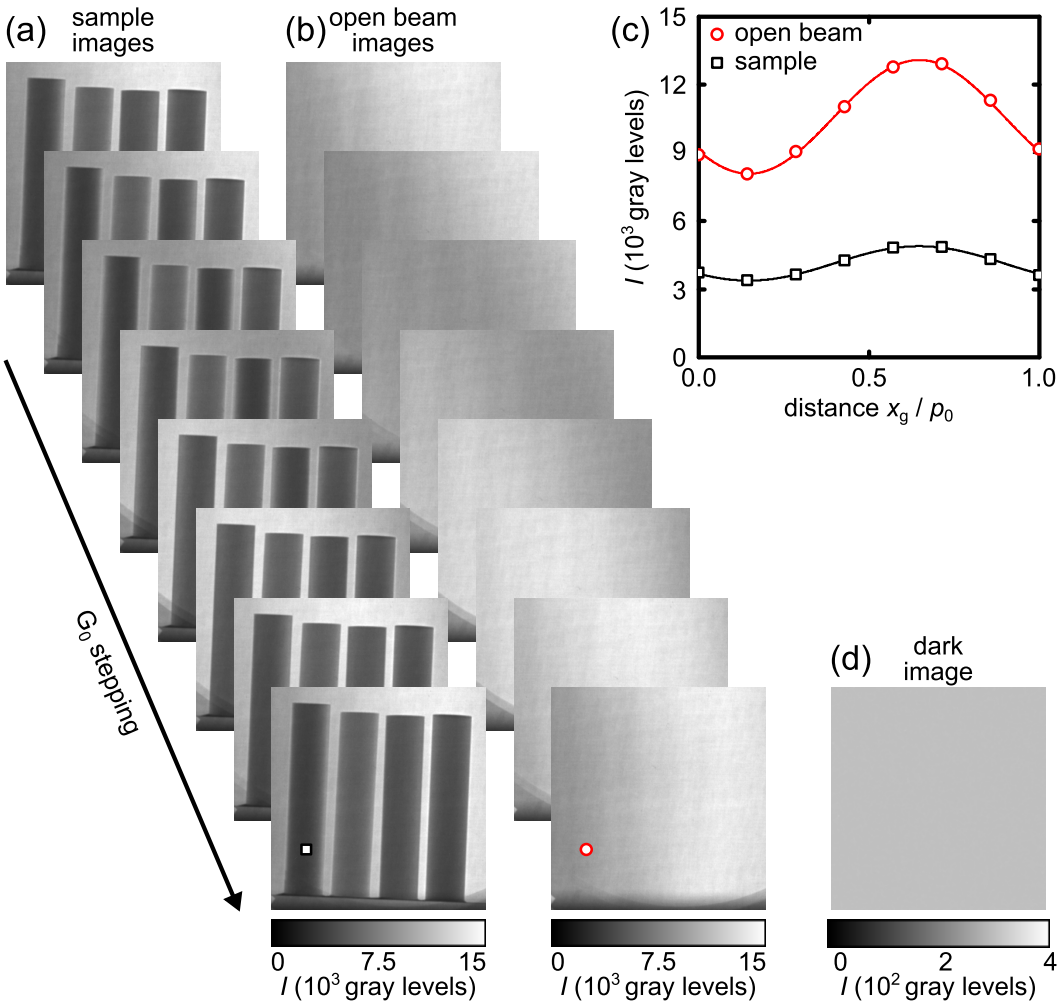

Figure 4.6.: Typical nGI dataset which consists of 8 sample images (a), 8 open beam images (b) and a dark image (d). Additionally, in panel (c), the intensity oscillation for the positions marked in (a) and (b) are shown as functions of the stepping distance x_g.

according to:

$$\mathrm{TI}(j,l) = \frac{a_0^{\mathrm{s}}(j,l)}{a_0^{\mathrm{f}}(j,l)} \ . \tag{4.4}$$

The TI evaluated from the data set shown in Fig. 4.6 is presented in Fig. 4.7 (b). The neutron attenuation is similar for all materials with the exception of brass, which reveals a slightly higher transmission. The TI corresponds to the transmission image measured by standard neutron radiography. Hence, its contrast depends exponentially on the local absorption and incoherent scattering cross-section σ_{abs} and σ_{inc} of the material, which were defined in Eq. 3.13 and 3.20. For an inhomogeneous solid, the TI is given by the integration of the cross-sections

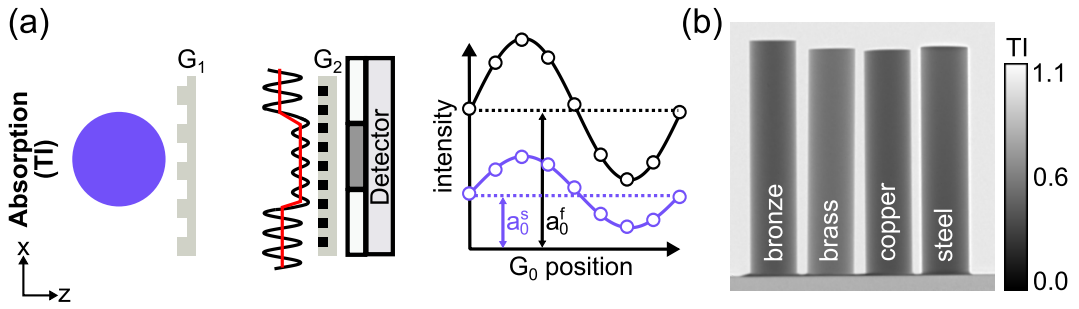

Figure 4.7.: The transmission image: (a) Illustration of the TI contrast modality. Neutron attenuation within the sample reduces the average intensity hitting the detector. Hence, the intensity oscillation measured by a stepping scan is diminished by a constant factor $a_0^{\mathrm{s}}(j,l)/a_0^{\mathrm{f}}(j,l)$. (b) Evaluated TI of the dataset shown in Fig. 4.6. Experimental details are given in Sec. 5.1.2.

along the neutron path through the sample:

$$\mathrm{TI} = \exp\left\{ -\int_{\mathbf{path}} \left[\sigma_{\mathrm{abs}}(z) + \sigma_{\mathrm{inc}}(z)\right] N dz \right\} \ . \tag{4.5}$$

However, in the case of strong coherent neutron scattering within the material, the TI can also provide a scattering contrast, which is demonstrated in Sec. 6.2 and explained in A.5.

4.2.2. The differential phase contrast image

The differential phase contrast image is defined as the phase shift of the interference pattern which is caused by the presence of the sample in the interferometer:

$$\mathrm{DPC}(j,l) = \varphi^{\mathrm{s}}(j,l) - \varphi^{\mathrm{f}}(j,l) \ . \tag{4.6}$$

Fig. 4.8 (a) illustrates the DFI contrast modality. If the sample has an index of refraction higher (lower) than unity, the neutron phase will be shifted by Φ within the sample. The neutron wave front profile will then be advanced (delayed) behind the sample, and a gradient is introduced to the neutron wave front. This gradient is connected to the phase of the interference pattern φ by [130]:

$$\varphi = -\frac{\lambda d}{p_2}\frac{\partial \Phi}{\partial x} \ , \tag{4.7}$$

in which λ is the neutron wavelength. Hence, the DPC maps the gradient of the neutron phase introduced by the sample. However, due to the one-dimensionality of the gratings, only phase shifts in x-direction perpendicular to the grating lines

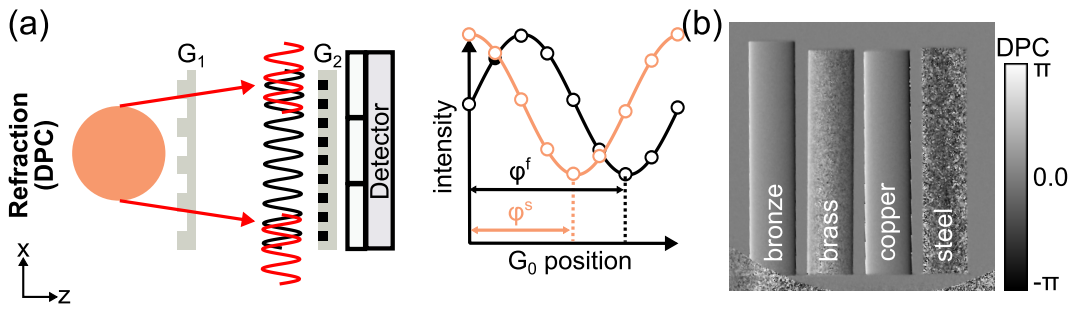

Figure 4.8.: The differential phase contrast image: (a) Illustration of the DPC contrast modality. Neutron refraction within the sample distorts the neutron wavefront. A gradient in the neutron wavefront causes a neutron deflection that is proportional to the phase shift $\varphi^{s}(j,l) - \varphi^{f}(j,l)$ of the interference pattern. (b) Evaluated DPC of the dataset shown in Fig. 4.6. Experimental details are given in Sec. 5.1.2.

can be detected.
The evaluated DPC for the data of Fig. 4.6 is shown in Fig. 4.8 (b). The arising contrast is attributed to the refraction within the rods ($n < 1$) that leads to a delay of the neutron wave front downstream the samples. This is illustrated in Fig. 4.9 (a). Horizontal line profiles of the DPC are presented in Fig. 4.9 (b): For the bronze, brass and copper samples, the DPC is extremal at one edge, but gradually changes its sign to the other edge leading to a vanishing signal in the center. The peculiar shape of the DPC is caused by the spherical cross-sections of the rods, as the thickness t of the sample in beam direction gradually increases to the center of the samples (compare Fig. 4.9 (a)). For a sphere, $\Phi(x)$ and $\mathrm{DPC}(x)$ can be easily calculated by introducing the thickness profile $t(x)$ into Eq. 3.12:

$$\Phi(x) \propto t(x) = \sqrt{(r^2 - (r-x)^2} \tag{4.8}$$

$$\mathrm{DPC}(x) \propto -\frac{dt(x)}{dx} = \frac{r-x}{\sqrt{(r^2 - (r-x)^2}} \ . \tag{4.9}$$

A fit of the line profile to Eq. 4.9 is exemplarily shown in Fig. 4.9.
The determination of the phase shift, however, requires a finite intensity modulation within the stepping can. If this modulation is too small, the phase determination becomes imprecise and the DPC noisy. This is the case for the brass, and in particular for the steel rod, which both reveal a low DFI contrast (see Sec: 4.2.3). The phase contrast image that shows the phase profile of the sample can be received by a one-dimensional integration [126]:

$$\Phi(j,l) = -\int \varphi \frac{p_2}{\lambda d} dx \ . \tag{4.10}$$

However, although the DPC has a high significance in x-ray radiography due to its high contrast for soft tissue, only minor applications have been identified for neutrons so far. This is why the rest of this thesis will focus on the TI and DFI contrast modalities.

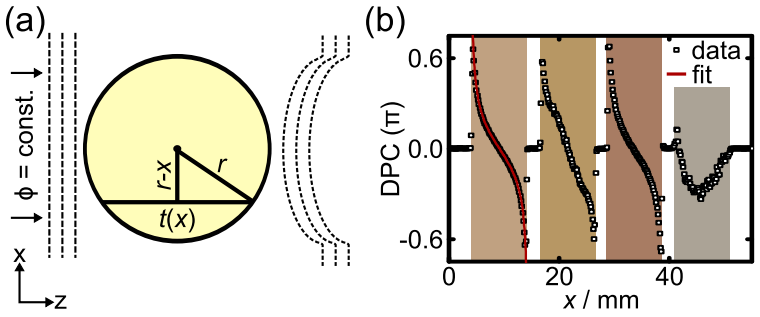

Figure 4.9.: The origin of the DPC contrast in Fig. 4.8 (b). (a) Illustration of the neutron wave front before and after passing the sample. Due to an index of refraction smaller than one, the neutron wave front is delayed after the rod shaped sample. The negative gradient of the wave front is mapped in the DPC. (b) Horizontal profile of the DPC. The peculiar shape of the DPC profile is caused by the spherical cross-section of the rods. The red curve is a fit to Eq. 4.9. The position of the samples is indicated by the rectangular areas in the background of the graph.

4.2.3. The dark-field image

The dark-field contrast is caused by scattering within the sample that degrades the visibility of the interference pattern, but does not influence the absorption image (Fig. 4.10 (a)). In analogy to optical interferometry, the visibility in nGI is defined as:

$$V = \frac{I_{\max} - I_{\min}}{I_{\max} + I_{\min}} = \frac{a_1}{a_0}, \tag{4.11}$$

and therefore quantifies the ratio of neutron intensity forming an interference pattern to the average intensity.
The dark-field image maps the local relative degradation of the visibility due to the sample in the interferometer:

$$\mathrm{DFI}(j,l) = \frac{V^{\mathrm{s}}(j,l)}{V^{\mathrm{f}}(j,l)} = \frac{a_1^{\mathrm{s}}(j,l)a_0^{\mathrm{f}}(j,l)}{a_0^{\mathrm{s}}(j,l)a_1^{\mathrm{f}}(j,l)} \,. \tag{4.12}$$

Because of the normalization with a_0, the DFI is not affected by pure neutron absorption. Instead, only processes reducing the visibility cause such a contrast. The evaluated DFI for the data presented in Fig. 4.6 is shown in Fig. 4.10 (b). The most striking detail is the strong DFI contrast reduction in the brass and steel

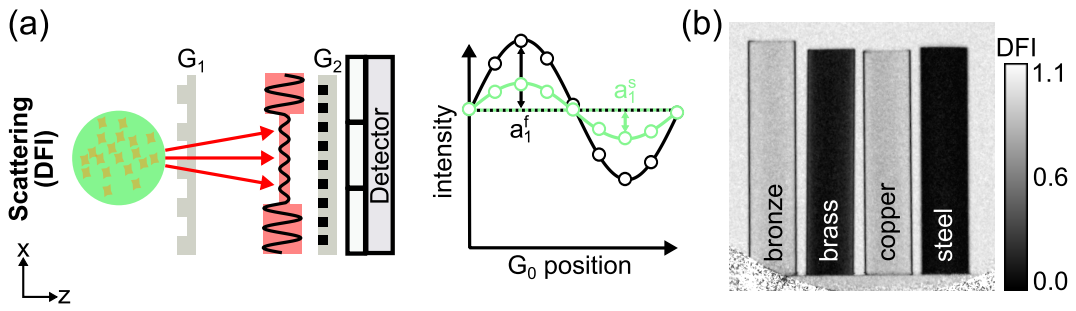

Figure 4.10.: The dark-field image: (a) Illustration of the DFI contrast modality. Scattering under ultra-small angles smears the interference pattern, but does not change the average intensity that reaches a detector pixel. (b) Evaluated DFI of the dataset shown in Fig. 4.6. Experimental details are given in Sec. 5.1.2.

rod, compared to bronze and copper, where only the sample edges contribute to the DFI. This contrast degradation in copper and steel can be linked to scattering at small precipitations [131] and magnetic domain walls [132], respectively. A more quantitative discussion of the DFI contrast is given below.

Nomenclature used in this thesis

In explaining the DFI modality, confusion may arise when the term 'contrast' is being used. The reason is that the DFI can be described in terms of an imaging contrast, where a lower DFI value would correspond to a higher contrast, but also in terms of the reduction of the intensity modulation, in which a low DFI signal implies a small contrast[1]. In this thesis, the latter nomenclature is used. Hence, a high DFI contrast corresponds to a high DFI value close to 1.

The origin of the DFI scattering contrast

The following section discusses how the DFI contrast is linked to the setup parameters and the microstructural properties of the sample. For x-ray grating interferometry, the DFI contrast has been treated by rigorous wave propagation calculations in Ref. [134] and [135]. Their results demonstrate a connection between the DFI contrast and the autocorrelation function of the refraction index within the microstructure of the sample.
A complementary, but more general theoretical approach given in Ref. [136] will be followed and further developed. In this approach, it has been assumed that scattering within the sample, involving a momentum transfer q_x perpendicular to the grating lines, leads to a fractional deflection of the neutron beam. Hence, the

1 The nomenclature is for example used in the Modulation of Intensity with Zero Effort (MIEZE) technique [133].

scattering is accompanied by a phase shift $\Delta\varphi$ of a part of the interference pattern, generated by G_1. Consequently, the DFI reduction results from a superposition of the undisturbed and the deflected parts of the interference pattern, and thus from scattering within the sample.
At first, the simplest case of a sample which elastically scatters all neutron under the same angle ϑ will be considered. In the small-angle approximation ($\tan\vartheta \approx \vartheta \approx \sin\vartheta$), the scattering angle is proportional to a momentum transfer q_x:

$$\vartheta \approx \frac{q_x \lambda}{2\pi} \,. \tag{4.13}$$

This scattering angle is directly connected to the phase shift $\Delta\varphi$ of the interference pattern: It has been derived in Ref. [137] that $\Delta\varphi$ depends on the position of the sample in the interferometer, according to:

$$\Delta\varphi = \begin{cases} \frac{2\pi\vartheta}{p_2}\frac{d}{L}\left(L + d - L_s\right) & \text{if sample is placed between } G_0 \text{ and } G_1 \\ \frac{2\pi\vartheta}{p_2} L_s & \text{if sample is placed between } G_1 \text{ and } G_2 \end{cases} \tag{4.14}$$

In defining an effective sample-to-detector distance L_S^{eff}

$$L_s^{\text{eff}} = \begin{cases} (L + d - L_s)\frac{d}{L} & \text{for } L_s > d \\ L_s & \text{for } L_s < d \end{cases} \tag{4.15}$$

the connection of the interference phase shift $\Delta\varphi$ (Eq. 4.13) and q_x (Eq. 4.14) can be expressed in an elegant way:

$$\Delta\varphi = \frac{\lambda L_s^{\text{eff}}}{p_2} q_x = \xi_{GI} q_x \,. \tag{4.16}$$

Hence, the phase shift of the interference pattern caused by neutron scattering is proportional to the momentum transfer q_x and a setup specific constant ξ_{GI} denoted as autocorrelation length of the setup:

$$\xi_{GI} = \frac{\lambda L_s^{\text{eff}}}{p_2} \,. \tag{4.17}$$

For most nGI setups, ξ_{GI} typically amounts a few micrometers [122, 138–140].
If one assumes scattering in equal parts to $\pm q_x$, the visibility is degraded as:

$$V^s = V^f \cos\left(\Delta\varphi\right) = V^f \cos\left(\xi_{GI} q_x\right), \tag{4.18}$$

since $\frac{1}{2}\left[\cos\left(\varphi + \Delta\varphi\right) + \cos\left(\varphi - \Delta\varphi\right)\right] = \cos\left(\varphi\right)\cos\left(\Delta\varphi\right)$. The discussed degradation of intensity modulation caused by a single q_x scattering event is illustrated in Fig. 4.11.

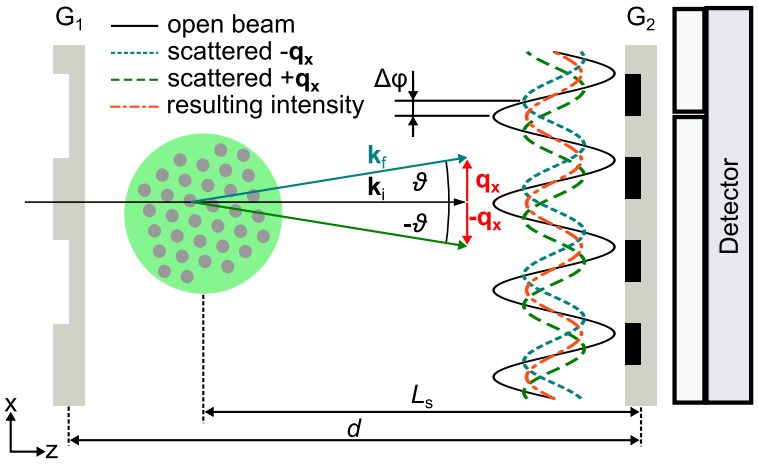

Figure 4.11.: The origin of the DFI contrast. Shown is a sample which perfectly scatters neutrons involving only a single momentum transfer q_x. In this case, the original open beam intensity modulation is splitted into two oscillations (blue and green) revealing a phase shift $\pm\Delta\varphi$. The resulting intensity oscillation is their superposition (orange). It is again a sinusoidal modulation, but with reduced amplitude.

The assumed approximation of symmetric scattering is commonly used in small-angle scattering, where the scattering pattern is mostly influenced by the form factor instead of the structure factor. However, it excludes the description of Bragg scattering within this approximation.
If the assumption of a single q-transfer is rejected, the whole scattering distribution $S(q_\mathrm{x})$ has to be taken into account:

$$V^\mathrm{s} = V^\mathrm{f} \int_{-\infty}^{\infty} S(q_\mathrm{x}) \cos\left(\xi_\mathrm{GI} q_\mathrm{x}\right) dq_\mathrm{x} \ . \tag{4.19}$$

The introduced function $S(q_\mathrm{x})$ can be interpreted as the probability that a neutron is scattered in the direction q_x. This probability is independent of the scattering parallel to the grating lines[1]. Hence, $S(q_\mathrm{x})$ will be proportional to the slit-smeared differential scattering cross-section $\left(\frac{d\sigma}{d\Omega}\right)_\mathrm{slit}$ defined in Eq. 3.42. In order to fulfill the probability condition $\int S(q_\mathrm{x}) dq_\mathrm{x} = 1$, the scattering cross-section has to be scaled by

$$S(q_\mathrm{x}) = \frac{1}{4\pi^2 G(0)} \left(\frac{d\sigma}{d\Omega}\right)_\mathrm{slit} \ , \tag{4.20}$$

1 In Sec. 4.5, it will be shown that the same holds true for USANS using a Bonse-Hart camera.

since according to Eq.3.32, the integral of $\left(\frac{d\sigma}{d\Omega}\right)_{\text{slit}}$ is given by:

$$\int_{-\infty}^{\infty} \left(\frac{d\sigma}{d\Omega}\right)_{\text{slit}} dq_y = 4\pi^2 G(0) \ . \tag{4.21}$$

Inserting $S(q_{\text{x}})$ into Eq. 4.19 rearranges the DFI signal to:

$$DFI = \frac{V^{\text{s}}}{V^{\text{f}}} = \frac{1}{4\pi^2 G(0)} \int_{-\infty}^{\infty} \left(\frac{d\sigma}{d\Omega}\right)_{\text{slit}} \cos\left(\xi_{\text{GI}} q_{\text{x}}\right) dq_{\text{x}} \tag{4.22}$$

$$= \frac{1}{G(0)} \frac{1}{4\pi^2} \int_{-\infty}^{\infty} \left(\frac{d\sigma}{d\Omega}\right)_{\text{slit}} \exp\left(\xi_{\text{GI}} q_{\text{x}}\right) dq_{\text{x}} \tag{4.23}$$

$$= \frac{G(\xi_{\text{GI}})}{G(0)} \ . \tag{4.24}$$

The cosine function was replaced by an exponential function, as this does not change the transform for a symmetric argument. In the last line, the correlation function $G(\xi_{\text{GI}})$ of Eq. 3.36 has furthermore been identified. Hence, the DFI contrast is directly linked to the real space correlation function $G(x)$ evaluated at the setup correlation length $x = \xi_{\text{GI}}$. Therefore, the nGI is closely related to spin-echo small-angle neutron scattering, which also measures $G(x)$ directly [108]. In a realistic scenario, some neutrons will pass the sample without scattering, and only a fraction $1 - \Sigma t$ of the beam might be scattered within the sample of thickness t. In this case, Eq. 4.24 expands to:

$$DFI = (1 - \Sigma t) + \Sigma t \frac{G(\xi_{\text{GI}})}{G(0)} \ . \tag{4.25}$$

Finally, according to the idea introduced by Schelten and Schmatz [141], multiple (n-fold) scattering in a sample can be handled as an n-fold convolution integral of the reciprocal space differential scattering cross-section. These convolutions elegantly reduce to a multiplication of the real space correlation functions. Applied to the DFI contrast, multiple scattering can be included to Eq. 4.25 by [136, 142]:

$$DFI = \exp\left[\Sigma t \left(\frac{G(\xi_{\text{GI}})}{G(0)} - 1\right)\right] \tag{4.26}$$

which is the final equation defining the DFI contrast[1].
Four distinct conclusions can be drawn from the derivation above: (i) The DFI

1 Note that Eq. 4.25 is the expansion of Eq. 4.26 for small Σ or t, and high $G\left(\xi_{\text{GI}}\right)$.

contrast depends exponentially on the sample thickness in beam direction. Tomographic DFI reconstructions can therefore be based on the same algorithms as attenuation based tomography [143]. (ii) A variation of ξ_{GI} via a wavelength or distance scan allows to directly measure the real space correlation function of the material within the boundaries given by the accessible wavelength band or setup distances. Hence, the deduction of quantitative information is possible, even in combination with high spatial resolution (Sec. 4.4). (iii) As the dark-field signal is generated by the microstructure of the sample, a material specific dark-field extinction coefficient can be defined [131] which differs from the attenuation coefficient and provides additional imaging contrast. (iv) The DFI is insensitive to scattering contributions parallel to the grating lines. Consequently, if the scattering function and hence the underlying microstructure of an object are anisotropic, its DFI will depend on the rotation angle ω of the grating lines around the beam axis. Detailed information about the microstructural orientation can thus be obtained by a DFI(ω) scan (Sec. 4.3).

4.3. Directional dark-field imaging

Directional dark-field imaging evaluates the variation of the DFI signal with the rotation angle ω of the grating lines around the beam axis. The DFI is insensitive to the scattering components parallel to the grating lines. Hence, this rotation of the gratings will result in an oscillation of the DFI contrast if the microstructure of the sample is anisotropic. From the shape of the oscillation, detailed information about the microstructural orientation within a sample can be obtained. Depending on the scattering strength and the number of predominant scattering directions, different evaluation procedures have been published [144–146]. However, it will be shown that all of them naturally arise from the dependence of the DFI signal on the correlation function $G(x)$ which was derived in Sec. 4.2.3. A direct connection to results from scattering experiments can consequently be established.

The DFI contrast of an arbitrary differential cross-section depends on its autocorrelation function $G(x,y=0)$. As shown in Sec. 3.2.4, $G(x)$ is simply given as the Fourier transform of the slit-smeared differential scattering cross-section. If the setup or the sample is rotated by an angle ω around the beam, the slit-smearing has to be performed along a different path in the reciprocal space to calculate the correlation function G. This situation is sketched in Fig. 4.12, in which an arbitrary differential scattering cross-section $\frac{d\sigma}{d\Omega}(\boldsymbol{q})$ is shown together with the integration path to perform the required slit-smearing (red line). However, for this consideration, it is non-relevant if the sample or the gratings are rotated, as only their relative rotation matters. The discussion is therefore restricted to the case where the sample is turned relative to the gratings.

If the sample is rotated at an angle ω around the beam axis, the scattering function is given by $\frac{d\sigma}{d\Omega}\left(q'_{\mathrm{x}},q'_{\mathrm{y}}\right)$ (Fig. 4.12 (b)). The correlation function then changes to

$G^R(x)$, according to:

$$G^R(x,y=0) = \frac{1}{4\pi^2} \int\limits_{q_x,q_y} \frac{d\sigma(q'_x,q'_y,0)}{d\Omega} \exp\left(\mathrm{i}q_x x\right) dq_x dq_y \ . \tag{4.27}$$

Here, q'_x and q'_y are coordinates in the rotated coordinate system. The two-dimensional Fourier transform of a rotated function equals the Fourier transform rotated by the same angle which is why Eq. 4.27 can be rewritten as:

$$G^R(x,y=0) = G(x',y') = G(x\cos\omega, -x\sin\omega) \ , \tag{4.28}$$

in which x and y were substituted according to:

$$(x',y') = (x\cos\omega + y\sin\omega, -x\sin\omega + y\cos\omega) \tag{4.29}$$

$$= (x\cos\omega, -x\sin\omega) \ . \tag{4.30}$$

Finally, the ω dependence of the DFI contrast results as:

$$\mathrm{DFI}\,(\omega) = \exp\left[\Sigma t \left(\frac{G(\xi_{\mathrm{GI}}\cos\omega, -\xi_{\mathrm{GI}}\sin\omega)}{G(0)} - 1\right)\right] \ . \tag{4.31}$$

The DFI(ω) variation under the simplified assumptions of a bi-gaussian scattering distribution is derived in Ap. A.2. Corresponding data are e.g. published in Ref. [147].

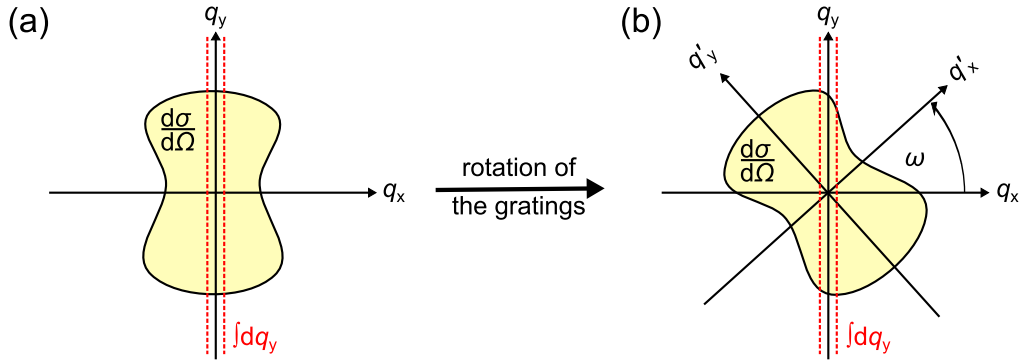

Figure 4.12.: Directional dark-field imaging of an anisotropic sample: (a) The correlation function measured by the DFI depends on the differential scattering cross-section of the sample (yellow) integrated along the direction of the grating lines $\boldsymbol{q_y}$ (red line). If the sample is rotated, the coordinate system of the differential scattering cross-section ($\boldsymbol{q'}$) is rotated against the system of the grating setup (b) and the integrated, slit-smeared differential scattering cross-section as well as $G(x)$ change. Hence, information about the anisotropy within the sample can be gained by a DFI(ω) scan.

4.4. Quantitative dark-field imaging

It has been shown in Sec. 4.2.3 that the DFI contrast depends on the correlation function G evaluated at a setup specific correlation length ξ_{GI}. A single nGI measurement only provides information in form of a single point of the correlation function, which is insufficient in order to link the contrast to any structural parameters. However, ξ_{GI} depends on the neutron wavelength, as well as on the sample-to-detector distance $L_{\mathrm{s}}^{\mathrm{eff}}$. A variation of these quantities allows to measure the correlation function on a wider range and to draw microstructural conclusions on the morphology of the sample. This approach is denoted as ´quantitative dark-field imaging'. Its feasibility and potential has been demonstrated in Refs. [147], [148] and [149]. The accessible parameter space is however restricted, since the visibility of nGI also depends on the wavelength and the setup geometry. In the following section, the limits on V set by λ and $L_{\mathrm{s}}^{\mathrm{eff}}$ will be discussed.

4.4.1. The effects of the wavelength onto the visibility

An nGI setup is normally tuned to one specific wavelength, as the analyzer grating G_2 is fixed at the wavelength dependent first fractional Talbot distance $d_1 = p_1^2/8\lambda$ (Eq. 4.2) behind G_1. A variation of λ for quantitative DFI will result in a detuning of the G_1-G_2-distance d and d_1 and therefore in a diminishing of the visibility[1]. However, a variation of the wavelength will also change the phase modulation of the neutron wave front introduced by G_1, which influences the visibility as well, and leads to a complex $V(\lambda)$ dependence.
For x-rays, this problem has been treated numerically in Ref. [125], in which the visibility of a perfectly coherent grating interferometer was calculated as function of the reduced propagation distance $\eta_{\mathrm{d}} = \frac{d}{d_{\mathrm{T}}}$ and the phase shift Φ introduced by G_1. While not explicitly stated in Ref. [125], their data clearly suggest that the visibility V_{T} of a perfectly coherent setup is well described by:

$$V_{\mathrm{T}}(\Phi,\eta_{\mathrm{d}}) = \frac{1}{2}\left(1-\cos\Phi\right)\left|\sin(8\pi\eta_{\mathrm{d}})\right| \ . \tag{4.32}$$

Applied to neutrons, both η_{d} as well as Φ linearly depend on the wavelength [122]:

$$\Phi = n_{\mathrm{sld}} h_1 \lambda \tag{4.33}$$

$$\eta_{\mathrm{d}} = \frac{d}{2p_1^2}\lambda \ , \tag{4.34}$$

1 For a visualization compare the Talbot carpet shown in Fig. 4.4. The amplitude modulation of the interference pattern is maximal only at the fractional Talbot distances.

in which $n_{\mathrm{sld}} = Nb_{\mathrm{c}} = 2.079 \times 10^{14}\,\mathrm{m}^{-1}$ (Eq. 3.12) is the scattering length density of the G_1 material Si [150] and h_1 is the height of the grating lines of G_1. Hence, the wavelength dependence of the visibility can be evaluated by combining Eq. 4.32, 4.33 and 4.34 in order to yield:

$$V_{\mathrm{T}}(\lambda,d) = \frac{1}{2}\left[1 - \cos\left(n_{\mathrm{sld}} h_1 \lambda\right)\right] \left|\sin\left(\frac{4\pi d}{p_1^2}\lambda\right)\right| \ . \tag{4.35}$$

The above equation models the wavelength dependence of the visibility in an ideal setup. However, in a real nGI, the absorption within the absorption gratings G_0 and G_2 will be wavelength dependent, too. The associated visibility degradation will be derived in Ap. A.3. For the gratings G_{i} ($i = 0,2$), it is given by:

$$V_{\mathrm{Gi}}(\lambda) = \frac{DC_{\mathrm{i}}}{DC_{\mathrm{i}} + \left[\exp(h_{\mathrm{i}}\sigma_{\mathrm{t}}\frac{\lambda}{1.8\,\text{Å}}) - 1\right]^{-1}} \ , \tag{4.36}$$

in which DC_{i} is the duty cycle of the grating i, h_{i} is the height of the grating lines and σ_{t} is the macroscopic absorption cross-section of the grating material at 1.8 Å.

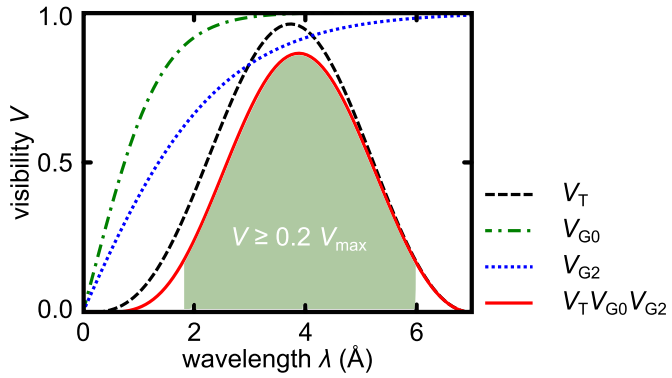

Figure 4.13.: Quantitative DFI by a variation of the neutron wavelength. Shown is the wavelength dependence of the visibility caused by the modifications of the Talbot carpet $V_{\mathrm{T}}(\lambda,d)$ as well as by the finite transmission through the grating lines $V_{\mathrm{G0}}(\lambda)$ and $V_{\mathrm{G2}}(\lambda)$. The red curve is the product of these single contributions and corresponds to the total visibility variation. A quantitative DFI measurement is possible within the green wavelength band in which the visibility did not drop below 20 % of its maximum value V_{max}.

The overall wavelength dependence of the visibility is finally given by:

$$V\,(\lambda) = V_0 V_{\mathrm{T}}(\lambda,d) V_{\mathrm{G0}}(\lambda) V_{\mathrm{G2}}(\lambda) \ . \tag{4.37}$$

V_0 can be interpreted as maximal achievable visibility of the setup, which depends on the quality of the gratings [151], the coherence of the beam hitting G_1 [152], and the smearing of the interference pattern due to the beam divergence [121]. The visibility $V(\lambda)$ as function of the wavelength is plotted in Fig. 4.13 for a set of actual setup parameters (see Sec. 5.1.2). Additionally, the single contributions $V_T(\lambda,d)$, $V_{G0}(\lambda)$, $V_{G2}(\lambda)$ are shown. The resulting visibility is a peaked function with a maximum around 4 Å and a fast degradation towards higher and lower wavelengths. Compared to V_T, the resulting visibility V is reduced and slightly shifted to higher wavelengths by the finite transmission through the absorption gratings. If one assumes that the visibility should not drop below one fifth of its maximum value in order to obtain a sufficient signal-to-noise ratio in the DFI [128], a quantitative DFI investigation is only reasonable between 2 and 6 Å. Hence, wavelength-dispersive dark-field imaging allows to map the correlation function only in the range of $(\frac{\xi_{GI}}{2},\frac{3\xi_{GI}}{2})$ around its value ξ_{GI} of maximum visibility.

4.4.2. The effects of the setup distance onto the visibility

The second possibility to change the correlation length, is by tuning the effective sample-to-detector distance L_s^{eff}. However, for the configuration that is mostly used, where the sample is positioned between G_0 and G_1, an increasing of L_s only slightly reduces L_s^{eff} and hence ξ_{GI} (compare Eq. 4.15). A stronger influence on the correlation length ξ_{GI} arises from the total length of the grating setup $L+d$. This parameter cannot be arbitrarily changed, though, because: (i) L and d have to fulfill the theorem of intersecting lines [126]:

$$p_0\frac{d}{L} = p_2 \ , \tag{4.38}$$

to guarantee that the interference pattern originating from different slits of G_0 are constructively superimposed onto the detector (See. Fig. 4.14 (a)), and (ii) L and d have to be scaled according to:

$$\frac{d}{L} = \left(\frac{2p_2}{p_1} - 1\right) = \text{const.} \ , \tag{4.39}$$

since otherwise the interference pattern would be magnified onto the grating G_2, which would result in vertical Moiré-fringes at the detector (see Fig. 4.14 (b) and caption within)[1]. Therefore, L and d have to be scaled equally.
In Fig. 4.15, the visibility according to Eq. 4.37 is plotted for arbitrary wavelengths and distances under the condition that d/L remains constant. The orange line

1 Moiré-fringes are periodical patterns that develop when periodic objects are overlaid in a slightly misaligned way. If the reader is interested in a visualization, he might take a look onto a curtain nearby.

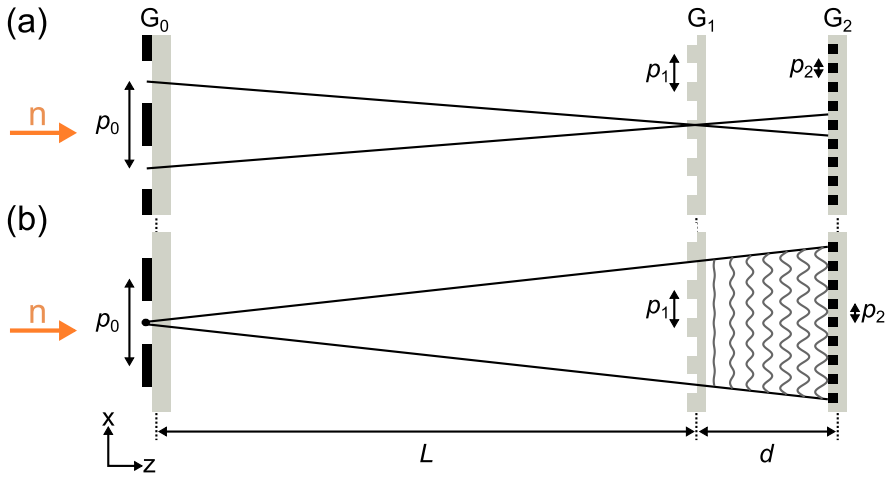

Figure 4.14.: Geometrical restriction on an nGI. Illustrated are the nGI setup, consisting of the source, phase and analyzer grating. (a) The distances L, d, p_0 and p_2 have to fulfill the theorem of intersecting lines 4.38 to ensure that the interference patterns from different slits are constructively added together. (b) The neutron wave front emanating from the slits of G_0 is slightly spherically distorted, leading to a cone beam geometry. The interference pattern produced by G_1 will be consequentially magnified and the periodicity of the intensity modulation behind this grating (black waved lines) increases with the distance. Therefore, if the magnification relation 4.39 is not fulfilled, the periodicity of the interference pattern and p_2 will not match, resulting in Moiré patterns at the detector.

again surrounds the parameter space with $V > 0.2V_{\max}$ and thus marks the region where an nGI scan is possible.
Clearly, the distance d can be varied between 5 and 25 mm and hence, the total length of the setup is fairly adjustable as well. However, for a given fixed L_S, the correlation length will vary according to

$$\xi_{GI}(d) = \frac{\lambda}{p_2}\left[\frac{2p_2 d}{p1} + L_s(1 - \frac{2p_2}{p1})\right] , \tag{4.40}$$

and in this way, a distance variation can only provide a moderate extension of the probed correlation length.
The above results implicate that a general structure determination is limited in grating based methods by the restrictions on the probed correlation length ξ_{GI}. Nonetheless, the quantitative DFI approach provides spatially resolved information which are strongly complementary to results from scattering methods such as SANS and USANS. Structural information obtained by means of these scattering techniques can be used to determine an averaged correlation function [108] of the microstructure, which can then be checked by means of nGI for local deviations in e.g. shape, concentration or structure size. In addition, an nGI is surprisingly

stable to a variation of the setup parameters and can flexibly be adjusted to different experimental conditions.

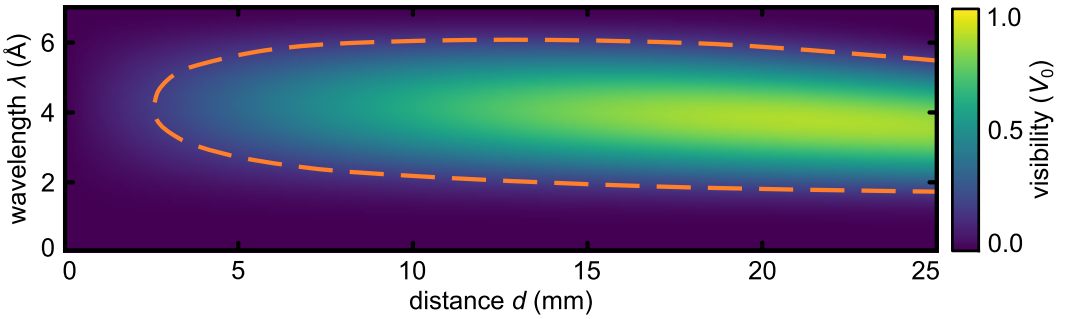

Figure 4.15.: Visibility as a function of the wavelength and the G_1-G_2-distance d. Data were calculated using Eq. 4.37 for typical setup parameter (see Sec. 5.1.2). It was assumed that d/L is kept constant. The maximum accessible distance d within the nGI setup has been assumed to be $25\,\mathrm{mm}$. The orange dotted line corresponds to a visibility reduction to $20\,\%$. Within the line, the visibility is sufficient for an nGI measurement. Hence, an nGI can be flexibly adopted to various setup geometries.

4.5. Ultra-small-angle neutron scattering using a Bonse-Hart camera

A conventional pinhole SANS instrument is not capable of probing the micrometer length scale of superconducting domains, since the corresponding neutron scattering angles of a few 0.1 mrad (momentum transfer $q_{\mathrm{min}} \approx 1 \times 10^{-4}\,\mathrm{Å}^{-1}$) cannot be resolved without the use of additional focusing neutron optical devices [107]. Instead, ultra-small-angle neutron scattering using a Bonse-Hart camera [153] has become the standard tool for the investigation of such low scattering angles and allows to cover a q-range down to $1 \times 10^{-5}\,\mathrm{Å}^{-1}$.
As shown in Fig. 4.16, a Bonse-Hart camera is a double crystal diffractometer: Neutrons are Bragg reflected by a monochromator crystal onto the scattering sample. Behind the sample, the angular distribution of the neutron beam is measured by rotating an analyzer crystal, which is known as 'rocking scan'. The difference in the angular intensity variation without (a) and with (b) a sample introduced to the diffractometer correlates with its neutron scattering function.
For an infinitely thick and transparent single crystal, the reflectivity function R_D around a nuclear Bragg peak is given as [154]:

$$R_D(y) = \begin{cases} 1 & |y| \leq 1 \\ \left(|y| - \sqrt{y^2 - 1}\right)^2 & |y| > 1 \end{cases} \tag{4.41}$$

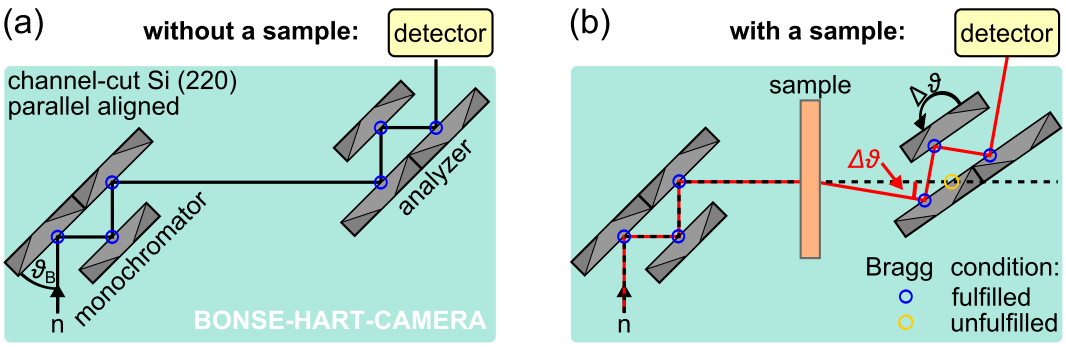

Figure 4.16.: Illustration of a Bonse-Hart camera. (a) Top view of the empty setup. In principle, a Bonse-Hart camera is a double crystal diffractometer, but with channel-cut crystals that scatter the neutron beam multiple times. Neutrons that were initially Bragg scattered at an angle ϑ_B within the first monochromator crystal, will be deflected by the analyzer into the detector if the crystals are oriented perfectly parallel. (b) If a sample is introduced between the crystals, a part of the neutrons will be scattered and the analyzer has to be rotated by the corresponding scattering angle to deflect these neutrons into the detector.

in which $y = (\vartheta - \vartheta_\mathrm{B})/\delta\vartheta_\mathrm{D}$ is the angular parameter depending on the incidence angle ϑ and the Bragg angle ϑ_B of the corresponding crystal plane. The Darwin width $\delta\vartheta_\mathrm{D}$ depends on the Debye-Waller factor, the structure factor and the angle of the corresponding Bragg reflection. It typically lies in the range of 1×10^{-2} mrad. The reflectivity curve of a crystal according to Eq. 4.41 is shown in Fig. 4.17 (a). Clearly, the Darwin width can be interpreted as half the angular range of total reflection. However, the single reflectivity curve R_D is not a perfect rectangular function, but has broad wings outside the Darwin plateau. If the finite thickness of the monochromator and analyzer crystals is additionally taken into account, the angular distribution will be smeared out further, due to successive scattering at the back and front faces of the crystal. The necessary corrections of Eq. 4.41 have been derived in Ref. [155] to:

$$R_E(y) = \frac{2R_\mathrm{D}(y)}{1 + R_\mathrm{D}(y)} \ . \tag{4.42}$$

This result corresponds to the reflectivity curve for thin crystals originally derived by Ewald [156]. It is additionally plotted in Fig. 4.17 (a).
The angular resolution of a double crystal diffractometer is given by the width of the rocking curve. It is calculated as the convolution of the reflectivity curves of the monochromator (M) and analyzer (A) crystal [157]:

$$I(\Delta\vartheta) = \int_{-\infty}^{\infty} R_\mathrm{E}^\mathrm{M}(y(\vartheta)) R_\mathrm{E}^\mathrm{A}(y(\vartheta - \Delta\vartheta)) dy \ . \tag{4.43}$$

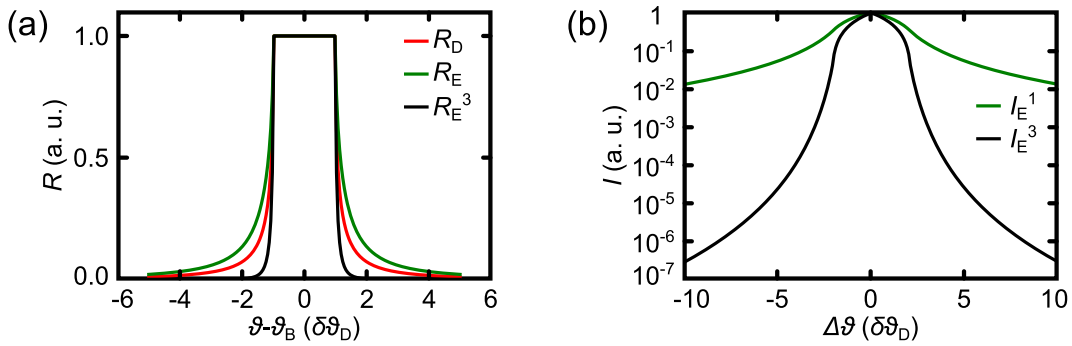

Figure 4.17.: Reflectivity of a single crystal and rocking curve of a double crystal monochromator. (a) Reflectivity curve for a single Bragg reflection at an infinitely thick crystal R_{D}, a single Bragg reflection of a thin crystal R_{E}, and a triple Bragg reflection at a thin crystal R_{E}^3. (b) Rocking curves of a double crystal diffractometer consisting of single and triple-bounce crystals, respectively.

Here, $\Delta\vartheta$ is the angular difference between the crystal orientations. The rocking curve of a double crystal monochromator with a single Bragg reflection I_{E}^1 is shown in Fig. 4.17 (b). Clearly, the angular resolution of the diffractometer is influenced by the Darwin width, but, more importantly, by the wings of the reflectivity curves outside the Darwin plateau. Consider e.g. an angle of $\approx 10\delta\vartheta_{\mathrm{D}}$ that corresponds to typical scattering angles measured by USANS. The rocking curve only drops down to 1 % of its maximum value, which is highly insufficient to measure weakly scattering samples.

In a Bonse-Hart camera, the single reflecting crystals are replaced by channel-cut crystals in which the neutron beam is reflected m-times. In this way, the reflectivity curve of the crystals is given by $I_{\mathrm{E}}^{\mathrm{m}}$. As shown for the case $m = 3$ in Fig. 4.17, the manifold reflection suppresses the wings in the reflectivity curve (a) and strongly reduces the background in the rocking curves (b), which finally enables the measurement of USANS. However, in a realistic Bonse-Hart camera, the simple channel-cut crystals have to be carefully surface treated and slightly modified by additional shielding in order to reduce parasitic effects by surface induced, air and thermal diffused scattering. Details can be found in Ref. [31]. A typically used, modified crystal geometry is shown in Fig. 4.18 (a), in which it is tried to block all neutron trajectories that deviate from the triple-bounce path.

In a USANS experiment, rocking curves have to be measured for the empty beam (I_{EB}) and for the sample inserted to the diffractometer (I_{SA}). The scattering curve is then calculated according to [158]:

$$I\left(q_{\mathrm{x}}\right) = I_{\mathrm{SA}}\left(q_{\mathrm{x}}\right) - T_{\mathrm{rock}} I_{\mathrm{EB}}\left(q\mathrm{x}\right) \ , \tag{4.44}$$

as the rotation angle of the analyzer corresponds to the measured scattering angle (compare Fig. 4.16 (b)). T_{rock} is the measured transmission of the sample.

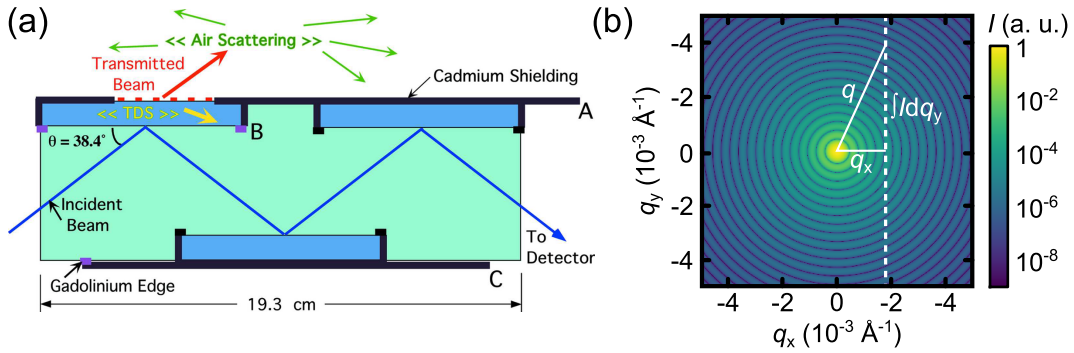

Figure 4.18.: Details of USANS. (a) Top view of a typical analyzer crystal. Several modifications are necessary on a simple channel-cut design to reduce parasitic effects increasing the background in a rocking scan. Cadmium and Gadolinium shielding on the back faces and the edges of the crystal, prevent neutrons which were scattered in the surrounding air or which were thermally diffused scattered (TDS) within the crystals to reach the detector. Reprinted from [157] with permission of the International Union of Crystallography. (b) The effect of slit-smearing in a USANS experiment. Shown is the differential scattering cross-section of a system of diluted spheres of radius $1\,\mu\mathrm{m}$. The rocking curve of a Bonse-Hart camera is insensitive to scattering components in vertical direction y. Hence, the measured rocking curve for a given q_x is the integral of the differential scattering cross-section along the q_y-direction (dashed white line).

The Bonse Hart technique strongly decreases the measurable momentum resolution to the $1 \times 10^{-5}\,\text{Å}^{-1}$ regime, while still providing sufficient counting rates. This is caused by three reasons: Firstly, a rather polychromatic neutron spectrum can be used, as the reflection on the monochromator introduces an angular-wavelength correlation to the neutron beam that is completely canceled by the analyzer [159]. Secondly, contrary to SANS, the resolution in USANS is independent of the aperture size. Finally, the high momentum resolution in horizontal q_x-direction is reached at the expense of resolution in vertical direction. Hence, a point of a USANS rocking curve corresponds to the integration in q_y-direction of all scattering vectors that have the same q_x-component (see Fig. 4.18 (b)). Consequently, the scattered intensity is proportional to the slit-smeared differential scattering cross-section defined in Eq. 3.33.

5. Experimental details

In the following chapter, the technical details of the experimental methods used in this thesis are considered with a focus on the neutron grating interferometer that has been newly implemented at the ANTARES beamline at Heinz Maier-Leibnitz Zentrum (MLZ). The experimental setup is introduced, the manufacturing of the gratings is discussed and the instrument is extensively characterized in terms of visibility and particle size sensitivity. A comparison to the nGI of the ICON beamline at the Paul-Scherrer-Institut (PSI) is given, since parts of this thesis are based on results obtained with this instrument. Furthermore, the sample environment, which has been used in most of these studies, will be presented. The section will close with a brief summary of the (ultra-)small-angle neutron scattering instruments BT-5 at the National Institute of Standard and Technology (NIST), SANS-1 and KWS-3 at the MLZ, and TPA at the Laboratoire Léon Brillouin (LLB), where experiments were conducted during this thesis.
Parts of this chapter have been already published in [147].

5.1. The neutron grating interferometer at the ANTARES beamline

5.1.1. The ANTARES beamline

ANTARES is a multi-purpose imaging beamline located at the beam port 4a of the FRM II reactor [160]. It provides a mixed spectrum of cold and thermal neutrons, peaked at $\lambda = 1.3\,\text{Å}$ [161]. The pinhole diameter can be varied between 2 and 36 mm to adjust the geometrical resolution of the instrument (Sec. 4.1). A drawing of the beamline is shown in Fig. 5.1[1]. The beamline is separated in three chambers. The first chamber (a) contains various beam shaping devices: a neutron velocity selector (Astrium NVS) providing a minimum wavelength of 2.95 Å with a wavelength spread $\Delta\lambda/\lambda$ of 10 %, a double crystal monochromator (1.4 Å -6.0 Å, $\Delta\lambda/\lambda \approx 3$ %), and a neutron filter wheel which includes a bismuth, a lead, a sapphire and a beryllium filter.
Helium filled flight tubes transport the neutron beam to the remaining chambers

1 Furthermore, a Cartesian coordinate system is defined in this figure, which will be used in the remainder of this thesis. The z-axis corresponds to the direction of the neutron beam, while the y-axis defines the vertical direction.

(b & c), each of which contains a sample position equipped with a neutron imaging detector, which is composed of a ^{6}LiF/ZnS scintillator and a CCD camera (Andor IkonL 4Mpix). The maximal achievable neutron flux amounts to $1 \times 10^8\,\mathrm{cm^{-2}s^{-1}}$ at L/D = 400.

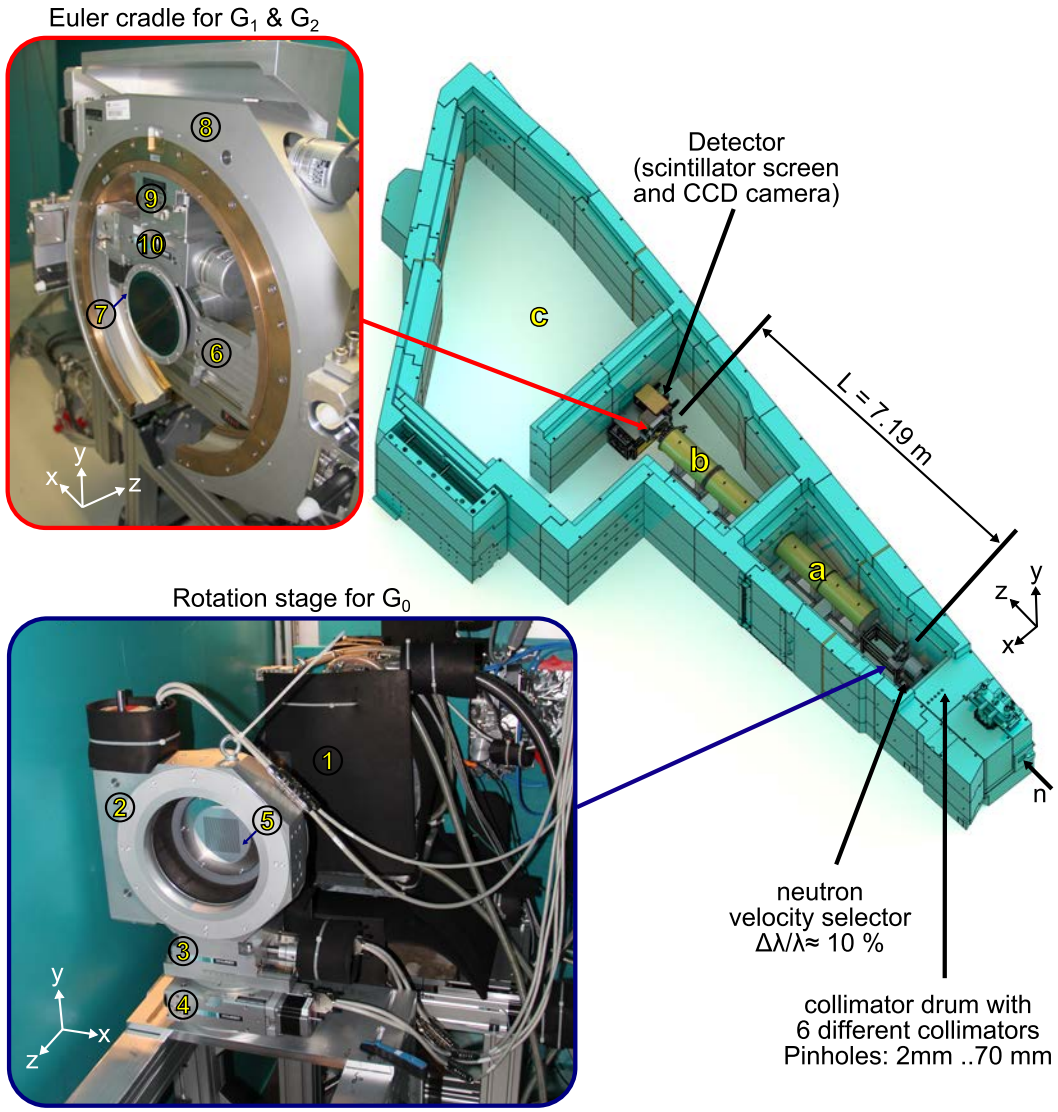

Figure 5.1.: The nGI-setup at ANTARES: Drawing of the ANTARES beamline, showing the main components of the nGI. a: Beam formation chamber, b: Chamber 1, c: Chamber 2, 1: Neutron wavelength selector, 2: Horizontal z-rotation stage of G_0, 3: Linear x-translation stage, 4: Vertical y-rotation stage, 5: Grating G_0, 6: Mounting of G_2, 7: Grating G_1, 8: z-Euler cradle of G_1 and G_2, 9: z-translation stage of G_1 and 10: z-goniometer head for G_1.

5.1.2. The nGI setup

For the absorption grating G_0, a polished, single crystalline quartz wafer (diameter = 102 mm, thickness = 1 mm) was used as substrate. An adhesive layer of 25 nm chromium followed by a neutron absorbing layer of 20 µm gadolinium and a protective cover layer of 50 nm aluminum was deposited onto the wafer by Ar sputtering. Gd has been chosen as absorbing material, because it has the highest absorption cross-section for thermal and cold neutrons [150]. The grating lines were subsequently incorporated into the layers by laser ablation. The resulting absorption grating has a periodicity of $p_{G0} = 1.6$ mm and a duty cycle DC_0 of 0.4. It is shown in Fig. 5.2 (a). The grating is mounted in a rotation stage (see Fig. 5.1), allowing for 360° rotation around the beam axis. Furthermore, the grating can be rotated around y by an angle χ_{G0} to change its effective periodicity $p_0 = p_{G0}\cos(\chi_{G0})$ seen from the detector. The whole G_0 setup is mounted on an x-translation stage, allowing a high precision movement perpendicular to the neutron beam.

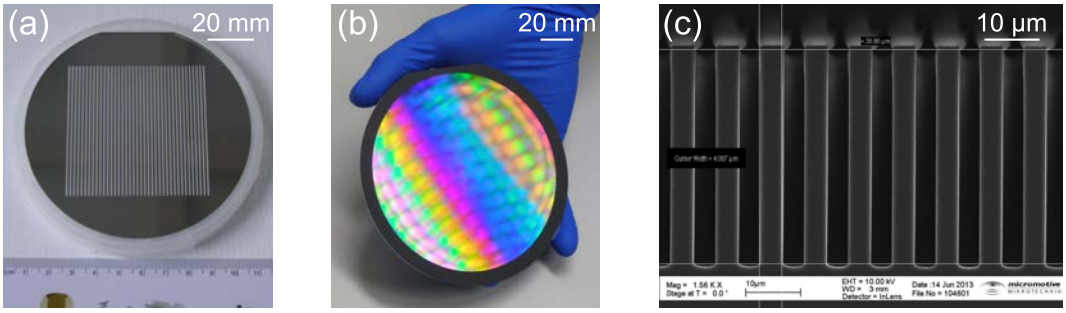

Figure 5.2.: Gratings G_0 and G_1. (a) Picture of the absorption grating G_0 which has been incorporated into a 50 nm Al/20 µm Gd/25 nm Cr layer by laser ablation. (b) Picture of the phase grating G_1 which has been structured into an Si single crystalline wafer. (c) Cross-sectional SEM image of the grating structure of G_1 (by courtesy of Micromotive Mikrotechnik [162]).

The phase grating G_1 is made from Si, since this material reveals negligible attenuation for neutrons [150]. The grating was commercially obtained from Micromotive Mikrotechnik [162]. The rectangular grating lines were dry etched into the surface of the Si wafer (diameter = 127 mm, thickness = 0.5 mm), leading to a grating periodicity of $p_1 = 7.98$ µm, a duty cycle of 0.5 and a structure height of $h_1 = 43$ µm. A picture as well as a scanning electron microscope (SEM) image of the grating are shown in Fig. 5.2 (b) and (c), respectively.
The fabrication of the analyzer grating G_2 is most challenging, since it has the smallest periodicity. So far, these gratings were produced following the method described in [122], in which Gd is sideways evaporated onto a Si grating with the required periodicity p_2. However, especially for large wafers, this procedure results in an inhomogeneous distribution of Gd on the substrate. To avoid this

inhomogeneity, a different approach based on Ar sputtering has been followed, which is illustrated in Fig. 5.3 (a): A collimator was introduced between the Gd sputtering target and the substrate grating, which is continuously moved back and forth during the sputtering. The substrate grating has been structured on top of a 127 mm diameter Si wafer similar to G_1, and has a periodicity of $p_2 = 4\,\mu m$, a height of 6 µm, and a grating line thickness of 1 µm. The collimator consisted of thin brass lamellae inclined at $\varepsilon = 25°$. In this geometry, only Gd atoms leaving the target at an angle of $\varepsilon = 25 \pm 2.5°$ can reach the substrate, allowing for a specific sidewall deposition. An SEM image of the resulting grating is shown in Fig. 5.3 (b). The image was recorded on the cross-section of a small 1 cm × 2 cm test piece of the grating covered with 3 µm of Gd. A well defined absorption grating was obtained. On top of the Si lines, the angle ϑ is recovered as the diagonal of the Gd deposition. The height of the Gd lines amounts to $h_2 = 9\,\mu m$ resulting in a maximal neutron transmission of 7 % at $\lambda = 3.5$ Å. The sputtered G_2 revealed a total neutron transmission of 59 % at $\lambda = 3.5$ Å with an inhomogeneity of ±1.5 % over the whole grating. Hence, an effective duty cycle can be calculated by $DC_2 = \frac{59\,\%-7\,\%}{1-7\,\%} = 0.56$. The gratings G_1 and G_2 are mounted together on a large Euler cradle, which is situated in the second chamber right in front of the detector (compare Fig. 5.1). This setup allows a simultaneous rotation of both gratings around the beam axis. Furthermore, G_1 is fixed on a goniometer head and a linear stage, which enables to tune the distance d of the gratings and to rotate G_1 against G_2, which is necessary to adjust the setup.

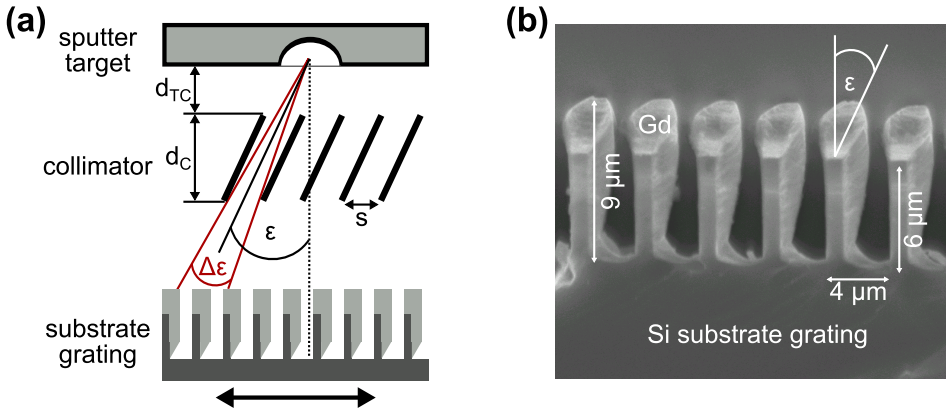

Figure 5.3.: The fabrication of G_2 by Gd sputtering on an Si grating: a: Schematic of the sputtering geometry ($d_{TC} = 29\,mm$, $d_C = 10\,mm$ and $s = 4.1\,mm$) b: SEM cross-sectional image of the obtained Gd absorption grating.

5.1.3. Geometry of the nGI setup at ANTARES

In x-ray grating interferometry, especially at a synchrotron source, the setups are mostly optimized to exhibit a maximum visibility. This is guaranteed as long as the geometric relations of Sec. 4.4.2 are fulfilled and d corresponds to a fractional Talbot distance [122]. However, neutron radiography suffers from the low neutron flux available, even at high brilliance neutron sources. Therefore, the setup optimization cannot be based on visibility considerations only, as a reduction of the setup length will strongly increase the neutron flux ($\propto (L+d)^2$) at the sample position. Based on these considerations, the setup length $L+d$ has been reduced. As discussed in Sec. 4.4.2, this is possible, as long as the ratio L/d is kept constant. The setup parameters were subsequently adjusted according to Eq. 4.37 to maximize the visibility for this setup length. In Tab. 5.1, the actual parameters are shown and compared with the parameters calculated according to Ref. [122] in which the neutron flux has not been considered. By using Eq. 4.37, the maximum visibility reduction caused by these improvements can be quantified to only 1.5 %. However, this is compensated by a flux enhancement of 24 % at the detector, due to a reduced distance to the pinhole.

parameter	**value according to Ref. [122]**	**actual value**
λ	3.5 Å	4.0 Å
p_0	1.596 mm	1.596 mm
DC_0	0.4	0.4
p_1	7.98 µm	7.98 µm
p_2	4.00 µm	4.00 µm
d	22.7 mm	18.0 mm
L	9.10 m	7.19 m

Table 5.1.: Parameters of the nGI setup: λ neutron wavelength, p_i periodicity of grating G_i, DC_0 duty cycle of G_0, L distance between G_0 and G_1 and d distance from G_1 to G_2.

5.1.4. Visibility of the nGI setup at ANTARES

Fig. 5.4 (a) shows the wavelength dependence of the visibility of the setup. As the neutron velocity selector is unable to reach wavelengths below 2.95 Å in its default configuration (wavelength spread $\Delta\lambda/\lambda = 0.1$), the NVS was tilted by 5° to access lower λ [163] in a second scan. However, this is accompanied by an increase of $\Delta\lambda/\lambda$ to 0.2. The visibility was determined for each pixel from a stepping scan over one period in 9 ($\Delta\lambda/\lambda = 0.2$) or 8 steps ($\Delta\lambda/\lambda = 0.1$), respectively, and subsequently averaged over the whole image. The exposure time was set to 80 s per step. The maximum of the visibility is found between $\lambda = 3.9$ Å and $\lambda = 4.0$ Å.

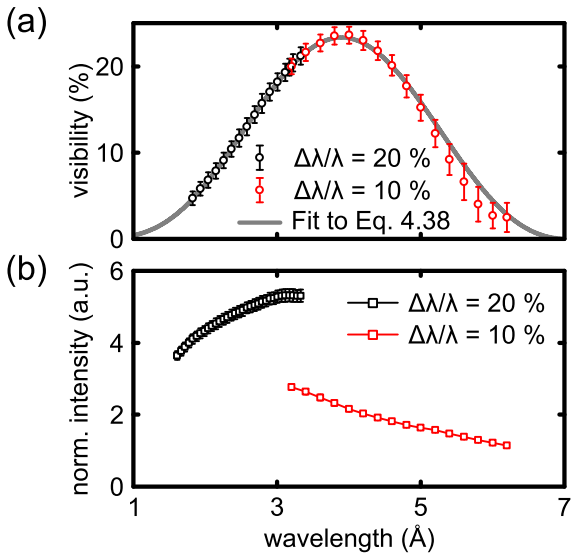

Figure 5.4.: Characterization of the nGI: Visibility of the current setup (a) and normalized intensity at the detector (b) vs. wavelength for two different $\Delta\lambda/\lambda$. The visibility was extracted by averaging the visibility of the full field of view. Error bars correspond to the standard deviation of the visibility. The intensity was determined at a scintillator position next to the gratings and normalized to the exposure time. Error bars correspond to the statistical counting error.

The data were fitted using Eq. 4.37 and the setup parameters defined in Tab. 5.1 and Sec. 5.1.2. The maximal achievable visibility V_0 has been determined to be $28.2\,\%$[1, 2].
The trend of the visibility is very well described by the derived relation 4.37, although the wavelength was not purely monochromatic. Deviations from the monochromatic visibility V are, however, expected to be smaller than $1\,\%$ for $\Delta\lambda/\lambda = 0.1$ and $1.7\,\%$ for $\Delta\lambda/\lambda = 0.2$ in the particular wavelength range [147]. Hence, the deviations caused by the finite wavelength spread of the NVS lie well below the error bars obtained in Fig. 5.4. Therefore, especially below $\lambda = 3.3\,\text{Å}$, it is preferable to perform experiments with a higher wavelength spread, as the gain in the detected intensity is a factor of 2 in the case of increasing $\Delta\lambda/\lambda$ from $10\,\%$ to $20\,\%$ (see Fig. 5.4 (b)).

1 V_0 is the parameter defined in Eq. 4.37 which describes $V\,(\lambda,d)$, not the maximum of the curve shown in Fig. 5.4 (a), in which $V\,(\lambda,d = \text{const.})$ has been measured.
2 Note that a theoretical limit of 0.5 exists for the visibility of the ANTARES setup [121]. This value is not reached, since the transmission profile of the analyzer grating is not binary. However, this visibility is comparable to values reached at other facilities [120].

5.1.5. The sensitivity of the DFI to structures of different sizes

In order to define the sensitivity of the DFI contrast to different structure sizes, it has been proposed to use diluted spherical particles as reference material [134]. Although the DFI contrast might be slightly different for arbitrarily shaped microstructures, this referencing has general significance for diluted systems. The reason is the discussed property of the correlation function G (Eq. 3.39) to decay to zero at the longest distance characterizing the microstructure, which is the diameter for spheres (see e.g. Ref. [108]). The DFI sensitivity to different structure sizes can be calculated via Eq. 4.26 with the correlation function and macroscopic cross-section of spheres already given in Eq. 3.45 and 3.48.
Following the discussed approach, nGI experiments were performed on different, diluted mono-dispersed polystyrene particles, similar to the ones used in Ref. [148]. The spherical particles with a diameter of 110 nm, 510 nm, 740 nm, 1.0 µm, 2.0 µm, 3.0 µm, 4.0 µm and 5.0 µm, respectively, were dissolved in a mixture of 56 % H_2O and 44 % D_2O, and each sample was filled in a 5 mm thick quartz cuvette. The particle volume concentration ϕ_V was set to 9 % for each particle diameter. $\Delta\rho$ has been calculated to be $1.082 \times 10^{14}\,\mathrm{m}^{-2}$ [164]. nGI scans (16 steps, 1 period p_0, exposure time per step = 60 s) were performed on all of the colloides and on three cuvettes filled with H_2O, D_2O and the H_2O/D_2O solvent, respectively.

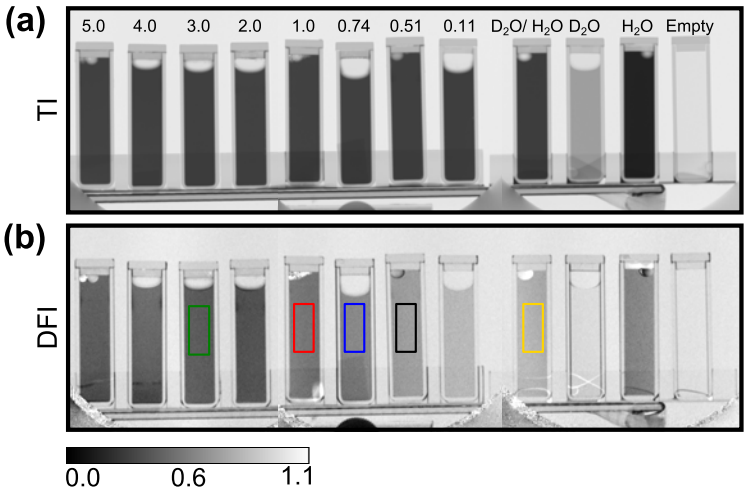

Figure 5.5.: DFI sensitivity to different particle sizes. TI (a) and DFI (b) of cuvettes filled with diluted spherical colloids of different diameters, an empty cuvette and three cuvettes filled with H_2O, D_2O and H_2O/D_2O, respectively. The particle diameters in the figure are given in units of µm. The images were merged from different TIs and DFIs recorded at $\lambda = 3$ Å. Clearly, the DFI contrast depends on the diameter of the spheres, whereas the TI contrast is not influenced by the particle size.

Fig. 5.5 (a) and (b) show the TIs and DFIs of all the samples, respectively, taken at a wavelength of 3 Å. The images were merged from three TIs (DFIs), recorded

separately. The TI contrast is identical for all colloids, as their chemical composition and concentration is equal. In contrast, the DFIs shown in Fig. 5.5 (b) reveal strong deviations in the signals of the different colloids: the high contrast for the 0.1 µm particles strongly decreases with enhanced particle sizes. To quantify the contrast degradation, Fig. 5.6 (a) shows the average DFI of the colloids as function of the particle diameter $d_{\mathrm{col}} = 2R$ for a neutron wavelength of 3.9 Å, corresponding to the value generating maximal visibility (see Sec. 5.1.4). To eliminate the DFI contrast contribution arising from incoherent scattering at the hydrogen within the solvent [148], the DFI values were normalized to the DFI within the H_2O/D_2O mixture taken to the power of 91 %. This fractional normalization accounts for the fact that in the colloids 9 % of the solvent are replaced by polystyrene but is slightly different to the normalization performed in Ref. [148][1].

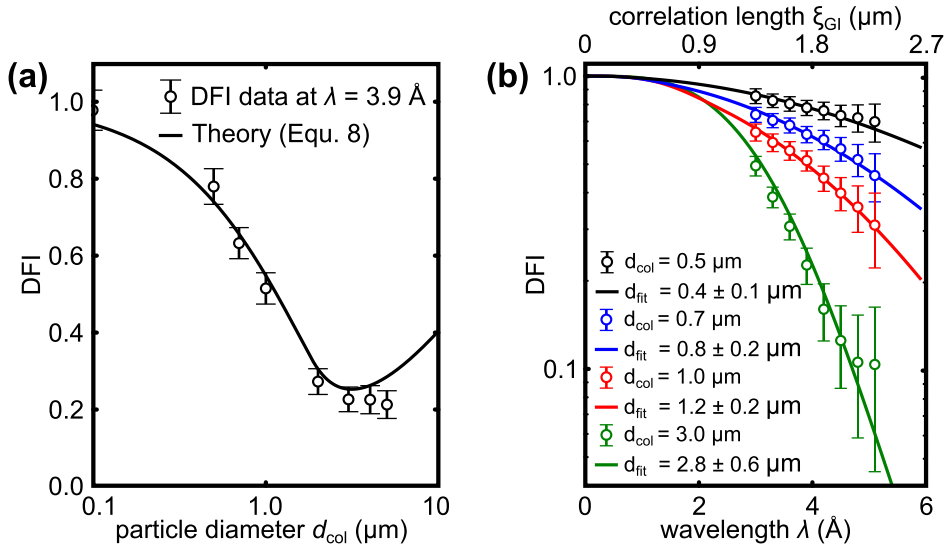

Figure 5.6.: Quantitative evaluation of the DFIs vs. wavelength. (a) DFI versus particle diameter of the colloids at $\lambda = 3.9$ Å. The averaged DFI within each colloid was normalized to the contrast of the H_2O/D_2O mixture. The solid curve represents the theoretical sensitivity calculated for spherical particles. Error bars are calculated by error propagation from the DFI standard deviation in the probed areas. (b) Wavelength dispersive imaging of the colloids. The DFI signal was averaged within the regions marked in Fig. 5.5 (b), normalized to the DFI contrast of the H_2O/D_2O mixture (yellow box) and plotted against the wavelength. The data were fitted according to Eq. 3.45 and 3.48. The d_{fit} values are given in the legend. Error bars are calculated by error propagation from the DFI standard deviation in the probed areas.

The DFI contrast clearly decreases from nearly unity at a particle diameter of

1 As the effective thickness of the incoherently scattering solvent is reduced by 10 %. However, the correct normalization of DFI data is still a question of debate that is currently investigated.

0.11 µm towards 0.2 at 3 µm, in agreement with the theory curve calculated by introducing Eqs. 3.45 and 3.48 into 4.26. The expected increase of the DFI for large d_{col} cannot be deduced from the presented data of colloids with $d_{\mathrm{col}} < 5\,\mu\mathrm{m}$, but has been observed for larger particles in Ref. [148]. The data clearly confirms that the DFI is insensitive to structures smaller than 0.1 µm and is mostly sensitive to particles in the micron range generating USANS scattering.
As discussed in Sec. 4.4, structural information about the samples' microstructure can be obtained by quantitative dark-field imaging. The accuracy of this approach is demonstrated in Fig. 5.6 (b) which shows the wavelength dependence of the DFI signal for colloids with particle diameter of 0.51 µm, 0.74 µm, 1.0 µm and 3.0 µm, respectively. The DFIs were normalized to the solvent as discussed above. The evaluated regions within the cuvettes are marked in Fig. 5.5 (b). The DFI data was fitted using Eq. 3.45 and 3.48, and the particle diameters of the colloids d_{fit} were determined. The resulting diameters are given in the figure.
In conclusion, the presented model describes the contrast variation well and provides a good estimate of the particle diameters. The data confirms the theoretical consideration on the DFI contrast and shows the potential of the nGI method. However, this size determination is based on the a priori knowledge of the underlying structure (shape, concentration and chemical composition).

5.1.6. Magnetic sample environment

For the investigation of superconducting samples, the nGI was combined with a cryomagnetic sample environment. The setup consists of a water-cooled electromagnet, reaching a maximal field of 0.4 T, and a cryostat (Fig. 5.7). The magnet was specially constructed to perform nGI experiments. It is characterized by a central bore of 84 mm to allow a large field of view, a compact design to reduce the sample-to-detector distance, and a passive magnetic shielding to avoid any influences of the magnetic field onto the mechanics of the grating interferometer. The inhomogeneity of the magnetic field is smaller than ±1.0 % over a sample volume of $2 \times 2 \times 2\,\mathrm{cm}^3$. Its maximum remanence has been determined to 0.6 mT. A hysteresis of the magnetic field can hence be excluded as origin of any hysteretic behavior observed in the sample[1].
Two kinds of cryostats were used: (i) a closed cycle cold head cryostat (Sumitomo SHI-RDK-2025D), and (ii) a closed cycle refrigerator cryostat. Both provide a base temperature smaller than 3.7 K. The sample temperature was monitored either by a Lakeshore Cernox CX-1030-CU or a CX-1050-CU, mounted near the sample. If not stated otherwise, the temperature stability amounted ±0.1 K.
The cryomagnetic sample environment was mounted on a sample stage, allowing for automated translation in y and x direction and vertical rotation around the

1 Further details on the magnetic homogeneity are given in App. A.4.

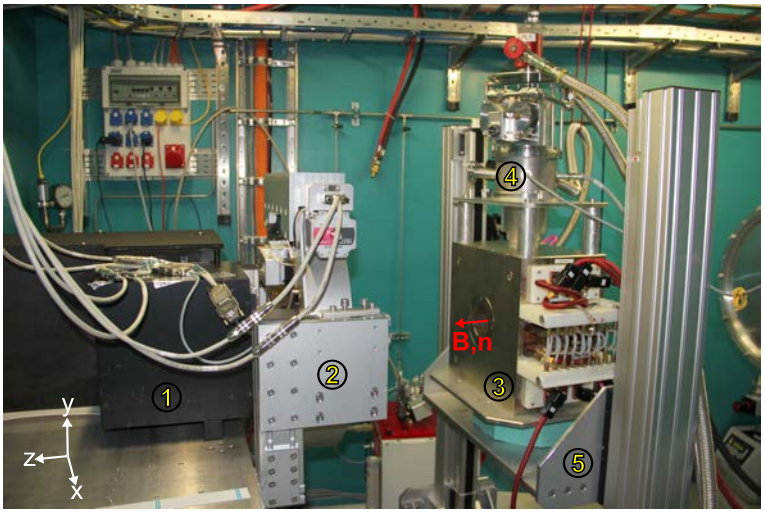

Figure 5.7.: nGI combined with a cryomagnetic setup at the ANTARES beamline. 1: Neutron imaging detector, 2: nGI (compare Fig. 5.1), 3: Water-cooled electro magnet, 4: Cold head cryostat, 5: Cryo-manipulator. For an nGI measurement, the magnet is placed immediately in front of the grating setup.

y-axis.
Although the magnet is shielded, the cryomagnetic setup slightly interferes with the grating setup mainly due to the heat which is caused by the magnet and the compressor of the cryostat. A small thermal drift in the grating alignment occurs as a consequence which can lead to weak Moiré-streaks in the nGI data. This effect is most pronounced for long exposures or a long time span between the data and the open beam images. In fact, this effect defines an upper boundary for the exposure time.

5.2. The neutron grating interferometer at the ICON beamline

The first nGI setup has been implemented at the ICON beamline [165] of the Swiss Spallation Neutron Source (SINQ) at the Paul-Scherrer-Institut [121, 122, 126]. Parts of the measurements included in this thesis were conducted at this setup. Compared to the ANTARES beamline, the neutron flux at the sample position of ICON is approximately eight times smaller for equal L/D=400. Its nGI parameters are given in Tab. 5.2. Although the setup length is slightly shorter, the sensitivity curves (Fig. 5.6 (a)) of both setups are nearly equal since similar correlation lengths are probed ($\xi_{\mathrm{GI}}^{\mathrm{ICON}}(L_{\mathrm{s}} = 90\,\mathrm{mm}) \approx 1.1 \times \xi_{\mathrm{GI}}^{\mathrm{ANTARES}}(L_{\mathrm{s}} = 90\,\mathrm{mm})$). Measurements revealed an only slightly higher visibility of approx. 25 % at the ICON setup, probably caused by the thicker analyzer grating. Yet, the setup has a smaller field of view of 64 mm×64 mm. Furthermore, as the neutron flux at the spallation

source is not constant over time, all images obtained at the ICON beamline have to be normalized to a region of the image, where neither G_1 nor G_2 are in the beam.

parameter	**value**	**parameter**	**value**
d	19.4 mm	L	5.23 m
λ	4.1 Å	$\Delta\lambda/\lambda$	15 %
p_0	1.076 mm	h_0	20 µm
p_1	7.97 µm	h_1	37 µm
p_2	4.00 µm	h_2	11 µm
DC_0	0.4	DC_1	0.5
DC_2	≈ 0.25		

Table 5.2.: Setup parameters of the nGI at the ICON beamline, taken from Ref. [121]

All experiments performed at PSI used the same sample environment as described in Sec. 5.1.6. Images of the grating setup and the sample position are shown in Fig. 5.8 (a) and (b), respectively. A drawback of the ICON beamline compared to ANTARES for investigations at low temperature is that the sample position was not decoupled from the grating setup. Hence, vibrations of the cold head cryostat strongly influenced the nGI performance and degraded the image quality.

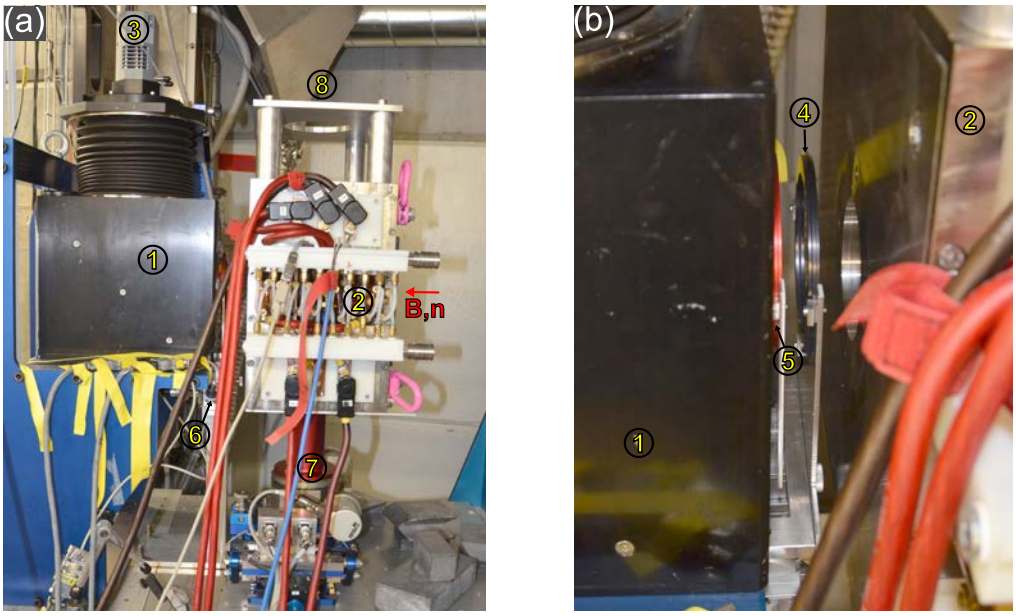

Figure 5.8.: The experimental setup at ICON. 1: Detector box including the scintillator and a mirror, 2: Electromagnet, 3: CCD-camera Andor DV434, 4: Grating G_1, 5: Grating G_2, 6: Goniometer heads and linear stage of G_1 and G_2, 7: Rotation stage for the cryomagnetic setup, 8: Holder for the cold head cryostat

5.3. The USANS beamline BT-5 at NIST

USANS experiments (compare Sec. 4.5) were performed on the BT-5 beamline at the Center for Neutron Research at the National Institute of Standards and Technology (NIST) [157]. Fig. 5.9 (a) depicts the instrument layout. The beamline is designed for a wavelength of 2.38 Å. To optimize both the neutron flux at the sample position and the signal-to-noise ratio, different beam shaping devices are implemented in the neutron beam: An Al_2O_3 sapphire filter (SF) is located close to the beam port to reduce the flux of fast neutrons. Higher order contamination of the beam is reduced by a pyrolytic graphite filter (GF). The neutron beam is focused onto the beam position by a doubly curved graphite (002)-oriented pre-monochromator (PM). The focusing leads to a peak neutron flux of $17\,300\,\mathrm{cm^{-2}s^{-1}}$ in the center of the beam at the sample position. The monochromator (M) and analyzer (A) consist of channel-cut Si crystals, grown by the float-zone technique. Each crystal uses a triple reflection at a (220) plane. The wavelength distribution of the reflected beam amounts $\Delta\lambda/\lambda = 5.9\,\%$ at the sample position. To prevent a misalignment of the crystals due to external vibrations, the whole Bonse-Hart camera is placed on a vibration isolated table (T), decoupled from the sample position. The detector composed of 5 counting tubes is shielded by 0.5 m high-density polyethylene. In total, a noise-to-signal ratio of 1×10^{-7} is achieved for $q > 5 \times 10^{-4}\,\mathrm{Å}^{-1}$ with a horizontal and vertical beam divergence of 7.4×10^{-6} rad and 0.023 rad per wavelength[1], respectively.
For USANS measurements, the sample was placed in a Janis closed cycle refrigerator reaching a base temperature of approximately 3.0 K. The temperature was controlled using a similar equipment as described in Sec. 5.1.6. To reduce USANS scattering at the aluminum tail, the cryostat possessed silicon single crystalline windows. The cryostat was placed in a water-cooled electromagnet reaching a maximum field of 0.5 T. The magnet revealed a high remanence of 5 mT, which necessitated a careful demagnetization after every field sweep.
The raw data were evaluated to the USANS scattering curves by using the Igor Pro USANS macro provided by NIST [158].

1 Since the crystals entangle the wavelength with the angle of reflection, the total divergence at the sample position is larger. This does not influence the resolution of the USANS method.

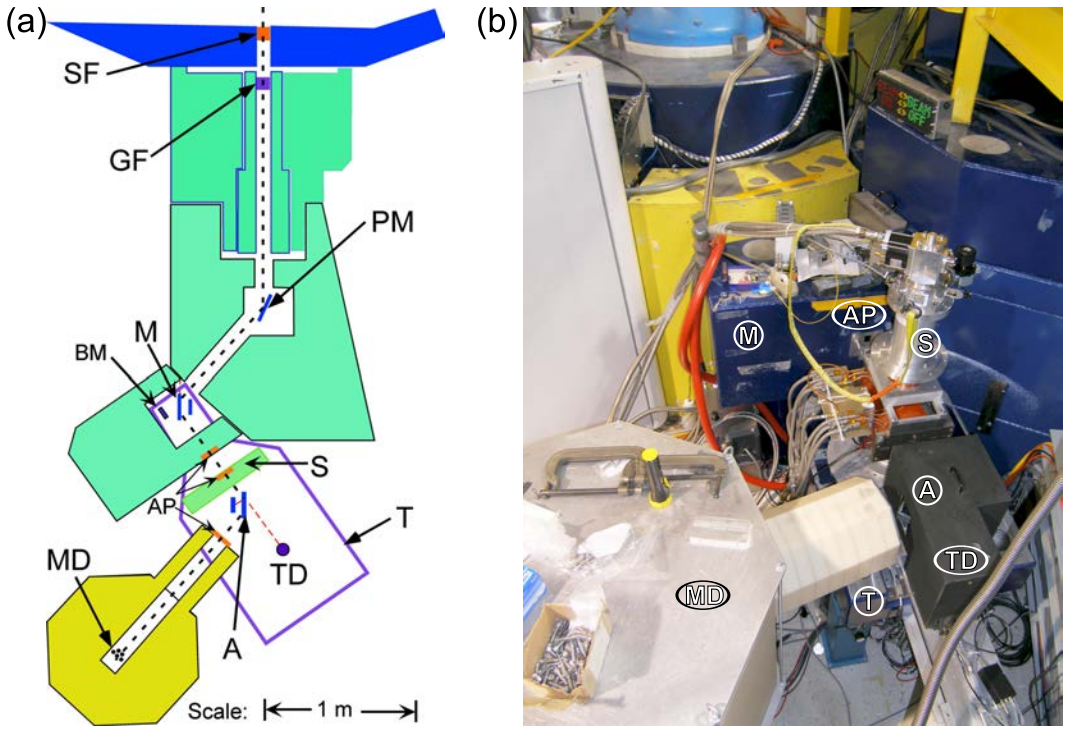

Figure 5.9.: The BT-5 USANS beamline at NIST. Drawing (a) and picture (b) of the beamline. SF: Sapphire filter, GF: Pyrolytic graphite filter, PM: Graphite premonochromator, M: Silicon monochromator, BM: Beam monitor, S: Sample position with cryostat and magnet, A: Silicon analyzer, TD: Transmission detector, T: Vibration isolation table, AP: Beam apertures, MD: Main detector. (a) is reprinted from [157] with permission of the International Union of Crystallography.

5.4. Small-angle neutron scattering at SANS-1, KWS-3 and TPA

Small-angle neutron scattering results discussed in this thesis were obtained at the SANS-1 [166] and the KWS-3 [32] instruments of the Maier-Leibnitz-Zentrum (MLZ), and the TPA beamline [167] at the Laboratoire Léon Brillouin (LLB).
SANS-1 is a pinhole instrument. Its setup is schematically sketched in Fig. 5.10: The neutrons are monochromatized by a neutron velocity selector providing a wavelength spread of 10 % in its standard configuration. The sample is placed downstream a 20 m collimation distance which can be adjusted by the insertion of neutron guides. A 128 x 128 pixel position sensitive ^{3}He tube detector which provides a resolution of 8 mm, detects the neutron scattering pattern. The distance between detector and sample can be increased from 1.2 m up to 20 m, which allows to access a minimum q-range of 5×10^{-4} Å^{-1}. Further information on the beamline can be found in Ref. [168]. All SANS-1 experiments presented in this thesis were performed using a wavelength of $\lambda = 11.9$ Å and the maximum sample-to-detector

distance of 20 m. The cryomagnetic sample environment corresponded exactly to the one described in Sec. 5.1.6. Scattering data were evaluated using the software package Grasp 6.9 [169].

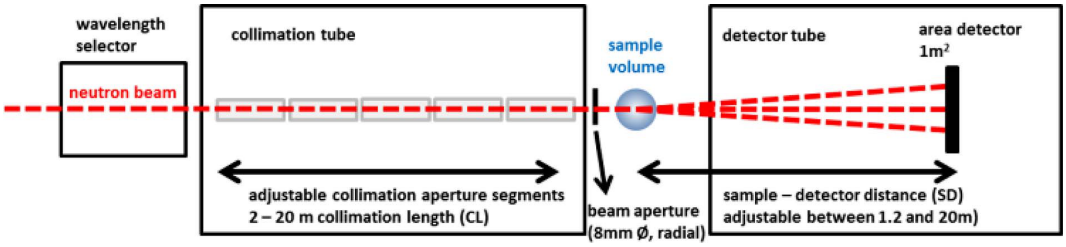

Figure 5.10.: Schematic view of the SANS-1 instrument at MLZ (Taken from Ref. [170]).

The minimal accessible wavevector on a pinhole SANS machine depends on the aperture size, as well as on the collimation and sample-to-detector distances. It is hence mainly limited by the neutron flux and the total setup length. A further expansion of the q-range can be obtained by the use of neutron focusing devices. At KWS-3, a toroidal focusing mirror is used for this purpose. A schematic sketch of the instrument is presented in Fig. 5.11: The neutron beam is shaped by an entrance aperture after passing the neutron velocity selector ($\Delta\lambda/\lambda = 20\,\%$). Afterwards, these neutrons are focused on a position sensitive detector by the toroidal mirror. The shape of this 1.2 m long neutron mirror covered with 80 nm ^{65}Cu is approximately elliptic, with the aperture and the detector located in its focal points (total focal distance 22 m). In this way, the q-resolution is expanded down to the 1×10^{-4} Å^{-1} range. Further information on the instrument is summarized in Ref. [171].

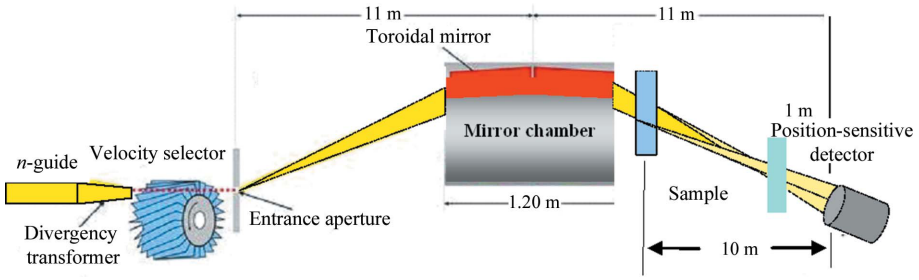

Figure 5.11.: Layout of the VSANS experiment KWS-3 at the MLZ (reproduced from Ref. [32] with permission of the International Union of Crystallography).

In the presented KWS-3 experiments, the sample environment described in Sec. 5.1.6 was placed in 8.5 m distance in front of the detector. With a neutron wavelength of 12.8 Å, the instrument was sensitive to length scales up to approximately 3 µm.

A different approach to decrease the accessible scattering angle is pursued at the TPA instrument. A scheme of the instrument is presented in Fig. 5.12: At TPA, neutron focusing is not achieved by mirrors or lenses. Instead, the initial beam is split into multiple beams by a pinhole mask. The individual beam fragments are each further collimated downstream by six successive masks, having pinhole diameters between 1.6 and 1.0 mm. These masks are arranged in a way that the multiple beams are superimposed in a single spot on the image plate detector. Hence, the neutron beam is not focused by reflection, like at the KWS-3 beamline, but filtered of all neutrons which would not have hit the detector in the focal point. In this way, a minimum momentum transfer of $2 \times 10^{-4}\,\text{Å}^{-1}$ can be reached. The advantage of the multibeam collimation design is a high flexibility in the choice of the neutron wavelength.
The experiments discussed in this thesis were performed using a neutron wavelength of 6 Å which has been selected via a double reflection supermirror ($\Delta\lambda/\lambda = 11\,\%$). The instrument was combined with a 7 T ^{4}He bath cryomagnet providing a base temperature of 3.5 K. The temperature was regulated by the usual combination of a cernox temperature sensor attached to the sample volume, and a Lakeshore 340 temperature controller for the resistive heating of the sample stick. The data evaluation has been performed using Grasp [169].

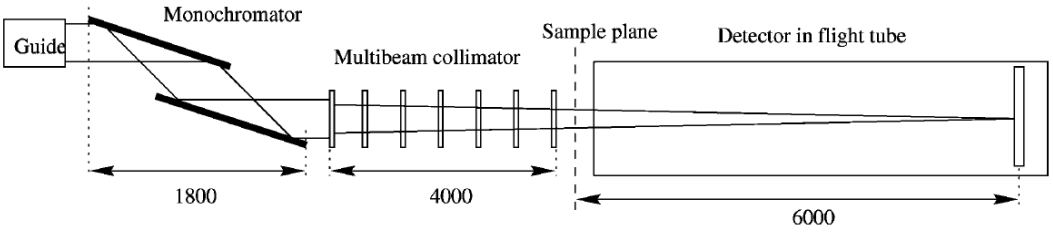

Figure 5.12.: Scheme of the spectrometer TPA at LLB (units in mm, drawing not to scale). The figure was reproduced from Ref. [167] with permission of the International Union of Crystallography.

6. Results

In this chapter, the impact of the combination of neutron grating interferometry, diffractive neutron imaging and (ultra-)small-angle neutron scattering is demonstrated by studying three model systems for vortex matter: (i) the intermediate state in type-I superconducting Pb, (ii) the intermediate mixed state in type-II superconducting Nb and (iii) the A-phase in MnSi. By combining integral scattering techniques which provide structural information about the vortex phase with imaging methods that map its spatial distribution, comprehensive pictures about the nucleation, distribution, and destruction of the domain structure in the IS and the IMS as well as of the skyrmion lattice in MnSi are obtained, covering a length scale of 0.01 to 10 µm.
This chapter is structured as follows: In Sec. 6.1, the nucleation of the intermediate state in the bulk of a pure lead sample is recorded by means of neutron grating interferometry. This example provides an ideal introduction as the obtained results on the IS distribution in the bulk can be compared to a multitude of magneto-optical data published in the literature. Afterwards, in Sec. 6.2 and 6.3, the nucleation and morphology of the IMS phase in Nb are extensively studied in the case of an ultra-pure sample and for a sample showing significant pinning. Thereafter, it is demonstrated how the IMS phase can be used as contrast agent to observe the field penetration in the critical state of a type-II/1 superconductor by means of nGI (Sec. 6.4). The chapter closes with a demonstration of a new experimental approach to study the spatial distribution and distortion of a skyrmion lattice by diffractive imaging. In the future, this approach might be used for the spatially resolved investigation of vortex matter in arbitrary type-II superconductors.
Parts of this chapter have been already published in [33] and [172].

6.1. Domain structure of the intermediate state in a pinning free type-I superconductor

The formation of the intermediate state in type-I superconductors and how it is provoked by an interplay of condensation and field energy has been addressed in Chap. 2. As an extensively studied problem [19, 66, 80], the nucleation of the intermediate state in pure lead is a well suited starting point to demonstrate the capabilities of nGI for µm domain investigations. Although first decoration and magneto-optical observations of the IS structure reach back to the 1960s (see

e.g. [173]), measurements of the IS distribution in the bulk of a sample have not been reported so far. However, the expected size range of the IS structure in lead (see Fig. 2.14 (a)) corresponds well to the sensitivity of nGI (Fig. 5.6 (a)). In the following section, it will be shown that nGI can be used as a complementary technique for IS investigations, since (i) it probes the bulk of the sample and is hence not influenced by parasitic effects like Landau branching (Sec. 2.3.2) or surface pinning (Sec. 2.2.3), and (ii) it has little restrictions on the shape of the investigated sample compared to the aforementioned methods which mostly require flat surfaces.

6.1.1. Experimental setup

The nGI measurements were performed at the ICON imaging beamline (Sec. 5.2) using the equipment described in Sec. 5.1.6. Each DFI was calculated from a stepping sequence of grating G_0 over one complete period in 8 steps. The total exposure time for one DFI was set to 1080 s. The spatial resolution of the setup was approximately 0.5 mm caused by the sample environment leading to a L_S of 300 mm.
The studied sample was a single crystalline Pb disc (diameter $d = 20$ mm, thickness $t = 1.9$ mm). A picture and a neutron image of the Pb sample mounted in its holder is shown in Fig. 6.1 (a) and 6.2, respectively. The sample was cut from a large single crystal by spark erosion and subsequently etched in a mixture of acetic acid and hydrogen peroxide to remove surface impurities introduced by the cutting process. A crystallographic $\langle 100 \rangle$ axis was perpendicular to the disc face. A small piece of the same crystal ($a \times b \times c = 3.5 \times 2.5 \times 1.5\,\mathrm{mm}^3$) was used for magnetization measurements along the c-axis in $\langle 100 \rangle$ direction using a Quantum Design Physical Properties Measurement System (PPMS).

6.1.2. Neutron grating interferometry on the IS

The phase diagram of the Pb disc deduced from magnetization measurements on the small cuboid is shown in Fig. 6.1 (b). Typical magnetization data for $T = 5$ K are depicted in Fig. 6.1 (c). At first, the initial magnetization curve is considered. Hysteretic behavior will be discussed in Sec. 6.1.4. All superconducting phases sketched in Fig. 2.10 (a) were identified: The IS to NS transition at $B_C(T)$ was determined by the vanishing of the diamagnetic magnetization in $M(B,T = \mathrm{const})$ and $M(B = \mathrm{const},T)$ measurements. The solid line in the phase diagram is a fit of $B_C(T)$ according to the standard BCS theory [34], providing $B_C(T = 0\,\mathrm{K}) = 83$ mT and $T_C = 7.3$ K in agreement with literature [174]. In contrast, the MS-IS transition depends on the sample geometry. For the cubic test piece, it corresponds to the triangular minimum in the $M(B,T = \mathrm{const})$ data shown in Fig. 6.1 (c). Note that the drawn IS boundary at $(1 - D)B_C(T)$ was calculated using the demagnetization coefficient of the disc $D = 0.84$ (dashed line in Fig. 6.1 (b)).

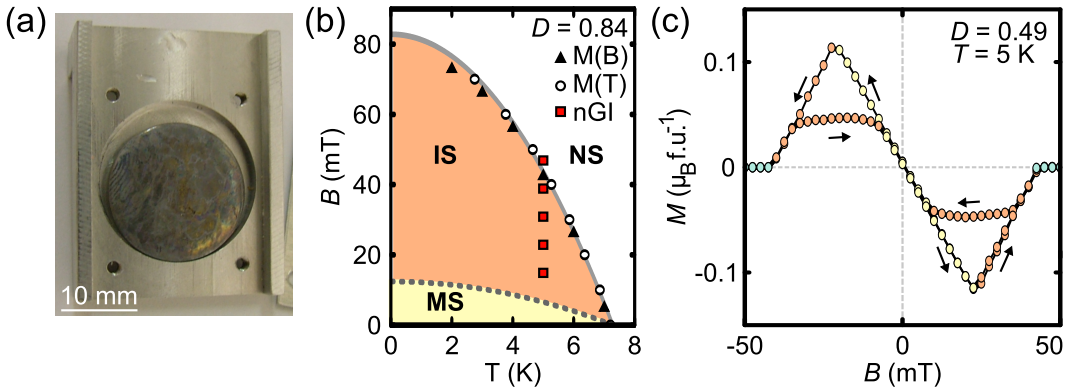

Figure 6.1.: Properties of the lead sample. (a) Picture of the sample in its holder. The staining might be caused by a reaction of the sample and its holder during the rewarming after the nGI measurement. (b) Phase diagram of the superconducting Pb disc deduced from magnetization measurements. The solid line is a fit to the BCS predictions whilst the dashed line shows the calculated MS to IS transition for the disc geometry. (c) Typical magnetization loop of Pb at 5 K. Its minimum marks the transition from the MS to the IS in the cuboid sample. Since the hysteresis closes in zero field, it is of topological nature and not caused by pinning.

DFIs of the Pb disc were taken at various fields between 14 mT and 46 mT as marked in the phase diagram. In a first set of measurements, the field was applied after zero field cooling (ZFC) to 5 K in order to exclude hysteretic effects. These are addressed in the following section. The DFI results are presented in Fig. 6.2. Stepping scans taken in zero field were used as reference data, hence, only additional contributions caused by magnetic scattering at the IS domain structure are visible. Fig. 6.3 (a) shows radial profiles of the DFI data depicted in Fig. 6.2. To extract these data, the DFI were median filtered and radially averaged. The averaging was performed over circular rings with a width of 6 pixel. A pixel corresponds to 0.44 mm.

At 14 mT, no DFI contrast is seen. At 22 mT, a ring-like feature is visible at the edge of the disc that has moved inwards at 30 mT. This feature is also seen as pronounced dip in the radial profiles at $r = 16$ mm (22 mT) and $r = 14$ mm (30 mT), respectively. Additionally, a small signal in the center of the sample arises for 22 mT and 30 mT leading to a minimum at $r = 0$ in the DFI profiles. At 38 mT, the ring feature has vanished. However, a reduced averaged DFI signal is still detectable at the sample position as revealed by the radial profiles in Fig. 6.3 (a). Finally, at 46 mT (above B_C) the DFI contrast is completely lost.

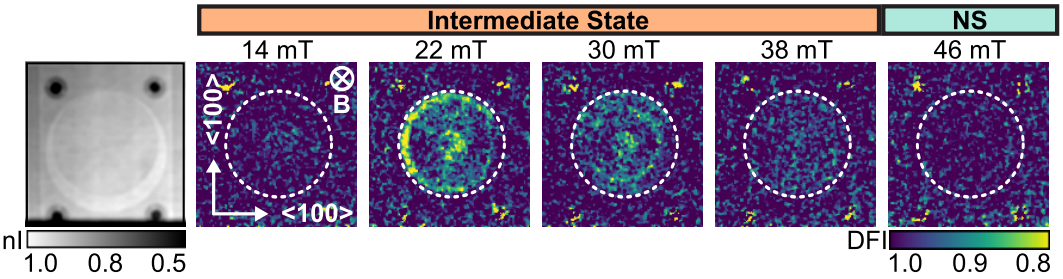

Figure 6.2.: Left: Neutron image (nI) of the Pb disc. It was normalized to unity since due to the experimental setup no open beam correction was possible. Right: DFI of the Pb disc in different fields applied after ZFC to 5 K. The data were normalized to zero field. A DFI contrast smaller than one marks the IS domain structure. The sample position is drawn as white circle in each DFI.

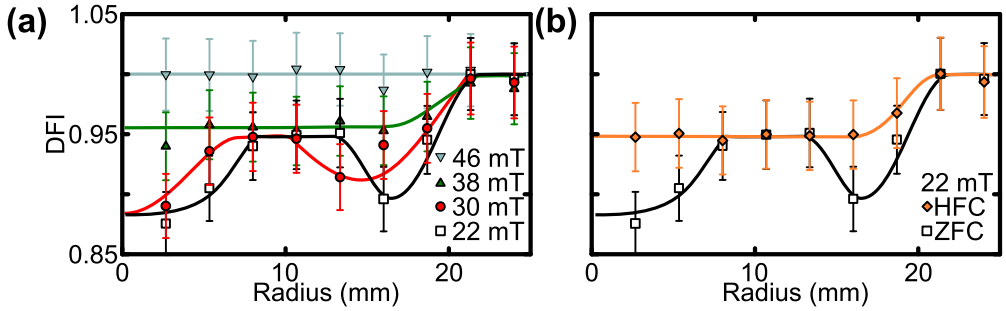

Figure 6.3.: Radial DFI profiles of the sample. The solid lines are guides to the eye. (a) Profiles for different fields applied after ZFC to 5 K. (b) DFI profiles at 22 mT after ZFC and HFC to 5 K. The error bars are estimated errors of 3 %.

.

6.1.3. Field penetration after zero field cooling

In the following, a consistent picture of how the magnetic field penetrates the sample at the MS to IS border is deduced from the data. At 14 mT, the amount of domains is either too small to generate significant DFI contrast or the sample is still in the MS. The field begins to penetrate the disc at 22 mT via a domain structure which nucleates at the edge of the disc, causing the ring in the DFI. However, the domains are partially driven to the center of the disc by Lorentz forces acting on closed flux structures (Sec. 2.2.4), causing the additional DFI signal in the middle of the sample. For increased fields of 30 mT, the domain front is shifted inwards and a much coarser domain structure is left behind, which causes a higher DFI contrast. At 38 mT, the whole sample is filled with an IS domain structure as a higher, but homogeneous DFI contrast arises all over the disc. The general tendency of increasing DFI contrast for increasing fields is attributed to a coarsening of the IS structure. At 46 mT, the entire sample is in the NS and thus the DFI contrast equals one all over the sample.

6.1.4. Hysteretic behavior

The hysteretic behavior is finally addressed as a general hallmark of systems forming domains. The hysteresis loop presented in Fig. 6.1 (c) only deviates in fields between 8 and 33 mT from the initial magnetization, as the decreasing magnetization branch lies below the increasing one. No signs of trapped flux are found at $B = 0\,\mathrm{mT}$. Hence, the crystal used for the nGI experiments reveals neglectable pinning and hysteretic effects seen with nGI cannot be linked to an insufficient sample quality (Sec. 2.2.3), but to a changed IS morphology.
Fig. 6.3 (b) compares DFI profiles taken at 22 mT and 5 K, following i) ZFC to 5 K and subsequent field ramp (white), and ii) high field cooling (HFC) at 46 mT $> B_\mathrm{C}$ to 5 K and subsequent field decrease (orange). The profiles show a constant DFI inside of the sample after HFC, whereas the sample reveals two minima after ZFC. At first glance, this behavior seems reasonable as the field has to penetrate the sample from the edges after ZFC. However, as no pinning hampers the sample to reach the IS configuration of minimal energy, the differences in DFI distribution can only be caused by the additional topological barrier described in Sec. 2.2.4, which inhibits the field penetration into the Pb disc [7, 63, 67]. Furthermore, the DFI signal averaged over the entire sample is lower after ZFC than after HFC. As the DFI contrast is immediately linked to the neutron scattering function of the IS domain structure (Sec. 4.4), this suggests a change of the IS domain size or/and the domain morphology during a hysteresis loop, which is also seen in the magnetization data of the cubic sample (Fig. 6.1 (c)). An analogous behavior has also been observed in surface sensitive magneto-optical observations on a similar Pb sample by Prozorov [19] (compare Fig. 2.15).

6.1.5. Conclusion

The results of the previous section demonstrate the potential of nGI. The domain distribution during field penetration into a single crystalline Pb sample could be recorded. Moreover, a change of the IS from a domain front behavior to a homogeneous distribution within a hysteresis loop has been observed. All data are in agreement with literature [19, 66]. Moreover, because of its unique contrast mechanism, nGI probes the domain structures in the *bulk* of a type-I superconductor on a length scale which has not been accessible so far by neither neutron scattering nor neutron imaging.

6.2. Domain structure of the intermediate mixed state in a pinning free type-II superconductor

Like the intermediate state of type-I superconductors treated in Sec. 6.1, the intermediate mixed state of type-II superconductors has been extensively investigated,

both theoretically [45, 46, 175] as well as experimentally [16, 49, 50, 176]. However, early studies mostly concentrated on the reasons for an attractive vortex-vortex interaction and the associated changes of the thermodynamic observables. In contrast, examinations on the morphology of the vortex lattice within the IMS domains are rare. To the authors' knowledge, they are exclusively based on local decoration pictures [83, 177] and small-angle neutron scattering [16, 178]. The details of the IMS domain nucleation, i.e. the change of the IMS distribution and the domain morphology, have not been addressed so far. This problem is considered in the following sections by studying the low-κ superconductor niobium. As a prototype of a type-II/1 material, the vortex lattice in this classical, phonon mediated superconductor has already been studied in detail [16, 93, 178].
In this section concerned with the IMS, it will be shown how neutron grating interferometry combined with small- and very-small-angle neutron scattering yields detailed information on the vortex lattice and its domain structure in the intermediate mixed state of a Nb sample of ultra-high purity and non-ellipsoidal shape. The results prove the capability of nGI to resolve the IMS domain distribution, but also to obtain information about the vortex lattice morphology. Furthermore, they reveal strong indications of a topological hysteresis in the structure of the IMS.

6.2.1. Experimental setup

For the experimental study of the IMS phase distribution, SANS, VSANS and nGI results obtained at the SANS-1, the KWS-3, the ICON and the ANTARES beamline were combined. Their experimental setups are extensively described in Sec. 5.4, 5.2 and 5.1.2. To exclude effects arising from slightly different magnetic field or temperature conditions, the same sample environment described in Sec. 5.1.6 was used for all measurements.
For SANS, a Cd aperture mask with a small diameter of 3 mm was placed in front of the sample position after a collimation distance of 20 m. In previous studies, the aperture was chosen so that most of the sample was illuminated [93]. Hence, an integral signal over the whole sample was obtained. The use of the 3 mm aperture permitted to perform locally resolved SANS investigations. The position of the neutron spot on the sample could be determined with an accuracy better than 1 mm.
The DFI and TI results were calculated from a stepping sequence of grating G_0 over one complete period in 8 (ICON) or 26 (ANTARES) steps. The total exposure time for one DFI was set to 1080 s (ICON) and 780 s (ANTARES). However, whilst at ICON a wavelength of 4.1 Å was used, the measurements at ANTARES were performed using the white beam. In both cases, the spatial resolution of the setup was approximately 0.5 mm, caused by the restriction on L_S to 300 mm due to the bulky sample environment.
A cylindrical rod of ultra-high purity niobium ($\kappa \approx 0.74$, $T_C = 9.2$ K) with a length

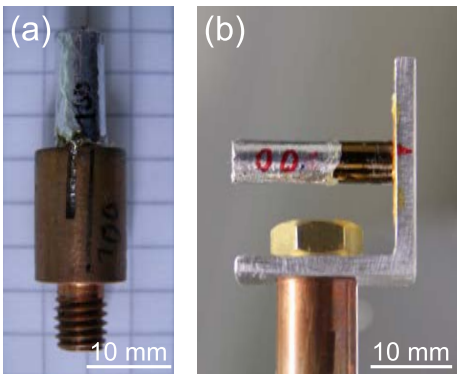

Figure 6.4.: The high purity niobium sample. Pictures of the sample in its holder for the measurements at ICON (a) and at ANTARES (b).

of 20 mm and a diameter of 4.5 mm had been selected (Fig. 6.4). The residual resistivity ratio (RRR) was measured with an eddy current decay method and was found to exceed $\approx 10^4$, underlining the exceptional crystallographic quality. In previous neutron scattering experiments [93, 179], no signs of volume pinning and trapped flux have been found. The cylinder axis of the sample corresponds to a crystalline [110] direction. Unless stated otherwise, the magnetic field was applied in the (110) plane, parallel to the incident neutron beam and perpendicular to the cylinder axis. The demagnetizing factor was calculated to be $D = 0.47$.

6.2.2. Experimental results

Small-angle neutron scattering

Fig. 6.5 shows typical SANS patterns measured in magnetic fields $75\,\mathrm{mT} \leq \mu_0 H \leq 153\,\mathrm{mT}$ after ZFC to 4 K. Each data set corresponds to a sum over a rocking scan with respect to the vertical sample axis. The data was corrected for background using the zero field pattern. By introducing a small aperture mask of only 3 mm in diameter, two different sample positions were probed, as indicated in Fig. 6.5. Data, originating from the position close to the upper sample edge (blue marker), is shown in the top row, data from the center of the sample (red marker) is shown in the bottom row in Fig. 6.5, respectively. The six-fold symmetry of the vortex lattice along this field direction agrees with literature [93].
The direct comparison of the two measurement positions reveals that the scattering patterns of the vortex lattice strongly depend on their position. A clear sixfold pattern is observed in the middle of the sample already at 75 mT. In contrast, there is no sign of a vortex lattice from the SANS pattern determined at the edge of the rod until the field reaches a value of 89 mT.
The q-spacing of the vortex lattice g_{VL} (Eq. 3.56) extracted from the SANS data is presented in Fig. 6.6 (a) as a function of the applied magnetic field. The hallmark of the IMS, a constant spacing of the vortex lattice [16] corresponding

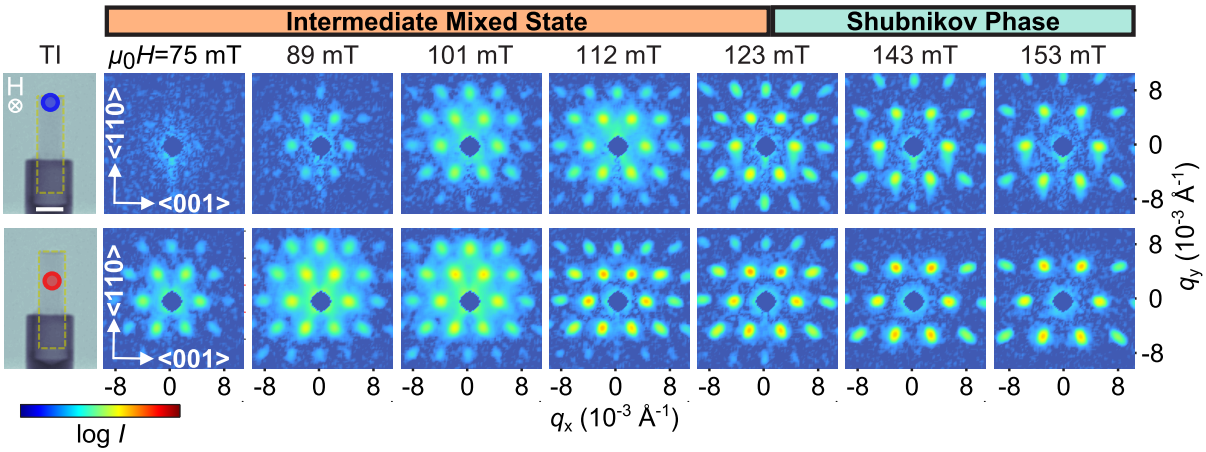

Figure 6.5.: Local SANS patterns of an ultra-high purity Nb rod vs. magnetic field. The data were obtained after ZFC to 4 K. Measurement positions at the upper edge (top row) and in the center (bottom row) of the sample were selected using a 3 mm Cd aperture as shown in the TI images on the left side. The scale bar corresponds to 5 mm.

to $g_{\mathrm{VL}} = 3.9 \times 10^{-3}\,\mathrm{Å}^{-1}$ is obvious for both positions. The data reveal that the spacing of the vortex lattice in the IMS is independent of the position on the sample. However, the field regions of the IMS phase differ: For the center position, the IMS domain nucleation sets in at 75 mT and persists up to 112 mT. At the edge position, the vortex lattice appears first at 89 mT and is constant until $\mu_0 H$ reaches 123 mT. The IMS field span corresponds well to the expected value of $DB_0 \approx 32$ mT (see Ap. A.1). In higher fields, both data sets follow a $(\mu_0 H - B_{\mathrm{off}})^{\frac{1}{2}}$ [16] behavior. The parameter B_{off} describes an offset to the local induction and reveals a difference of 14 mT for the two positions.

It has to be emphasized that the delay in appearance of the vortex lattice at the top of the sample cannot be explained by an inhomogeneity of the magnetic field (compare Ap. A.4). After a careful examination of different rocking angles, a missing scattering signal at the edges due to a bending of the vortex lines can be ruled out as well.

Fig. 6.6 (b) shows the integrated intensity of the first order Bragg peaks as extracted from rocking scans for both positions indicated in the inset. A well-defined maximum marks the transition from the IMS-phase to the Shubnikov phase at H_{C1}. Again, the shift in magnetic field in between the two positions is clearly visible. The maximum is found between 105 and 112 mT for the middle position and between 123 and 133 mT for the upper edge of the sample. The $I(\mu_0 H)$ trend as well as $g_{\mathrm{VL}}(\mathrm{IMS})$ are in agreement with previous measurements [93].

However, a closer inspection of the intensity curve of the middle position reveals a nonlinear behavior with a downward dip at 90 mT. This dip was not observed in former experiments, where the entire volume of the sample was probed using a

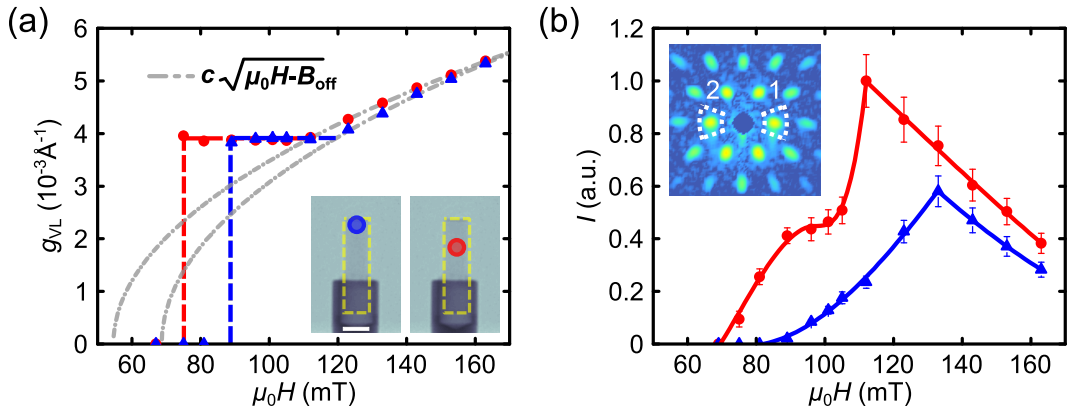

Figure 6.6.: Quantitative analysis of the SANS data from the Nb rod. The two measurement positions are indicated in the inset of (a). The scale bar in the inset corresponds to 5 mm. (a) q-position of the first order Bragg peak of the vortex lattice g_{VL} as function of the applied magnetic field. The grey line indicates the field dependence $(\mu_0 H - B_{\mathrm{off}})^{\frac{1}{2}}$ at high fields. The dashed lines are a guide to the eye of the constant q behavior in the IMS. (b) Integrated intensity of the first order Bragg peak versus magnetic field. The error bars correspond to the standard error of the mean (s.e.m.). The lines are guides to the eyes. The evaluated Bragg peaks are exemplarily shown in the inset of (b) for $\mu_0 H = 153\,\mathrm{mT}$.

larger aperture. If the intensities of the top and center positions are added, the dip is washed out leading to close agreement with literature [93].
In Fig. 6.7 (a), the integrated intensity of the first order Bragg peak for the center position of the sample is complemented by data measured after high field cooling (HFC) at the same temperature. The ZFC and HFC intensity coincide well, unless in a small field interval between 89 and 112 mT, where the ZFC data reveal the described kink, whereas the HFC data show a nearly linear behavior up to the IMS-SH transition. A similar hysteresis has been observed in former measurements [93]. Its emergence at the upper boundary of the IMS is an indication of a topological hysteresis.
Typical SANS rocking curves of the vortex lattice are exemplarily shown in Fig. 6.7 (b) for the center position. The curves belong to the peak 1 shown in the inset of Fig. 6.6 (b). The curves were normalized to the maximal intensity found in the data. The rocking curves of the rod reveal an unusual, asymmetric double peak structure in small fields. However, the peaks slowly converge in increasing fields. The strong positional dependence of the $g_{\mathrm{VL}}(\mu_0 H)$ and the $I(\mu_0 H)$ curves indicates a strongly inhomogeneous domain distribution in the IMS of non-ellipsoidal sample that additionally shows some signs of history dependence. Furthermore, SANS revealed an unexpected broad variation of rocking angles within the IMS, indicating a distortion of the flux line lattice in longitudinal direction. Both assumptions are further investigated by means of nGI.

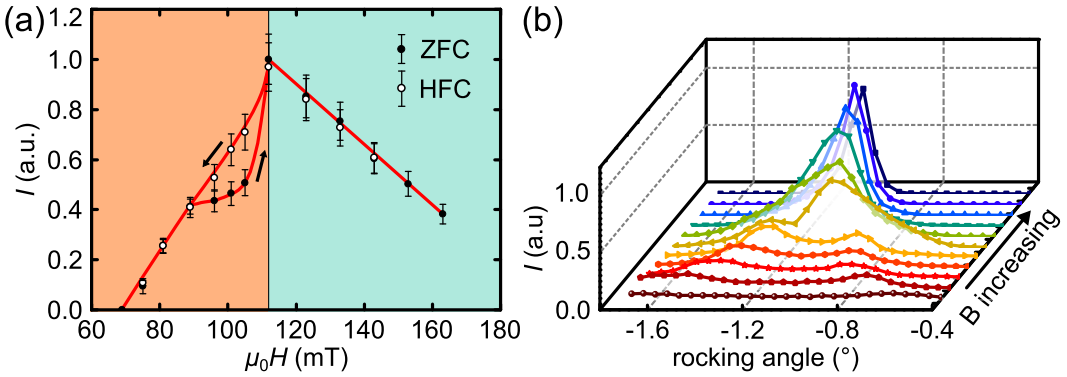

Figure 6.7.: Details of the SANS results. (a) Integrated intensity of the first order Bragg peak versus magnetic field for the center position. The data were obtained after ZFC (filled circles) and high field cooling (open circles) to 4 K. At high and low fields, the intensities perfectly match. However, in between 89 and 112 mT, a strong hysteretic behavior is observed. (b) Rocking curves for the center position in fields of 81 mT, 89 mT, 96 mT, 101 mT, 105 mT, 112 mT, 123 mT, 133 mT, 143 mT, 153 mT and 163 mT, respectively. The rocking curves have the shape of a double peak which slowly evolves into a singly peak for increasing fields. The zero-point of the rocking angle is arbitrarily defined.

Neutron grating interferometry on the IMS

Results of the nGI experiments performed at ICON are presented in Fig. 6.8. The nGI data are grouped in the TI in the top row and DFI in the bottom row. Their contrast modalities are explained in Ap. A.5 and Sec. 4.2.3, respectively. At 0 mT, the contrast seen in the TI is caused by the attenuation of the beam by the sample and its holder. In the DFI, residual background scattering from the sample holder and the edges of the sample is seen. All TIs and DFIs for finite magnetic fields were normalized to the data for 0 mT, thus, the shown TI- and DFI- contrasts for $\mu_0 H \geq 75\,\mathrm{mT}$ are caused by the appearance of the vortex lattice only, and are of purely magnetic origin.
If the magnetic field is increased after ZFC to 4 K, the sample passes through the different superconducting phases. At 75 mT, the sample enters the IMS phase since a vortex lattice is present in the sample as indicated by the SANS experiments from Fig. 6.5. However, the scattered intensity is too weak to produce sufficient contrast in the TI and DFI. At 89 mT and above, both DFI and TI show a clear contribution caused by the vortex lattice and its IMS domains inside the sample. The TIs show a line shaped contrast persisting up to the highest field of 205 mT, with its maximum at 112 mT. A pronounced signal in the DFIs originating from the IMS domains exists for magnetic fields between $89\,\mathrm{mT} \leq \mu_0 H \leq 123\,\mathrm{mT}$ with a maximum at 101 mT. For 89 mT and 101 mT, a homogenous DFI contrast is observed except for the top and bottom ends. At 112 mT, a homogenous contrast is formed where also the top and bottom ends contribute to the DFI. The variation

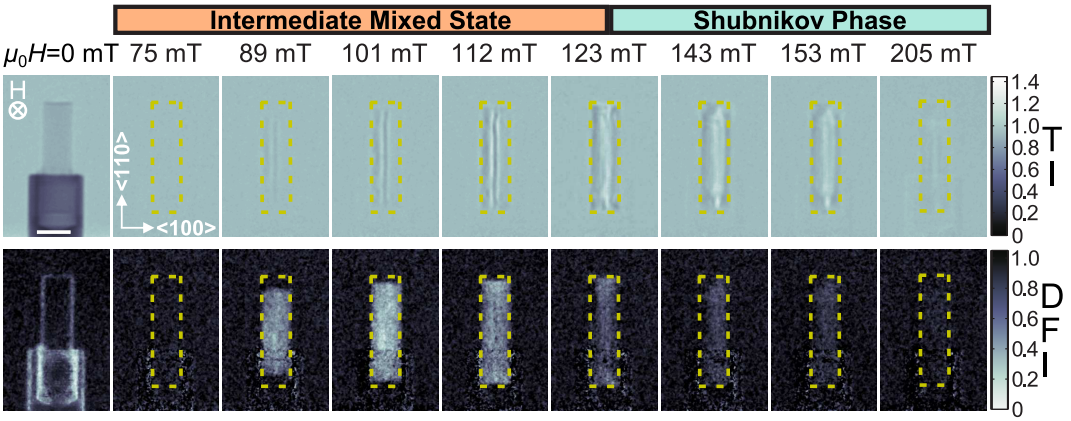

Figure 6.8.: Transmission and dark-field images of an ultra-pure niobium rod as a function of magnetic field. The magnetic field was successively increased after ZFC to $T = 4\,\mathrm{K}$. The contour of the sample is indicated by the yellow dashed boxes. The scale bar corresponds to $5\,\mathrm{mm}$. The TI (top row) and DFI (bottom row) results for $B > 0$ are normalized to the results at $\mu_0 H = 0\,\mathrm{mT}$, hence, only the pure magnetic contribution from the vortex lattice is visualized. The TI and the DFI provide information about the flux line lattice within the vortex domains and the domain formation in the IMS phase, respectively.

of the contrast of the DFI with increasing magnetic field inside the IMS phase is attributed to the increasing filling factor of the sample leading to an enlargement of the domain sizes beyond the sensitivity range of the nGI setup (compare Fig. 5.6 (a)). At 123 mT, the sample is characterized by a phase coexistence of IMS and Shubnikov phase. The interpretation of the TI signal together with DFI and SANS indicates that the bottom and top part are still in the IMS phase causing a DFI signal, whereas in the central part of the sample, only a weak indication for a domain structure is detected.
At high magnetic fields $\mu_0 H \geq 143\,\mathrm{mT}$, the Shubnikov phase completely fills the sample and contrast is seen in the TI only. Similar to the SANS data, the decreasing intensity observed with increasing field is explained by the field dependent form-factor of the vortices [16]. The remaining contribution in the DFI is attributed to the crosstalk originating from a TI signal greater than unity. A detailed quantitative explanation of the crosstalk is given in Ap. A.5, in which also its influence on the DFIs of Fig. 6.8 is visualized.
The crosstalk can be avoided by choosing a geometry with the field perpendicular to the beam direction, aligned along the grating lines[1]. In this case, the vortex lattice is rotated out of the Bragg condition preventing SANS scattering which

1 Notice that magnetic scattering arises perpendicular to the magnetic field [103]. Hence, the field cannot be applied perpendicular to the beam direction **and** the grating lines, since in this geometry the scattering is not detected by nGI.

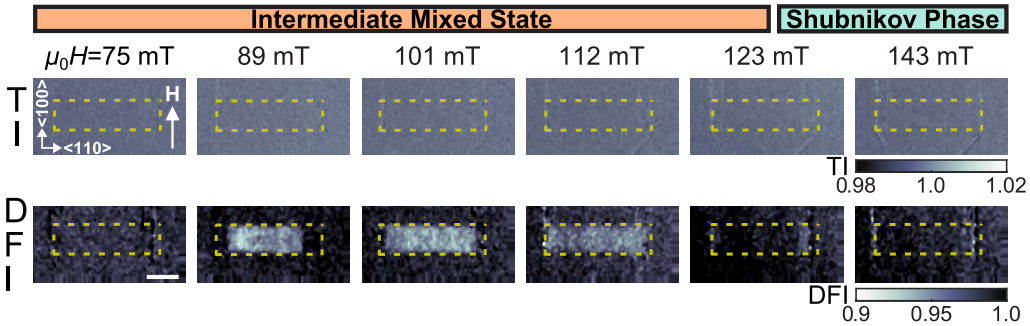

Figure 6.9.: TI and DFI results of an ultra-pure niobium rod as a function of increasing magnetic field after ZFC to $T = 4\,\mathrm{K}$. The field was applied perpendicular to the neutron beam. The contour of the sample is indicated by the yellow dashed boxes. The TI (top row) and DFI (bottom row) results are normalized to $\mu_0 H = 0\,\mathrm{mT}$, hence, only the pure magnetic contribution is visualized. As the vortex lattice is rotated away from the Bragg condition, no TI contrast arises. However, USANS scattering at the IMS domains still causes a pronounced DFI contrast. The scale bar corresponds to $5\,\mathrm{mm}$.

influences the TI and causes the crosstalk effect. However, the isotropic USANS signal of the IMS, which is largely invariant under this rotation, will still cause a DFI contrast. nGI measurements in this geometry were performed at the ANTARES beamline and are shown in Fig. 6.9. This time, the magnetic field was applied in vertical direction along $\langle 100 \rangle$ and perpendicular to the neutron beam along $\langle 110 \rangle$. Again, the data for finite magnetic fields are normalized to the data for 0 mT and grouped into the TI in the top row and the DFI in the bottom row. As discussed, no magnetic TI contrast arises apart from small contributions due to a slight displacement of the sample holder in higher magnetic fields. However, a pronounced DFI contrast is still visible. Moreover, the field dependence of the DFI contrast variation on the magnetic field is in complete agreement with Fig. 6.8. Especially at 123 mT, the delayed IMS to Shubnikov phase transition near the cylinder faces is clearly visible as remaining DFI contrast at the left and right edge of the sample. The presented data further supports the proposed peculiar IMS distribution, since other contributions to the DFI contrast than USANS scattering are ruled out.
Although not systematically investigated, it should finally be noted that after HFC, a residual DFI signal has been detected in the center of the sample for small fields of 75 mT, whereas no signal occurs after ZFC. However, in both cases, the TIs lack any scattering contributions. Corresponding data are shown in Fig. 6.10 (a).

Very-small-angle neutron scattering

Fig. 6.10 (b) shows typical VSANS data. Normalized, radially averaged scattering curves are shown as a function of the momentum transfer q for magnetic fields

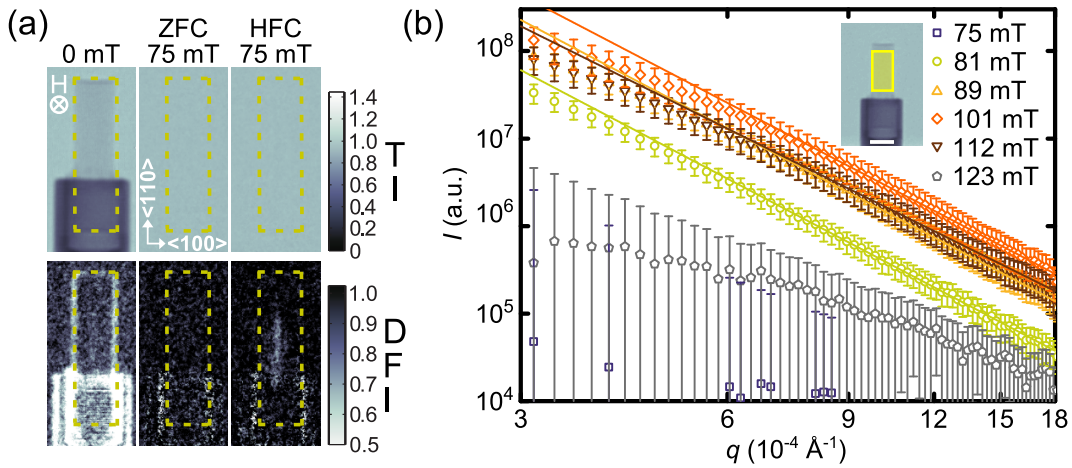

Figure 6.10.: DFI hysteresis and VSANS scattering curves. (a) TI and DFI of the rod at $4\,\mathrm{K}$ in a field of $75\,\mathrm{mT}$, applied after ZFC and HFC. The data were normalized to $0\,\mathrm{mT}$. In contrast to the ZFC, a remaining DFI signal is found after HFC, while no signal is detected in the TI. The unnormalized, zero field TI and DFI are shown in order to compare. (b) VSANS scattering curves of the ultra-high purity Nb rod. The data were obtained after ZFC to $4\,\mathrm{K}$ in different magnetic fields. The Cd aperture mask is depicted as the yellow area seen in the inset. The scale bar corresponds to $5\,\mathrm{mm}$. Error bars are calculated from the propagation of uncertainty of the sample transmission and the s.e.m. of the scattering curves measured at $B = 0$ and in the corresponding field, respectively. The high q regime can be approximated via a power law behavior $I \propto q^{-4\pm0.2}$, which is shown as solid lines in the graph.

between $75\,\mathrm{mT}$ and $123\,\mathrm{mT}$ after ZFC to $4\,\mathrm{K}$. The radial averaging was performed over two 30° sectors in horizontal direction. For each magnetic field, the sample transmission was obtained by normalization to the direct beam. The scattering curves were extracted by normalization of the scattering pattern measured in an applied field to its transmission and subsequent subtraction of the zero field scattering pattern. Consequently, the data presented in Fig. 6.10 (b) show only magnetic scattering contributions.

Likewise in the DFI in Fig. 6.8, no additional scattering is observed at $75\,\mathrm{mT}$. In the field region between $81\,\mathrm{mT}$ and $112\,\mathrm{mT}$, a scattering signal is found which vanishes in fields above $123\,\mathrm{mT}$. The VSANS signal in intermediate fields is caused by neutrons scattered off the IMS domains and precisely coincides with the DFI contrast seen with nGI. Moreover, as seen in Fig. 6.10 (b), the scattering curves decrease as a power law $q^{-\alpha_\mathrm{P}}$ for $q > 6 \times 10^{-4}\,\mathrm{Å}^{-1}$ in this field range. The exponent α_p slightly varies between 4.1 ± 0.1 for fields from $81\,\mathrm{mT}$ to $101\,\mathrm{mT}$ and 3.9 ± 0.1 at $112\,\mathrm{mT}$. In higher fields, the scattering vanishes again as the sample enters the Shubnikov phase. SANS scattering off the vortex lattice still exists but the scattering angles are too large to hit the VSANS detector. The scattering shows up as a correction to the transmission of the sample. The domain structure

at the edges of the sample seen with DFI at 123 mT is not detectable by VSANS, because it is not covered by the Cd aperture placed in front of the Nb rod as shown in Fig. 6.10 (b) (yellow box seen in the inset).
The VSANS signal in the IMS phase cannot be explained by neutrons scattered off the vortex lattice itself or by a large distribution of the vortex lattice parameter d_{VL}, as the complementary SANS data reveals well defined Bragg peaks with high intensity at much larger q-values ($q \approx 4 \times 10^{-3}\,\mathrm{Å}^{-1}$). The high transmission of the sample of 0.9 even in the IMS phase indicates that multiple scattering can be neglected as source of the VSANS signal. The q-resolved VSANS data hence clearly reveal µm sized magnetic scattering contributions for field values attributed to the IMS via nGI and indirectly by SANS.

6.2.3. IMS nucleation in the absence of pinning

The spatial distribution of the IMS

A comprehensive interpretation of the domain structure of the IMS and its evolution with increasing field based on the combination of nGI, SANS and VSANS data is given in the following paragraphs. The visualization of the IMS domain distribution obtained by means of nGI is in perfect agreement with the SANS and VSANS results. Hence, this study clearly demonstrates the capability of nGI to image the IMS nucleation and to determine the phase boundaries in the superconducting phase of Nb. For the case of the IMS nucleation in a cylindrical specimen, it could be shown that (i) the IMS domain nucleation starts in the center of the rod and the IMS region propagates along the cylinder axis to the edges, (ii) the IMS lastly evolves into the Shubnikov phase at the edge of the sample, (iii) the induction at the top and bottom part of the sample reveals a considerably delay with respect to the central part, and (iv) a coexistence of pure Shubnikov phase and IMS is possible due to demagnetization effects in non-ellipsoidal geometries. Note that after ZFC, the vortices can only penetrate the sample from the outside of the superconducting sample. Therefore, the observed IMS nucleation in the middle is peculiar. However, in the absence of pinning, the Lorentz force pushes the vortices to the middle of the sample once the flux lines have penetrated the sample and overcome the geometrical barrier at the top and bottom edges of the rod (Sec. 2.2.4) [69, 180, 181]. As the vortex lattice nucleation in the middle of the sample generates a dipolar field opposed to the applied one, the induction at the edge of the samples is reduced. Hence, the IMS nucleation as well as the IMS to Shubnikov transition is delayed at these positions. For the presented Nb sample with cylindrical geometry, this delay could be quantified to be 14 mT.
Besides these qualitative arguments, it has to be pointed out that the process of the IMS nucleation is not well understood. A successful theory for IMS modelling has to include the detailed nature of the vortex-vortex interaction, the disturbance of the applied field by the IMS structure, the surface tension between Shubnikov and

Meissner domains (similar as in the case of the IS (Sec.2.3)) and the geometrical constrains in the rod. Here, the presented results can be directly compared to theoretical models, and the nGI method provides unique access to the bulk domain distribution in this pinning free, cylindrical sample. This study hence may serve as nucleation point to stimulate further detailed experimental and theoretical work. Quantitative information obtained by VSANS can serve as further input parameter. In flat samples, magneto-optical investigations [12, 13] as well as numerical calculations [84] suggest the existence of a preferred thickness-dependent IMS domain size similar to the case of the IS [38]. However, for this sample it was not possible to extract an exact size distribution of the IMS domains from the VSANS scattering curves. Although a clear magnetic scattering signal is present between 81 and 112 mT in the $I(q)$ data, no sign of a preferred domain length is observed. Domain sizes larger than the VSANS sensitivity or a too broad domain size distribution due to the cylindrical shape of the sample may explain this behaviour. However, the Porod q^{-4} [111] dependence of the scattering curve at large q indicates that regularly shaped domains exist, having a smooth surface on a sub µm scale. Furthermore, the high scattered intensity and deviations from the power law behavior at small q, give a hint that the domain sizes are slightly larger than the range probed by VSANS.
Finally, some effects arising in the data have not been addressed so far. The upward kink in the $I(B)$ SANS dataset (Fig. 6.6 (b)) recorded at the middle position of the sample is unexpected. The form factor of the vortex lattice is independent of the field due to a constant magnetic induction B_0 in the IMS. Hence, according to Eq. 3.57, the integrated intensity of a vortex lattice Bragg peak inside the IMS phase only depends on the volume fraction of the IMS and increases linearly with the applied magnetic field [178]. The presence of an upward kink of the integrated intensity recorded at the center position of the sample reveals that a changing local distribution of IMS domain regions is required in addition to the linear increase of volume fraction to explain this behaviour.

The distortion of the vortex lattice

The peculiar contrast variation in the TI of Fig. 6.8 requires special attention as it directly links to a distortion of the vortex lattice in the horizontal plane of the sample. Considering the TI for 101 mT, the vertical, high and low intensity streaks are roughly separated by 0.7 mm. With an L_s of approximately 300 mm, the scattering angle can be estimated to 0.13° which corresponds to the Bragg angle of the vortex lattice taken from Fig. 6.6 (a) to be 0.14° for $\lambda = 4.1$ Å. Hence, the TI contrast is clearly caused by the SANS signal of the vortex lattice. However, for the case of a vortex lattice which is aligned strictly parallel to the external magnetic field direction over the entire sample volume, a TI signal different than unity would only arise if the vortex lattice is rotated to the Bragg angle. In this case, the TI would decrease at one sample edge and increase at the other, since

the intensity is just slightly shifted in the horizontal plane. This is obviously not the case for the TI of the Nb rod presented in Fig. 6.8. In order to generate the distinct TI contrast variations of high and low intensity streaks seen between 89 and 112 mT, a spatial variation of the vortex lattice orientation (mosaic) is additionally required.

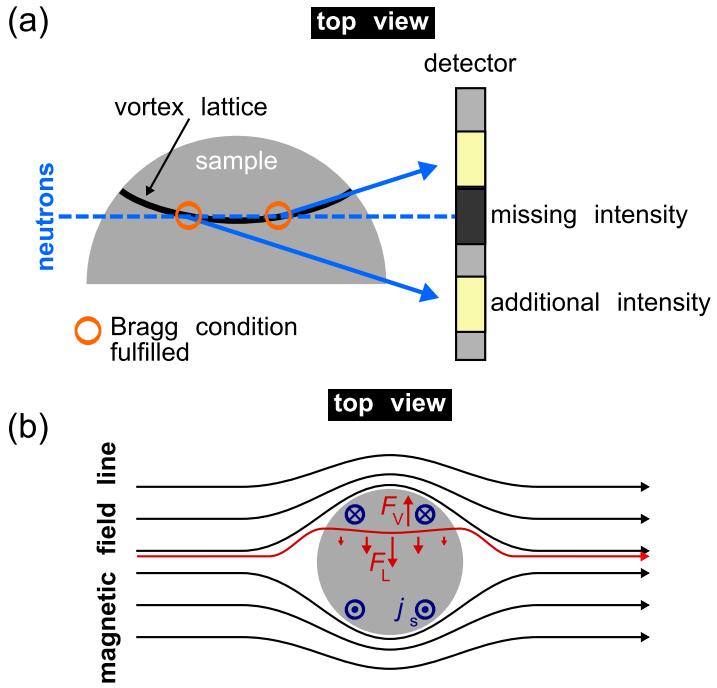

Figure 6.11.: On the origin of the TI contrast. (a): Schematic sketch, explaining how the curvature of the vortex lattice generates a line-shaped contrast variation in the TI. (b): Top view sketch of the forces acting on a vortex line upon field penetration.

The TI pattern can concisely be explained by introducing a symmetrical bending of the vortices in the Nb rod within the horizontal plane, as schematically indicated in Fig. 6.11. In this case, neutrons are Bragg scattered twice inside the sample. This leads to the observed arrangement of high and low intensity streaks separated by twice the Bragg angle. For this effect to occur, a bending in the range of the vortex lattice Bragg angle ($\approx 0.1°$) is sufficient.
The existence of a small curvature of the vortices can be understood by simplified arguments based on the sample geometry and the balance of forces acting on a flux line penetrating a superconducting sample (Fig. 6.11 (b)): Due to the cylindrical geometry of the sample, magnetic flux lines can enter the sample in the horizontal plane without being hampered by a geometrical barrier at the edge of the sample (compare Fig. 2.7 (c)). However, as explained in Sec. 2.2.4, a further penetration of the flux line into the bulk of the sample requires an elongation of the vortex lines and hence a loss of condensation energy, which results in an outward directed

force F_V. On the other hand, the flux line is directed to the center of the sample by the Lorentz forces F_L acting on the vortex lines. As discussed in Sec. 2.2.2, these forces are proportional to the local screening current density j_s which is maximal in the vertical mirror plane of the rod perpendicular to the applied field. Hence, they do not act homogeneously on the vortex line, but their magnitude increases towards the center of the sample which gives rise to the observed flux line distortion.

The proposed bending of the vortex lattice is directly confirmed by the SANS rocking curve shown in Fig. 6.7 (b). Normally, the rocking width is reciprocally linked to the longitudinal correlation length of the vortex lattice. Hence, for the ultra-pure bulk sample, one would expect a single Gaussian-shaped rocking curve which corresponds to the instrumental resolution function. However, in the presented case, the rocking curve of the vortex lattice shows a peculiar double peak structure which can only be explained by a distribution of vortex lattice orientations (mosaic) and hence of Bragg angles. Nonetheless, a smooth spherical distortion of the vortex lines cannot account for the double peak structure as will be demonstrated in Sec. 6.5.

The rocking curves can be modeled accurately by two Lorentzian profiles as exemplarily shown in Fig. 6.12 (a) for fields of 101 mT and 123 mT, respectively. Here, the intensity of the right diffraction peak (Nr. 1 in Fig. 6.6 (b)) has been plotted against the vertical rocking angle. By fitting these data, one obtains the center position of each peak which is plotted against the magnetic field in Fig. 6.12 (b). However, in fields higher than 143 mT, the rocking curve can also be reproduced by a single Lorentzian, since the peaks have nearly merged. The error bars in Fig. 6.12 (b) correspond to the numerical error of the fit, but might be underestimated due to the high amount of fit parameters.

As seen in Fig. 6.12 (b), the angular peak distance is reduced in increasing fields.

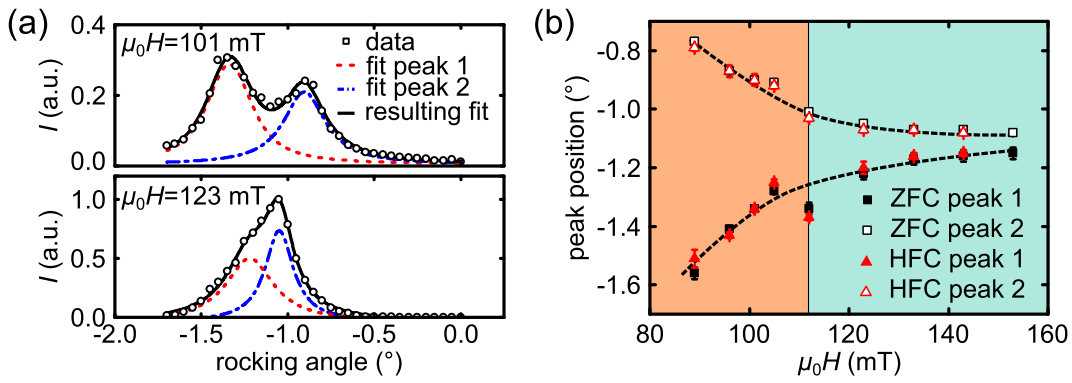

Figure 6.12.: Double peak structure of the rocking curve. (a) Rocking curves for 101 and 123 mT which were fitted by two Lorentzians. (b) Center position of the Lorentzian peaks as function of the magnetic field after ZFC and HFC. The dashed line is a guide to the eye. The zero-point of the rocking angle is arbitrarily defined.

This behavior can be expected, since the rigidity of the vortex lattice strengthen in increasing fields [7]. However, the rate of convergence changes in between 105 and 123 mT where the IMS (orange)-SH (blue) transition takes place. Hence, the orientational distribution of the vortex lattice in beam direction clearly changes as the Meissner domains are filled with the vortex lattice. The same morphology change is seen in Fig. 6.8 as a variation of the TI contrast between 112 and 143 mT, where the streaked pattern is replaced by a more homogeneous one. The most likely explanation for the correlation between the vortex distortion and the IMS is that Shubnikov domains in small applied fields, which can be visualized as a bundle of vortex lines, are deformed easier by the Lorentz forces than larger ones formed in high applied fields. As the field approaches the border to the Shubnikov phase, the domain structure is replaced by a rigid vortex lattice which is to a lesser extent influenced by the screening currents.

Hysteretic behavior

Finally, the hysteretic behavior has to be considered. Like in former measurements, no sign of vortex pinning could be detected in the Nb rod, since (i) the $I(q)$ curve shows no difference after HFC compared to ZFC in small fields, and (ii) the longitudinal orientation of the flux lines in the sample is not influenced by HFC, as the peak position of the rocking curves is unaffected by the magnetic history (see Fig. 6.12 (b)). However, the sample reveals a higher integrated intensity in fields between 89 and 112 mT after HFC, which directly indicates that the ratio of Meissner domains is smaller on the downward hysteresis branch. As this ratio shows a different field characteristic in tubular or laminar domain structures (compare Eq. 2.26 and 2.28), this is an indication for a changed domain morphology after HFC. The remaining DFI signal at 75 mT can be seen as a second evidence of a structural transition, since the DFI contrast is directly linked to the morphology of the vortex lattice on the micrometer scale. Unfortunately, VSANS failed to provide information on the detailed microstructure of the IMS. Hence, the proposed domain metamorphosis is only based on indirect evidences. However, as the nGI data strongly suggest a penetration of the vortices from the top and bottom end of the cylinder, the same geometrical barrier causing a hysteresis in the IS [66] might be responsible for a similar behavior in the IMS of the cylindrical sample.

6.2.4. Conclusion

In summary, the previous part of this thesis presented a systematic approach to study the properties of the vortex lattice of the bulk type-II superconductor niobium in the absence of pinning. The combination of nGI, SANS and VSANS coherently merges the spatial resolution of real space methods with the quantitative statistical information obtained by reciprocal space techniques. In this way, a wide

length scale from 10 nm to 10 µm could be covered. Furthermore, the applicability of nGI to image the IMS domain distribution in the bulk has been proven. Indeed, the shown nGI measurements provide the first direct visualization of the IMS domain nucleation in bulk samples.
As a main finding of this investigation, an unconventional domain volume filling of the sample within the bulk IMS phase could clearly be identified and explained by geometrical barriers discussed in Sec. 2.2.4. Furthermore, a hysteretic behavior was found, which is most likely linked to a topological hysteresis. The rocking data moreover reveal a peculiar distribution of Bragg angles within the sample, caused by a bending of the vortex lines. This bending is most pronounced within the IMS and quickly reduces within the Shubnikov phase. These data raised the questions, if it is possible to directly measure and quantify the local distortion of the vortices within the sample, which will be readdressed in Sec. 6.5.
Finally, the results presented in this section have an important impact on the general interpretation of SANS data of type-II superconductors: these data show that the geometry of the sample influences the local vortex lattice configuration even far away from the sample edges. Hence, both the sample shape as well as its illuminated region should always be carefully considered for the interpretation of SANS data.

6.3. Domain structure of the intermediate mixed state in a type-II superconductor in the presence of pinning

The results discussed in Sec. 6.2 have shown the importance of geometrical effects to understand the nucleation of the IMS in a pinning free material: On the microscopic scale, the IMS formation is caused by the crossover of a repulsive to an attractive vortex-vortex interaction. In contrast, the spatial distribution of the domains is strongly determined by the macroscopic geometrical constraints. As a next step, it will be examined, how the IMS nucleation will change if effects of vortex-pinning (Sec. 2.2.3) are taken into account that collectively act on an intermediate length scale on the vortex lattice. Based on the considerations of Sec. 2.3.6 and 2.2.3 a disordered or suppressed final IMS state [87, 89, 90] as well as the appearance of strong magnetic irreversibilities [56] are expected.
In the following section, the structure and the formation of the IMS in the presence of pinning is addressed by combining results of SANS, USANS and nGI with bulk magnetization measurements. For the sake of clarity, these considerations are split into three parts.
Firstly, the process of the IMS nucleation is discussed with a special focus on the procedure of field cooling, since it turned out that in the ZFC and HFC cases, an IMS formation is completely suppressed by pinning and no sign of vortex lattice domains could be detected by either of the used methods. Previous works on this

topic are rare. The IMS stabilization during field cooling has only recently been studied using SANS in Ref. [182], in which a phase coexistence of vortex (IMS) clusters and vortex lattice has been reported.
In the second part 6.3.3, the field dependence of the IMS domain structure, which is stabilized during field cooling, is examined. Although the IMS morphology has been investigated several times (e.g. in [83] and [177]), these studies are rather old. Consequentially, the data are usually based on the decoration method which neither allows a comprehensive investigation of the field dependence nor a recording of the situation within the whole sample. Again, the role of pinning has not been tackled so far. Finally, in Sec. 6.3.4, the distribution of the IMS structure within a wedge shaped sample is examined for different fields by means of nGI.

6.3.1. Experimental setup

The experimental study on the IMS formation was performed on the SANS instruments SANS-1 and TPA, the USANS beamline BT-5 and the nGIs at the ANTARES and ICON beamlines. The setups are described in Sec. 5.4, 5.3, 5.1.2 and 5.2, respectively. Exactly the same sample environment has been used at SANS-1 and for nGI.
At SANS-1, the experimental configuration was the same as described in Sec. 6.2.1. Again, different positions of the sample were probed by a 3 mm Cd aperture. However, as the results are similar for all positions, the attention is restricted to the center position of the specimen. At BT-5 and TPA, the beam size has been reduced to an area of 14 mm diameter in the center of the sample by using a Cd aperture. Hence, only the edges of the samples were masked in these measurements.
The nGI results were calculated out of a stepping sequence of grating G_0 over one complete period in 15 (ANTARES) or 21 (ICON) steps, respectively. The total exposure time for one DFI was set to 3000 s (ANTARES) and 3780 s (ICON). Wavelengths of 4.0 Å (ANTARES) and 4.1 Å (ICON) were used. Additionally, quantitative dark-field imaging has been performed on one sample. For this purpose, nGI scans (17 steps, 60 s exposure time per step) have been conducted for different wavelengths between 3 and 6 Å. In all cases, the spatial resolution of the setup was approximately 0.5 mm.
Four Nb samples were investigated. All samples were prepared from the same single-crystal commercially obtained from MaTeck [183]. The sample was of lower crystallographic quality (RRR $\approx$ 100) than the one examined in Sec. 6.2. A list summarizing the shapes, sizes and demagnetization coefficients of the investigated samples is given in Tab. 6.1. The samples were cut with a diamond wire saw and subsequently polished. Three of the samples were finally etched in a mixture of 50 % HF and 50 % HNO_3 for 30 s in order to reduce surface impurities introduced by the cutting and polishing. A $\langle 110 \rangle$ direction was found to correspond to the normal vector of the discs and of the largest face of Nb 5. In all measurements,

the magnetic field was applied parallel to this crystallographic direction.
The demagnetization coefficient of the cuboid was calculated using the equation given in Ref. [184], while for the disc samples, it was estimated by approximating the discs as flat ellipsoidals (i.e. $D = 1 - \pi t/(4r)$ [40]). A definition of the demagnetization coefficient of the wedge is difficult, as an elliptical approximation is technically speaking not possible, due to the non-parallel surfaces. However, the coefficient should lie between the values of discs with thickness 0.6 ($D = 0.95$) and 2.8 mm ($D = 0.76$).
The Nb wedge, Nb 2 and Nb 3 have been used for neutron investigations, while Nb 5 was solely cut for magnetization measurements on a Quantum design PPMS.

sample	**shape**	**dimensions** (mm)	**etched**	D
Nb wedge	disc shaped wedge	$r = 9.3$, $t = 0.6 - 2.8$	no	0.76 - 0.95
Nb 2	disc	$r = 9.3$, $t = 2.0$	yes	0.83
Nb 3	disc	$r = 9.3$, $t = 0.6$	yes	0.95
Nb 5	cuboid	$1.9 \times 3.7 \times 4.0$	yes	0.50

Table 6.1.: List of niobium samples. D demagnetization coefficient for the studied field geometry, r radius and t thickness of the sample. Nb 2 and Nb 3 originate from adjacent parts, while the Nb wedge was cut from the other side of the 5 cm long original crystal. Nb 2 and Nb 3 are slightly flattened which leads to an error of the radius of approx. 0.1 mm.

6.3.2. The IMS nucleation during field cooling

Magnetization

The magnetic characterization of niobium is presented in Fig. 6.13. In (a), the magnetization of the sample Nb 5 is shown as function of the applied magnetic field for various temperatures between 2 and 9 K. The field was applied after ZFC to the required temperature. A half hysteresis loop has been measured, hence, the data show the initial magnetization curve and the first branch of the irreversible magnetization. The second branch results from an inversion at the origin. As predicted by the critical state theory (Sec. 2.2.3), the magnetization is diamagnetic after the initial field ramp and paramagnetic in decreasing fields. For all temperatures, the remanent magnetization at 0 T is roughly half the maximum $M(B)$ value. The magnetization loop decreases with increasing temperature, as the sample becomes less diamagnetic. The signal completely vanishes above 9 K.
The upper critical field B_{C2} is marked by the disappearance of the magnetization, since normal conducting niobium is only slightly diamagnetic. At 4 K, B_{C2} is determined to 420 mT which is considerably higher than values reported in literature for pure niobium (e.g. $B_{C2}^{\mathrm{Lit}}(4.2\,\mathrm{K}) = 275\,\mathrm{mT}$ [15] or $B_{C2}^{\mathrm{Lit}}(4.1\,\mathrm{K}) = 278\,\mathrm{mT}$ [185]). A determination of B_{C1} is not possible from the kink in the $M(B)$

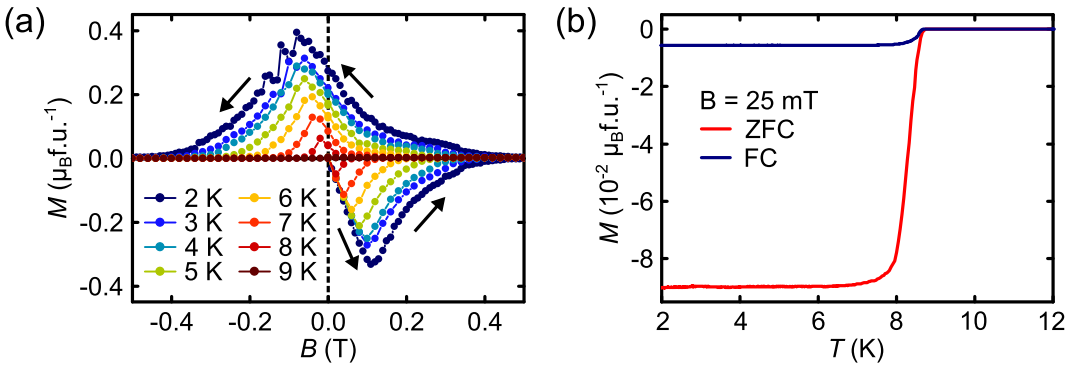

Figure 6.13.: Magnetization data of the cuboid sample Nb 5. (a) Magnetization as function of the applied magnetic field, measured for different temperatures between 2 and 9 K. Shown are the initial magnetization curve after ZFC and half a hysteresis loop. (b) Temperature dependence of the magnetization at $B = 25\,\mathrm{mT}$. The curve was measured once for increasing temperatures, after ZFC to 2 K, and successive application of the magnetic field, and once for decreasing temperature in an applied field (FC).

dataset, as the field of first flux penetration is typically strongly increased by pinning. The critical temperature can be determined to $T_\mathrm{C} = 9.1 \pm 0.1\,\mathrm{K}$ by extrapolating the upper critical field $B_{\mathrm{C2}}(T)$ to zero [186]. This value is only slightly reduced compared to pure samples ($T_\mathrm{C}^\mathrm{Lit} = 9.3\,\mathrm{K}$ [50]). Although the impurity composition and concentration of the crystal have not been investigated, the critical field and temperature correspond well to values of $T_\mathrm{C}^\mathrm{Lit} = 9.03\,\mathrm{K}$ and $B_{\mathrm{C2}}^\mathrm{Lit} = 415\,\mathrm{mT}$, found for a contamination with 0.14 atomic percent of interstitial oxygen [187].

Typical $M(T)$ data are exemplarily presented in Fig. 6.13 (b) for an applied field of 25 mT. The red curve has been measured for increasing temperatures after the sample had initially been cooled down in zero field. In contrast, the blue curve has been measured field cooled i.e. for decreasing temperature in an applied field. In a pinning free sample, both curves would overlay (neglecting geometrical barriers), since the thermodynamic equilibrium is reached independently of the used cooling path. Moreover, the magnetization would continuously decrease with decreasing temperature, since the sample becomes more diamagnetic. In contrast, the presented Nb sample is less diamagnetic after FC, as pinning prevents a complete expulsion of magnetic flux during cooling. Furthermore, the magnetization is temperature independent in most of the superconducting phase. Deviations from a constant magnetization firstly emerge above 6.3 K and 7.8 K for ZFC and FC measurements, respectively. Interestingly, a reversible state where both curves coincide, is not found below $T_\mathrm{C}(25\,\mathrm{mT}) = 8.8\,\mathrm{K}$ underlying that the studied situation does not correspond to the thermodynamic equilibrium.

The presented data strongly suggest that the vortex configuration is frozen below 6.3 K at 25 mT, as the macroscopic magnetization experiments do not show any further temperature dependence. In particular, no sign of an IMS nucleation

is seen in the data. These predictions are tested in the following by means of small-angle scattering which probes the vortex lattice on the sub-micrometer scale.

Small-angle neutron scattering

Typical SANS results obtained on the Nb wedge are presented in Fig. 6.14 (a). Each scattering pattern corresponds to the sum of a rocking scan performed after the sample had been cooled down in an applied field of 26 mT (top row) and 41 mT (bottom row), respectively. The data have been normalized to the zero field pattern, hence, only magnetic contributions are visible. The hexagonal symmetry of the vortex lattice along the ⟨110⟩ direction is in agreement with the results of Sec. 6.2 and with literature [93].

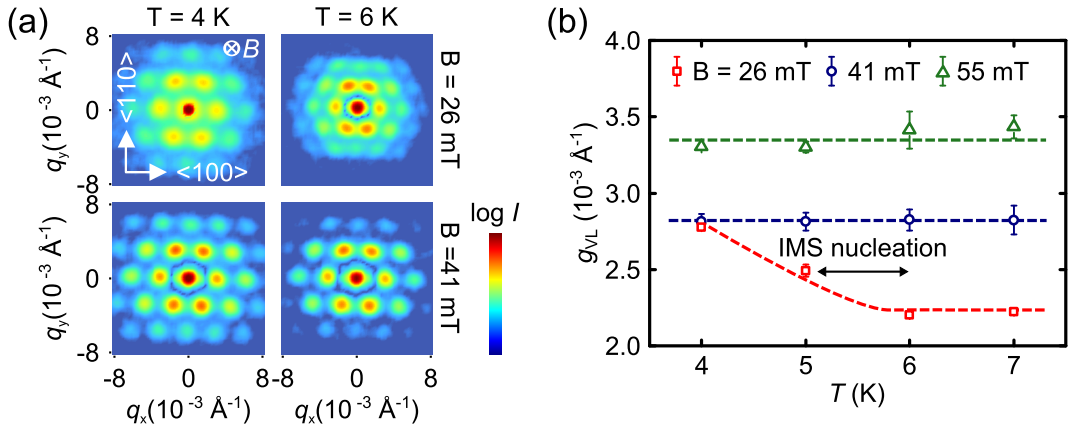

Figure 6.14.: SANS results of the niobium wedge. (a) Typical SANS pattern of the vortex lattice in Nb for different fields and temperatures. The vortex lattice parameter is temperature independent for 41 mT (bottom row). In smaller fields, however, a shrinking of the vortex lattice is observed for decreasing temperatures. (b) Quantitative evaluation of the reciprocal vortex lattice spacing g_{VL} which corresponds to the position of the horizontal first order Bragg peaks. g_{VL} is drawn as function of the temperature for three different field values. The error bars correspond to the differences of the spacing extracted from the left and the right peaks. These errors are slightly larger than the errors associated with the determination of the peak position.

Comparing the data for 26 and 41 mT shows that the reciprocal vortex lattice spacing g_{VL} is temperature dependent only for the lower field, where g_{VL} increases for decreasing temperature. In contrast, g_{VL} is constant in higher field.
This can be seen in Fig. 6.14 (b), where g_{VL} is plotted as function of the temperature for three different field values. At 55 and 41 mT, g_{VL} takes a constant value of 3.4×10^{-3} and 2.8×10^{-3} Å^{-1}, and no variation of the lattice parameter could be detected between 4 and 7 K. This observation is in agreement with magnetization data which suggested a freezing of the vortex lattice below 7 K. However, cooling in a field of 26 mT is accompanied by a continuous increase of g_{VL}

from $2.2 \times 10^{-3}\,\text{Å}^{-1}$ to $2.8 \times 10^{-3}\,\text{Å}^{-1}$ below 6 K. The local magnetic induction within the flux line lattice, as given in Eq. 3.56, hence, dramatically increases from 22 mT to 36 mT. As the macroscopic magnetization at 25 mT, shown in Fig. 6.13 (b), did not change in this temperature range, the data clearly indicate a microscopic rearrangement of flux below 6 K. Although the development of a vortex lattice superstructure in form of microscopic IMS domains seems most likely at this point, the SANS data alone could not exclude a macroscopic redistribution of flux. However, the typical field independence of the vortex lattice parameter in the IMS is found at 4 K for 26 and 41 mT.

Ultra-small-angle neutron scattering

The formation of IMS domains can be directly verified using ultra-small-angle neutron scattering. Typical USANS rocking curves are shown in Fig. 6.15 and 6.16 for a magnetic field of 20 and 17 mT, respectively. Presented is the scattered intensity as function of the wavevector transfer q. The data were taken during FC to 4 K. Only magnetic scattering is presented in the data, as the scattering curves are normalized to the curves above T_C using Eq. 4.44.

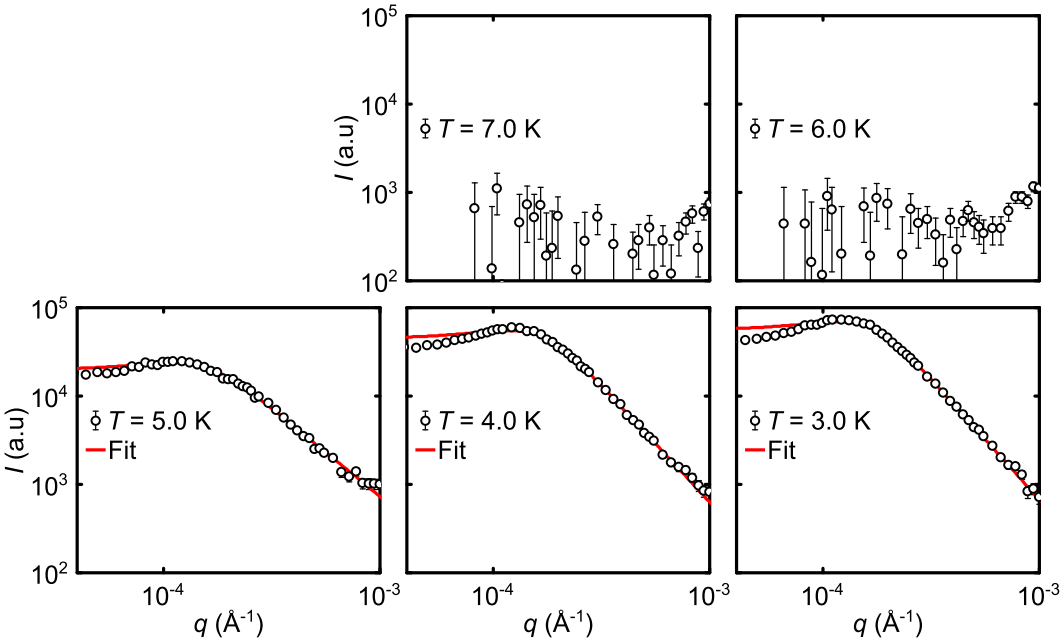

Figure 6.15.: USANS scattering curves at $B = 20\,\text{mT}$ for various temperatures after FC. The data are normalized to curves above T_C. B was applied along $\langle 110 \rangle$, parallel to the neutron beam, while the crystallographic $\langle 100 \rangle$-direction was rotated into the horizontal plane. Pronounced scattering can only be detected below 6 K. The red curve is a fit to Eq. 6.4, whose underlying model will be discussed in Sec. 6.3.3.

Considering the data taken at 20 mT, pronounced USANS scattering is not found

for temperatures above 5 K. Only at high q, a weak scattering signal appears that might be a signature of the vortex lattice Bragg peak, observed slightly above the probed q-range in Ref. [182]. The situation changes at smaller temperatures. Here, a scattering curve develops that is characterized by a peak around $1.2 \times 10^{-4}\,\text{Å}^{-1}$ and a decreasing intensity following a power function for high momentum transfers. The position of the peak remains nearly constant in the probed temperature range. However, the scattered intensity strongly increases with decreasing temperature.

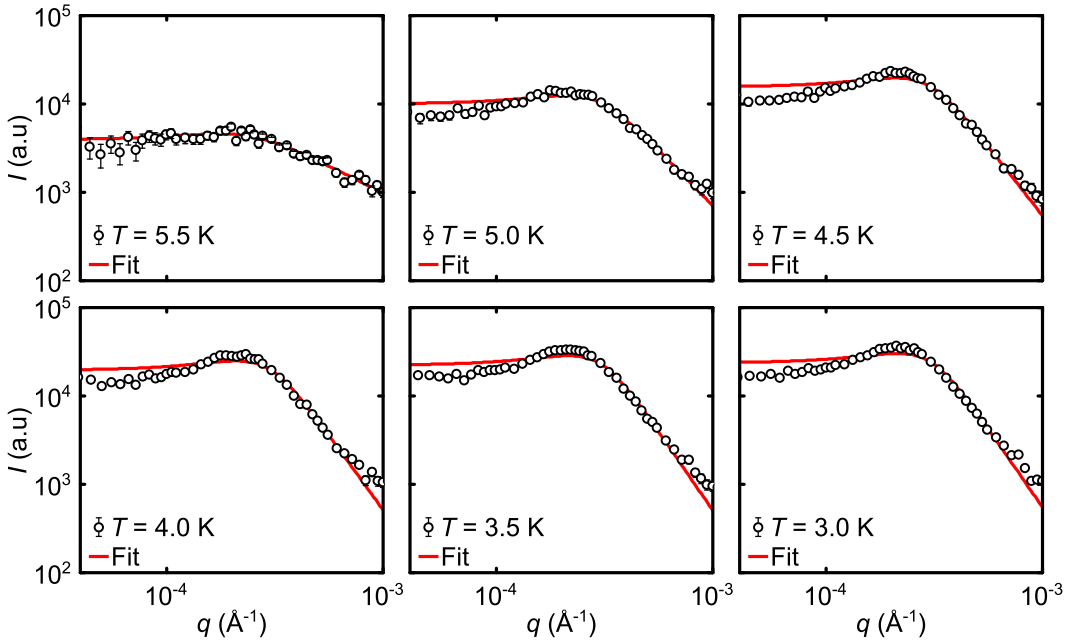

Figure 6.16.: USANS scattering curves at $B = 17\,\text{mT}$ for various temperatures after FC. The data are normalized to curves above T_C. The crystal was oriented as in Fig. 6.15. The red curve is a fit to Eq. 6.4, whose underlying model will be discussed in Sec. 6.3.3.

A quite similar behavior is found in an applied field of 17 mT which has been measured with smaller temperature steps. Again, the scattered intensity significantly increases for decreasing temperature. Furthermore, the width of the peak seems to decrease moderately by lowering T. Note that the position of the scattering peak at approximately $2.8 \times 10^{-4}\,\text{Å}^{-1}$ is shifted to higher values compared to 20 mT. Although the origin of this scattering curve will be discussed extensively in the next Sec. 6.3.3, the shift of the peak position to lower q for increasing field directly confirms that micrometer-sized magnetic structures in the sample act as scattering centers, which grow in size with increasing field. Hence, in agreement with SANS, the USANS data can only be interpreted as a second indication of a nucleating IMS structure below 6 K.

Neutron grating interferometry

The results of magnetization and SANS have revealed that below 6 K, the vortex lattice seems to rearrange on the microscopic level, overcoming pinning, while macroscopically no flux is expulsed. At the same time, a peak shows up in USANS indicating a further correlation length of a few micrometer. These observations give a strong hint for a build up of the IMS structure. Neutron grating interferometry can provide further insight into the IMS nucleation process, as it visualizes how the IMS is distributed within the sample during domain formation.

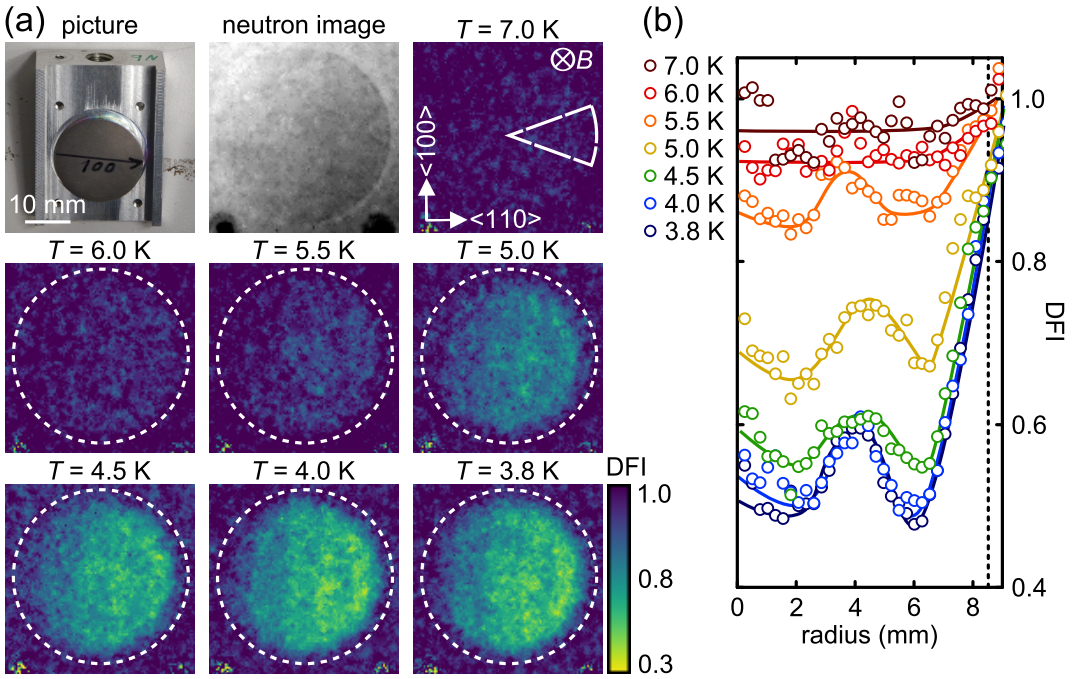

Figure 6.17.: Results of nGI on the Nb wedge in a field of 20 mT. The measurements were performed at ICON. (a) Shown is a picture of the sample in its holder, a neutron radiography as well as DFI results. The DFI data were taken after field cooling to the specified temperature. The sample position is marked by the white circle. The crystal has been aligned following the procedure described in Ap. A.6. (b) Radial profiles of the DFI at various temperatures. Averaging was performed over the segment of a circle marked for the DFI at 7.0 K. The lines are a guide to the eye. The DFI contrast strongly decreases for decreasing temperature and is characterized by two minima corresponding to the contrast degradation in the center of the sample and to the ring near the edges.

In Fig. 6.17 (a), the nGI results obtained at the Nb wedge are presented. Shown is a picture of the sample in its holder, a neutron radiography of the sample, and DFI for various temperatures between 7.0 and 3.8 K. The sample was cooled down in an applied magnetic field of 20 mT. The data were normalized to the normal state at 10 K. The DFI at low temperatures are superimposed by weak vertical

streaks which are an experimental artifact, arising due to a slight thermal drift in the setup during the long time of the field cooled measurement.
The presented data are in complete agreement to the USANS results: No contrast in the DFI is seen at 7.0 K, while in between 6.0 and 5.0 K a distinct contrast develops that further decreases with cooling to the base temperature of 3.8 K. The contrast variation within the sample at 3.8 K is characterized by a contrast minimum in the center of the wedge and a ring-shaped contrast decrease near the edge of the sample[1]. These two features are observed as dips in the radial DFI profiles of Fig. 6.17 (b). In order to obtain these profiles, the DFIs of (a) have been radially averaged within the segment of a circle marked for 7.0 K. For the sake of clarity, error bars have been skipped. The errors lie in the range of 10 % besides for low radii below 2 mm, where they strongly increase due to the reduced averaging area. Both the DFI and the corresponding profiles reveal that the contrast does not suddenly drop down at the sample edge (dashed line in (b)), but a region of slowly decreasing DFI signal is formed at the sample boundary. The observed spatial variation in the DFI and hence in the IMS domain distribution already seems to have developed during the IMS nucleation below 5.0 K.

A comprehensive picture of the IMS nucleation out of a homogeneous, pinned vortex lattice

Based on the experimental results of the Nb wedge at $B \approx 20\,\mathrm{mT}$, a coherent picture about the FC nucleation of the IMS is obtained. The FC process is schematically illustrated in Fig. 6.18 and can be summarized as follows: For $10\,\mathrm{K} \geq T \geq 7\,\mathrm{K}$, the sample enters the Shubnikov phase from the normal conducting state (1-2). With decreasing temperature, the magnetic field is macroscopically expelled from the sample as seen by magnetization measurements. Microscopically, the vortex lattice distance is expected to increase.
In the region $6\,\mathrm{K} \leq T \leq 7\,\mathrm{K} = T_\mathrm{F}$, the expulsion of flux is stopped, as $M(T)$ has reached a constant value and the vortex lattice parameter probed by SANS remains constant. In this temperature range, the magnetic flux is trapped inside the sample (3), since the material has been cooled below the temperature T_F at which the vortex lattice is pinned by imperfections within the material. Hence, the magnetic properties of the sample have to be described using the critical state model [56] (Sec. 2.2.3) which assumes that the flux lines can only be further moved along a field gradient sufficiently high to overcome the pinning forces. The effects of field cooling on the macroscopic field distribution have been treated in terms of the critical state theory in Ref. [188] and [189]. Although, geometric effects have been neglected in these works, it has been shown that during field cooling, the induction within a superconductor, and hence the vortex lattice parameter, is only

1 Hence, the contrast distribution is comparable to the one obtained during the nucleation of the IS (Sec. 6.1).

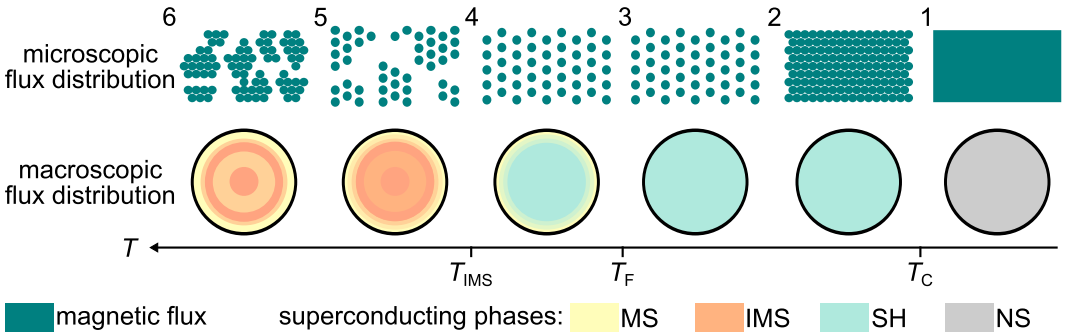

Figure 6.18.: Illustration of the IMS nucleation during FC. For decreasing temperature, the sample first becomes superconducting at T_C and the vortex lattice is formed (1-2). Further cooling initially decreases the vortex lattice parameter (3). When the temperature is sufficiently reduced to pin the vortices, the vortex lattice configuration is frozen in the center of the sample, but flux is still expelled on the edges (4). At T_{IMS}, the crossover to an attractive vortex interaction takes places. Consequently IMS domains are formed and a peculiar ring shaped IMS distribution arises (5). Further cooling of the sample only slightly influences the domain morphology and distribution. However, the vortex lattice parameter within the domains is further decreased (6).

reduced along a small area near the edge of the sample, whereas it is completely unaffected in its center. This peculiarity arises, since a magnetic gradient, which is sufficient to deplete the vortex lattice, can only be generated in a small region near the surface of the sample (4).

For $T \leq 6\,\mathrm{K} = T_{IMS}$, the characteristics of the microscopic vortex lattice change. (i) Its lattice parameter is reduced as indicated by SANS, and (ii) a magnetic µm domain structure nucleates as shown by USANS and nGI. The sample has hence entered the IMS (5). This change of the vortex configuration is remarkable, since the macroscopic magnetization is unaffected. Obviously, the pinning within the sample prevents a further expulsion of the vortex lattice, but not an internal rearrangement of it. This might be expected, since it has been discussed in Sec. 2.2.3 that pinning forces act collectively on an elastic vortex lattice and not on individual vortices. The presented data suggest that below 6 K the crossover from a repulsive to an attractive vortex-vortex interaction occurs. While for pure niobium this crossover has been observed [190] and predicted [46] very close to T_C, it can be considerably shifted to lower temperatures in impure samples, because of their higher κ [46]. This seems to be the case in the presented study. The crossover is accompanied by a strong influence on the elastic properties of the vortex lattice, as has already been proven by means of stroboscopic SANS [191], allowing for the observed rearrangement of the vortex lattice.

The spatial distribution of the IMS phase, as recorded by means of nGI, exhibits three distinctive features (5). (i) A diminished DFI contrast in the center of the sample, (ii) a reduced DFI contrast on a ring, and (iii) a smooth increase of DFI contrast to the edges of the sample. While the latter simply seems to be

a manifestation of the discussed macroscopic flux depletion at the sample edge during FC [188, 189], the other two observations cannot be definitely explained. They contradict the simple assumption of the critical state theory which supposes a frozen vortex configuration in most of the sample. This problem might be clarified by numerical simulations as such calculations (e.g. Fig. 7 of Ref. [69]) showed that field decreasing after initial penetration of a disc shaped sample results in a similar ring-like structure.

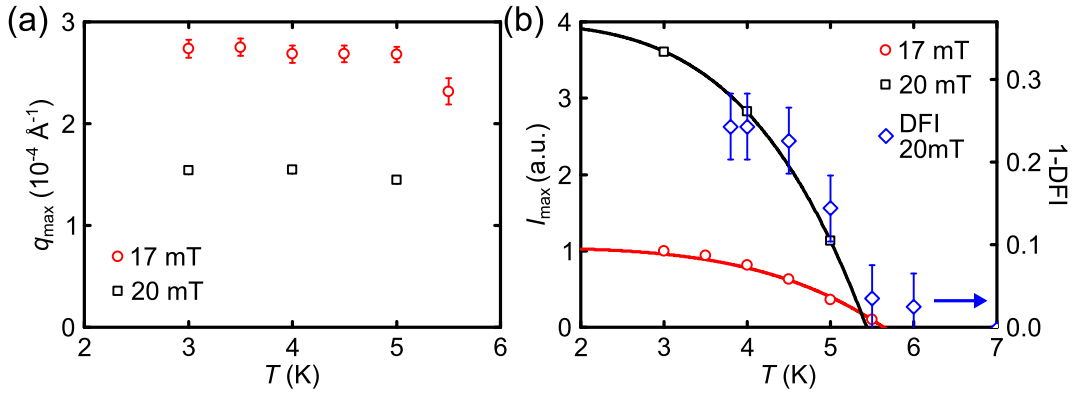

Figure 6.19.: Quantitative evaluation of the USANS data shown in Fig. 6.16 and 6.15. (a) Maximum of the scattering curves $q_{\max}$ as function of the temperature. The maximum is nearly temperature independent, only for 17 mT, the peak is slightly shifted to lower q at 5.5 K. The error bars for 20 mT lie within the symbols. (b) Temperature dependence of the parameter $I_{\max}$ for 17 and 20 mT, extracted from the USANS scattering curves. The solid lines are fits to $\propto T^4 + \text{const}$. Additionally plotted are the mean values of the DFI shown in Fig. 6.17. For comparison they are drawn as 1-DFI. Clearly the data agree qualitatively well.

Further structural information can be obtained from an evaluation of the USANS data presented in Fig. 6.16 and 6.15. Fits of the data to Eq. 6.4 are shown as red lines in theses figures. From such a fit, the peak position $q_{\max}$[1], which is a measure of the average domain size and the maximal scattered intensity $I_{\max}$ that quantifies the magnitude of scattering, can be obtained. While the regression seems to be inaccurate at low q, the fit succeeds in determining the peak position and the maximal peak intensity. These parameters are presented as function of the temperature in Fig. 6.19 (a) and (b), respectively. The details of the fitting and a physical motivation of the used model will be shifted to Sec. 6.3.3 since at this point only a qualitative discussion is necessary.

The peak position remains nearly constant for decreasing temperature. Hence, as the sample enters the IMS, stable domains of the energetically preferred size

1 Note that $q_{\max}$ cannot be directly extracted from the data, as USANS scattering curves are slit-smeared. Hence, the fitting is necessary.

(see Sec. 6.3.3) are formed. On the other hand, the scattered intensity strongly increases with decreasing temperature, suggesting either (i) a scattering contrast enhancement of the domains, (ii) an increase of the domain number, or both. The increase of scattering length density contrast can be easily estimated: According to Eq. 3.50, the scattering amplitude f will depend on the averaged magnetic induction $B_0 \propto g_{\mathrm{VL}}^2$ (Eq. 3.56) within the domains. Consequentially, the scattered intensity should behave as: $I_{\max} \propto f^2 \propto B_0^2 \propto g_{\mathrm{VL}}^4$. Assuming a linear behavior of g_{VL} as suggested by SANS (Fig. 6.14), the scattered intensity should reveal a T^4-temperature dependence. In Fig. 6.19 (b), $I_{\max}$ is accordingly fitted by $I_{\max}(T) \propto T^4 + \mathrm{const}$. As can be seen, this simple relation qualitatively describes the data. Hence, USANS suggests that the morphology of the formed IMS domains is not strongly changed after initial nucleation, but the density of the vortex lattice within the domains is continuously increased (6).
Finally, the close agreement of USANS data and quantitative DFI observations should be mentioned. As USANS indicates a rather constant domain structure during FC, the corresponding IMS correlation function $G(x)$ (Eq. 3.36) should not strongly vary with temperature. Hence, $1 - \mathrm{DFI}$ should be proportional to $I_{\max}$ as:

$$(1 - DFI) = 1 - \exp\left[\Sigma t \left(\frac{G(\xi_{\mathrm{GI}})}{G(0)} - 1\right)\right] \tag{6.1}$$

$$\approx 1 - 1 + \Sigma t \left(\frac{G(\xi_{\mathrm{GI}})}{G(0)} - 1\right) \tag{6.2}$$

$$= \mathrm{const} \times \Sigma \propto I_{\max} \tag{6.3}$$

The average DFIs of the data presented in 6.17 are additionally plotted against the temperature in 6.19 (b). According to Eq. 6.3, the $(1 - \mathrm{DFI})$ trend is in good qualitative agreement with $I_{\max}$.

6.3.3. Field dependence of the IMS morphology

The previous section has revealed that the IMS nucleation in a sample showing significant pinning only takes place during field cooling. Hence, IMS domains are formed out of the regular vortex lattice of the Shubnikov phase. This transition, which arises below 6 K, is characterized by the appearance of a broad peak in the USANS scattering curve indicating that a domain structure of a preferred domain size has developed. In the following, the morphology of this domain structure and its field dependence is studied by means of SANS and USANS.

Small-angle neutron scattering

The field range of the IMS within the different samples can be deduced by SANS. In Fig. 6.20, results obtained at TPA are presented for Nb 2 and Nb 3, respectively.

In (a) and (c), the scattered intensity of the samples is plotted versus the modulus of the wavevector transfer q for different magnetic fields between 10 mT and 180 mT. The sample has been field cooled to 4 K. Only magnetic scattering is present in the graphs, since the data have been normalized to zero field. The curves correspond to radial profiles of the scattering pattern achieved by integrating a SANS rocking scan. The maximum marks the position of the first order Bragg peak of the vortex lattice g_{VL}. Its value has been determined by a Gaussian approximation of the scattering curves and is plotted against the applied field in (b) and (d). The errorbars correspond to the FWHM of the Gaussian distribution. The hallmark of the IMS, a constant g_{VL} and an increasing scattered intensity for increasing field, is observed in both samples. In higher fields, g_{VL} is proportional to $\sqrt{B}$ as indicated by the red fits shown in Fig. 6.20 (b) and (d), while the intensity of the Bragg peaks slowly decreases with increasing field (compare (a) and (c)).
Various sample parameters can be obtained from the $g_{\mathrm{VL}}(B)$-curves: The field of transition from the IMS to the Shubnikov phase B_2 can be deduced from the intersection of the high field curve with the constant q value of the IMS. This constant value $g_{VL}(IMS)$ is furthermore connected to the induction within the Shubnikov domains B_0 via Eq. 3.56. Finally, the lower critical field B_{C1} can be calculated from these quantities (Eq. A.7). Values for B_2, g_{VL}, B_0 and B_{C1} are summarized in Tab. 6.2 for both samples. All values depend on the sample geometry and are considerably reduced compared to pure Nb (Sec. 6.2). The latter fact underlines that the vortex lattice configuration is frozen at higher temperatures where B_{C1} and B_0 are smaller. In pure Nb, comparable B_{C1} values are found around $T = 7\,\mathrm{K}$ [185].

	Nb 2	Nb 3
B_2(mT)	45 ± 1	34 ± 1
$g_{\mathrm{VL}}(IMS)(10^{-3}\text{Å})$	3.0 ± 0.1	2.6 ± 0.1
B_0(mT)	41 ± 2	32 ± 1
B_{C1}(mT)	65 ± 4	72 ± 20

Table 6.2.: Field of the IMS to Shubnikov transiton B_2, reciprocal lattice parameter g_{VL} of the vortex lattice within the IMS, induction within the Shubnikov domains B_0 and lower critical field B_{C1} of the Nb samples.

Ultra-small-angle neutron scattering

The domain structure nucleated during FC was probed by means of ultra-small-angle neutron scattering. Typical USANS rocking curves for different applied fields between 1 and 34 mT are shown in Fig. 6.21 on the example of the Nb 2 disc. Corresponding data of Nb 3 and Nb wedge are given in Ap. A.7. All data

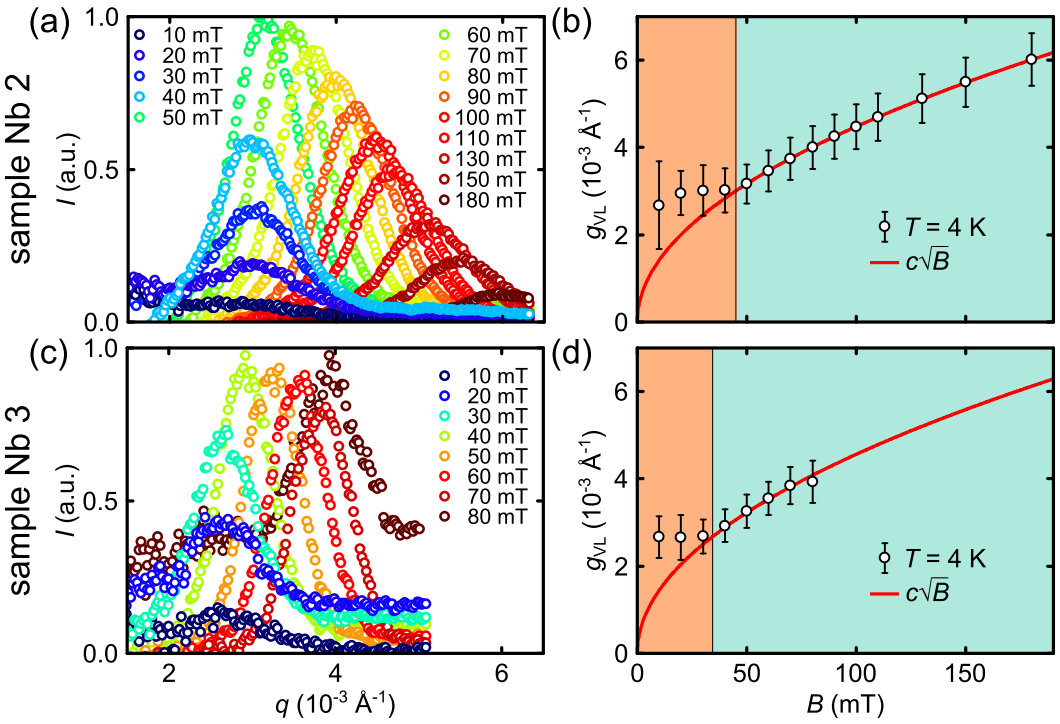

Figure 6.20.: SANS results of Nb 2 and Nb 3 for different applied fields after FC to 4 K. In (a) and (c), the scattered intensity is plotted as a function of the wave vector transfer q. The data were normalized to zero field and scaled to the maximal intensity. The position of the peaks corresponds to the vortex lattice parameter g_{VL} which is plotted against the magnetic field in (b) and (d). In low fields, the sample is in the IMS, and the typical constant q behavior is observed. In higher fields, g_{VL} is proportional to $\sqrt{B}$. The field range of the IMS varies for the two samples due to their different thicknesses. The parasitic offset for 80 mT in (c) is most probably caused by a small displacement of the cryomagnetic setup during He filling. It does not influence the determination of g_{VL}.

were obtained after field cooling to 4 K. Presented is the scattered intensity as function of the wavevector transfer q. The data were normalized to zero field. For 1 mT, the scattering curve of Fig. 6.21 is characterized by weak and diffuse scattering representing background. In increasing fields between 9 and 26 mT, a distinct scattering signature, indicating the nucleation of IMS domains, has developed. As in Fig. 6.15 and 6.16, the scattering curve is distinguished by a broad peak at low q, followed by a power law decrease at higher q. With enhanced field, the peak position moves to lower q-values, while the overall scattered intensity increases. Finally, the intensity strongly drops down at $B = 34$ mT and no peak is observed in the scattering curve. A qualitatively similar behavior is found in all investigated samples (Fig. A.7 and A.8).

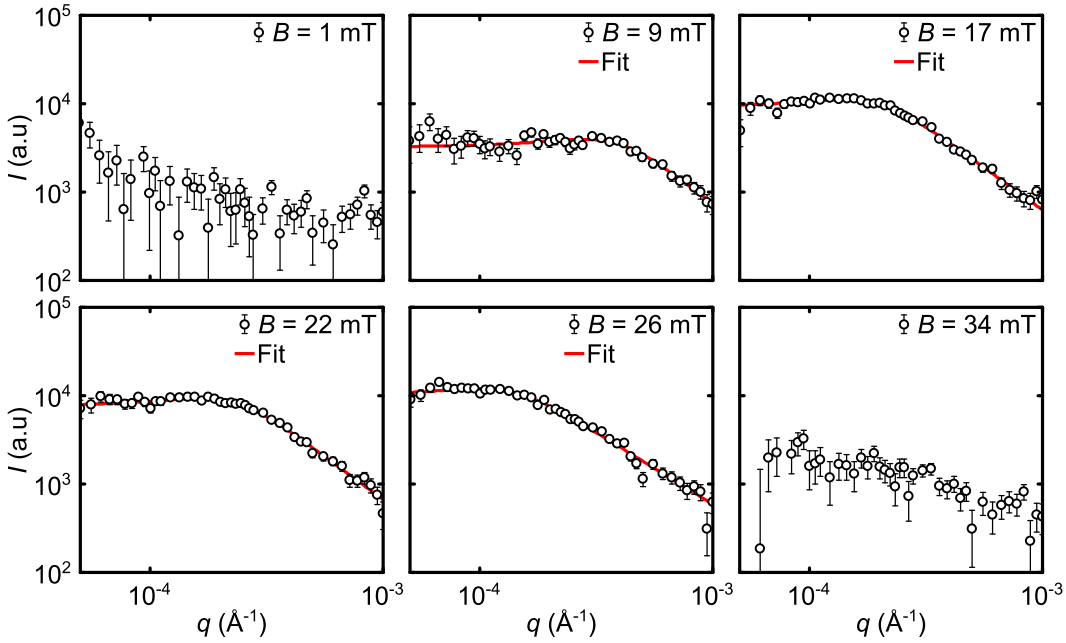

Figure 6.21.: USANS scattering curves of the Nb 2 sample for different magnetic fields. The sample has been field cooled to 4 K. B was applied along $\langle 110 \rangle$, parallel to the neutron beam, while another crystallographic $\langle 110 \rangle$-direction was rotated into the horizontal plane. The red curves are fits to Eq. 6.4.

The IMS domain morphology

Two distinct characteristics of the scattering curve arise already from the fact that USANS particularly probes the micrometer range: (i) The field modulation within the vortex lattice of the IMS domains takes place on a smaller length scale of 100 nm. The IMS structure can hence be described as a two phase system characterized by a homogeneous scattering length density within the domains. (ii) Since the coherence length of the neutron beam is comparable to the IMS size of a few microns, USANS particularly probes the form factor, but is largely insensitive to the structure factor of the IMS.
A description of the IMS domains as cylindrical objects seems likely from Fig. 1.1. However, the corresponding form factor [192] does not reproduce the obtained USANS data. A more satisfactory approximation is reached by the empirical formula given in Ref. [193]:

$$I_{\mathrm{unsmeared}}(q) = I_{\mathrm{max}} \frac{\left(1+\frac{\gamma_s}{2}\right)\left(\frac{q}{q_{\mathrm{max}}}\right)^2}{\frac{\gamma_s}{2}+\left(\frac{q}{q_{\mathrm{max}}}\right)^{2+\gamma_s}} \ , \tag{6.4}$$

in which q_{max} is the position of the peak and I_{max} is the corresponding intensity. The parameter γ_s, describing the power law decrease at high q values, is connected

to the dimensionality of the system [193]. This scattering function is typically used to describe phase-separating mixtures [193] that develop during spinodal decomposition [194]. Hence, the underlying model describes an irregular, isotropic two-phase system which is however characterized by a preferred correlation length. In order to obtain consistency with the data, a smearing of Eq. 6.4 is required (compare Sec. 4.5 and Eq. 3.42). The shown data are thus fitted according to:

$$I(q) = \frac{1}{q_\mathrm{v}} \int_0^{q_\mathrm{v}} I_\mathrm{unsmeared}\left(\sqrt{q^2 + q_\mathrm{y}^2}\right) dq_\mathrm{y} \ . \tag{6.5}$$

The integration is performed up to $q_\mathrm{v} = 0.117\,\text{Å}^{-1}$ which is an instrumental parameter describing the maximal vertical scattering angle under which neutrons can reach the detector [158].
Fits of the data to Eq. 6.5 are shown as red lines in Fig. 6.15, 6.16, 6.21, A.7, and A.8. For Nb 2 and Nb 3, the scattering curves are well approximated by the fit. Small deviations only arise for the wedge shaped sample in the low q range. The parameter γ_s is deduced to $\gamma_\mathrm{s} \approx 3$ for sample Nb 2 and Nb 3, which is expected for scattering at a two dimensional structure below the percolation threshold of multiple domains [194]. For the Nb wedge, $\gamma_\mathrm{s} \approx 4$ is found, but an accurate determination of γ_s is hampered by the arising vortex lattice Bragg peak. In all samples, γ_s slightly decreases for high fields. Since the high q behavior usually arises from the surface of the scattering structure [111], this either indicates an elongation or a coalescence of the domain structure in higher fields.

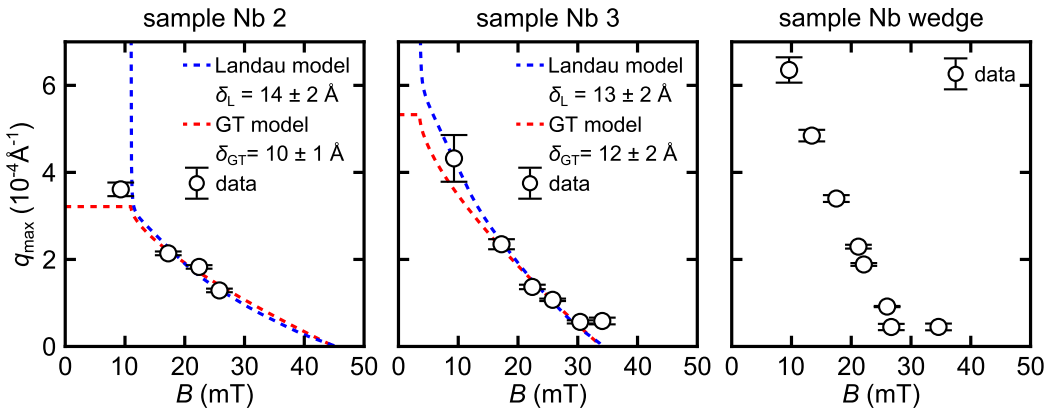

Figure 6.22.: Field dependence of the domain size. The graphs show the parameter q_max, extracted from USANS, as a function of the magnetic field for the samples Nb 2, Nb 3 and Nb wedge. Error bars correspond to the uncertainty of the fit. The red and blue dashed curves correspond to fits to the Landau (Sec. 2.3.2) and the Goren-Tinkham (Sec. 2.3.3) model. A reasonable fitting of the wedge data was not possible, since neither the sample thickness nor the demagnetization coefficient are homogeneous over the sample volume.

The correlation length increases with increasing field and is hence attributed to growing Shubnikov domains. Consequently, even without any assumptions on the domain morphology, the position of the peak $q_{\max}$ provides a measure of the domain size that can be compared to theoretical predictions. The parameter $q_{\max}$, extracted by fitting the data to Eq. 6.5, is plotted against the applied field in Fig. 6.22. For all samples, a qualitatively similar decrease of $q_{\max}$ with the field is found. In agreement to SANS, the IMS nucleation takes place in a slightly different field range for the different samples.

In order to compare the data to the models given by Landau, as well as by Goren and Tinkham (compare Sec. 2.3.2 and 2.3.3), the assumption $q_{\max} = \frac{2\pi}{a_{\mathrm{SH}}}$ is reasonable[1]. In Fig. 6.22, $q_{\max}$ has been fitted to the Landau (blue) and Goren-Tinkham (red) model by means of Eq. 2.27, 2.29 and 2.35. Values of B_0, B_{C1}, D and t were taken from Tab. 6.1 and 6.2, respectively. Thus, only the wall-energy parameter δ remained undefined. Its values, extracted via the Landau and the Goren-Tinkham approaches, are given in the graphs and are denoted by δ_{L} and δ_{GT}, respectively.

In the case of Nb 2 and Nb 3, both models approximate the data well. In contrast, a meaningful fitting of the Nb wedge data was not possible as neither D nor t were homogeneously defined. However, the trend of the data is comparable to Nb 2 and Nb 3, but the IMS is slightly shifted to lower fields. Since USANS scattering already arose at 9 mT in the Nb 2 sample, which is not expected using the IMS borders determined by SANS, B_{C1} might have been slightly overestimated, or a small offset existed in the calibration of the magnetic field. Interestingly, $q_{\max}$ remains approximately constant for 30 and 34 mT in Nb 3 and for 27 and 35 mT in the Nb wedge.

A further determination of the domain morphology from the field dependence of the domain size is not possible, since (i) the errors in $q_{\max}$ are too large as to allow for an unambiguous attribution of the domain size behavior to a specific model, and (ii) the IMS morphology does not seem to be characterized by either of the pure laminar or tubular patterns underlying the models. Nonetheless, the determined wall-energy parameter $\delta \approx 12 \pm 4$ Å is rather independent of the used model. Via Eq. 2.33, this value can be further used to provide a rough estimation of the vortex-vortex interaction energy per unit length $U_{\mathrm{bond}} \approx (2 \pm 1) \times 10^{-13}$J/m. This result corresponds well to the binding energy of 0.6×10^{-13} - 3×10^{-13} J m^{-1} given in Ref. [83] for lead-thallium alloys with a similar Ginzburg-Landau-parameter $0.71 < \kappa < 0.82$.

The good agreement of the USANS curves to Eq. 6.4 rather suggests an irregular but isotropic mixture of Shubnikov and Meissner domains within the IMS than pure tubular or laminar morphologies given by the Goren-Tinkham (Sec.2.3.3) and the Landau model (Sec. 2.3.2), respectively. Although USANS does not allow

1 Notice that a_{SH} replaces a_{n} in Eq. 2.26 and 2.28.

any conclusions on the isotropy of the scattering structure, the assumption of an approximately isotropic IMS domain morphology seems reasonable in the present case: (i) The scattering curves are of similar shape for Nb 2, Nb 3 and Nb wedge although the latter one has been measured in a different crystalline orientation, and (ii) molecular-dynamics simulations [87, 89, 90], discussed in Sec. 2.3.6, have shown that the anisotropy of the vortex domains can be considerably reduced by pinning (compare Fig. 2.18).
In summary, even though the presence of strong pinning distorts the IMS domain structure, it is still characterized by a single correlation length. Since the $q_{\max}$ variation follows the prediction of *both* the Landau and the Goren-Tinkham model, and realistic values of the wall-energy parameter are obtained by means of these methods, the (macroscopic) correlation length of the IMS is still governed by the energy minimization between the interfacial energy of the domains and the energy attributed to the distorted magnetic field (Sec. 2.3). Compared to pinning free Nb at 4 K, the upper critical field is enhanced for the samples revealing pinning due to a higher amount of impurities [186]. In contrast, both the lower critical field and B_0, which are relevant for the IMS nucleation, seem considerably reduced. This discrepancy occurs, since the configuration studied on the samples revealing pinning, does not correspond to the thermodynamic equilibrium reached in the pinning free samples (Fig. 6.23 (a)). Instead, pinning freezes the vortex configuration at higher temperatures. The probed vortex structure is hence in a metastable state which has been frozen at higher temperatures, where all field scales are accordingly reduced (b).

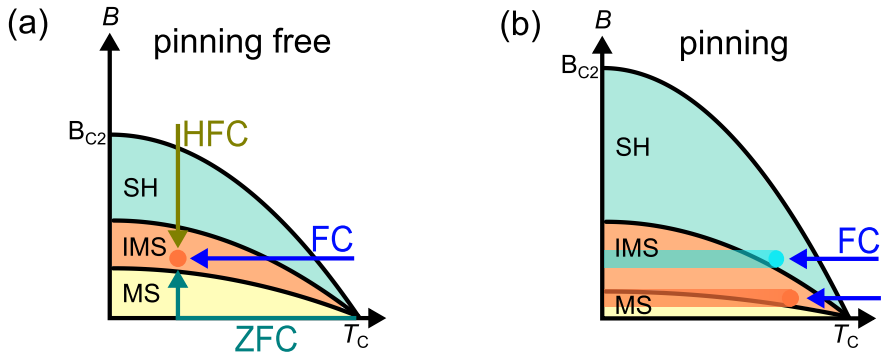

Figure 6.23.: Schematic phase diagram of Nb for the pure and pinning free sample (a), and for the samples revealing significant pinning (b). In the absence of pinning, the vortex lattices reaches the thermodynamic equilibrium independently of the field and temperature history (under the assumption that geometrical barriers are negligible). In contrast, pinning prevents the sample from reaching equilibrium and metastable states are frozen during FC. This is exemplarily sketched by the orange and blue streaks in (b).

6.3.4. Distribution and local variations of the IMS structure

In the subsequent section, spatial variations of the IMS structure are examined by means of quantitative dark-field imaging. In particular, the focus will lie on the wedge shaped sample, since both the Landau as well as the Goren-Tinkham model derived a distinct dependence of the domain size on the sample thickness. Moreover, the consistency of nGI and USANS as well as their high complementarity will be demonstrated.

Neutron grating interferometry

DFIs obtained on the Nb wedge, field cooled to 5 K in different magnetic fields between 0 and 35 mT, are presented in Fig. 6.24. The data were acquired at the ANTARES beamline. In contrast to Fig. 6.17, the DFIs were normalized to the open beam. Hence, the IMS signature is superimposed by some weak residual contrast arising from the sample, its holder, and the tail of the cryostat. In order to obtain a quantification, the mean DFI value is plotted against the magnetic field in Fig. 6.26 (a). The DFI values correspond to the average DFI contrast within the circle marked in Fig. 6.24, normalized to 0 mT.
In zero field, only a small contrast is seen within the sample, since only very weak USANS and incoherent scattering arises in Nb [164]. In between 7 and 35 mT, neutron scattering at the IMS generates an additional magnetic contrast. The mean DFI strongly decreases for increasing fields, until a minimum is reached at 25 mT. For 29 mT, the contrast has reincreased. No further change is observed for 35 mT.
For low and high fields, the DFI contrast homogeneously decreases from left to right in the sample, while between 17 and 25 mT, a contrast variation develops that is characterized by a diminished DFI in the center, as well as on a ring near the edge of the sample. The same peculiar contrast modulation has already been observed in Fig. 6.17.
In order to eliminate the implicit dependence of the DFI contrast on the sample thickness t, the dark-field images presented in Fig. 6.24 have been corrected for each pixel (j,l) according to:

$$\mathrm{DFI}_{\mathrm{cor}}(j,l) = \mathrm{DFI}(i,j)^{\frac{1}{t(j,l)}} \ , \tag{6.6}$$

in which $t(j,l)$ is the local thickness of the sample in beam direction. Results of this correction are shown in Fig. 6.25. These data were additionally normalized to zero field.
The thickness correction completely removes the horizontal DFI gradient apart from the region close to the left edge, where the low signal-to-noise ratio hampers an unambiguous interpretation of the data. The DFI for 22 mT even suggests that the ring-like contrast degradation is sustained in the thinnest parts. On first glance, both observations contradict the predictions of a distinct thickness

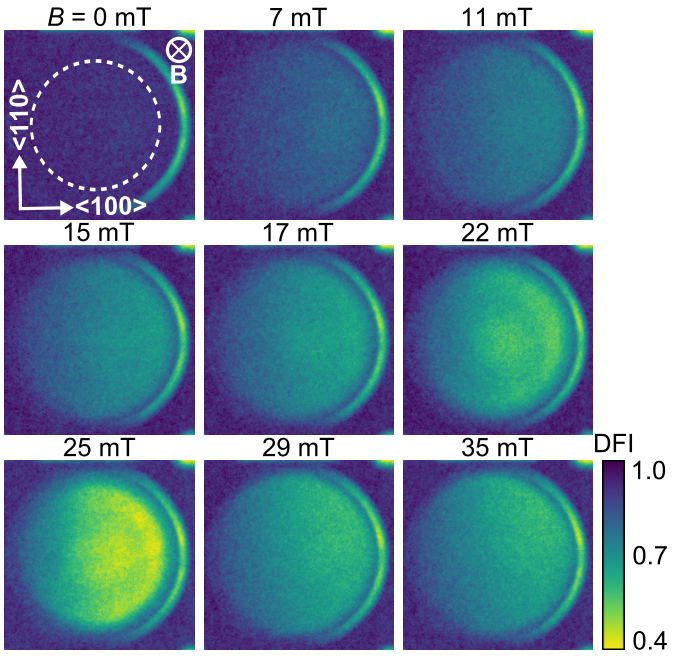

Figure 6.24.: Results of nGI on the Nb wedge at a temperature of 5 K in different magnetic fields applied before cooling. The wedge thickness increases from left to right. A wavelength of 4 Å has been chosen. The shown DFI were normalized to the open beam. Hence, the DFI are superimposed by residual contrast arising from the sample, the sample holder and the tail of the cryostat. The circular region of lower contrast on the right side of the sample is caused by edge refraction at the thicker side of the wedge.

dependence of the IMS morphology, since the DFI contrast is directly linked to the autocorrelation function of the IMS structure. However, a comparison of USANS and nGI, performed in the following, will show that such a conclusion can indeed not be drawn from the nGI data.

Consistency of nGI and USANS

According to Eq. 4.26, the DFI contrast depends on the macroscopic scattering cross-section Σ, the autocorrelation function of the microstructure $G(\xi_{\mathrm{GI}})$, as well as on the sample thickness t. For isotropic scattering, the autocorrelation function G can be obtained from the differential scattering cross-section via Eq. 3.40. In principle, Σ can be calculated from the differential scattering cross-section as well. However, since a USANS measurement provides the neutron transmission of the sample, denoted as T_{rock} in Eq. 4.44, Σ can be directly obtained. The neutron transmission is solely reduced by the scattering and not by the absorbing part of the macroscopic cross-section, since zero field data have been used as reference in

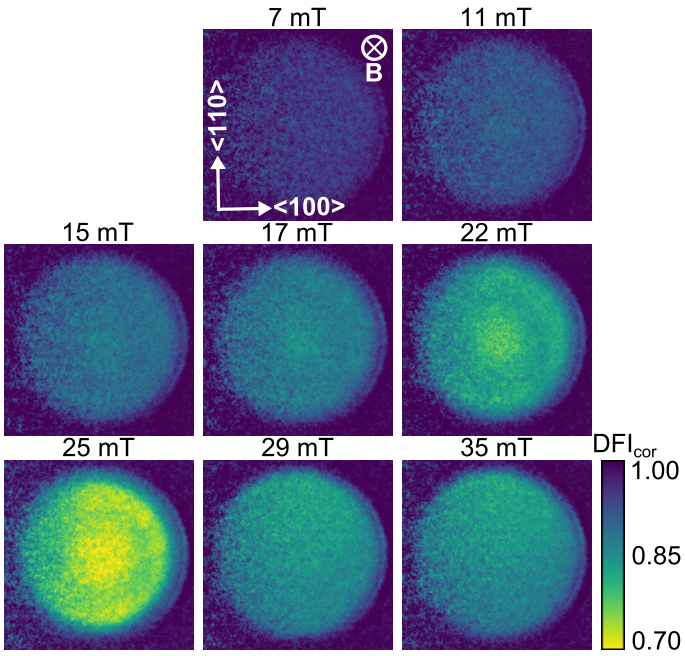

Figure 6.25.: DFI from Fig. 6.24, corrected for the sample thickness according to Eq. 6.6 and normalized to zero field.

the presented study. Consequentially, T_{rock} provides a measure of Σ via:

$$T_{\mathrm{rock}} = \exp\left[-\Sigma\left(\lambda_1\right) t\right] \ . \tag{6.7}$$

The different wavelengths used for USANS (λ_1) and nGI (λ_2) are accounted for by:

$$\Sigma\left(\lambda_1\right) = \left(\frac{\lambda_1}{\lambda_2}\right)^2 \Sigma\left(\lambda_2\right) \ , \tag{6.8}$$

because $\Sigma \propto \lambda^2$ (Eq. 3.32). Consequentially, T_{rock} can be identified in the DFI formula:

$$DFI = \exp\left[\Sigma\left(\lambda_2\right) t \left(\frac{G\left(\xi_{\mathrm{GI}}\right)}{G\left(0\right)} - 1\right)\right] \tag{6.9}$$

$$= \exp\left[-\Sigma\left(\lambda_1\right) t \left(\frac{\lambda_2}{\lambda_1}\right)^2 \left(1 - \frac{G\left(\xi_{\mathrm{GI}}\right)}{G\left(0\right)}\right)\right] \tag{6.10}$$

$$= T_{\mathrm{rock}}^{\left(\frac{\lambda_2}{\lambda_1}\right)^2 \left(1 - \frac{G\left(\xi_{\mathrm{GI}}\right)}{G\left(0\right)}\right)} \ . \tag{6.11}$$

The procedure to calculate a DFI contrast value from the USANS data based on

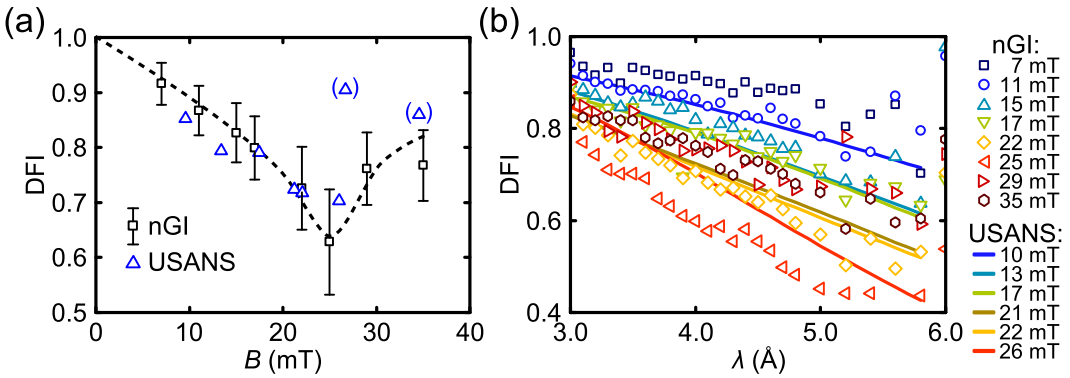

Figure 6.26.: Comparison of USANS and nGI on the example of the field cooled Nb wedge sample. (a) Mean value within the DFI shown in Fig. 6.24 as function of the applied magnetic field. The averaging was performed within a 14 mm circular area in the center of the sample (see Fig. 6.24), which corresponds to the aperture used for the USANS investigations. Additionally, the DFI values calculated by means of Eq. 6.11 from the USANS scattering curves are plotted. For low fields, the values coincide well. At high fields, the calculated values (in parentheses) deviate, since the accuracy of the USANS fit is degraded. Notice that the nGI and USANS experiments were obtained at 4 K and 5 K, respectively, which explains the small deviations in the DFI. The dashed curve is a guide to the eye. (b) Wavelength dependence of the measured and calculated DFI values. Error bars are skipped for the sake of clarity. Notice the slightly different field values for USANS and nGI.

the above considerations, is demonstrated on the example of the Nb wedge in Fig. 6.27. The data corresponds to the scattering curve presented in Fig. A.8, which has been taken at 22 mT after field cooling to 4 K. Firstly, the scattered intensity I is fitted to the model presented in Eq. 6.5. This fit is shown as red curve in (a). The obtained unsmeared scattering intensity $I_{\mathrm{unsmeared}}$ (Eq. 6.4) is given in (b). In order to obtain the correlation function G, $I_{\mathrm{unsmeared}}$ is Hankel transformed according to Eq. 3.40[1]. The autocorrelation function shown in (c) is a damped oscillating function, since $I_{\mathrm{unsmeared}}$ describes a modulated two phase system with a defined correlation length. Finally, using Eq. 6.11, the DFI value at a specific neutron wavelength can be obtained via insertion of T_{rock} and $\xi_{\mathrm{GI}}(\lambda)$ (Eq. 4.17). DFI values calculated from the USANS scattering curves are additionally marked in Fig. 6.26 (a). In low fields, the calculated DFIs (blue triangles) agree well with the measured values (black squares). Considering that nGI scans were conducted at 5 K, a slightly smaller DFI would be expected for 4 K, further reducing the difference of the measured and calculated DFI values at low fields. At high fields, the calculated values strongly differ from the measured ones (points in parentheses),

1 In principle, the USANS data could be directly Fourier transformed to obtain G (Eq. 3.34). Nonetheless, this would increase the noise in the correlation function.

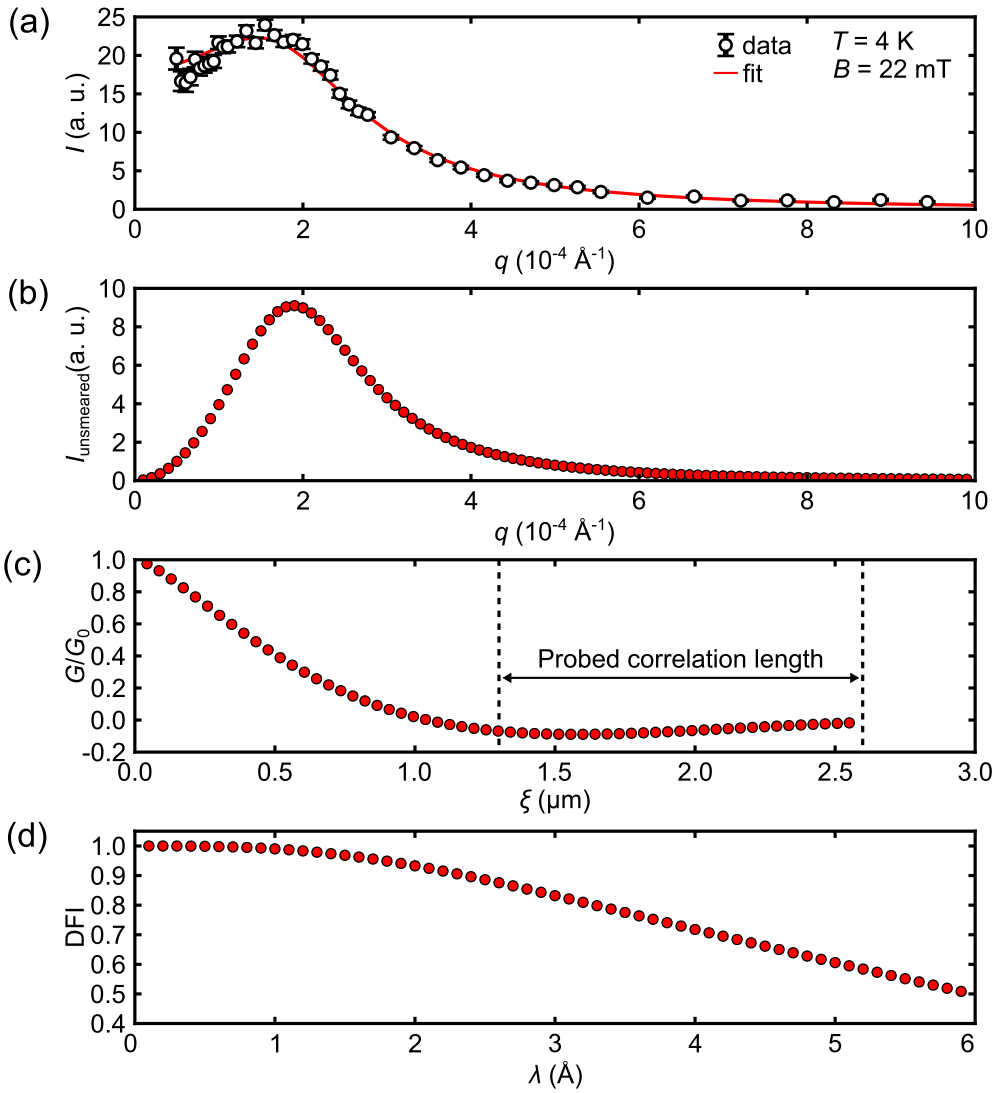

Figure 6.27.: Transformation of USANS results into DFI values on the example of Nb wedge, field cooled to 4 K at $B = 22\,\mathrm{mT}$. (a) USANS scattering curve and corresponding fit to Eq. 6.5. (b) Unsmeared scattered intensity according to Eq. 6.4. (c) The normalized autocorrelation function G results as the Hankel transform of the scattering function shown in (b). (d) Calculated $\mathrm{DFI}(\lambda)$ curve according to Eq. 6.11.

since the correlation peak in the USANS data vanished. The accuracy of the fit is hence strongly reduced, which hampers the data evaluation.
The nGI scans shown in Fig. 6.24 have been repeated for different wavelengths between 3 and 6 Å. The wavelength dependence of the DFI is presented in Fig. 6.26 (b). As in (a), the DFI has been normalized to 0 mT and averaged over the circular region shown in Fig. 6.24. Additionally, DFI curves calculated from the USANS data are shown. They were evaluated similarly to the example shown in Fig. 6.27 (d).

For increasing wavelength, a continuously decreasing signal is obtained in all studied applied fields between 7 and 35 mT. Comparing the wavelength dependence of the measured DFI, a good agreement with the calculated curves is found. Only for 26 mT, the calculated DFI values strongly differ from the measured ones (25 mT). On the one hand, this results from the beginning disappearance of the correlation peak and the accompanying increase in the error of the DFI calculation. On the other hand, the small field difference of the USANS and nGI data might have a higher impact, since the DFI contrast variation with the field is highest near the DFI minimum.
The presented data demonstrate the good consistency of USANS results and nGI. Apart from the colloid data shown in Sec. 5.1.5, these data provide a second verification of the quantitative dark-field imaging approach and the underlying theory of the DFI contrast.
Moreover, the complementary USANS results enable the correct interpretation of the above nGI data. The correlation length ξ_{GI} probed by the nGI setup varies from 1.3 to 2.6 µm for $3\,\text{Å} \leq \lambda \leq 6\,\text{Å}$ (Eq. 4.17). At these correlation lengths, the autocorrelation function G is nearly zero (compare marked interval in Fig. 6.27 (c)). Although the correlation function becomes broader for higher fields, G is only marginally changed near ξ_{GI}. Consequentially, any field and position dependence of the contrast variation seen in Fig. 6.25 is particularly attributed to the variation of Σ and not to the changes of G. The peculiar DFI contrast variation within the sample (Fig. 6.25) thus rather maps differences in the local domain number than in the domain size, since particularly Σ is probed. In order to probe the local domain size, a reconfiguration of the nGI would be required to access a slightly smaller correlation length.

Spatial variations of the domain structure

The previous considerations have revealed that the DFI results of Fig. 6.25 do not allow a conclusion on the spatial variation of the domain size. Instead, an interpretation of the DFI contrast variation as manifestation of an inhomogeneously distributed domain structure seems more likely. The peculiar ring-shaped contrast variation arising between 17 and 25 mT cannot be explained based on the simple principles introduced in Chap. 2. However, the occurrence of this contrast modulation for intermediate fields underlines the complex interplay of demagnetization fields, pinning interactions and vortex-vortex interactions governing the IMS nucleation during field cooling.

6.3.5. Conclusion

In summary, the systematic approach to study the IMS nucleation in the bulk of type-II superconducting niobium presented in Sec. 6.2 has been expanded to study the effects of pinning. Furthermore, the morphology of the IMS has been

systematically studied by means of USANS and SANS. The nucleation of the IMS is hampered by pinning and is only possible via field cooling. In this case, the IMS formation takes place in different stages: (i) a partial expulsion of the magnetic field accompanied by the nucleation of the vortex lattice, (ii) freezing of the vortex lattice and trapping of the magnetic flux within the sample, and (iii) rearrangement of the vortex lattice into the IMS domain structures. Based on the presented data, the nucleated IMS is given as an irregular but isotropic mixture of Shubnikov and Meissner domains, which is characterized by a single, field dependent correlation length.
The presented data reveal that both the IMS structure as well as the IMS distribution within the sample are strongly influenced by the magnetic field. The correlation length of the IMS increases with the field, following the predictions of both the Landau and the Goren-Tinkham model. Although pinning influences the morphology of the IMS, its correlation length is still governed by the competition of surface tension and the magnetic field energy. Intriguingly, for low and high fields, the IMS seems to be rather uniformly distributed within the sample, while in intermediate fields, a strongly inhomogeneous distribution is suggested by nGI. This unconventional volume filling of the IMS is not expected form existing theoretic models [188].
The nature of the transition from the Shubnikov to the IMS is yet unclear and should be further addressed in a subsequent study. Normally, pinning acts collectively on the vortex lattice and freezes its configuration in the sample. However, since the elasticity of the vortex lattice is strongly changed by the occurrence of the attractive part in the vortex-vortex interaction [191], this should also strongly influence the collective pinning of the vortex lattice. How this process promotes or even only enables the IMS formation is still unclear. The experimental approach necessary for such further investigations has been introduced in this section.

6.4. Imaging the critical state: field penetration into a niobium superconductor

The magnetic properties of superconductors are strongly influenced by the strength of vortex pinning within the material, which has already been discussed and demonstrated in Sec. 2.2.3 and 6.3. An understanding of the various pinning mechanisms and their impacts on the superconducting properties is hence of high scientific relevance, e.g. to differentiate intrinsic properties of a material from impurity induced. However, vortex pinning is also one of the most important effects governing the technical applicability of superconducting materials, since a non-dissipative electrical transport is only possible as long as pinning prevents a motion of the flux line lattice [37]. Vortex pinning and the associated phenomena do thus belong to the most studied fields in superconductivity: (i) microscopic vortex imaging

techniques are utilized to observe and even quantify the interaction of a single vortex with different pinning potentials [195], (ii) transport measurements are employed to identify and investigate different regimes of the voltage-current characteristics (flux creep, flux jump and flux flow) [54], (iii) magnetization and magnetic susceptibility measurements are employed to determine the penetration field and the critical current density [196], and (iv) magneto-optical methods are used to directly observe the field penetration into a superconductor [197]. With this large number of experimental methods, the simple predictions of the critical state model introduced in Sec. 2.2.3 have been extensively reviewed and extended. However, it has also been realized that flux penetration is a full three-dimensional problem [198], and the sample shape as well as the attributed demagnetization coefficient, which are not considered in the original Bean model [56], play a significant role for its understanding [60, 69].

By use of imaging approaches, the field penetration process is now believed to be caused by a complex interplay of the sample geometry and pinning [69]. However, while advanced numerical simulations allow to study the field distribution in the whole bulk of an arbitrarily shaped sample (see e.g. [68, 69, 181]), all listed techniques fail to verify them, except in thin specimen. The reason is that in thick samples, the applied field not only penetrates the specimen from the edges parallel to the field, but also from the perpendicular edges (see Fig. 2.8). Hence, the measured surface induction does not necessarily reflect the penetration front in the center of the sample [69].

Neutron methods could provide novel insight into the field penetration and distribution within a superconductor, but studies addressing these questions are rare. Most approaches to obtain bulk information on the magnetic field distribution are based on polarized neutron radiography [3, 199, 200]. However, due to the stray field of the sample, which rotates the neutron polarization vector, the acquired data require a complex evaluation and are difficult to interpret.

In the following section, it will be demonstrated that at least for type-II/1 superconductors, nGI can be used for the direct observation of field penetration into a bulk superconductor. The presented approach is based on the conclusion drawn in Sec. 6.2 and 6.3 that nGI is capable to directly measure the IMS domain distribution. Since the IMS can be frozen by field cooling, if pinning cannot be neglected, the idea arose to use the IMS domain structure as contrast agent to visualize the critical state (Sec. 2.2.3).

The principle of this experiment is illustrated in Fig. 6.28 (a). The sample is cooled down in an applied field sufficient to nucleate and freeze an IMS structure at point (1). Afterwards, the field is successively increased (2,3,4). Further magnetic flux can only enter the sample from the edges, which locally fills up the voids in the IMS structure (compare Fig. 6.28 (b)). Since the magnetic USANS scattering contrast is lost in these filled regions, they will vanish in the DFI.

Within the Bean critical state theory, the phase front separating the frozen IMS from the penetrated flux, corresponds to the flux front which would be expected

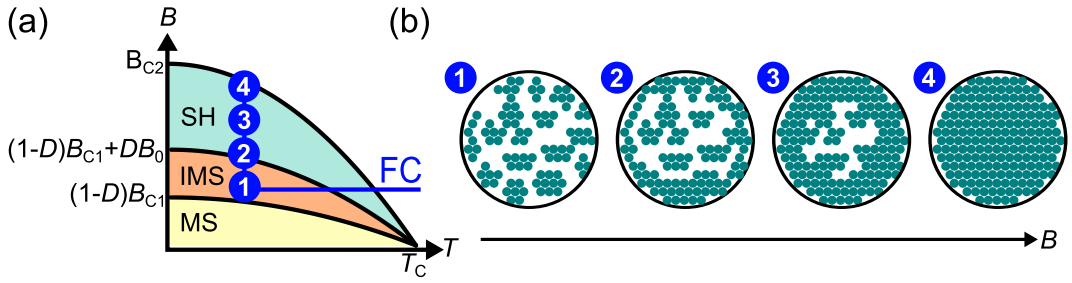

Figure 6.28.: Experiment scheme to observe the field penetration into a type-II/1 superconductor. (a) Schematic phase diagram of type-II/1 material. Shown is the cooling path into the phase diagram that freezes the IMS structure and allows an observation of field penetration. (b) Illustration how the IMS structure acts as contrast agent. If the field is increased after FC to the IMS, flux can only penetrate the sample from the edges by filling the domain structure. As this is accompanied by a loss of DFI contrast, the field penetration can be studied by nGI. Notice that in a realistic scenario, the vortex lattice of the penetrating flux does not equal the one within the IMS.

for initial field penetration into the Meissner state of the superconducting sample. This is due to the fact that in the Bean model [56], the final vortex configuration is generated by gradients in the magnetic induction only (Sec. 2.2.3). The macroscopically homogeneous flux distribution within the field cooled IMS will thus not strongly influence the field penetration, besides adding a constant offset to all relevant field scales.

6.4.1. Experimental setup

The investigation of field penetration into a niobium superconductor is based on USANS experiments performed at the BT-5 instrument and nGI performed at the ANTARES beamline. The experimental setups are described in Sec. 5.3 and 5.1.2. The same samples as introduced in Sec. 6.3.1 have been studied. The nGI experiments were performed either at a wavelength of 4.0 Å (Nb 2, 10 steps, total exposure time: 3000 s) or in the white beam (Nb 3 and Nb wedge, 20 steps, total exposure time: 1200 s). The crystals were aligned following the procedure described in Ap. A.6. In order to guarantee a high DFI quality, the open beams were taken above T_C, individually for every field. Hence, the nGI experiments were conducted via the following protocol: (i) Set temperature to $T = 10\,\mathrm{K} > T_\mathrm{C}$, (ii) set required field, (iii) perform open beam nGI measurement, (iv) set field to 24 mT, (v) field cooling of the sample to the IMS, (vi) set required field, and (vii) execute nGI data measurement.

6.4.2. Experimental results

Ultra-small-angle neutron scattering

The suggested experiment assumes that the field cooled IMS structure in the center of the sample is not modified by a subsequent field enhancement. This assumption is verified in the following. For this purpose, a USANS investigation has been performed on the sample Nb 2, in which the IMS scattering pattern has been recorded once after initial field cooling to 4 K in a field of 26 mT, and once after a subsequent field increase to 60 mT. In the latter case, the sample is not expected to be in the IMS anymore, as seen from from SANS results in Fig. 6.20 (b). Corresponding USANS rocking curves are presented in Fig. 6.29 (a), in which the scattered intensity I is plotted against the momentum transfer q. Clearly, doubling the applied field has no impact on the scattering curve (and hence on the IMS morphology) after the domain structure has been field cooled.

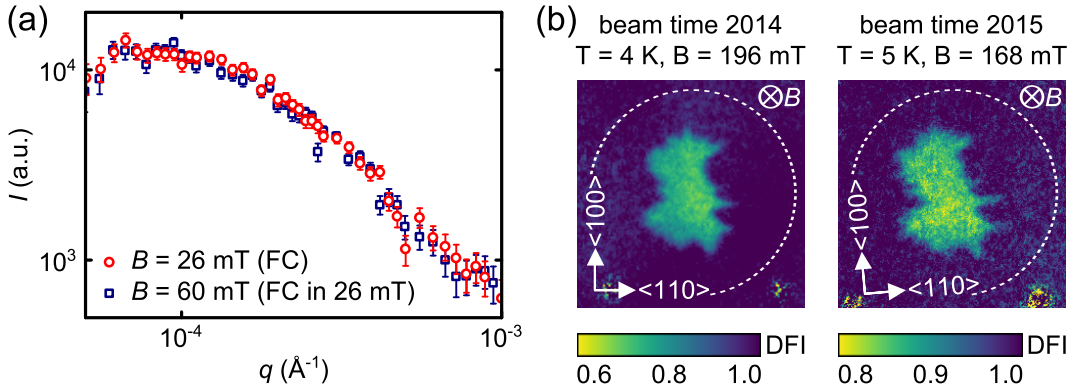

Figure 6.29.: Preconsideration of the nGI experiments. (a) USANS rocking curves of the Nb 2 at 4 K once measured after cooling in a field of 25 mT, and once after successive field enhancement to 60 mT. Clearly, the curves are identical within the error bars. (b) Comparison of nGI measurements on Nb 2 performed during different beam times. The DFI images are quite similar, which reveals that the field penetration pattern is not random but defined by the sample and linked to the crystal lattice, since a slight rotation of the crystal turned the DFI pattern as well. Different applied fields are required for the same pattern due to the weaker pinning strength at higher temperatures. White circles mark the sample position.

Neutron grating interferometry

In Fig. 6.30, DFIs of the sample Nb 2 are presented for fields between 73 and 225 mT taken at 5 K following the cooling procedure discussed in Sec. 6.4.1. In fields between 24 and 73 mT no change in the DFI pattern has been detected. As verified in Sec. 6.1, a contrast in the DFI marks the presence of IMS domains. If the DFI has locally increased to one, the IMS structure has consequentially

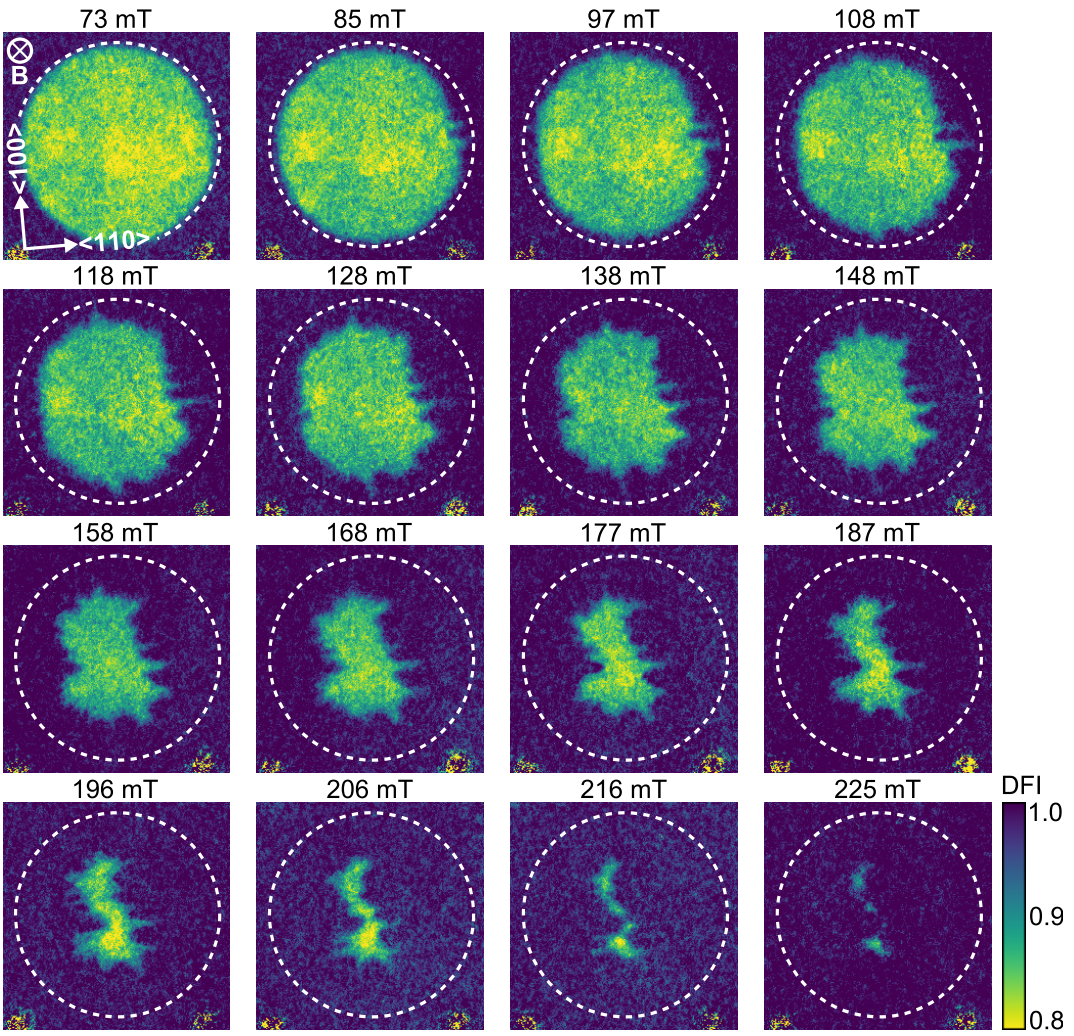

Figure 6.30.: DFI mapping of the field penetration into Nb 2. The sample was initially cooled to 5 K in a field of 25 mT. Afterwards, the field was ramped to the specified values. Regions of low DFI contrast correspond to positions which have not been penetrated by the applied field so far. The white circle marks the sample position.

been filled with penetrating flux. In increasing fields, the region of contrast in the DFI continuously shrinks until at 225 mT only three isolated small areas of DFI $\neq 1$ remain. The flux does not penetrate circular as expected from the disc shape of the sample, but plenty of spikes are formed during field entrance which are directed outward (seen e.g. at 108 mT). Furthermore, a clear anisotropy in the flux front develops and flux penetration along the $\langle 100 \rangle$ direction is distinctly delayed compared to the $\langle 110 \rangle$ direction.

The observed 'inkblot'-pattern is not random, but linked to the crystal lattice of the sample as demonstrated in Fig. 6.29 (b). Shown are the DFI for 168 mT taken from Fig. 6.30 and a DFI obtained in a previous beam time, measured using

the same experimental procedure, but at a slightly lower temperature[1]. Although the applied field necessary for a similar penetration distance is higher at lower temperature, the observed flux front patterns are quite similar in both cases. The samples were aligned slightly differently, but the flux front pattern clearly follows this misalignment. Therefore, it can be concluded that the spikes preferentially formed along the $\langle 100 \rangle$ and $\langle 110 \rangle$ directions.

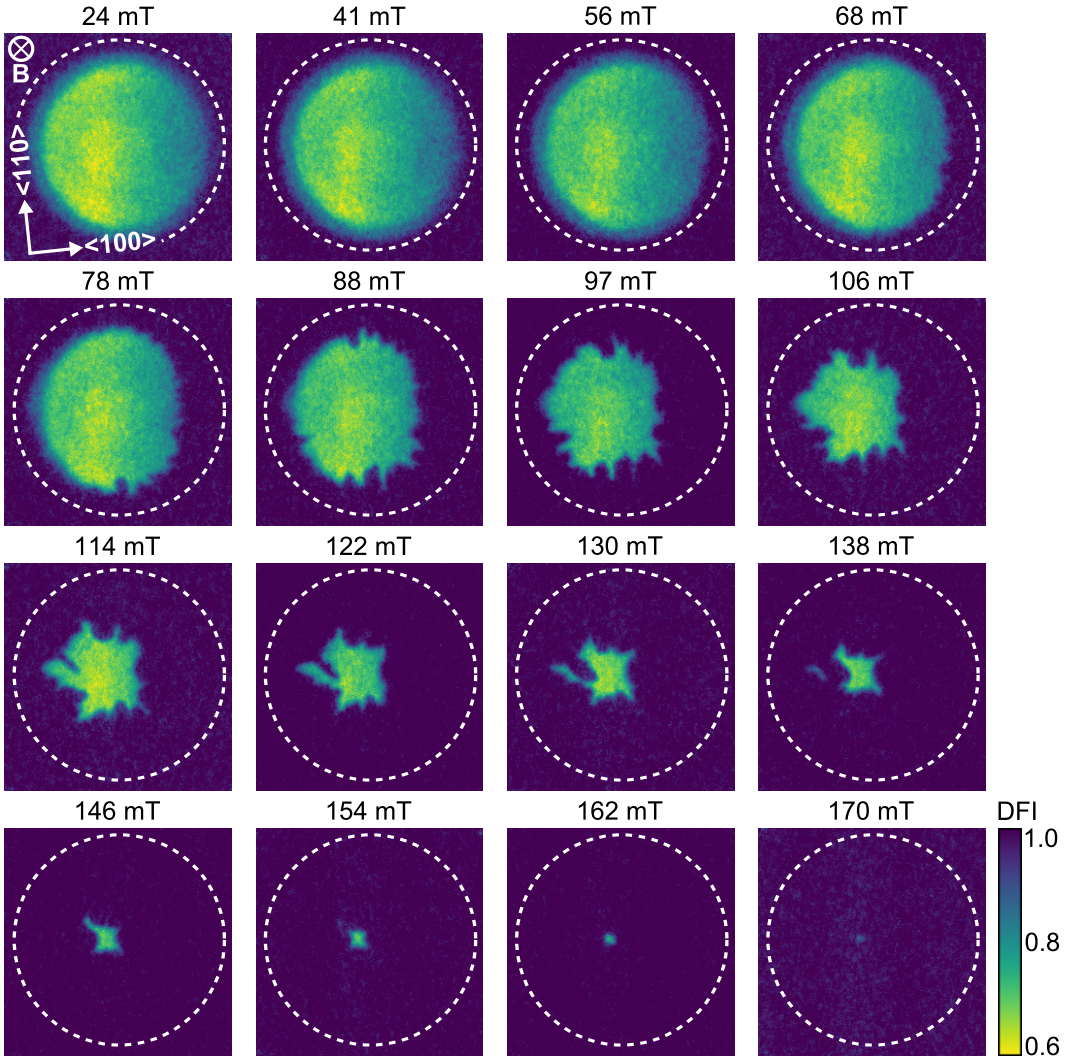

Figure 6.31.: DFI mapping of the field penetration into the Nb wedge. The thickness of the wedge decreases from left to right. The sample was initially cooled to $5\,\mathrm{K}$ in a field of $25\,\mathrm{mT}$. Afterwards, the field was ramped to the specified values. Regions of low DFI contrast correspond to positions which have not been penetrated by the applied field so far. The white circle marks the sample position.

1 Notice that the data from 2014 are also 2×2-binned.

Corresponding nGI data for the Nb wedge are shown in Fig. 6.31. The DFI were obtained at 5 K in fields between 24 and 170 mT. The flux-depleted region at the edge of the sample, discussed in Sec. 6.3, is clearly seen at low fields. In increasing fields, the flux front becomes irregular as well, but preferably penetrates the sample from the thinner side of the wedge. Again, emerging spikes in the flux front are primarily aligned along ⟨100⟩ and ⟨110⟩. The field of full penetration is reached around 170 mT, which is considerably lower than in the Nb 2 sample.

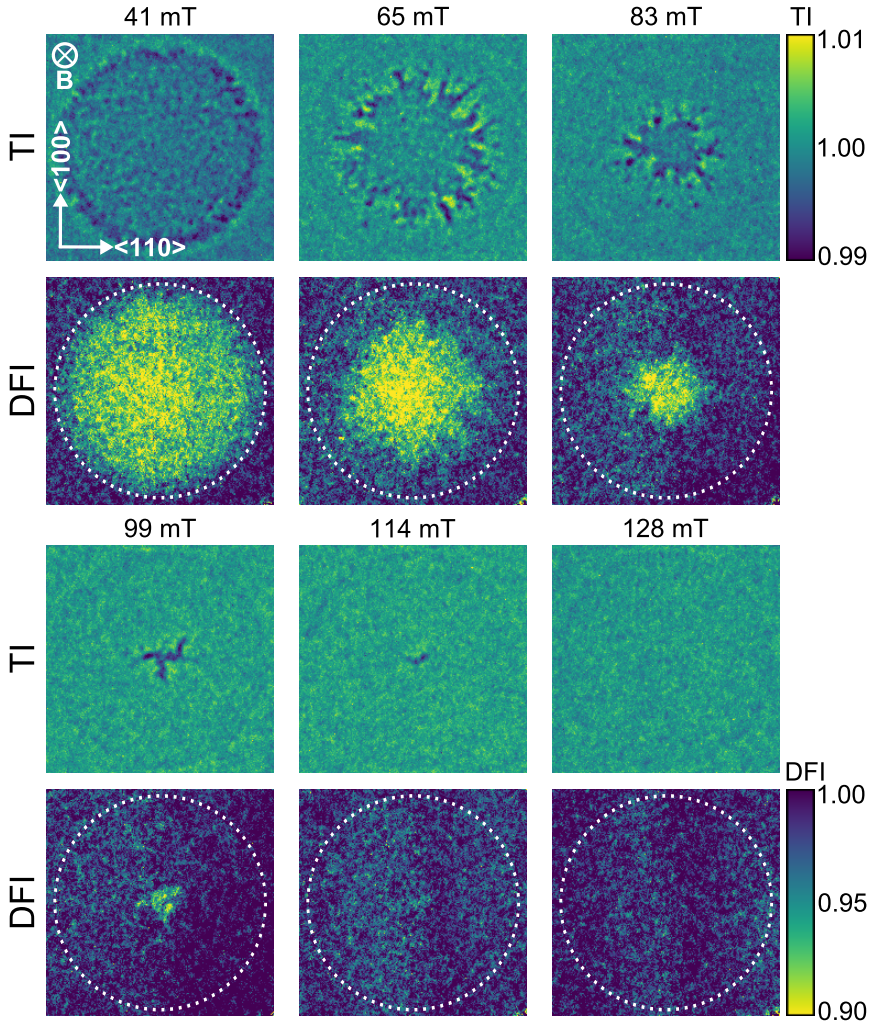

Figure 6.32.: Field penetration into Nb 3. The sample was initially cooled to 5 K in a field of 25 mT. Afterwards, the field was ramped to the specified values. Shown are DFI data which mark the non-penetrated IMS phase and TI data marking the IMS-Shubnikov boundary. The white circle marks the sample position.

The Nb 3 sample is addressed hereafter. Corresponding nGI results are shown in Fig. 6.32. This time, the dataset is grouped into the TI and DFI taken at 5 K in fields between 41 and 128 mT. As Nb 3 is the thinnest sample, the DFI contrast

degradation is considerably reduced compared to Fig. 6.31 and 6.30, and the TI can be consulted to obtain additional information on the flux front position.
The region of DFI contrast smaller than one shrinks isotropically for increasing fields and vanishes above 114 mT. As expected from the higher demagnetization coefficient, the thinnest sample has the lowest field of full penetration. However, details at the flux front are strongly blurred caused by the weak scattering.
As discussed in Sec. 6.2, the TI is influenced by small-angle scattering at the vortex lattice itself and marks regions on the detector, where neutrons are scattered to or scattered away from their original trajectory. As seen in Fig. 6.32, a TI contrast that is different to one only appears at the edges of the IMS region within the sample, which therefore allows a clearer determination of the penetrated flux front. The observed flux penetration is isotropic, but the flux front is strongly irregular. In small fields below 99 mT, the observed spikes cannot unambiguously be linked to a crystallographic axis, in contrast to the thicker samples. Only near the field of full penetration, at 99 mT, the IMS boundary seems to coincide with $\langle 100 \rangle$ and $\langle 110 \rangle$ directions.

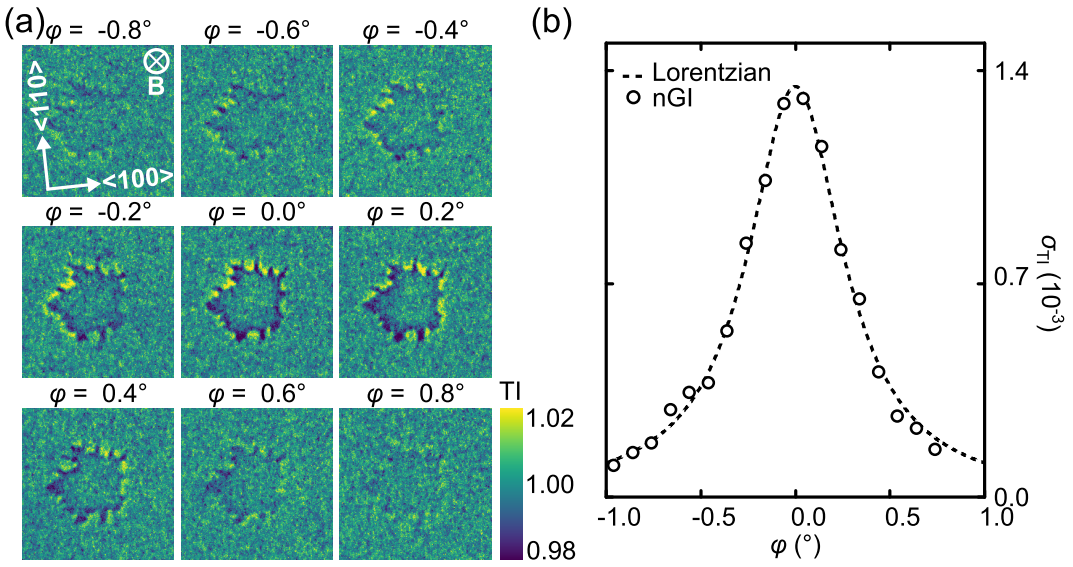

Figure 6.33.: An nGI rocking scan. (a) TIs of the Nb wedge at $B = 106\,\mathrm{mT}$ after the sample has been cooled down to $T = 5\,\mathrm{K}$, following the procedure described in Sec. 6.4.1. The TI, hence, corresponds to the DFI for 106 mT shown in Fig. 6.31. The magnetic setup was rotated together with the sample around the vertical axis and TIs were recorded for various rocking angles φ. (b) Standard deviation σ_{TI} of the TIs shown in (a) as function of the rocking angle.

The arising TI contrast needs to be considered in more detail, since it is still undefined why it marks the penetrating flux front. Further information can be obtained by a rocking scan of the vortex lattice. Hence, in analogy to SANS, the cryomagnetic sample environment was rotated with the sample, and TIs were

acquired at different vertical rotation angles φ. Results of an nGI rocking scan are shown in Fig. 6.33 (a) on the example of the niobium wedge at 106 mT. The field has been applied after field cooling to 5 K, following the procedure described in Sec. 6.4.1. The observed state of the sample thus corresponds to the one shown in Fig. 6.31 at 106 mT. Since the TI is sensitive to SANS scattering off the vortex lattice, a distinct dependence on the rocking angle arises. A maximum contrast variation occurs for $\varphi = 0°$, while the TI contrast slowly vanishes to higher (positive as well as negative) rocking angles. In the TI, the penetration front is characterized by a line of lower intensity at the inside surrounded by a halo of high intensity. As the sample is rotated from $\varphi = -0.2°$ to $0.2°$, the halo becomes less intense on the left side and more intense on the right side. Outside of the flux front, no TI contrast variation exceeding the noise level is detected.

The presented TI can be interpreted as a second strong indication that the vortex lattice inside the penetrating flux front is frozen. The ordered vortex lattice within the IMS generates strong coherent scattering. The corresponding scattering image seen on the detector is a mapping of the IMS region. However, this image is slightly deflected by a horizontal distance of 0.5 mm which corresponds to the scattering vector of $2.8 \times 10^{-3}\,\text{Å}^{-1}$ found within the IMS (see Fig. 6.20). The resulting TI contrast is the superposition of this scattering image (TI>1) with the attenuation image (TI<1) of the sample showing the local intensity degradation due to absorption and scattering. As the TI has been normalized to zero field, and the vortex lattice is homogeneously distributed on a macroscopic scale within the IMS region, the attenuation and scattering contrast completely cancel each other besides on the edges of the IMS. Depending on the preferential scattering direction, determined by the rocking angle of the vortex lattice, one side of the sample thus shows the halo, while the other one reveals the line of lower TI contrast. Only if the sample is rotated to $\phi = 0°$, scattering into both directions arises equally, as the beam divergence of approximately $0.2°$ is comparable to the Bragg angle of the vortex lattice.

No TI contrast is found at the edge of the sample. This suggests that the penetrating vortex lattice is not sufficiently ordered to produce a high amount of coherent scattering, most probably due to the expected gradient in the vortex lattice parameter (Sec. 2.2.3).

In order to quantify the TI information in terms of scattered intensity, its mean value is inappropriate as the averaged scattering and attenuation signals cancel each other. However, the scattered intensity can be quantified by the standard deviation σ_{TI} of the TIs measured over the full image size. This is demonstrated in Fig. 6.33 (b), in which σ_{TI} is plotted as a function of the rocking angle φ. As shown by the dashed line, the standard deviation can be approximated by a Lorentzian function. Its peak marks the position where the field is completely parallel to the neutron beam. In principle, such an evaluation of the rocking scan should provide similar information as a SANS rocking scan. This is suggested

by the Lorentzian shape of the curve, which has been found in SANS data on the same sample as well. The full width at half maximum of 0.6° is comparable to twice the Bragg angle. However, in contrast to SANS, σ_{TI} (i) includes the scattering information of all horizontal Bragg peaks, (ii) is convolved by a broader resolution function, defined by the beam divergence, and (iii) is influenced by a strong background signal, defined by the signal-to-noise ratio of the TI. This problem will be readdressed in Sec. 6.5, where a complementary approach to obtain rocking data by neutron imaging is demonstrated.

6.4.3. Flux penetration into a bulk niobium sample

The discussed results prove the validity of the presented method for the observation of flux penetration into type-II/1 superconductors: (i) USANS has shown that the field cooled IMS morphology is not influenced by a subsequent field variation (Fig. 6.29 (a)) and (ii) during the field enhancement, a clear boundary between a well ordered vortex lattice inside the IMS and a distorted one develops, as seen in the TI (Fig. 6.33). Consequentially, the penetration of flux can be evaluated quantitatively based on the presented data.

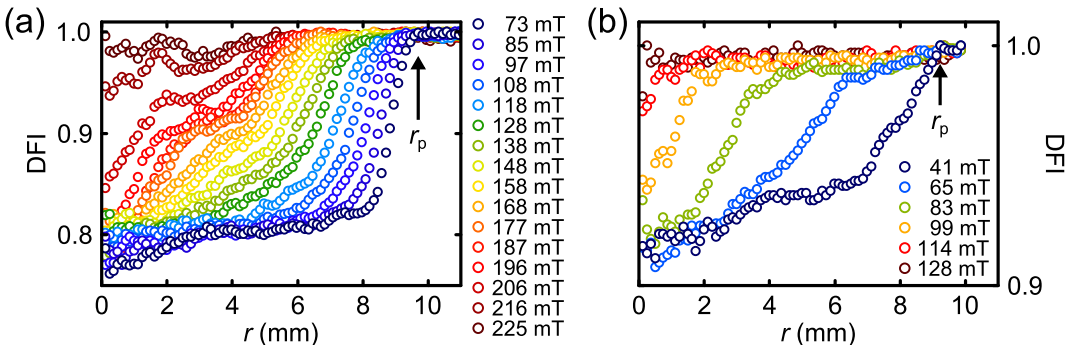

Figure 6.34.: Radial profiles to determine the flux front radius. Shown is the radially averaged DFI signal as function of the radius for sample Nb 2 (a) and Nb 3 (b). The data were calculated from the DFI in Fig. 6.32 and 6.30. r_{p} is determined as the radius, where the DFI signal firstly deviates from the constant background. For the lowest fields, it is exemplarily marked with arrows.

The flux penetration is usually quantified in terms of the radius of penetration r_{p} of the flux front [201]. Its extraction from the data presented in Fig. 6.32 and 6.30 is possible via a radial averaging of the DFI signal. In Fig. 6.34, radial profiles for both Nb 2 (a) and Nb 3 (b) are presented. Shown are the radially averaged DFIs as a function of the radial position r on the sample. In both cases, the DFI is strongly degraded inside the penetrated flux front, while the DFI equals one outside. Obviously, in increasing field, a continuous decrease of the penetrated flux front radius is detected. However, the DFI value inside this front, remains

mainly unaffected. For Nb 2, a peak develops in high fields above 206 mT, which marks the emerging islands of residual IMS phase, seen in Fig. 6.30.
An average flux front radius might be determined from the middle position of the sharp drop in the DFI(r) curves. However, especially for low fields, a high error is to be expected due to the fringed penetration front. Hence, for the sake of simplicity, r_p is defined as the radius of first deviation from the background DFI, as exemplarily marked in Fig. 6.34.
In Fig. 6.35, r_p is drawn against the applied magnetic field for both samples. As the flux penetration is highly anisotropic for the thicker Nb 2 sample, the flux front position has been determined separately along the ⟨100⟩ and ⟨110⟩ direction. For the latter one, r_p (⟨110⟩), has been calculated from a radial averaging over a 40° sector along ⟨110⟩, only. However, its value is also found in Fig. 6.34 (a), as the position of the kink which develops in the data above 118 mT. Along ⟨100⟩, r_p corresponds to the value deduced from Fig. 6.34 (a).

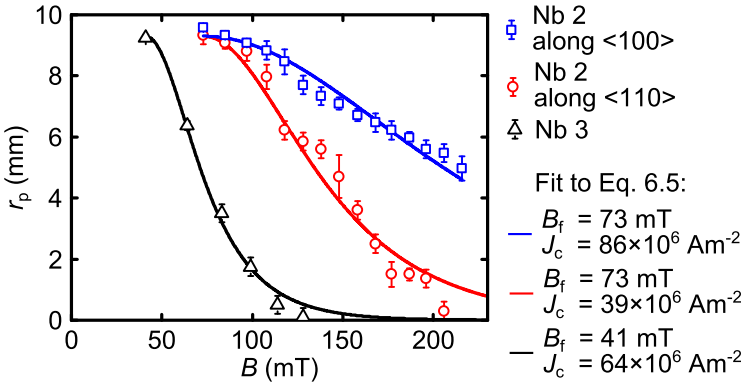

Figure 6.35.: Quantitative evaluation of the flux front radius. Shown is r_p as a function of the magnetic field. The data were extracted from the profiles presented in Fig. 6.34. Error bars are visual estimations on how well r_p is defined in the radial profiles.

The flux penetration into a cylindrical sample has been studied e.g. in Ref. [202–204]. It has been derived that in a cylindrical sample (radius r, thickness t, critical current density J_c), the field of full penetration B_p is generally given by [203]:

$$B_\mathrm{p} = \frac{\mu_0 J_\mathrm{c} t}{2} \ln\left(\frac{2r}{t} + \sqrt{1 + \frac{4r^2}{t^2}}\right) \tag{6.12}$$

A complete flux penetration is thus expected at $2.9\mu_0 J_\mathrm{c}$ (for Nb 2) and $1.2\mu_0 J_\mathrm{c}$ (for Nb3). Therefore, under the assumption of an equal J_c, the penetration field of the thicker Nb 2 should approximately be twice as high as in the thin Nb 3. This prediction is in rough agreement to the presented data. In contrast, regarding the partially penetrated state, analytic expressions for the magnetic field profile within the sample only exist in limited cases which can be simplified to only one

dimension. E.g. for thin discs ($r \gg t$), the flux front radius is given as [204]:

$$r_{\mathrm{p}}(B) = \frac{r}{\cosh\left[\frac{2\zeta(B)}{\mu_0 J_c t}\right]} \tag{6.13}$$

in which $\zeta(B) = B$. An applicability of Eq. 6.13 on discs with $\frac{t}{2r} \ll 0.25$ has been numerically verified in Ref. [202]. Sample Nb 3 ($\frac{t}{2r} \approx 0.03$) clearly fulfills this condition, while slight deviations might be expected for Nb 2 ($\frac{t}{2r} \approx 0.1$). However, for a usage of Eq. 6.13 in the presented case, several modifications are required, since (i) the formula has been derived under the assumption $H_{\mathrm{C1}} = 0$, and (ii) the magnetic flux, frozen in the IMS phase, has to be accounted for. An appropriate correction to Eq. 6.13 can be implemented by empirically introducing $\zeta(B) = B - B_{\mathrm{f}}$. Here, B_f is the field, at which the flux penetration sets in.
In Fig. 6.35, the flux front position r_{p} has been fitted to the modified model 6.13. The fit parameters are included in the legend of the figure. B_{f} was fixed to the value where a first penetration of flux had been observed. Although, the flux front is not unambiguously defined due to the multitude of spikes that arose near the boundary, the general trend of the data is well described by Eq. 6.13. Small deviations exist in high fields. However, the possible requirement to introduce a cut-off at high fields to describe the field penetration in thicker samples has already been recognized by Brandt [202]. The estimated values of J_c between 30×10^6 and $90 \times 10^6\,\mathrm{Am}^{-2}$ have been reported for slightly impure Nb single crystals [205]. The physical content of B_{f} is still unclear, but a connection to the demagnetization coefficient D, the lower critical field B_{C1}, and the frozen magnetic induction B_0 seems obvious. However, no correlation of B_{f} to these data could be established so far. An in depth investigation would require samples that are better defined in terms of impurity content and homogeneity. However, this was beyond the scope of this thesis.
Finally, the deviations from a circular penetration front should be considered. The observed anisotropy of the flux front in Nb 2 might be caused by its slightly flattened edge along the $\langle 100 \rangle$ direction, which privileges a field penetration perpendicular to it. A similar ellipsoidal cross-section is found for Nb 3, but the small thickness of the sample might reduce its effect on the field penetration. Spikes in the flux front are routinely observed by means of magneto-optical imaging [198]. They might be caused by crystallographic dislocations or grain boundaries [47]. The orientation of the spikes along crystallographic directions might support the first assumption. However, also textured normal precipitations could link the flux penetration boundary to crystal directions. Another explanation might even be small indentations on the sample edge [203] which arose since the used Nb discs were primarily produced for the investigations of Sec. 6.3, where such effects were of minor importance for the data interpretation.

6.4.4. Conclusion

In the previously discussed experiment, it has been clearly demonstrated that nGI can be used to image the field penetration of superconducting vortices. In contrast to all other investigation techniques, solely nGI is capable of probing the bulk of the material. Furthermore, the method allows for a tomographic reconstruction of various different DFI projections and hence for a one-to-one comparison of numerically obtained data on the bulk flux distribution and experimental results. The presented approach might also trigger studies on the extension of the Bean model for a finite H_{C1}. This problem has been sparsely considered, since in thin samples, normally studied by magneto-optics, the Meissner phase is strongly suppressed due to demagnetization.
Moreover, although the focus of this first study lies in the demonstration of the imaging capability of this approach, also quantitative information in form of a rough estimation of the critical current density could be obtained. Finally, it has to be stressed that the chosen approach is not restricted to type-II/1 superconductors. Its general idea, to prepare a sample in a metastable state, which provides a scattering contrast, and to observe the subsequent spatial degradation of this phase due to changing external conditions, might be useful for other physical problems. Examples include the spatial degeneration of ferromagnetic domain structures, skyrmion lattices or multiferrorics.

6.5. Distribution and morphology of the skyrmion lattice in MnSi: A case study for further vortex matter investigations

The skyrmion lattice in MnSi, introduced in Sec. 2.4, has been intensively investigated during the last years [101]. Most of these studies focused either on the nucleation, stability [206], dynamics [207, 208] and elasticity [209] of the skyrmion lattice, or on its influence on electrical properties of the material [210, 211]. In contrast, the impact of geometric effects on the skyrmion distribution has not been addressed so far. Since the skyrmion lattice bears some strong resemblance to the vortex lattice found in type-II superconductors, a similar impact of the sample shape might also be expected. Hints of the influence of demagnetization effects have already been mentioned in the first experimental observation of skyrmions [98] by means of SANS. In this work, the SANS rocking width has been found to strongly depend on the sample shape. A similar correlation has been reported in Ref. [212], in which magnetization data have revealed that the A-phase is surrounded by a region of phase coexistence whose extent crucially depends on the sample geometry. Neither a quantification nor a further discussion on how demagnetization influences the skyrmion lattice and its nucleation could be given

in the aforementioned studies.
Diffractive neutron imaging can be used to shed some light on the impact of demagnetization effects on the distribution of the skyrmion lattice within the sample. The idea and motivation of the presented study resulted from experimental observations on type-II/1 superconductors, discussed in Sec. 6.2 to 6.4. In these examinations, it has been verified that coherent small-angle neutron scattering off the vortex lattice can cause a significant scattering contrast in the transmission image (compare e.g. Fig. 6.8 or 6.33). A similar contrast variation will occur for the skyrmion lattice, as its small-angle scattering signature solely differs by a ten times larger reciprocal lattice spacing. However, a distinct interpretation of the SANS signal within the TI was hampered so far by the fact that (i) the TI is the superposition of the attenuation image and the diffracted image, (ii) the diffracted image itself can be composed of scattering contributions arriving from various directions, and (iii) the TI only reveals contrast at positions where the angle enclosed by the neutron beam and the skyrmion (vortex) lattice fulfills the Bragg condition.
An easy experimental approach to overcome these limitations can be based on the usage of a borated micro-channel plate (MCP). An MCP is a neutron collimator consisting of several million micro-channels which are fused together (see Fig. 6.37 (a))[213]. In this way, the obtained collimator can provide a high collimation ratio L_C/D_C exceeding 200, whereas its thickness in beam direction amounts only a few millimeters. In contrast to the usually used Soller slit collimators, the MCP collimation is obtained in vertical as well as in horizontal direction, and the structure of the MCP is too fine to be directly resolved by neutron radiography. The obtained images are consequentially not interspersed with streaks as in the case of Soller slits, and a high resolution can be reached.
MCP have been discussed for a long time as neutron collimators or lenses [214]. Recently, they have been utilized in neutron radiography to increase the spatial resolution [215, 216] via a decrease of the beam divergence. They have been used additionally to *suppress* scattering contributions arising in the transmission image [161].
In the following section, the capabilities of MCPs in *selecting* particular scattering directions by absorbing the direct beam are demonstrated. Hence, the MCP is used for diffractive [217] instead of transmission imaging. In this way, a mapping of the skyrmion lattice distribution with high spatial resolution is possible. Moreover, it will be shown how the local directional distortion and in principle also the local lattice parameter of a skyrmion lattice can be deduced. The demonstrated approach thus provides information complimentary to the usually used small-angle neutron scattering.
The presented experiment can be seen as a proof-of-principle. For the sake of convenience, this capability test has been performed on the skyrmion lattice of MnSi, because its Bragg angle is comparably large and could be studied by the available MCP with $L/D = 250$. An adaption of the presented approach to the

vortex lattice in type-II superconductors is simple and straightforward. It only requires a better collimation ratio of the MCP. However, it has to be emphasized that the manufacturing of MCPs with L_C/D_C up to 2000 has been considered to be feasible [218] and a verification of their applicability to various different physical problems should trigger further developments.

6.5.1. Experimental setup and its alignment

A setup for diffractive imaging has been implemented at the ANTARES beamline (Sec. 5.1.1). It is illustrated in Fig. 6.36: The sample was positioned at a distance of $L_R = 8.3\,\mathrm{m}$ to the instruments' pinhole and of $L_S = 54\,\mathrm{cm}$ to the detector. A pinhole diameter of $D_R = 18\,\mathrm{mm}$ was chosen, leading to a L_R/D_R-ratio of 460. The sample was placed in the cryomagnetic setup described in Sec. 5.1.6. This setup could be vertically rotated by the angle φ which enabled rocking scans of the sample. By placing absorbing beam limiters in front of the entrance to the magnet, the neutron beam could be restricted to the sample area.

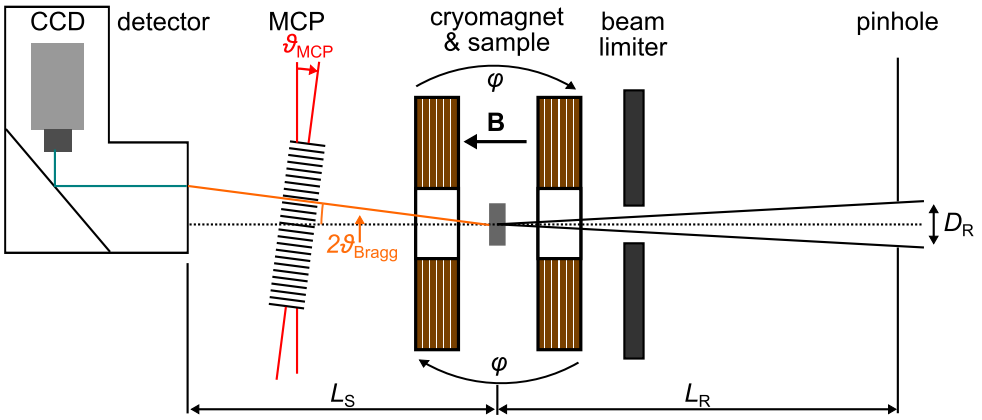

Figure 6.36.: Schematic of the setup used for diffractive imaging on the skyrmion lattice. The illustration is not to scale. The direct neutron beam is blocked by an MCP, while neutrons scattered at the skyrmion lattice can pass and reach the detector if $\vartheta_{MCP} = 2\vartheta_{Bragg}$. The intensity transmitted through the setup to the detector strongly depends on the rocking angle φ which regulates the fulfillment of the Bragg condition. The spatial resolution depends on the convolution of the geometrical resolution of the beamline (Sec. 4.1) and the mosaicity of the skyrmion lattice.

The MCP was placed in front of the detector. A schematic of this collimator which measures 5 cm in diameter and $L_C = 2\,\mathrm{mm}$ in thickness, is shown in Fig. 6.37 (a). The MCP consists of glass fibers enriched with a mixture of Gd_2O_3 and B_2O_3 that were hexagonally packed, leading to a center-to-center distance of 10 µm. Within the fibers, pores of 8 µm diameter had been etched forming the micro-channels. Due to the composition of the glass, the MCP reveals a high absorption for cold neutrons outside the pores. The same MCP has been used in Ref. [161], in which

its peak transmission has been deduced to 56 % [161] for a white beam spectrum. A picture of the experimental setup is shown in Fig. 6.37 (b): The MCP was placed in an aluminum holder and mounted on the sample manipulation stage of the ANTARES beamline that allowed for a vertical rotation around the angle ϑ_{MCP} as well as for a tilting of the MCP in beam direction by the angle χ_{MCP}.

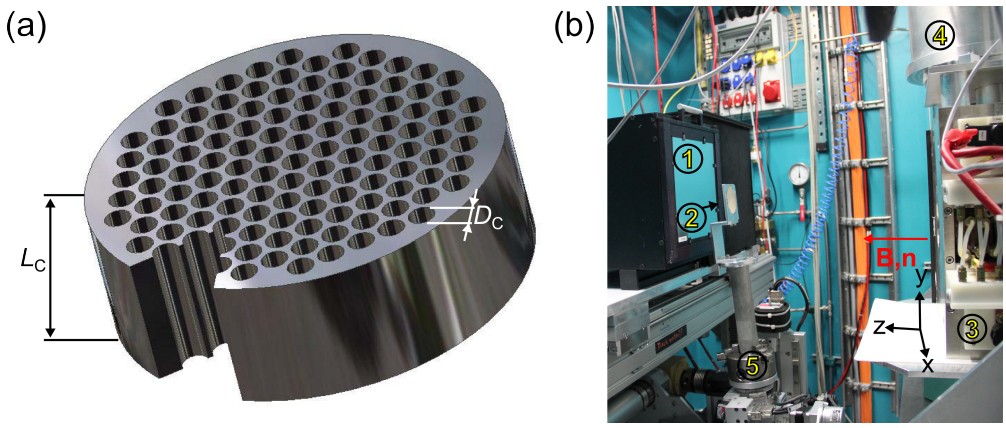

Figure 6.37.: The experimental setup for diffractive imaging at ANTARES. (a) Illustration of an MCP (not to scale), which consists of several micro-channels which were fused together. Reprinted from Ref. [213] (©2004 IEEE). (b) Photography of the experimental setup at ANTARES (compare Fig. 5.7): 1: Detector, 2: Micro-channel plate in aluminum holder, 3: Magnet, 4: Cryostat and 5: Sample manipulator.

An MnSi disc (thickness $t = 2.1\,\mathrm{mm}$, diameter $d = 9.3\,\mathrm{mm}$) had been chosen to demonstrate the performance of the MCP approach. A photography of the sample is shown in Fig. 6.39. The sample was cut from a single crystal which had been grown by the floating zone method. The flat faces of the sample have been polished to remove impurities introduced by the cutting. A crystallographic $\langle 100 \rangle$ direction corresponds to the normal of the disc.

Characterization of the multi-channel plate

Prior to any investigation on MnSi, the MCP was characterized. For this purpose, the sample and the sample environment were moved out of the beam, and the transmitted intensity of the MCP was measured as function of the vertical rotation angle ϑ_{MCP} and the tilt angle χ_{MCP} in 0.05° and 0.1° steps, respectively. Corresponding results are presented in Fig. 6.38. In (a) the transmitted intensity is plotted against ϑ_{MCP} and χ_{MCP}. The intensity has been averaged over the MCP and is specified in CCD gray levels per second. The data points are interpolated to obtain the presented intensity map. This measurement has been performed in the white beam.
The intensity map is strongly peaked and approx. of radial-symmetry around

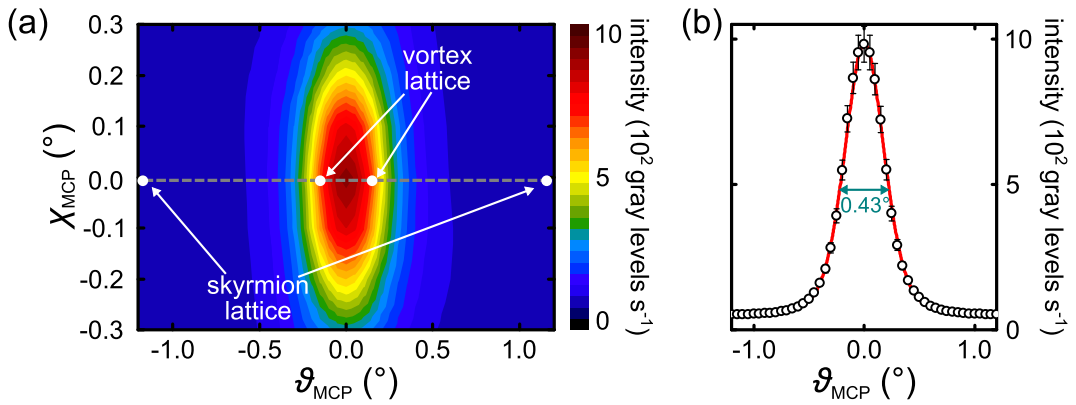

Figure 6.38.: Empty rocking curve of the MCP. (a) Neutron transmission of the used MCP as function of the vertical rocking angle ϑ_{MCP} and of the horizontal inclination angle χ_{MCP}. The Bragg angle of $0.2°$ ($\lambda = 4\,\text{Å}$) found for the vortex lattice in Nb (white inner spots) is too small to enable a separation of the scattered beam from the direct beam using the MCP. In contrast, the feasibility of the presented approach can be demonstrated on the skyrmion lattice in MnSi (white outer spots), as its Bragg angle of $1.2°$ ($\lambda = 4\,\text{Å}$) is much larger than the width of the rocking curve. (b) Profile along the gray line in (a). The full width of half maximum has been determined to amount $0.43°$ by fitting of the data to a Voigt profile.

the origin[1] (considering the different scaling of the axes). Outside the peak, the background intensity amounts to 5 % of the peak value. This constant background is mostly caused by epithermal neutrons, as the MCP absorption strongly decreases for increasing neutron energy [161]. A line profile for constant χ_{MCP} along the gray line in (a) is presented in Fig. 6.38 (b). The peak shape could be accurately fitted by a Voigt profile which yields a full width at half maximum (FWHM) of $0.43°$ in accordance to former measurements [161]. The distinct form of the intensity curve results as the convolution of the transmission function of the MCP [213] and the divergence of the neutron beam which is estimated to about $0.4°$ over the whole area of the collimator. The FWHM directly shows that in the case of a superconducting vortex lattice ($2\vartheta_{\mathrm{Bragg}} \approx 0.2°$ at $\lambda = 4\,\text{Å}$), it is impossible to separate the first order Bragg peaks from the direct beam with the used setup, since the Bragg angle lies within the angular range that passes the MCP. In contrast, the Bragg peak of the skyrmion lattice ($2\vartheta_{\mathrm{Bragg}} \approx 1.2°$ at $\lambda = 4\,\text{Å}$) can be well separated. For a visualization, the Bragg angles for both cases are additionally marked in Fig. 6.38 (a). The Bragg angles could be increased further by an increase of the neutron wavelength, however, this would strongly diminish the neutron flux.

1 Indeed, a closer inspection reveals a slightly hexagonal symmetry, which is however irrelevant for the present study.

Alignment of the skyrmion lattice

In order to align the setup, the MCP had to be rotated exactly to the Bragg angle of the skyrmion lattice: Firstly, the rocking angle φ revealing maximal scattering (i.e. $\varphi = \vartheta_{\mathrm{Bragg}}$) had to be determined, and secondly, the angle ϑ_{MCP} had to be scanned to maximize the transmission for scattered neutrons (i.e. $\vartheta_{\mathrm{MCP}} = 2\vartheta_{\mathrm{Bragg}}$).

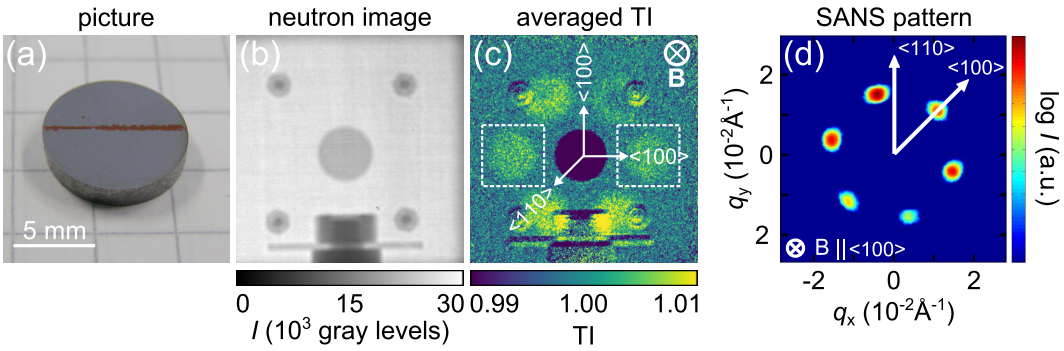

Figure 6.39.: Small-angle neutron scattering signatures in neutron radiography. (a) Picture of the used MnSi disc. (b) Neutron image of the sample in its sample holder taken at 28 K in a field of 200 mT. (c) Corresponding transmission image that is the average of 20 single TIs which were recorded for different rocking angles between $-2.5°$ and $1.3°$ and normalized to above T_{C}. The six diffracted images of the skyrmion lattice are seen around the sample position. (d) Corresponding integrated SANS pattern of the skyrmion lattice in MnSi for a similar orientation. As the detector is further away in a SANS instrument and of lower resolution, the diffraction images of (c) degenerate to diffraction spots. Hence, the real space information is lost for the gain of reciprocal space resolution. Picture taken from [219] with courtesy of T. Adams.

In the initial step, the MCP had been removed from the beam and neutron images of the sample were taken at a neutron wavelength of $\lambda = 4.0$ Å. In order to nucleate the skyrmion lattice, a magnetic field of 200 mT had been applied after zero field cooling to 28 K. In Fig. 6.39 (b), a corresponding neutron radiography of the sample is presented. The holder and the MnSi disc are clearly visible, however, no sign of a diffractive contribution is seen, since (i) the scattered intensity is very weak, and (ii) the sample has to be rotated around φ to obtain the complete scattering information.
In Fig. 6.39 (c), results of a φ-rocking scan are presented. The shown TI is the average of 20 single TIs taken at different equidistant angles φ between -2.5 and $1.3°$. Each TI has been corrected for the dark current and has been normalized to a neutron image taken above T_{C} and at the same φ. Hence, all non-magnetic contrast contributions have been eliminated. Some residual contrast at the screws and the border of the sample holder arose, which might be the result of thermal expansion, a slight movement of the sample in the magnetic field and a weak

afterglow of the scintillator. A distinct hexagonal scattering pattern occurs around the sample, which is separated by a distance of 12 mm from the center of the disc. The corresponding diffraction angle can be calculated to 1.3° which closely correlates to the Bragg angle of the skyrmion lattice in MnSi. The hexagon is aligned horizontally along an $\langle 100 \rangle$ direction of the crystal, in agreement with former SANS results. In Fig. 6.39 (d), a SANS pattern of the skyrmion lattice in MnSi is shown for comparison. The data have been taken from Ref. [219] and had been obtained on a similar sample in the same $B \| \langle 100 \rangle$-geometry of the crystal. Clearly, the orientation of the SANS Bragg peaks and the diffractive images match. The presented TI can hence be seen as a near field image of the SANS pattern which reveals a better real space, but a lack of reciprocal space resolution.
In Fig. 6.40 (a), the mean TI values within the areas marked in Fig. 6.39 (c) are plotted versus the rocking angle φ. Hence, the shown curve is the analogy of a SANS rocking scan of the horizontal first order Bragg peaks. The peaks of the rocking curves were fitted by a Gaussian peak function to obtain their angular distance of $1.51 \pm 0.05°$. The value roughly corresponds to the expectation value of $2\vartheta_{\mathrm{Bragg}}$, but its determination is defective since the small scattered intensity is overlaid by the direct beam.
Afterwards, the MCP has been aligned by turning φ to the maximum of the TI at the right peak position ($\varphi_{\mathrm{peak}} = 0.7°$) and subsequent scanning of ϑ_{MCP} from 0.5 to 2.0°. In Fig. 6.40 (b), the mean intensity reaching the detector during this scan is plotted as a function of ϑ_{MCP}. Towards low angles, the intensity increases, since the direct beam begins to pass the MCP. In contrast, the peak emerging at 1.3° corresponds to the desired configuration with $\vartheta_{\mathrm{MCP}} = 2\vartheta_{\mathrm{Bragg}}$.

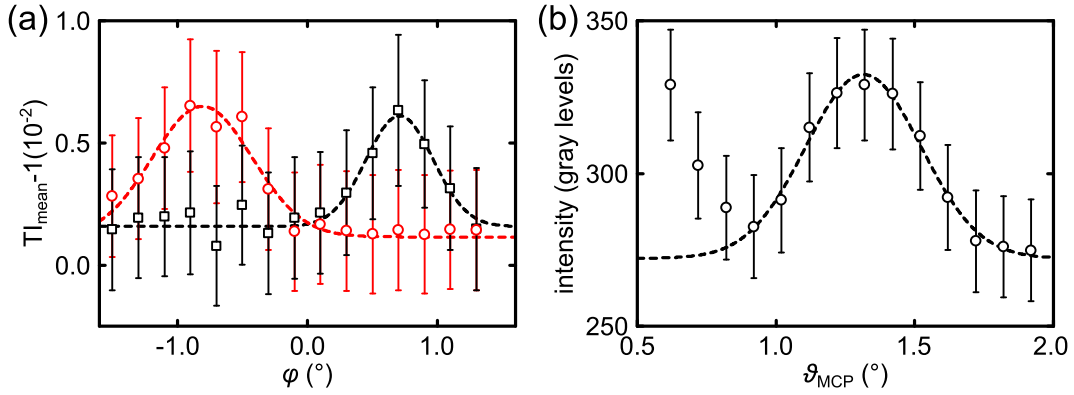

Figure 6.40.: Sample and MCP rocking curves at 28 K and 200 mT. (a) Mean TI value for the right (black) and left (red) areas of Fig. 6.39 (c) as function of the rocking angle φ. Error bars are estimated errors. (b) Intensity within the right area marked in Fig. 6.39 (c) as function of the MCP rocking angle ϑ_{MCP}. The sample has been rotated to $\varphi = 0.7°$ to scatter maximal intensity. Error bars correspond to the statistical error. In both cases, the dashed lines are Gaussian fits.

Recording diffractive images of the skyrmion lattice

The distribution of the skyrmion lattice within the MnSi disc has been studied in various magnetic fields between 150 and 260 mT, applied after the sample had been zero field cooled to 28 K. A neutron wavelength of $\lambda = 4$ Å has been selected. For each field, 41 single neutron images have been obtained at different rocking angles[1] $\Delta\varphi = \varphi - \varphi_{\mathrm{peak}}$ between -2 and 2°. The MCP was fixed at the angle revealing maximal transmission for the scattered beam, which has been deduced above. The exposure time per image was set to 300 s. Although the MCP filtered most of the direct beam, a number of epithermal neutrons could still pass the collimator. Therefore, a similar open beam scan has been conducted in fields above the A-phase. All subsequently shown data were filtered for gamma spots, corrected for the CCD dark current and normalized to this open beam measurement. Hence, although the consideration is restricted to the diffracted image of the sample, marked by the right box in Fig. 6.39 (c), the presented results are evaluated in a similar way as the transmission images and are consequentially also denoted TIs.

6.5.2. Diffractive imaging of the skyrmion lattice distribution

Proof-of-principle

Results of the diffractive imaging of the skyrmion lattice are exemplarily shown in Fig. 6.41 for $B = 200$ mT which lies deep in the A-phase of the material. In (a), single diffractive images of the MnSi disc are presented for different rocking angles $\Delta\varphi$ between -1.9 and 1.9°. For the sake of clarity, only a part of the 41 single TIs is shown. For low and high $\Delta\varphi$, these diffractive images are sickle shaped on the left and right edge of the sample. If the rocking angle nears zero, the two sickles become broader, converge, and increase in intensity until one single broad vertical streak remains close to $\Delta\varphi = 0°$. Clearly, the overall intensity of the diffractive images dramatically increases towards the origin of $\Delta\varphi$.
The peculiar shape of the TIs is attributed to a distortion of the skyrmion lattice: In the center of the disc, the lattice is aligned strictly parallel to the applied field. Hence, the Bragg condition is only fulfilled within a small angular range and once Bragg's law is satisfied, neutrons are scattered with high intensity. In contrast, the Bragg condition is partially fulfilled in a much broader angular range on the edge of the sample, which directly confirms that the skyrmion lattice is locally distorted.
The aforementioned distortion can be easily quantified from the dataset. In Fig. 6.41 (b), the TI values of the pixels marked in (a) are plotted as a function of $\Delta\varphi$. This time, all 41 images were evaluated. The presented data correspond to

1 For sake of clarity, the rocking angle is defined with respect to the angle of maximal scattered intensity φ_{peak}.

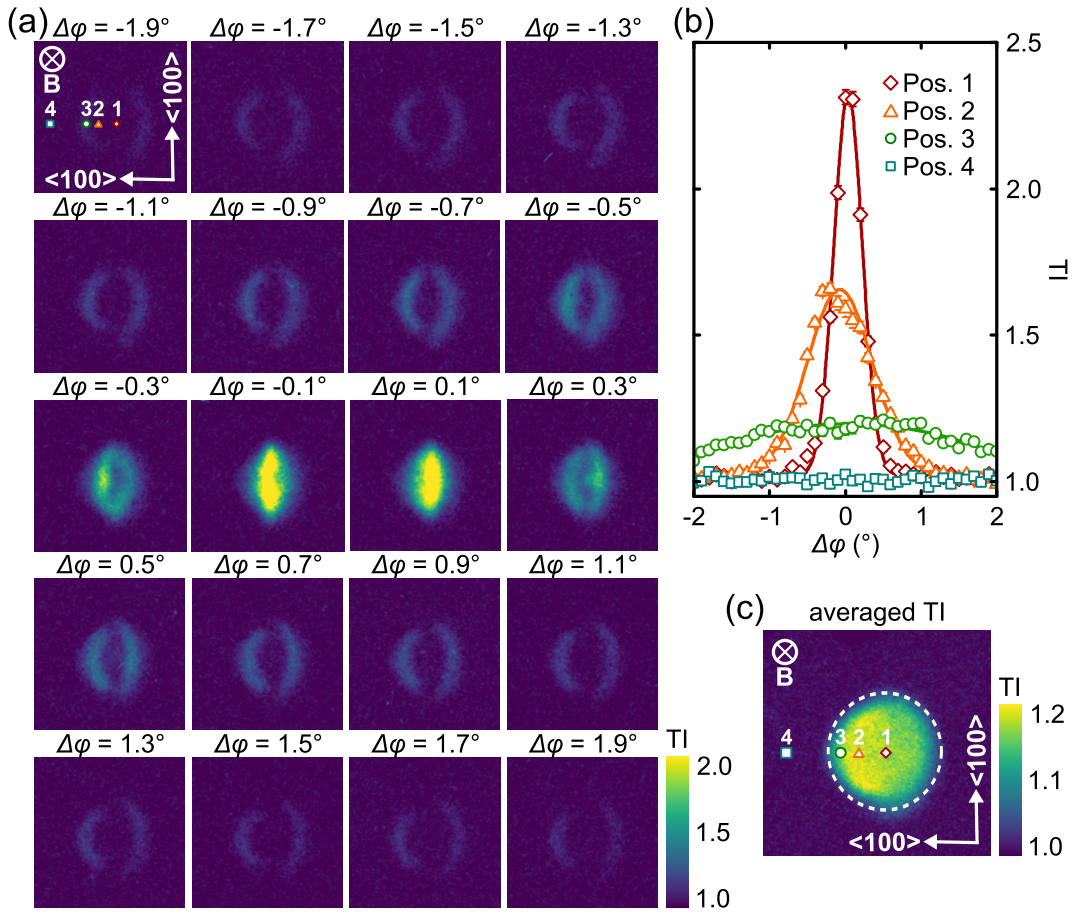

Figure 6.41.: Results of diffractive imaging on the MnSi sample at $28\,\mathrm{K}$ in a field of $200\,\mathrm{mT}$. (a) Single diffractive images of the skyrmion lattice for different rocking angles $\Delta\varphi$ between -1.9 and $1.9°$. (b) TI value as function of the rocking angle for the positions marked in (a). The lines correspond to Gaussian fits. Clearly, these rocking curves become broader from the center (1) to the edge (3) of the sample. Outside of the diffracted image (4), no contrast variation is observed and the TI equals one. Error bars correspond to the statistical error, but mostly lie within the symbols. (c) Average TI of the images shown in (a) which maps the distribution of the skyrmion lattice. The sample position is marked as white circle.

a SANS rocking scan, however, instead of the whole sample, only the scattering arising from one particular sample position is evaluated. In all cases, the rocking curves could be approximated by a Gaussian distribution.

In the center of the sample (1), the rocking curve is strongly peaked, revealing a maximal TI of 2.3 and a FWHM of $0.46 \pm 0.01°$. The width of the rocking curve gradually increases towards the edge of the disc from $1.1 \pm 0.1°$ at position (2) to $3.9 \pm 0.2°$ at position (3), while the maximum decreases accordingly. Furthermore, the peak position seems to be slightly shifted towards the edge. The rocking width

in the center approximately corresponds to the FWHM of the MCP rocking curve presented in Fig. 6.38 (b), and is hence limited by the instrumental resolution. In contrast, positions (2) and (3) clearly reveal a broadening above the instrumental curve. Outside of the diffractive image (4), no intensity modulation arises and the TI signal equals one.
In Fig. 6.41 (c), the average TI is presented, which corresponds to the mean of all 41 diffracted images of a rocking scan. It displays from which positions within the sample neutrons are scattered under the Bragg angle of the skyrmion lattice and, therefore, maps the distribution of the A-phase. Due to the MCP setup, the scattered intensity within the averaged TI could be increased drastically compared to Fig. 6.39 (c), since the background has been strongly reduced.
Clearly, for 200 mT, the skyrmion lattice is homogeneously distributed over the sample. A small drop in intensity is only found near the edge. This TI decrease is caused by the fact that, due to limited beam time, the rocking scan could not be extended until the TI contrast completely vanished. Some residual scattered intensity would still have appeared near the edges, as seen from the unsaturated rocking curve of position (3).

The nucleation and suppression of the skyrmion lattice near the boundaries of the A-phase

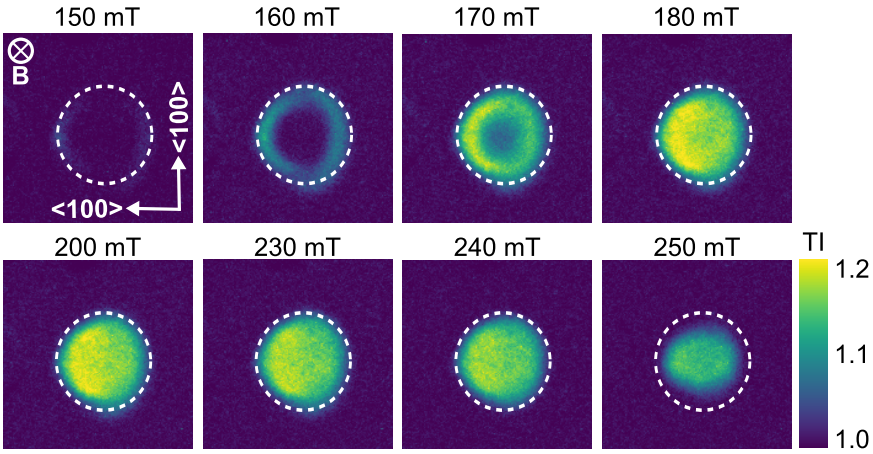

Figure 6.42.: Distribution of the skyrmion lattice for different fields. Shown are averaged TIs (compare Fig. 6.41), for different fields. The data were normalized to $B = 260\,\mathrm{mT}$, at which the scattering contrast has already vanished. The data evaluation which is required to calculate these images is explained in Sec. 6.5.2.

After the capacity of diffractive imaging has been demonstrated above, the nucleation and suppression of the skyrmion phase in the disc-shaped sample is studied in the remainder of this section. For this purpose, diffractive images have been obtained for different fields between 150 and 250 mT. Averaged TIs which mark

the skyrmion lattice are presented in Fig. 6.42. These images have been obtained in a similar way to the one shown in Fig. 6.41 (c).
At 150 mT the skyrmion lattice begins to nucleate at the edges of the sample, where a small sickle-shaped contrast arises. In increasing fields, the A-phase further penetrates the sample from the edge, which generates a ring-shaped contrast variation in the averaged TI for 160 mT. The connected penetration front has moved further inwards at 170 mT. In between 180 and 230 mT, the whole sample is in the A-phase, since a homogeneous contrast arises all over it. Above 240 mT, the skyrmion lattice shrinks and the A-phase only occupies the center of the disc. No scattering occurs at the region near the edge, where the sample is already in the conical state. At 260 mT, no scattering contrast could be detected anymore. These data have been used as reference (open beam) scan.

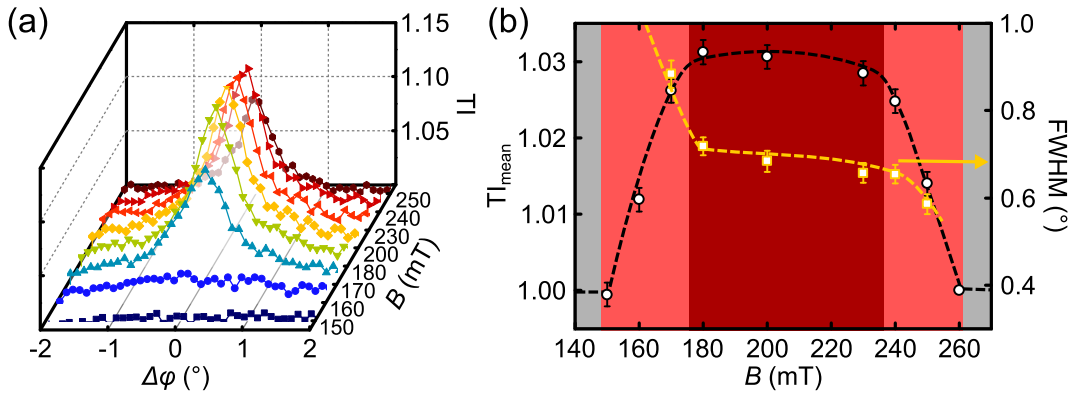

Figure 6.43.: Quantitative evaluation of the TI. (a) Rocking curves of the whole sample for different magnetic fields between 150 and 250 mT. (b) Mean TI of the rocking curves (black) shown in (a) and full width at half maximum (FWHM) of these curves (yellow). The dashed lines are guide to the eyes.

The diffractive images are quantitatively evaluated in Fig. 6.43. In (a), rocking curves of the sample are shown for all investigated fields. In each rocking curve, the mean TI value within a single diffractive image (compare Fig. 6.41 (a)) is plotted against the respective rocking angle $\Delta\varphi$. Since the scattering is averaged over the whole sample volume, these data correspond to a SANS rocking scan of the first order Bragg peak. In fields below 170 mT, the rocking curves are very broad and do not drop to one in the examined angular range. In contrast, above 170 mT, the rocking curves are strongly peaked around $\Delta\varphi = 0$, reveal a higher TI, and could be approximated by a Lorentzian distribution. The reason of this particular line shape will be discussed below.
The mean value $\mathrm{TI}_{\mathrm{mean}}$ of the averaged TIs, shown in Fig. 6.42, is plotted against the magnetic field in Fig. 6.43 (b). Additionally, the FWHMs obtained from Lorentzian fits of the rocking curves in (a) are plotted. $\mathrm{TI}_{\mathrm{mean}}$ is a measure for the overall scattered intensity and is hence analogous to the integrated intensity

measured in SANS. In contrast, the FWHM corresponds to the SANS rocking width.
Above 150 mT, the intensity increases with the field, since the volume of the A-phase within the sample grows. In contrast, a strong decrease is observed in the FWHM. In both quantities, a plateau develops between approximately 180 and 230 mT, which marks the field region in which the whole sample is filled by a skyrmion lattice. This plateau is routinely observed in the integrated intensity measured for the A-phase [220]. In high fields above 230 mT, the volume fraction of the A-phase again decreases leading to a diminishing $\mathrm{TI}_{\mathrm{mean}}$. The FWHM simultaneously drops down, until the contrast vanishes at 260 mT.
Taking advantage of the imaging approach, the mean TI value and the FWHM of the rocking scan can be extracted for each detector pixel. In this way, the local distortion and scattering power of the skyrmion lattice can be mapped. For this purpose, every detector pixel within a rocking scan has been fitted to a Gaussian function:

$$\mathrm{TI}(\Delta\varphi) = 1 + \frac{A_{\mathrm{G}}}{\sigma_{\mathrm{G}}\sqrt{2\pi}} \exp\left[-\frac{(\Delta\varphi - \Delta\varphi_{\mathrm{center}})^2}{2\sigma_G^2}\right] \tag{6.14}$$

Here, $\Delta\varphi_{\mathrm{center}}$ is the position of the peak, while the integrated intensity is given as the area A_{G} of the Gauss peak and the FWHM is defined as $2\sigma_{\mathrm{G}}\sqrt{2\ln 2}$. It has already been demonstrated in Fig. 6.41 (b) that this Gaussian approximation fits the data quite well.

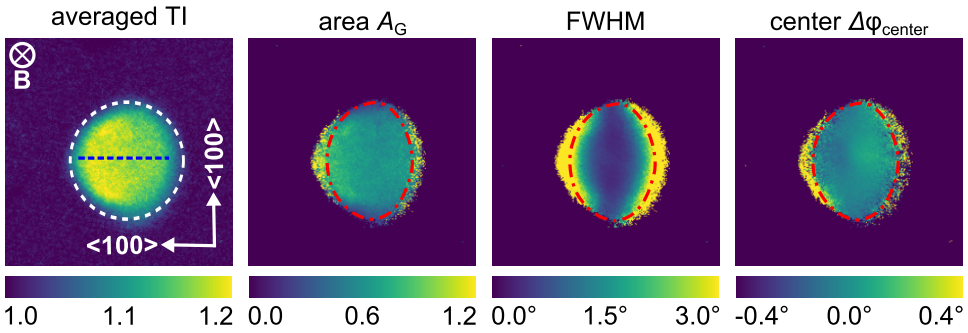

Figure 6.44.: Quantitative evaluation of the diffracted images for $B = 200\,\mathrm{mT}$ and $T = 28\,\mathrm{K}$. Shown are the average TI and results of a pixelwise fitting of the diffracted images to Eq. 6.14. These results are separated into maps of the area A_{G}, the FWHM, and the center $\Delta\varphi_{\mathrm{center}}$. The white dashed line and the red dotted-dashed lines correspond to the sample area and the area within which the error of the fits is smaller than 20 %.

Results of the pixelwise fitting of the diffracted images are presented in Fig. 6.44. The data are grouped in the averaged TI, maps of the area A_{G}, the local FWHM, and the local center of the rocking scan $\Delta\varphi_{\mathrm{center}}$. Within the red dashed-dotted

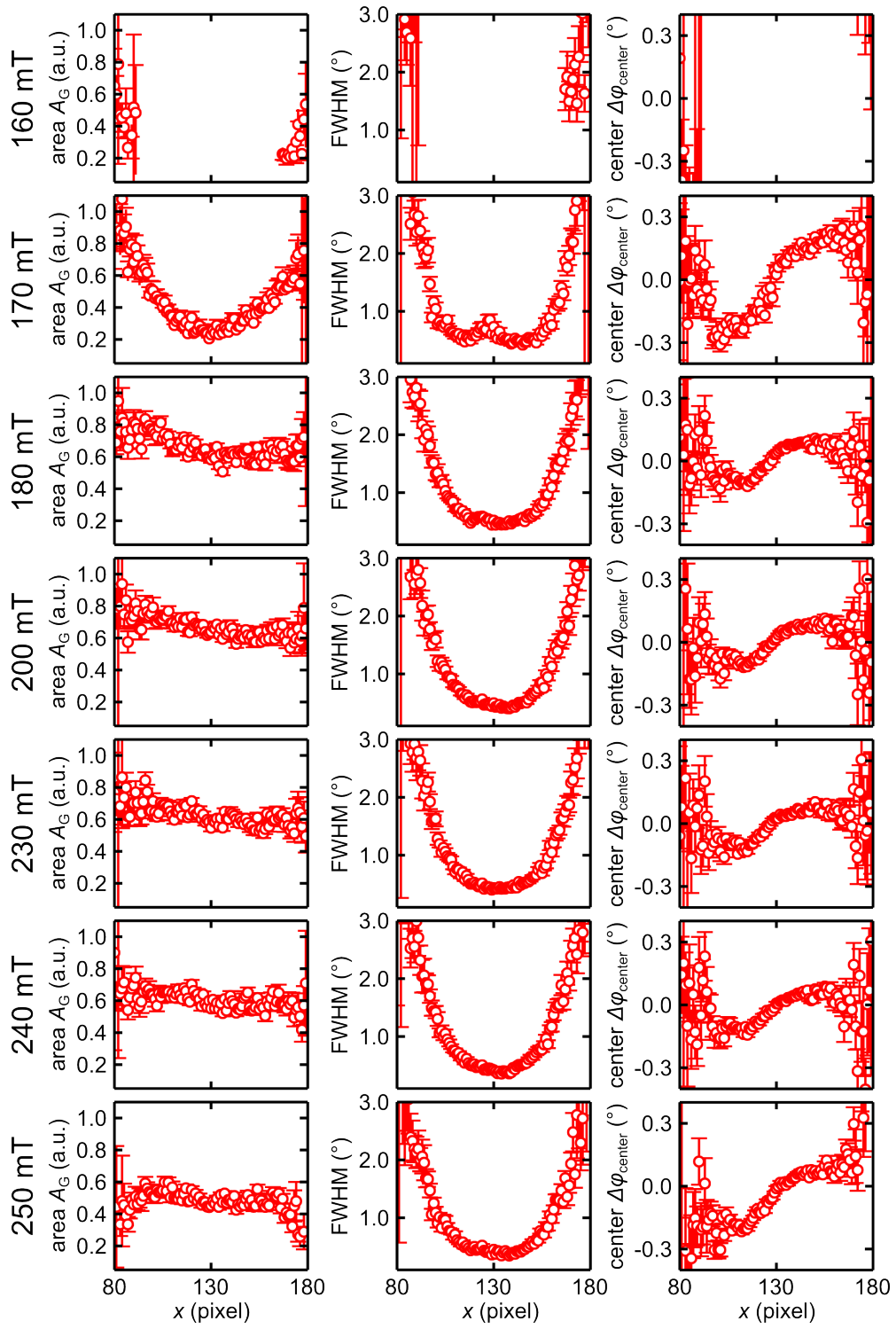

Figure 6.45.: Evaluation of the parameter maps. Shown are horizontal line profiles through the parameter maps for all investigated fields. A pixel corresponds to $76\,\mu\mathrm{m}$.

line, the error of the fit parameters is smaller than 20 %. The oval shape of the parameter maps is a consequence of the fact that rocking scans could only be conducted around the vertical axis. Therefore, only distortions in the horizontal direction are probed, but similar ones are expected in the vertical direction, due to the cylindrical symmetry of the sample.
The averaged TI has already been discussed in Fig. 6.41 (c). The map of A_G is flat in the center of the sample, suggesting a homogeneous skyrmion lattice at this field. Deviations are only observed near the edge. They are caused by the low scattered intensity at these positions which diminishes the fit accuracy. The center position $\Delta\varphi_{\text{center}}$ varies within the sample and shows a zero-point in the middle of it. Finally, the FWHM shows that the rocking curve is strongly smeared out at the edges of the samples and the rocking width continuously decreases towards the center of the sample. In the interior of the disc the instrumental resolution is reached at a value of 0.4°.
The cylindrical symmetry of the sample allows to restrict the attention on a horizontal profile. Therefore, in Fig. 6.45, the variation of A_G, FWHM, and $\Delta\varphi_{\text{center}}$ along the blue line in Fig. 6.44 is presented for fields between 160 and 250 mT. Data obtained for 150 mT could not be evaluated due to the low scattered intensity.
In the first column, the area A_G under the rocking curve is plotted against the horizontal position. At 160 mT, scattering arises only near the edge of the sample where A_G gradual decrease towards the middle. In the center of the disc, A_G equals zero. At 170 mT, the skyrmion lattice has completely penetrated the sample but a V-shaped profile is observed. For increasing fields, the profile is homogenized and A_G is finite as well as approximately constant all over the disc. The local degradation of the skyrmion lattice is seen at 250 mT as a reduction of A_G near the sample edge. All data (including the averaged TIs of 6.42) reveal a slight horizontal gradient in the integrated intensity. It could not be decided from these first measurements if this effect is parasitic and caused by the setup or an intrinsic property.
The FWHM of the rocking curves are presented in the middle column. Except for the smallest field, where no contrast arises in the center, the profiles show a pronounced U-shape with a FWHM variation between 0.4 and 3°. Once the skyrmion lattice has covered the whole sample above 180 mT, this profile does not change significantly. Only at 170 mT, a small reincrease occurs in the center. However, it has to be emphasized that no conclusions can be drawn about the angular distortion of the skyrmion lattice in the center of the sample, since the angular resolution limit of 0.4° is reached.
The center position of the rocking curves is shown in the right column. At the lowest field, an exact determination of $\Delta\varphi_{\text{center}}$ is hampered by the low intensity. In higher fields, the trend of the rocking curve width and area is confirmed since no deviations occur above 180 mT. However, the center of the rocking curve is clearly increasing throughout the disc from −0.1 to 0.1° (−0.3 to 0.3° at 170 mT)

and a linear slope arises in its center. This variation in the center position can be partially explained by the pinhole geometry of the setup sketched in Fig. 6.46 (b). The maximal divergence at each position within the sample is approximately given by $D_\mathrm{R}/L_\mathrm{R} = 0.12°$ as sketched by the dashed lines. However, the mean direction of the neutron beam (red) changes throughout the sample and is only zero in its center. The maximal variation over the sample diameter d is given by $d/L_\mathrm{R} \approx 0.07°$. The value can only partially account for the discrepancy in the data. However, a slight radial component of the magnetic field at the sample position of about $2 \times 10^{-3}B$ might already explain the further $\Delta\varphi_\mathrm{center}$ variation. This effect is most likely, as the sample was positioned approximately 3 mm out of the center of the magnet in the direction of the beam.
To conclude, it has to be noted that a similar investigation has been performed for decreasing fields. None of the determined quantities has shown a clear sign of hysteretic behavior. A topological hysteresis as arising in superconductors seems hence absent in the A-phase. However, a final assessment requires further investigations.

6.5.3. The influence of demagnetization effects on the skyrmion lattice

Nucleation of the skyrmion lattice

The nucleation of the skyrmion lattice is usually accompanied by several signatures which suggest a temporary coexistence between the A-phase and the conical state, underlining the first-order character of the phase transition: (i) In small-angle neutron scattering [98, 220], the transition to the A-phase takes place in a finite field interval, where the integrated intensity simultaneously increase for the Bragg peak related to the skyrmion lattice[1] and decrease for the peak connected to the conical state. (ii) The phase coexistence is also seen in magnetization data, as broad peaks in the field dependence of the real and imaginary magnetic susceptibility of the sample which develop at the A-phase boundary [101, 212]. Whether this coexistence is of microscopic or macroscopic nature cannot be detected by either of the methods. However, a distinct correlation of the width of the transition region to the sample shape has been verified in Ref. [212], which points to a strong influence of demagnetization effects. The imaging approach presented in this section allows to naturally address the influence of demagnetization on the skyrmion nucleation, since it allows to map the spatial distribution of the A-phase in the coexistence region.
A connection of the data presented in Fig. 6.42 to magnetization results is established in Fig. 6.46 (a) in which the phase diagram of MnSi near the A-phase is shown. The data are taken from Ref. [101] in which a cuboid sample of

1 In Ref. [220], the skyrmion Bragg peak was still believed to be cause by a reoriented helical structure.

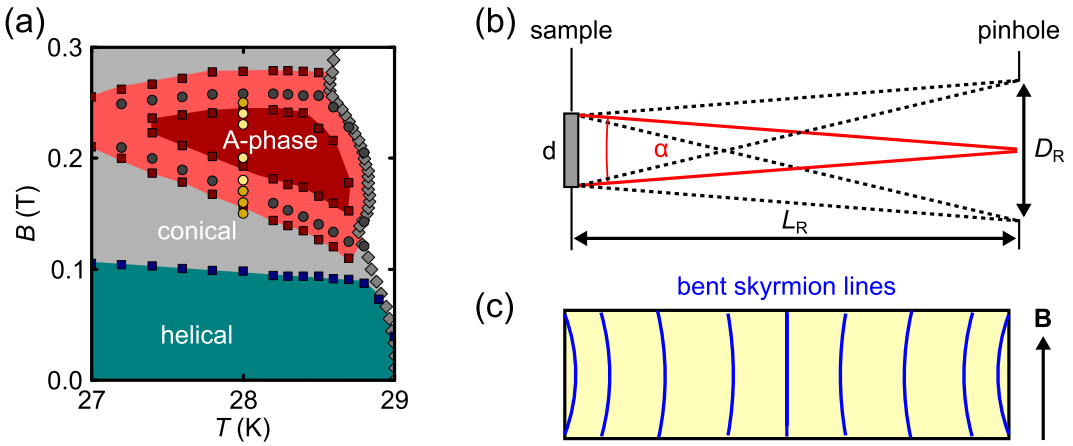

Figure 6.46.: Discussion on the skyrmion distribution. (a) Magnified phase diagram of MnSi near the A-phase (compare Fig. 2.19 (a)). Yellow circles mark the positions studied by diffractive imaging. Data with courtesy of A. Bauer [101]. (b) Illustration how the pinhole geometry influences the local center position of a rocking scan. (c) Illustration how the skyrmion lattice is distorted in the disc shape geometry.

comparable quality has been studied. The originally presented internal field $\mu_0 H_{\mathrm{int}}$ (compare Fig. 2.19 (a)) has been translated to applied fields by scaling according to $B = (1 + D\chi_{\mathrm{con}})\mu_0 H_{\mathrm{int}}$ [99]. Here, $D = 0.65$ is the demagnetization coefficient of the disc and $\chi_{\mathrm{con}} = 0.34$ is the magnetic susceptibility within the conical state [99]. The following discussion is based on these data, since no measurements on the MnSi disc were available, due to its large size.

The helical, conical and A-phase are seen in the phase diagram. The latter one has been subdivided into (i) a core region (dark red) where no signatures of a phase coexistence are found by magnetic bulk measurements and (ii) a boundary region (light red) in which broad peaks in the susceptibility arise and a phase coexistence is likely. Positions, at which diffractive images of the MnSi disc have been obtained, are marked by yellow circles. The onset of scattering within the TIs at 150 mT coincides well with the lower boundary of the A-phase. In contrast, the scattered intensity vanishes already at 260 mT slightly below the skyrmion suppression expected by magnetization data. In the A-phase, both data are in qualitative agreement. The region of phase coexistence found between 150 and 180 mT (dark yellow) and of pure A-phase between 180 and 230 mT (bright yellow) corresponds well to the phase diagram. The slight deviations in the absolute values might be caused by the different sample shape [212].

The presented coincidence of neutron and magnetization data suggests that the observed phase coexistence is mostly macroscopic and the A-phase nucleates via a skyrmion penetration from the sample edges. This behavior can be qualitatively well understood from the demagnetization field $\boldsymbol{H}_{\mathrm{d}} = -D\boldsymbol{M}$ within the disc, which decreases from the interior to the edge. The local field $\boldsymbol{H} = \boldsymbol{B}/\mu_0 + \boldsymbol{H}_{\mathrm{d}}$

is consequentially enhanced near the sample boundary, which provokes the local transition to the A-phase already in smaller applied fields.
It cannot be excluded that the skyrmion nucleation in the center takes place by the spontaneous formation of skyrmions out of the conical continuum. The opposite process has been observed in doped $Fe_{0.5}Co_{0.5}Si$, in which neighboring skyrmions have been shown to randomly merge, leading to a successive transition to the conical state [206]. However, the presented data strongly suggest that most of the signatures seen at the magnetic phase transition can be explained by demagnetization.

Bending of the skyrmion lattice

The observed broadening of the rocking curves of a few degrees clearly exceeds the experimental resolution of 0.4° which, contrary to $\Delta\varphi_{\text{center}}$, does not depend on the position on the sample. A widening of the rocking curve is usually connected to a loss of the longitudinal coherence of the skyrmion lattice. However, due to the strong spatial dependence of the rocking width, a local bending of the skyrmion lines seems to be more likely, since demagnetizing fields will provoke a distortion towards the sample edge. If one assumes a smooth variation of the skyrmion line direction, an alignment as sketched in Fig. 6.46 (c) seems most likely based on the presented data. The skyrmions are bent along the internal field which is directed outward, towards the corners of the sample, but is homogenized towards the center of the disc. From the rocking FWHM of more than 3°, typical radii of curvatures can be deduced to lie in the centimeter range at the sample edge.

The geometrical influence on SANS data

The presented spatially resolved data directly demonstrate how a SANS rocking curve is influenced by demagnetization effects. In Fig. 6.47 (a)-(f), the averaged TI taken at 200 mT is shown. Additionally, rocking curves evaluated only for the marked area in the associated TIs are presented. These data would correspond to SANS rocking scans with an aperture placed in front of the sample that has the shape of the particular white square. Clearly, the FWHM of the rocking curve, written above each graph, strongly increases once the aperture covers the edge of the sample (d). Furthermore, a peculiar transition in the line shape can be observed. For a demonstration, each rocking curve is fitted by a Gaussian (red) as well as a Lorentzian (blue) peak shape. The means of the squared residuals are denoted R^2_{Gauss} and R^2_{Lorentz}, respectively. While the data of (a) and (b) are more accurately described by the Gaussian shape ((a) $R^2_{\text{Gauss}} = 0.6R^2_{\text{Lorentz}}$, (b) $R^2_{\text{Gauss}} = 0.3R^2_{\text{Lorentz}}$), a better fit is reached by the Lorentzian, once the aperture covers the edge of the sample ((d) $R^2_{\text{Gauss}} = 16R^2_{\text{Lorentz}}$). If the whole sample is included, small deviations from the Lorentzian line shape arise, as well. Although this behavior seems remarkable, it has been directly observed in Ref. [98] where

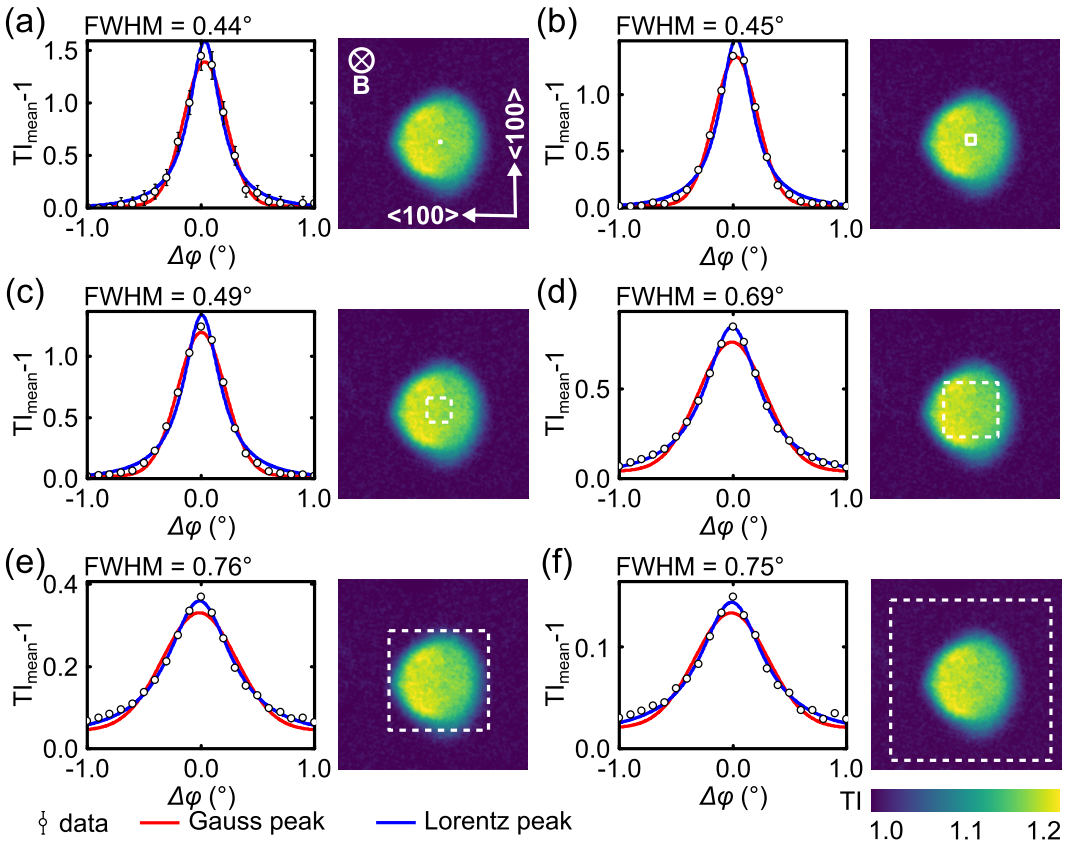

Figure 6.47.: The geometric influence on the rocking curve. Presented are the results of diffractive imaging for $B = 200\,\mathrm{mT}$. Each of the subfigures (a)-(f) shows a rocking curve evaluated for the area marked by the white square in the corresponding averaged TIs. Each rocking curve is fitted by a Gaussian and a Lorentzian distribution. The line shape remarkably changes if one extends the probed sample area to the edge of the sample. Error bars corresponds to the statistical error.

an approximately Lorentzian shape of the rocking curve was found for a cuboid sample, whereas a thin plate covered by a small aperture produces a distinct Gaussian shape. The transition in the line shape arises, as the rocking curve is the convolution of the Gaussian resolution curve, the Gaussian mosaicity of the skyrmion lattice [219] and the orientational distribution of the skyrmion lattice, which seems to be more of Lorentzian nature if the edges of the sample are included.

6.5.4. Conclusion and outlook

In conclusion, the presented approach using an MCP provides a simple way to use small-angle scattering arising from magnetic structures to obtain diffractive images. On the example of the skyrmion lattice in MnSi it could be recorded

how magnetization and scattering data are influenced by the sample shape. The demagnetization fields associated with the disc shape of the sample, (i) give rise to an inhomogeneous penetration of the skyrmion lattice and (ii) locally misalign the direction of the skyrmion lines from that of the applied magnetic field. Both effects have to be considered in the interpretation of SANS data. The presented study substantiates the necessity to always consider the sample shape in the interpretation of scattering data, either by the use of ellipsoidal samples which generate a homogeneous demagnetization field or by a simulation of the internal field distribution in non-elliptic samples. The approach to just mask the edges of a sample in a scattering experiment is obviously insufficient to exclude demagnetization effects.

Considering type-II superconductors, the presented study illustrated the potential of diffractive imaging to investigate the bulk distribution and alignment of magnetic vortices. A further technical improvement of the MCPs to higher collimation ratios will enable to directly test several of the theoretical prediction on the vortex distribution within superconductors of different shapes [68]. On the first glance, these problems seem quite academic. However, results of such theoretical computations are extensively applied in the interpretation of e.g magnetization or magneto-optical data, although their experimental verification is so far restricted to the sample surface.

7. Conclusion: New toys conquer the playground

In this thesis, a novel approach to study the bulk structure of vortex matter has been developed, which is based on the combination of neutron grating interferometry, diffractive imaging, small-angle neutron scattering, as well as ultra-small-angle neutron scattering. This approach enables to probe a broad range of length scales of 0.01 to 10 µm, which is not accessible by ordinary small-angle neutron scattering. By combining SANS and USANS, the differential scattering cross-section of the sample can be probed over an extended q-range, while nGI allows for a mapping of its local deviation. Hence, detailed information about the sample's microstructure are combined with high resolution images of its spatial distribution. By means of this approach, the properties of three different generic types of vortex matter have been investigated: (i) the intermediate state (IS) in type-I superconducting lead, (ii) the intermediate mixed state (IMS) in type-II superconducting niobium, and (iii) the skyrmion lattice in chiral magnetic MnSi.
This thesis consists of a methodical as well as an experimental part. In order to establish nGI as a tool for quantitative investigations of emergent micrometer structures, arising e.g. in the IS and IMS, a major goal of the present work was the implementation of a grating interferometer as user instrument at the ANTARES beamline of the Heinz Maier-Leibnitz Zentrum. The capability of the setup to perform novel experimental approaches like directional and quantitative dark-field imaging has been demonstrated. Since the developed setup allows for an easy insertion of additional sample environments, it can be generally adapted to investigate systems revealing a scattering length density that varies on the micrometer scale. Due to its good interferometric visibility, its comparatively high neutron flux and its discussed flexibility, the nGI at ANTARES provides a strong alternative to the few setups existing world wide[1].
As a further important point, a common theoretical framework covering nGI, SANS and USANS has been derived and experimentally verified within this thesis. It allows to extract detailed information about the sample's microstructure (like structure size and textures) by quantitative and directional dark-field imaging. The developed relations furthermore enable a coherent interpretation of USANS and nGI results which permits the combination of different techniques performed in this work.

1 Further nGI setups are available at the Paul-Scherrer-Institut (PSI), the Helmholtz Zentrum Berlin (HZB), the National Institute of Standards and Technology (NIST), and the High Flux Advanced Neutron Application Reactor (HANARO).

By applying nGI to the intermediate state in a type-I superconducting lead sample, its capability to image the nucleation of superconducting domain structures has been verified. In agreement with literature, a strong hysteretic behavior of the domain morphology has been found, which is of pure topological nature.
The impact of pinning and geometrical barriers on the IMS formation in type-II superconductors has been examined on niobium samples of different qualities and shapes. In the case of a pinning free Nb rod, an unconventional domain volume filling, which is accompanied by a strong variation of the internal field, has been found. It could be explained in terms of geometrical barriers arising due to the non-ellipsoidal sample shape. Furthermore, a first hint for a topological hysteresis in the morphology of the IMS has been detected.
The situation dramatically differs for samples revealing significant pinning. In this case, an IMS can only be nucleated via field cooling. Unlike in the pinning free sample, the IMS is formed out of the Shubnikov phase. It could be shown that the total flux is trapped in the sample already above the temperature at which the IMS nucleates. The observed rearrangement of the vortices to form domains is hence purely microscopic and linked to the changed lattice elasticity accompanying the onset of vortex attraction. Further investigations are required to uncover the nature of this transition.
The resulting IMS domain morphology is rather irregular due to the presence of pinning, but still characterized by a preferred domain size which increases with the field according to theoretical predictions of the Landau and Goren-Tinkham models. As for the pinning free case, the IMS is not homogeneously distributed within the sample after field cooling.
By using the IMS as contrast agent for nGI, the process of field penetration into the bulk of a Nb type-II superconductor has been studied. Actually, these results provide the first direct visualization of the critical state within the bulk of a type-II superconductor. The observed flux penetration can be described qualitatively by the existing theory. However, a quantitative treatment requires a modification of the existing models to account for the finite thickness of the samples and for a finite lower critical field. Since an additional signature of the flux front has been observed in the transmission image, the presented approach could be expanded to investigate also type-II superconductors not forming an IMS.
Finally, the potential of diffractive imaging using an MCP collimator has been demonstrated by imaging the nucleation of the skyrmion lattice phase in an MnSi disc. A strong influence of demagnetization effects on the magnetic phase diagram of MnSi has been visualized, since the observed skyrmion nucleation from the edge of the disc to its center correlates to the demagnetization field within the sample. As a second consequence of demagnetization, the skyrmion lattice is strongly distorted, even deep within the A-phase.
Besides providing detailed information about the morphology and nucleation of the vortex phase in the bulk of superconductors and chiral magnets, the presented study demonstrated the dramatic influence of the sample shape on vortex matter:

In particular, (i) an inhomogeneous distribution of vortices, (ii) a strong bending of vortex lines, as well as (iii) a macroscopic phase separation have been identified as common manifestations of geometrical effects. This strong impact of the sample shape onto vortex matter is rarely considered in literature. Instead, observations which cannot be satisfactorily explained are often only vaguely linked to demagnetizing effects. The methodical approach presented in this thesis now allows for a detailed quantification of such geometric effects. The additional usage of radiographic methods might hence be considered whenever the influence of the sample geometry is not sufficiently understood, and prevents an unambiguous interpretation of scattering data.

At last, it has to be emphasized that the presented general approach is by no means limited to vortex matter. It could be extended in order to investigate the rich variety of modulated phases appearing in densely packed, liquid and dilute physical, chemical or biological systems and systems near phase transitions (in particular first order phase transitions), as well as in emerging magnetic systems. All of them share the macroscopic domain formation on the micrometer or sub-micrometer scale as a common feature.

Acknowledgment / Danksagung

The amount of gratitude I feel cannot be expressed in a foreign language.

Prof. Peter Böni Vielen Dank dafür, dass du mir dir Gelegenheit gegeben hast, an diesem spannenden Thema zu forschen, mich die letzten Jahre mit Rat und Tat begleitet hast und uns immer sofort zur Seite standest, wenn sich Probleme ergaben. Ursprünglich wollte ich nur "etwas mit Neutronen machen". Mit der Vielzahl von Erfahrungen, die ich in den letzten Jahren sammeln konnte, hätte ich nie gerechnet.

Michael Schulz Vielen Dank für die schönen letzten Jahre in deiner Gruppe. Danke für die Einweisungen in die Geheimnisse der Neutronenradiographie, für deine stetige Bereitschaft meine Proposals, Anträge, Reports, Paper, etc. Korrektur zu lesen, für deine Hilfe und Unterstützung bei unzähligen Messzeiten sowie für die vielen wissenschaftlichen, wie privaten Gespräche.

Sebastian Mühlbauer Vielen Dank Basti, für deine Betreuung und Hilfe während der letzten Jahre. Ich habe nicht nur viel von dir über Supraleitung, Magnetismus und Neutronenstreuung gelernt, sondern auch immer sehr von deinen Ratschlägen und unseren intensiven Diskussionen profitiert. Dein Perfektionismus und dein Elan waren (meistens) ansteckend.

Christian Grünzweig Von wem könnte man Neutronengitterinterferometrie besser lernen, als von dir. Vielen Dank für die Einweisung in diese Technik, deine Betreuung während der Experimente am PSI sowie deine wichtigen Ratschläge zu dem Setup am ANTARES. Ein Highlight jeder Messzeit war das Grillen mit dir und deiner Familie. Danke für die Zusammenarbeit.

ANTARES-Gruppe Die schöne Zeit am FRM II verdanke ich besonders den alten und neuen Kollegen der ANTARES Gruppe. Lieber Alexander, Aureliano, Burkhard, Dominik, James, Marc, Martin, Michael (L.), Philipp, Stefan und Tobias. Danke für eure Hilfe bei so manchen technischen sowie physikalischen Problemen, für die unzähligen Konstruktionen, entgrateten Kanten und gebohrten Löcher, für die Hilfe beim Aufbau und der Durchführung meiner Experimente, für die wertvollen Diskussionen, Tipps und Lebensweisheiten. Es war immer eine tolle Stimmung auf unserem Gang und wir hatten viel Spaß zusammen.

NIAG Gruppe Bei meinen Besuchen am PSI wurde ich immer herzlich empfangen und mit Kräften unterstützt. Vielen Dank an Anders Kaestner für seine Hilfe bei der Datenauswertung, an Steven Peetermans für seine Ideen zum diffractive imaging und Ralph Harti für fruchtbare Diskussionen zum DFI Kontrast. Besonderer Dank gebührt Benedikt Betz, der sich viele Wochenenden um die Ohren geschlagen hat um mich bei meinen Messungen zu unterstützen.

NIST USANS team I am very grateful to David Mildner, Markus Bleuel and Alan Ye. Thank you for your support during my two beamtimes at the NIST neutron facility, but also for the nice evenings we shared, for some beautiful hikes or for the introduction to nearly every all-you-can-eat restaurant nearby NIST.

Annie Brûlet, Hartmut Lemmel, Vitaliy Pipich Thanks for your support in preparing and conducting experiments at TPA, S18 and KWS 3, respectively.

Alexander Lenz Ohne dein schnelles und unkompliziertes Lösen so mancher Softwareprobleme wäre wohl ein Großteil meiner Messungen ins Wasser gefallen. Danke für deine Hilfe.

Andreas Bauer und Georg Benka Vielen Dank an die beiden Kristallhexer für wertvolle Diskussionen, ihre Hilfsbereitschaft im Kristalllabor sowie die schnellen Messungen am PPMS.

E21 and E51 Vielen Dank an alle Kollegen vom Lehrstuhl, für vielfältige Unterstützung und das tolle Arbeitsklima (besonders beim Vorbereiten für FKP-Intro).

FRM II Danke auch an alle Kollegen vom FRM II (Wissenschaft sowie Betrieb), die indirekt zu meiner Arbeit beigetragen haben. Besonders bedanken möchte ich mich beim Strahlenschutz für das schnelle und zumeist spontane freimessen meiner Proben und Instrumente sowie bei den Herzog und Stiegel Werkstätten für ihre (meist kurzfristige) Fertigung diverser Bauteile und Probenhalter.

Kaffee (Mate)-Runde Liebe Kollegen (Andi, Christian, Elbio, Herbert, Linus, Peter...), danke für eure Hilfe bei so manchen Problemen sowie für die entspannte, witzige, lehrreiche aber manchmal auch beschämende Zeit jeden Mittag ab 11:30 Uhr. Solche Kollegen wie euch wünscht man niemandem. Aber ich werde es (euch) trotzdem sehr vermissen. Danke!

Das Beste kommt zum Schluss Sani, ich danke dir für deine Unterstützung und deine Geduld mit mir in den letzten Jahren. Du bist meine Stütze und mein Anker. Mit dir blicke ich lächelnd und voller Vorfreude in die Zukunft.

This project has received funding from the European Union's 7th Framework Programme for research, technological development and demonstration under the NMI3-II Grant number 283883.

List of publications

1. **The new neutron grating interferometer at the ANTARES beamline: design, principles and applications**
   T. Reimann, S. Mühlbauer, M. Horisberger, B. Betz, P. Böni and M. Schulz
   J. Appl.Cryst. 49, 1488-1500 (2016)

2. **Neutron Dark-Field Imaging of the Domain Distribution in the Intermediate State of Lead**
   T. Reimann, M. Schulz, C. Grünzweig, A. Kaestner, A. Bauer, P. Böni and S. Mühlbauer
   J. Low Temp. Phys. 182, 107-116 (2016)

3. **Visualizing the morphology of vortex lattice domains in a bulk type-II superconductor**
   T. Reimann, S. Mühlbauer, M. Schulz, B. Betz, A. Kaestner, V. Pipich, P. Böni and C. Grünzweig
   Nat. Commun. 6:8813 (2015)

4. **The New Neutron Imaging Beam Line ANTARES at FRM II**
   M. Schulz, B. Schillinger, E. Calzada, D. Bausewein, P. Schmakat, T. Reimann and P.Böni
   Proceeding of the 1st International Conference on Neutron Imaging and Neutron Methods in Archaeology and Cultural Heritage Research, accepted (2014)

5. **Enhenced critical fields in MnSi thin films**
   D. Menzel, J. Engelke, T. Reimann and S. Süllow
   JKPS, 62, 1580-1583 (2013)

6. **Spin-Spin Correlation Length in MnSi Thin Films**
   J. Engelke, T. Reimann, L. Hoffmann, S. Gass, D. Menzel and S. Süllow
   J. Phys. Soc. Jpn., 81, 124709 (2012)

A. Appendix

A.1. The phase boundaries of the IMS

The phase diagram of the intermediate mixed state was given in Fig. 2.10 (b). It has been stated that the IMS is characterized by a coexistence of Shubnikov and Meissner domains in the field region $(1-D)B_{\mathrm{C1}} \leq B \leq (1-D)B_{\mathrm{C1}} + DB_0$. In the following section, these boundaries are shortly justified [15, 178].
The magnetization within the sample is given by the magnetic induction $\boldsymbol{B}$ and the magnetic field $\boldsymbol{H}$:

$$\boldsymbol{M} = \frac{1}{\mu_0}\boldsymbol{B} - \boldsymbol{H} \ , \tag{A.1}$$

in which the magnetic field is composed of the applied field $\boldsymbol{H_a}$ and the demagnetization field $\boldsymbol{H_d} = -D\boldsymbol{M}$:

$$\boldsymbol{H} = \boldsymbol{H_a} + \boldsymbol{H_d} = \boldsymbol{H_a} - D\boldsymbol{M} \ . \tag{A.2}$$

In the Meissner state $\boldsymbol{B} = 0$, hence, Eq. A.1 simplifies to $\boldsymbol{M} = -\boldsymbol{H}$. Therefore, the field $\boldsymbol{H}$ reaches the critical value already at an applied field:

$$\boldsymbol{H_a} = (1-D)\boldsymbol{H_{C1}} \ , \tag{A.3}$$

which corresponds to the transition field to the IMS. Within the IMS, Shubnikov domains are formed. These domains are characterized by a constant, field independent vortex lattice parameter of:

$$a_{\mathrm{VL}} = \sqrt{\frac{2\Phi_0}{\sqrt{3}B_0}} \ . \tag{A.4}$$

The local induction of the domains is given by $\boldsymbol{B_0}$ that is defined by the equilibrium spacing of the vortices within the interaction potential of Eq. 2.20. In the IMS, $\boldsymbol{B_0}$ remains constant and only the filling factor of the domains increases. The magnetic field $\boldsymbol{H}$, consequently corresponds to the critical value $\boldsymbol{H_{C1}}$ as otherwise, the IMS would become unstable.
Clearly, the sample is entirely filled with vortex lattice, when the macroscopic

induction $\boldsymbol{B}$ is given by $\boldsymbol{B_0}$. This is the case at:

$$\boldsymbol{H_a} = \boldsymbol{H_{C1}} + D\boldsymbol{M} = \boldsymbol{H_{C1}} + D\left(\frac{1}{\mu_0}\boldsymbol{B_0} - \boldsymbol{H_{C1}}\right) \tag{A.5}$$

$$= (1-D)\boldsymbol{H_{C1}} + \frac{D}{\mu_0}\boldsymbol{B_0}\ . \tag{A.6}$$

The corresponding applied magnetic field $\boldsymbol{B_a}$ is given by:

$$\boldsymbol{B_2} = (1-D)\boldsymbol{B_{C1}} + D\boldsymbol{B_0}\ . \tag{A.7}$$

Above this value, the sample is in the Shubnikov state and completely filled with a vortex lattice. A further increase of the field reduces the vortex lattice parameter.

A.2. Directional DFI on a bi-gaussian scattering distribution

The formula for the ω-dependence of the DFI is derived under the assumption of a bi-gaussian differential scattering cross-section:

$$\frac{d\sigma(q_\mathrm{x},q_\mathrm{y})}{d\Omega} = A\exp\left[-\left(\frac{q_\mathrm{x}^2}{2\sigma_\mathrm{x}^2} + \frac{q_\mathrm{y}^2}{2\sigma_\mathrm{y}^2}\right)\right]\ . \tag{A.8}$$

By using Eq. 3.31, the correlation function $G(x,y)$ can be calculated to:

$$G(x,y) = \frac{A}{4\pi^2}\int\limits_{q_\mathrm{x},q_\mathrm{y}} \exp\left[-\left(\frac{q_\mathrm{x}^2}{2\sigma_\mathrm{x}^2} + \frac{q_\mathrm{y}^2}{2\sigma_\mathrm{y}^2}\right)\right]\exp\left[\mathrm{i}\left(q_\mathrm{x}x + q_\mathrm{y}y\right)\right]dq_\mathrm{x}dq_\mathrm{y} \tag{A.9}$$

$$= \frac{A}{4\pi^2}\int\limits_{q_\mathrm{x}} \exp\left(-\frac{q_\mathrm{x}^2}{2\sigma_\mathrm{x}^2}\right)e^{\mathrm{i}q_\mathrm{x}x}dq_\mathrm{x}\int\limits_{q_\mathrm{y}} \exp\left(-\frac{q_\mathrm{y}^2}{2\sigma_\mathrm{y}^2}\right)e^{\mathrm{i}q_\mathrm{y}y}dq_\mathrm{y} \tag{A.10}$$

$$= \frac{A}{\pi^2}\int\limits_0^\infty \exp\left(-\frac{q_\mathrm{x}^2}{2\sigma_\mathrm{x}^2}\right)\cos\left(q_\mathrm{x}x\right)dq_\mathrm{x}\int\limits_0^\infty \exp\left(-\frac{q_\mathrm{y}^2}{2\sigma_\mathrm{y}^2}\right)\cos\left(q_\mathrm{y}y\right)dq_\mathrm{y}\ . \tag{A.11}$$

(A.12)

In the last step, the fact that the differential scattering cross-section is an even function has been used, which allows to skip the imaginary part of the exponential function. The resulting integral is tabulated [221] and is solved to:

$$G(x,y) = \frac{A\sigma_x\sigma_y}{2\pi}\exp\left[-\left(\frac{x^2\sigma_\mathrm{x}^2}{2} + \frac{y^2\sigma_\mathrm{y}^2}{2}\right)\right]\ . \tag{A.13}$$

Hence, the correlation function is again a Gaussian distribution. The ω dependence of the DFI is connected to the correlation function through Eq. 4.31. Here, the normalized correlation function is given by:

$$\frac{G(x\cos\omega, -x\sin\omega)}{G(0{,}0)} = \exp\left[-\frac{x^2}{2}\left(\sigma_x^2\cos^2\omega + \sigma_y^2\sin^2\omega\right)\right] , \tag{A.14}$$

which can be rearranged to:

$$\frac{G(x\cos\omega, -x\sin\omega)}{G(0{,}0)} = \exp\left[-\frac{x^2}{2}\left\{\sigma_x^2 + \left(\sigma_y^2 - \sigma_x^2\right)\sin^2\omega\right\}\right] . \tag{A.15}$$

Neglecting multiple scattering (Eq. 4.25), the DFI dependence on ω is given by:

$$DFI(\omega) = 1 - \Sigma t + \Sigma t \exp\left(-\frac{\xi_{\mathrm{GI}}^2}{2}\left[\sigma_x^2 + \left(\sigma_y^2 - \sigma_x^2\right)\sin^2\omega\right]\right) . \tag{A.16}$$

Under the assumption, that most neutrons are scattered ($\Sigma t \approx 1$) the visibility is finally given by:

$$DFI(\omega) = \exp\left(-\frac{\xi_{\mathrm{GI}}^2}{2}\left[\sigma_x^2 + \left(\sigma_y^2 - \sigma_x^2\right)\sin^2\omega\right]\right) . \tag{A.17}$$

Note that Eqs. A.16 and A.17 exactly correspond to the results given by Jensen et al. [144] and Revol et al. [145]. The only difference is that here the starting point was a scattering distribution in reciprocal space, whereas in the aforementioned works, $DFI(\omega)$ has been calculated starting from a real space gaussian intensity distribution at the detector. The variance is hence once defined in reciprocal space and once as the variance of the resulting scattering pattern at the detector. However, the translation is given by:

$$\sigma_x = \frac{4\pi^2}{\xi_{\mathrm{GI}} p_2^2}\begin{cases}\sigma_m & \text{Revol et al.}\\ \sigma_1 & \text{Jensen et al.}\end{cases} \tag{A.18}$$

$$\sigma_y = \frac{4\pi^2}{\xi_{\mathrm{GI}} p_2^2}\begin{cases}\sigma_M & \text{Revol et al.}\\ \sigma_2 & \text{Jensen et al.}\end{cases} \tag{A.19}$$

A.3. The influence of finite grating transmission on the nGI visibility

The effect of the finite grating line transmission on the visibility can be estimated by the following considerations: The absorption gratings $\mathrm{G_i}$ (i=0,2) having periodicity p_i and a duty cycle of DC_i will have a transmission profile as illustrated in Fig.

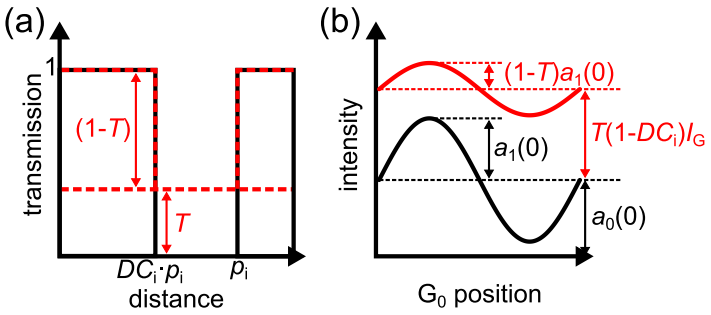

Figure A.1.: Reduction of visibility caused by finite transmission through the grating lines: (a) Simplified transmission profile of the absorption gratings. (b) If the transmission through the grating lines T is non-zero the intensity oscillation at the detector is reduced and superimposed by a constant background.

A.1 (a). In the case of a perfect grating, the transmission through the slits is unity, whereas the transmission of the grating lines, denoted as T, is zero. Therefore, the visibility will have an initial value $V_{\mathrm{Gi}}(T=0) = a_1(T=0)/a_0(T=0)$, in which $a_0(0)$ is given as DC_{i} multiplied by the neutron intensity incident on the grating I_{G}. However, if T is non-zero, the transmitted intensity will increase according to:

$$a_0(T) = \left[DC_{\mathrm{i}} + T(1 - DC_{\mathrm{i}})\right] I_{\mathrm{G}} \tag{A.20}$$

On the other hand, the intensity oscillation measured at the detector will correspond to the initial one, reduced by a factor of $(1-T)$, which is superimposed by a constant offset given as $T \cdot I_{\mathrm{G}}$ (compare red curve in Fig. A.1 (b)). Hence $a_1(T)$ scales as $(1-T)$:

$$a_1(T) = (1-T)a_1(0) = (1-T)V_{\mathrm{Gi}}(0)DC_{\mathrm{i}}I_{\mathrm{G}} \tag{A.21}$$

For low neutron energies, the wavelength dependence of the neutron transmission T can be approximated by:

$$T(\lambda) = \exp\left[-h_{\mathrm{i}}\sigma\frac{\lambda}{1.8\,\text{Å}}\right] \tag{A.22}$$

where $\sigma = 1502.645\,\mathrm{cm}^{-1}$ is the macroscopic absorption cross-section of Gd at 1.8 Å [150]. By combining Equations A.20,A.21 and A.22, the wavelength dependence of the visibility caused by the finite transmission through the grating lines is derived as:

$$\frac{V_{\mathrm{Gi}}(T(\lambda))}{V_{\mathrm{Gi}}(0)} = \frac{1}{V_{\mathrm{Gi}}(0)}\frac{a_1(T(\lambda))}{a_0(T(\lambda))} = \frac{DC_{\mathrm{i}}}{DC_{\mathrm{i}} + \left[\exp(h_{\mathrm{i}}\sigma\frac{\lambda}{1.8\,\text{Å}}) - 1\right]^{-1}}\,. \tag{A.23}$$

A.4. Magnetic field profiles of the ANTARES magnet

A brief characterization of the magnet used for most of the presented studies is given in Fig. A.2. Shown are profiles of the x-component of the field inside the magnet for different applied currents. By means of a Hall probe, the profiles were measured along the radial (a) and axial (b) cut through the center of the magnet (see inset in (a)). The sample position is marked by a dashed vertical line in each of the graphs.

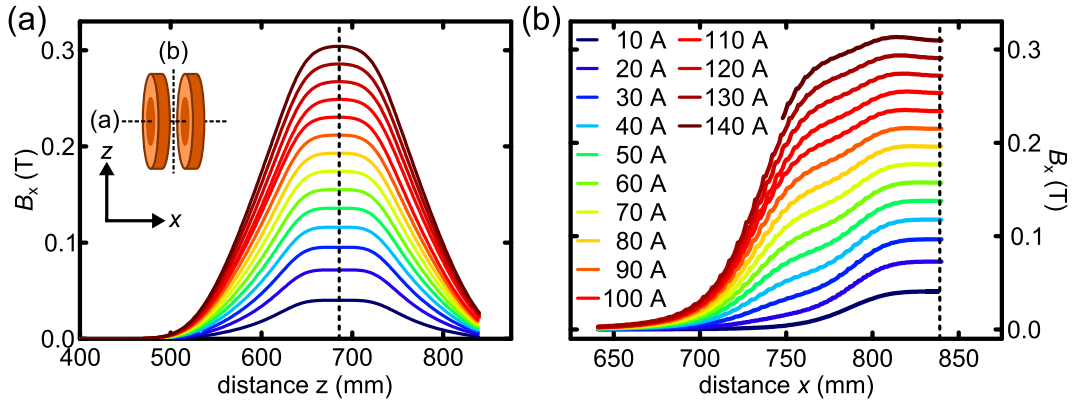

Figure A.2.: Characterization of the electromagnet used for most of the presented studies. Shown are radial (a) and axial (b) B_x profiles through the center of the magnet. The x-axis corresponds to the axial direction of the magnet.

The magnetic field profiles reveal a homogeneous region in the center of the magnet of at least 20 mm in length. For 100 mT, the inhomogeneity of the field amounts only 0.05 mT in this region. With increasing current, the region of constant field slightly shrinks, caused by deviations from the linear $M(B)$ characteristics of the iron yoke. However, even at a field of 300 mT the inhomogeneity amounts less than 1 mT. Unfortunately, the radial components of the magnetic field could not be quantitatively determined with the used Hall probe, since the axial component is distinctly larger and only a slight misalignment of the probe results in an exlusive measurement of this component. Nonetheless, up to 120 mT, no clear sign of a radial component has been detected at the sample position.

A.5. Scattering contrast in the TI and its crosstalk to the DFI

If the sample shows strong coherent scattering, the TI signal might not only be influenced by the neutron attenuation of the specimen but also by its scattering contributions. Positions in the sample where neutrons are scattered away, result in a reduced intensity at the detector, whereas additional intensity occurs in the

detector pixels where the neutrons are scattered to. In the case of the investigated vortex lattice, this implies that the TI locally shows where the angle enclosed by the incoming neutrons and the orientation of the vortex lattice fulfills the Bragg condition. Hence, neutrons that are locally scattered away from their original direction lead to a decrease of the intensity at the corresponding position on the detector (TI < 1) and an increase of the general background of diffuse scattering. Thereby, the TI contrast is complementary to integral scattering techniques such as SANS, as a localization of the scattering positions is possible.
For purely absorbing samples the TI shows contrasts smaller than unity. However, due to the discussed coherent scattering, the TI signal of the vortex lattice locally shows values larger than unity as shown in Fig. 6.8 (white lines). Referring to Eq. 4.12, the DFI remains smaller than unity as long as a_0^{f} is smaller than unity, which is the case if no coherent scattering is present in the sample. However, it is obvious that coherently scattered neutrons locally lead to a larger amplitude a_0^{f}. This larger value directly influences the calculated DFI signal as seen in Eq. 4.12. Under the assumption that the absorption of the sample is negligible, which holds in the presented case as the data are zero field normalized, as well as no USANS scattering in the sample is present ($a_1^{\mathrm{f}} = \text{const.}$) , the TI and the DFI signals are related by :

$$DFI(j,l)_{\mathrm{Crosstalk}} = \frac{a_1^{\mathrm{s}}(j,l)a_0^{\mathrm{f}}(j,l)}{a_0^{\mathrm{s}}(j,l)a_1^{\mathrm{f}}(j,l)} = \frac{1}{TI} \tag{A.24}$$

The crosstalk of the TI to the DFI can therefore be quantified as the inverted signal of the TI. An illustration of the crosstalk contrast mechanism is given in Fig. A.3.
In case of the nGI data as presented in Fig. 6.8, the crosstalk from the TI to the DFI can be better seen by taking horizontal line profiles through the individual TI and DFI images for each magnetic field. These line profiles show that the crosstalk can be directly compared as shown in Fig. A.4.

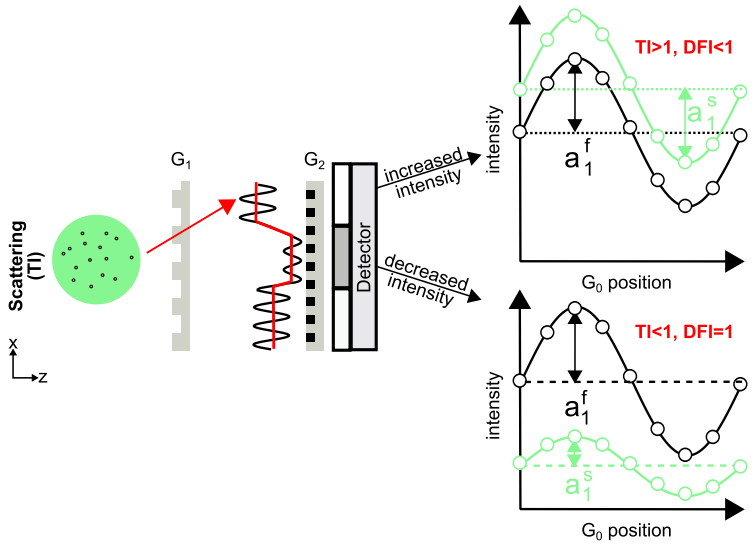

Figure A.3.: Illustration of the crosstalk of the DFI and the TI. If the sample reveals strong SANS scattering, neutrons are deflected in a different pixel when reaching the detector, which generates a scattering contrast in the TI. However, the additional neutron flux offsets the intensity oscillation in the corresponding detector pixel which leads to a DFI signal. In contrast, at the detector pixels where the intensity is reduced, the whole oscillation is degraded, which reduce the TI but leaves the DFI contrast unaltered.

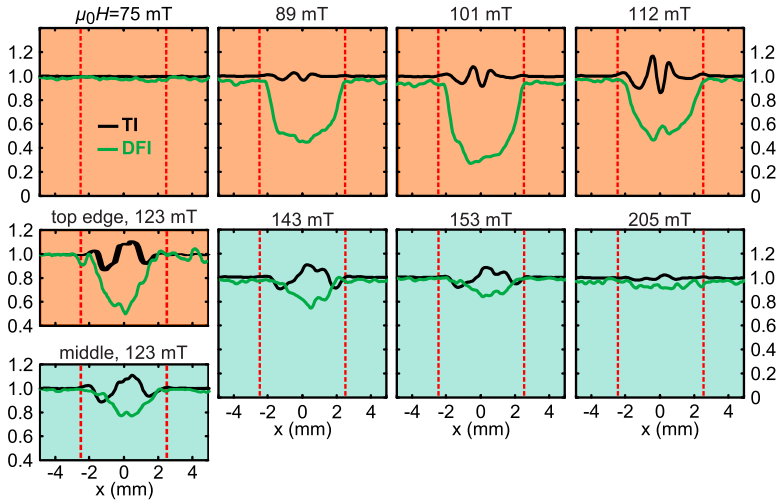

Figure A.4.: Profiles of the TI and DFI signals of the nGI data from Fig. 6.8. The TI (black) and DFI (gree) profiles were measured along a horizontal section in the center of the rod. The red dashed vertical lines indicate the boundary of the sample. Profiles measured along the top edge of the Nb rod are additionally shown for $123\,\mathrm{mT}$. They illustrate the delayed IMS to Shubnikov transition at the sample edge compared to the center of the sample.

A.6. Alignment of the vortex lattice for nGI

Experiments on superconductors require the precise knowledge how the magnetic field and, hence, the vortex lattice is aligned to the neutron beam. In small-angle scattering, this information is easily obtained by a rocking scan. A parallel field-to-beam configuration is reached at the middle of two opposite first order rocking peaks. However, in neutron radiography, the scattering pattern is hardly accessed, due to the low sample-to-detector distance.
In order to still allow an optimal orientation of the sample to the field, the used magnet has been constructed in a way that an asymmetrical operation of the two Helmholtz coils is possible. In this mode, the field at the sample position (and consequentially also the vortex lattice) is slightly spherically distorted as shown in the top view of Fig. A.5 (a). If the angle enclosed by the direction of the vortex lattice and the neutron beam fulfills Bragg's law, the neutrons will be scattered. As seen in Fig. A.5 (a), due to the spherical distortion, a peculiar scattering contrast at the detector develops which is characterized by a high intensity in the center where neutrons have been scattered to, surrounded by positions of lower intensity in which neutrons have been scattered away. As the vortex lattice has a hexagonal symmetry, this pattern repeats every 60°. Hence, at the detector, a six-fold star structure arises which is sketched in Fig. A.5 (b). The scattering vectors $\boldsymbol{k_1}$,$\boldsymbol{k_2}$ and $\boldsymbol{k_3}$ found in the hexagonal SANS pattern of the vortex lattice (see e.g. Fig. 6.5), are recovered as the scattering directions perpendicular to the low and high intensity streaks forming the star. They are drawn in Fig. A.5 (b), too.

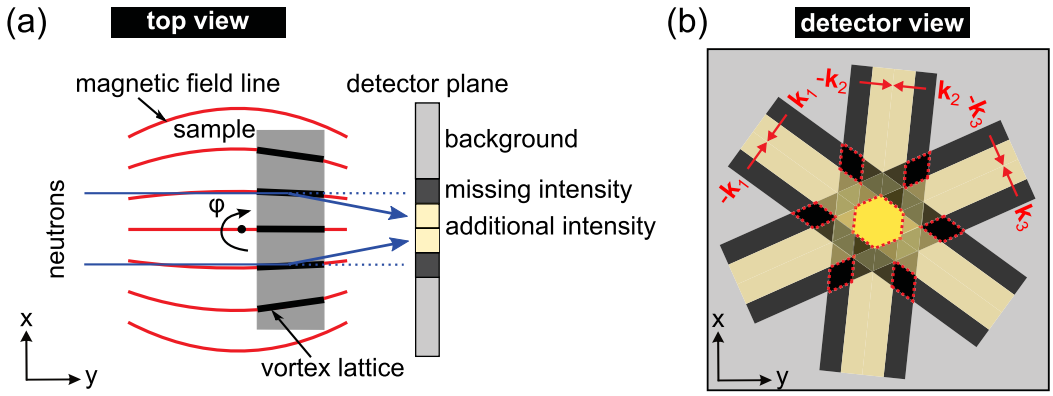

Figure A.5.: Vortex lattice orientation using an asymmetric magnetic field. (a) Top view of a sample in an asymmetric operated Helmholtz geometry. (b) View on the detector. A peculiar star-shaped transmission image arises due to the vortex lattice distortion Further explanation see text.

If the magnetic field and the sample are rotated by an angle ϕ around the vertical axis (rocking scan), the positions where the Bragg condition is fulfilled change

and hence the star moves along the sample. Fig. A.6 demonstrates this behavior on the example of the Nb wedge sample. The magnetic field is perfectly parallel to the neutron beam, if the center of the star coincides with the center of the sample. In the presented case, the sample was situated slightly below the middle position of the magnet. Furthermore, from the alignment of the star, one can perform a crystallographic fine orientation of the sample: As demonstrated in Fig. 6.14 (a), the scattering takes place along the $\langle 100 \rangle$ direction and hence, the nearly vertical streak must correspond to the perpendicular $\langle 110 \rangle$ direction. All Nb samples, probed by nGI were prealigned using this approach.

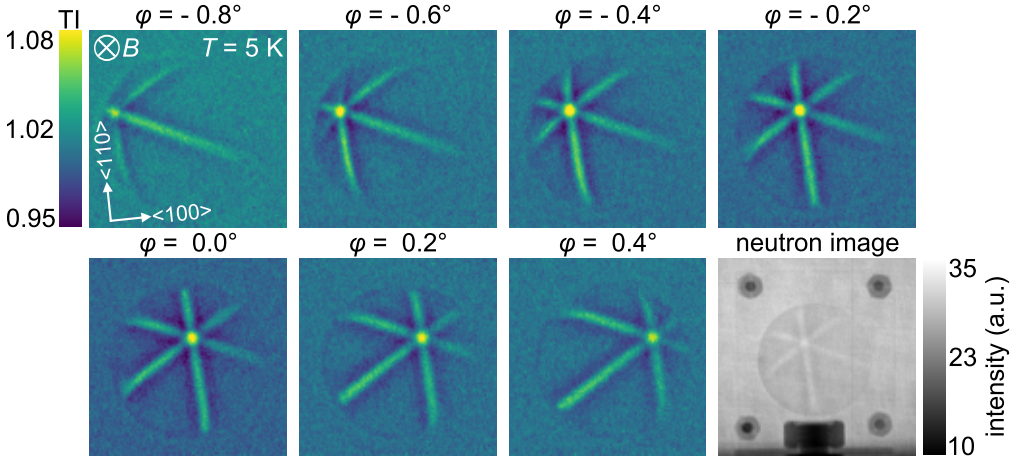

Figure A.6.: Sample alignment on the example the Nb wedge in a field of $140\,\mathrm{mT}$ and at a temperature of $5\,\mathrm{K}$. The data are open and dark image corrected. Additionally, a neutron radiography is shown.

A.7. Data substantiating the drawn conclusions

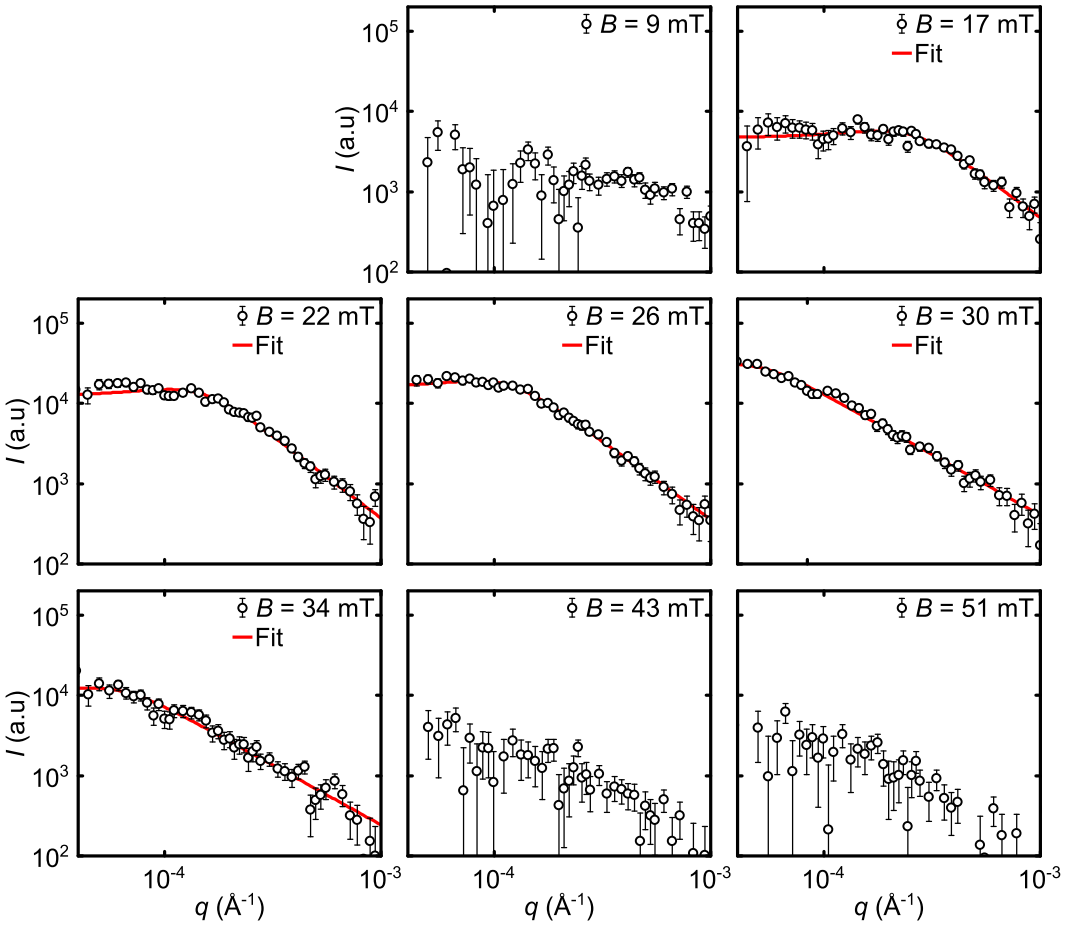

Figure A.7.: USANS scattering curves of the Nb 3 sample for different magnetic fields. The sample has been field cooled to $4\,\mathrm{K}$. B was applied along $\langle 110\rangle$, parallel to the neutron beam, while another crystallographic $\langle 110\rangle$-direction was rotated into the horizontal plane. The red curves are fits to Eq. 6.4.

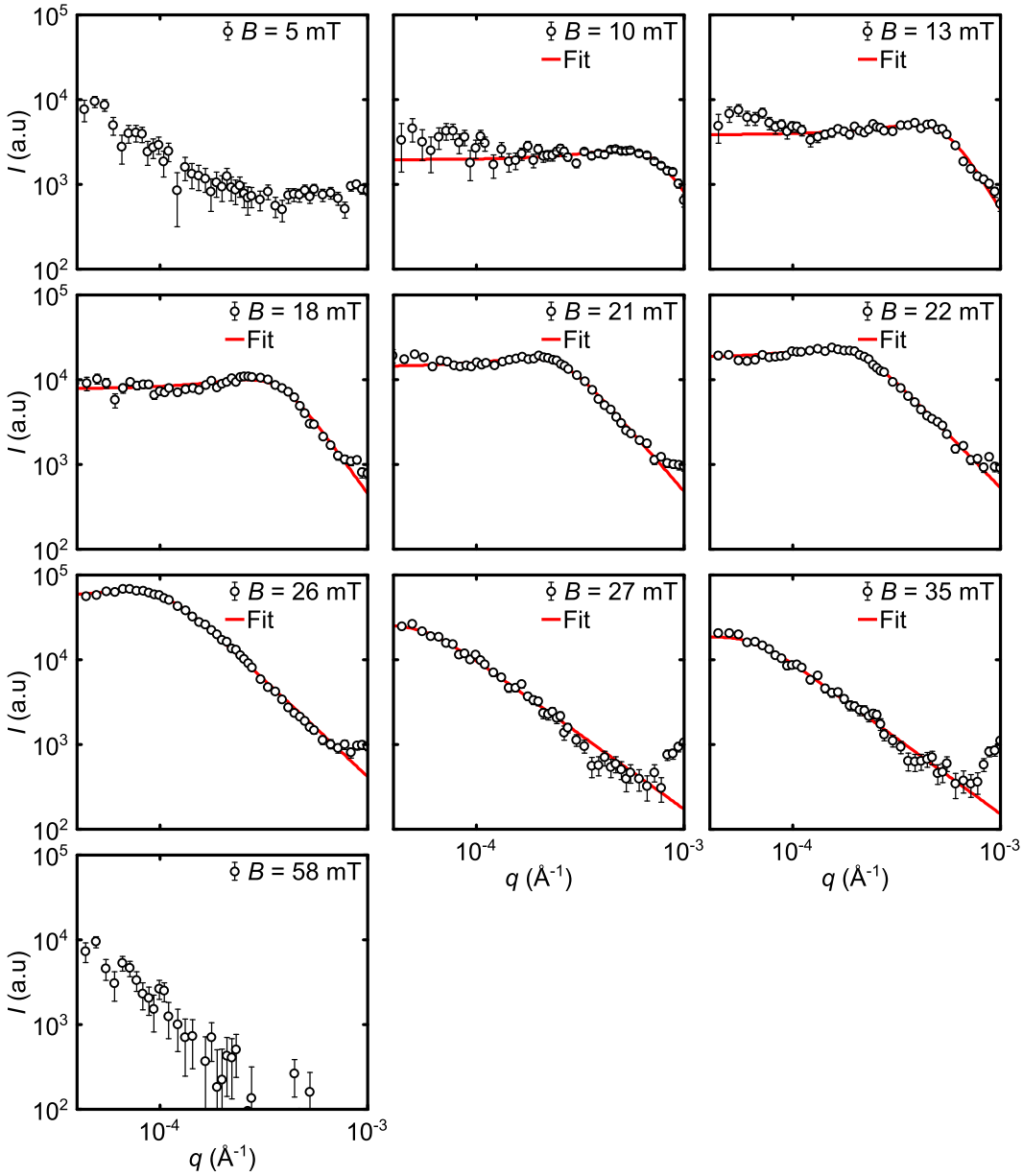

Figure A.8.: USANS scattering curves of the Nb wedge sample for different magnetic fields. The sample has been field cooled to $4\,\mathrm{K}$. B was applied along $\langle 110\rangle$, parallel to the neutron beam, while a crystallographic $\langle 100\rangle$-direction was rotated into the horizontal plane.The red curves are fits to Eq. 6.4. The increased intensity around $1 \times 10^{-3}\,\mathrm{\AA}^{-1}$ is attributed to the first order Bragg peak of the vortex lattice expected at $1.35 \times 10^{-3}\,\mathrm{\AA}^{-1}$.

Bibliography

[1] K Onnes. Furher experiments with liquid helium C. On the change of electric resistance of pure metals at very low temperatures etc. IV. The resistance of pure mercury at helium temperatures. *Leiden Comm*, 120b, 1911.

[2] F.M. Ašner. *High Field Superconducting Magnets*. Oxford science publications. Clarendon Press, 1999.

[3] S Aull, O Ebrahimi, N Karakas, J Knobloch, O Kugeler, and W Treimer. Suppressed Meissner-effect in Niobium: Visualized with polarized neutron radiography. *Journal of Physics: Conference Series*, 340(1):012001, 2012.

[4] M. Stemmle, F. Merschel, M. Noe, and A. Hobl. AmpaCity - Installation of advanced superconducting 10 kV system in city center replaces conventional 110 kv cables. In *Proceedings of 2013 IEEE International Conference on Applied Superconductivity and Electromagnetic Devices*, pages 323–326, 2013.

[5] H.S. Han and D.S. Kim. *Magnetic Levitation: Maglev Technology and Applications*. Springer Tracts on Transportation and Traffic. Springer Netherlands, 2016.

[6] W. Meissner and R. Ochsenfeld. Ein neuer Effekt bei Eintritt der Supraleitfähigkeit. *Naturwissenschaften*, 21(44):787–788, 1933.

[7] E H Brandt. The flux-line lattice in superconductors. *Reports on Progress in Physics*, 58(11):1465, 1995.

[8] G.W. Crabtree and D.R. Nelson. Vortex physics in high-temperature superconductors. 50(4):38–45, 1997.

[9] R Lortz and C Meingast. Vortex matter in high-temperature superconductors: a model system to study phenomena related to crystalline melting and fragile glass formation? *Journal of Non-Crystalline Solids*, 307-310:459 – 462, 2002.

[10] T. Giamarchi and P. Le Doussal. Elastic theory of flux lattices in the presence of weak disorder. *Phys. Rev. B*, 52:1242–1270, 1995.

[11] T. Klein, I. Joumard, S. Blanchard, J. Marcus, R. Cubitt, T. Giamarchi, and P. Le Doussal. A Bragg glass phase in the vortex lattice of a type II superconductor. *Nature*, 413(6854):404–406, 2001.

[12] U. Essmann. Observation of the mixed state. *Physica*, 55:83 – 93, 1971.

[13] E. H. Brandt and M. P. Das. Attractive Vortex Interaction and the Intermediate-Mixed State of Superconductors. *Journal of Superconductivity and Novel Magnetism*, 24(1):57–67, 2011.

[14] R. Radebaugh and P. H. Keesom. Low-Temperature Thermodynamic Properties of Vanadium. II. Mixed State. *Phys. Rev.*, 149:217–231, 1966.

[15] H. R. Kerchner, D. K. Christen, and S. T. Sekula. Equilibrium properties of the fluxoid lattice in single-crystal niobium. I. Magnetization measurements. *Phys. Rev. B*, 21:86–101, 1980.

[16] D. K. Christen, F. Tasset, S. Spooner, and H. A. Mook. Study of the intermediate mixed state of niobium by small-angle neutron scattering. *Phys. Rev. B*, 15:4506–4509, 1977.

[17] V. Moshchalkov, M. Menghini, T. Nishio, Q. H. Chen, A. V. Silhanek, V. H. Dao, L. F. Chibotaru, N. D. Zhigadlo, and J. Karpinski. Type-1.5 Superconductivity. *Phys. Rev. Lett.*, 102:117001, 2009.

[18] M. Seul and D. Andelman. Domain shapes and patterns: The phenomenology of modulated phases. *Science*, 267(5197):476–483, 1995.

[19] R. Prozorov. Equilibrium Topology of the Intermediate State in Type-I Superconductors of Different Shapes. *Phys. Rev. Lett.*, 98:257001, 2007.

[20] U. Essmann and H. Träuble. The direct observation of individual flux lines in type II superconductors. *Physics Letters A*, 24(10):526 – 527, 1967.

[21] K. Harada, T. Matsuda, J. Bonevich, M. Igarashi, S. Kondo, G. Pozzi, U. Kawabe, and A. Tonomura. Real-time observation of vortex lattices in a superconductor by electron microscopy. *Nature*, 360(6399):51–53, 1992.

[22] J.-Y. Ge, J. Gutierrez, A. Lyashchenko, V. Filipov, J. Li, and V. V. Moshchalkov. Direct visualization of vortex pattern transition in ZrB_{12} with Ginzburg-Landau parameter close to the dual point. *Phys. Rev. B*, 90: 184511, 2014.

[23] J. E. Bonevich, K. Harada, H. Kasai, T. Matsuda, T. Yoshida, and A. Tonomura. Direct measurement of single-vortex diameters by electron holography. *Phys. Rev. B*, 50:567–570, 1994.

[24] F.S. Wells, A. V. Pan, X. R. Wang, S. A. Fedoseev, and H. Hilgenkamp. Analysis of low-field isotropic vortex glass containing vortex groups in $YBa_2Cu_3O_{7-x}$ thin films visualized by scanning SQUID microscopy. *Scientific Reports*, 5:8677, 2015.

[25] P. J. Curran, W. M. Desoky, M. V. Milošević, A. Chaves, J.-B. Laloë, J. S. Moodera, and S. J. Bending. Spontaneous symmetry breaking in vortex systems with two repulsive lengthscales. *Scientific Reports*, 5:15569, 2015.

[26] P. E. Goa, H. Hauglin, Å. A. F. Olsen, M. Baziljevich, and T. H. Johansen. Magneto-optical imaging setup for single vortex observation. *Review of Scientific Instruments*, 74(1):141–146, 2003.

[27] H. Yang, B. Shen, Zh. Wang, L. Shan, C. Ren, and H.-H. Wen. Vortex images on $Ba_{1-x}K_xFe_2As_2$ observed directly by magnetic force microscopy. *Phys. Rev. B*, 85:014524, 2012.

[28] S. Mühlbauer, C. Pfleiderer, P. Böni, M. Laver, E. M. Forgan, D. Fort, U. Keiderling, and G. Behr. Morphology of the superconducting vortex lattice in ultrapure niobium. *Phys. Rev. Lett.*, 102:136408, Apr 2009.

[29] L. D. Landau. The intermediate state of supraconductors. *Nature*, 141:688, 1938.

[30] M R Eskildsen, E M Forgan, and H Kawano-Furukawa. Vortex structures, penetration depth and pairing in iron-based superconductors studied by small-angle neutron scattering. *Reports on Progress in Physics*, 74(12): 124504, 2011.

[31] M. Agamalian, G. D. Wignall, and R. Triolo. Optimization of a Bonse–Hart Ultra-Small-Angle Neutron Scattering Facility by Elimination of the Rocking-Curve Wings. *Journal of Applied Crystallography*, 30(3):345–352, 1997.

[32] G. Goerigk and Z. Varga. Comprehensive upgrade of the high-resolution small-angle neutron scattering instrument KWS-3 at FRM II. *Journal of Applied Crystallography*, 44(2):337–342, 2011.

[33] T. Reimann, S. Mühlbauer, M. Schulz, B. Betz, A. Kaestner, V. Pipich, P. Böni, and C. Grünzweig. Visualizing the morphology of vortex lattice domains in a bulk type-II superconductor. *Nat. Commun.*, 6:8813, 2015.

[34] J. Bardeen, L. N. Cooper, and J. R. Schrieffer. Theory of Superconductivity. *Phys. Rev.*, 108:1175–1204, 1957.

[35] V. L. Ginzburg and L. D. Landau. On the Theory of superconductivity. *Zh. Eksp. Teor. Fiz.*, 20:1064–1082, 1950.

[36] L. P. Gor'kov. Microscopic derivation of the Ginzburg-Landau equations in the theory of superconductivity. *Sov. Phys. JETP*, 9(36):1364, 1959.

[37] M. Tinkham. *Introduction to Superconductivity: Second Edition*. Dover Books on Physics. Dover Publications, 2004.

[38] R.P. Huebener. *Magnetic Flux Structures in Superconductors*. Springer Series in Solid-State Sciences. Springer Berlin Heidelberg, 2013.

[39] W. Buckel and R. Kleiner. *Supraleitung: Grundlagen und Anwendungen*. Lehrbuch Physik. Wiley, 2013.

[40] C.P. Poole, H.A. Farach, R.J. Creswick, and R. Prozorov. *Superconductivity*. Elsevier Science, 2010.

[41] F. London and H. London. The Electromagnetic Equations of the Supraconductor. *Proceedings of the Royal Society of London A: Mathematical, Physical and Engineering Sciences*, 149(866):71–88, 1935.

[42] K. Fossheim and A. Sudboe. *Superconductivity: Physics and Applications*. Wiley, 2005.

[43] L. V. Shubnikov, Khotkevich V. I., Shepelev Yu. D., and Ryabinin Yu. N. Magnetic properties of superconducting metals and alloys. *Ukr. J. Phys.*, 53 (Special issue), 2008. Translation and reprint of Zh. Eksper. Teor. Fiz. 7, 221-237 (1937).

[44] A. A. Abrikosov. On the magnetic properties of superconductors of the second group. *JETP*, 5(6):1174, 1957.

[45] E. H. Brandt. Microscopic theory of clean type-II superconductors in the entire field-temperature plane. *physica status solidi (b)*, 77(1):105–119, 1976.

[46] U. Klein. Microscopic calculations on the vortex state of type II superconductors. *Journal of Low Temperature Physics*, 69(1):1–37, 1987.

[47] T. Matsushita. *Flux Pinning in Superconductors*. Springer Series in Solid-State Sciences. Springer Berlin Heidelberg, 2014.

[48] E. H. Brandt. Elastic and plastic properties of the flux-line lattice in type-II superconductors. *Phys. Rev. B*, 34:6514–6517, 1986.

[49] J. Auer and H. Ullmaier. Magnetic Behavior of Type-II Superconductors with Small Ginzburg-Landau Parameters. *Phys. Rev. B*, 7:136–145, 1973.

[50] H.W. Weber, E. Seidl, M. Botlo, C. Laa, H.P. Wiesinger, and J. Rammer. Magnetization of low-κ superconductors II. The lower critical field H_{c1}. *Physica C: Superconductivity*, 161(3):287 – 293, 1989.

[51] J. Bardeen and M. J. Stephen. Theory of the Motion of Vortices in Superconductors. *Phys. Rev.*, 140:A1197–A1207, 1965.

[52] G. Antesberger and H. Ullmaier. Pinning of vortices in superconducting NbTa alloys due to normal conducting precipitates. *Philosophical Magazine*, 29(5):1101–1124, 1974.

[53] D. D. Morrison and R. M. Rose. Controlled Pinning in Superconducting Foils by Surface Microgrooves. *Phys. Rev. Lett.*, 25:356–359, 1970.

[54] A.M. Campbell and J.E. Evetts. Flux vortices and transport currents in type II superconductors. *Advances in Physics*, 21(90):199–428, 1972.

[55] P. W. Anderson. Theory of Flux Creep in Hard Superconductors. *Phys. Rev. Lett.*, 9:309–311, 1962.

[56] C. P. Bean. Magnetization of Hard Superconductors. *Phys. Rev. Lett.*, 8: 250–253, 1962.

[57] D. J. Thompson, M. S. M. Minhaj, L. E. Wenger, and J. T. Chen. Observation of Paramagnetic Meissner Effect in Niobium Disks. *Phys. Rev. Lett.*, 75: 529–532, 1995.

[58] A. I. Larkin and Yu. N. Ovchinnikov. Pinning in type II superconductors. *Journal of Low Temperature Physics*, 34(3):409–428, 1979.

[59] L. R. E. Cabral, C. C. de Souza Silva, E. H. Brandt, and J. Albino Aguiar. Magnetization curves and geometric barrier in BSCCO-2212. *Physica C: Superconductivity*, 369(1-4):196–199, 2002.

[60] E. H. Brandt, M. V. Indenbom, and A. Forkl. Type-II Superconducting Strip in Perpendicular Magnetic Field. *EPL (Europhysics Letters)*, 22(9): 735, 1993.

[61] R.B. Flippen, T.R. Askew, J.A. Fendrich, and C.J. van der Beek. Surface flux pinning in $YBa_2Cu_3O_{7-\delta}$. *Phys. Rev. B*, 52:R9882–R9885, 1995.

[62] L.M. Fisher, I.F. Voloshin, V.S. Gorbachev, S.E. Savelev, and V.A. Yampolskii. Nonlocal critical state model for hard superconductors. *Physica C: Superconductivity*, 245(3-4):231–237, 1995.

[63] E. Zeldov, A. I. Larkin, V. B. Geshkenbein, M. Konczykowski, D. Majer, B. Khaykovich, V. M. Vinokur, and H. Shtrikman. Geometrical Barriers in High-Temperature Superconductors. *Phys. Rev. Lett.*, 73:1428–1431, 1994.

[64] M.V. Indenbom, H. Kronmüller, T.W. Li, P.H. Kes, and A.A. Menovsky. Equilibrium magnetic properties and Meissner expulsion of magnetic flux in $Bi_2Sr_2CaCu_2O_x$ single crystals. *Physica C: Superconductivity*, 222(3):203 – 211, 1994.

[65] C. P. Bean and J. D. Livingston. Surface Barrier in Type-II Superconductors. *Phys. Rev. Lett.*, 12:14–16, 1964.

[66] R. Prozorov, R. W. Giannetta, A. A. Polyanskii, and G. K. Perkins. Topological hysteresis in the intermediate state of type-I superconductors. *Phys. Rev. B*, 72:212508, 2005.

[67] M. Benkraouda and J. R. Clem. Magnetic hysteresis from the geometrical barrier in type-II superconducting strips. *Phys. Rev. B*, 53:5716–5726, 1996.

[68] E. H. Brandt. Geometric edge barrier in the Shubnikov phase of type-II superconductors. *Low Temperature Physics*, 27(9):723–731, 2001.

[69] E. H. Brandt. Superconductor disks and cylinders in an axial magnetic field. I. Flux penetration and magnetization curves. *Phys. Rev. B*, 58:6506–6522, 1998.

[70] E. A. Matute. On the superconducting sphere in an external magnetic field. *American Journal of Physics*, 67(9):786–788, 1999.

[71] A. Aharoni, L. Pust, and M. Kief. Comparing theoretical demagnetizing factors with the observed saturation process in rectangular shields. *Journal of Applied Physics*, 87(9):6564–6566, 2000.

[72] D. X. Chen, J. A. Brug, and R. B. Goldfarb. Demagnetizing factors for cylinders. *IEEE Transactions on Magnetics*, 27(4):3601–3619, 1991.

[73] J. A. Osborn. Demagnetizing Factors of the General Ellipsoid. *Phys. Rev.*, 67:351–357, 1945.

[74] L. D. Landau. *Zh. Eksp. Teor. Fiz.*, 7:371, 1937.

[75] R. N. Goren and M. Tinkham. Patterns of magnetic flux penetration in superconducting films. *Journal of Low Temperature Physics*, 5(4):465–494, 1971.

[76] J.B. Sykes, D. Haar, and L.P. Pitaevskii. *Perspectives in Theoretical Physics: The Collected Papers of E. M. Lifshitz.* Elsevier Science, 2012.

[77] A. Hubert. Zur Theorie der zweiphasigen Domänenstrukturen in Supraleitern und Ferromagneten. *physica status solidi (b)*, 24(2):669–682, 1967.

[78] H. Träuble and U. Essmann. Der direkte Nachweis von Flußlinienbewegungen in stromdurchflossenen Supraleitern. *physica status solidi (b)*, 25(1):395–402, 1968.

[79] J. R. Hoberg and R. Prozorov. Current-driven transformations of the intermediate-state patterns in type-I superconductors. *Phys. Rev. B*, 78: 104511, 2008.

[80] J. R. Clem, R. Prozorov, and R. J. Wijngaarden. Equilibrium intermediate-state patterns in a type-I superconducting slab in an arbitrarily oriented applied magnetic field. *Phys. Rev. B*, 88:104504, 2013.

[81] X. B. Xu, H. Fangohr, S. Y. Ding, F. Zhou, X. N. Xu, Z. H. Wang, M. Gu, D. Q. Shi, and S. X. Dou. Phase diagram of vortex matter of type-II superconductors. *Phys. Rev. B*, 83:014501, 2011.

[82] R. Choksi, V. R. Kohn, and F. Otto. Energy Minimization and Flux Domain Structurein the Intermediate State of a Type-I Superconductor. *Journal of Nonlinear Science*, 14(2):119–171, 2004.

[83] U. Krägeloh. Der Zwischenzustand bei Supraleitern zweiter Art. *physica status solidi (b)*, 42(2):559–576, 1970.

[84] J. R. Clem. Intermediate mixed state in Nb. private communication, 2013.

[85] B. Mutaftschiev. *The Atomistic Nature of Crystal Growth*. Springer Series in Materials Science. Springer Berlin Heidelberg, 2013.

[86] J. A. Drocco, C. J. Olson Reichhardt, C. Reichhardt, and A. R. Bishop. Static and dynamic phases for magnetic vortex matter with attractive and repulsive interactions. *Journal of Physics: Condensed Matter*, 25(34):345703, 2013.

[87] C. Reichhardt, J. Drocco, C.J. Olson Reichhardt, and A.R. Bishop. The effect of pinning on vortex states with attractive and repulsive interactions. *Physica C: Superconductivity*, 479:15 – 18, 2012. Proceedings of VORTEX VII Conference.

[88] H. J. Zhao, V. R. Misko, and F. M. Peeters. Dynamics of self-organized driven particles with competing range interaction. *Phys. Rev. E*, 88:022914, 2013.

[89] X. B. Xu, H. Fangohr, Z. H. Wang, M. Gu, S. L. Liu, D. Q. Shi, and S. X. Dou. Vortex dynamics for low-κ type-II superconductors. *Phys. Rev. B*, 84: 014515, 2011.

[90] H J Zhao, V R Misko, and F M Peeters. Analysis of pattern formation in systems with competing range interactions. *New Journal of Physics*, 14(6): 063032, 2012.

[91] C.J. Olson Reichhardt, C. Reichhardt, I. Martin, and A.R. Bishop. Dynamics and melting of stripes, crystals, and bubbles with quenched disorder. *Physica D: Nonlinear Phenomena*, 193(1-4):303–309, 2004.

[92] A. Hubert and R. Schäfer. *Magnetic Domains: The Analysis of Magnetic Microstructures*. Springer Berlin Heidelberg, 2014.

[93] S. Mühlbauer, B. Binz, F. Jonietz, C. Pfleiderer, A. Rosch, A. Neubauer, R. Georgii, and P. Böni. Skyrmion Lattice in a Chiral Magnet. *Science*, 323 (5916):915–919, 2009.

[94] W. Münzer, A. Neubauer, T. Adams, S. Mühlbauer, C. Franz, F. Jonietz, R. Georgii, P. Böni, B. Pedersen, M. Schmidt, A. Rosch, and C. Pfleiderer. Skyrmion lattice in the doped semiconductor $Fe_{1-x}Co_xSi$. *Phys. Rev. B*, 81: 041203, 2010.

[95] T. Adams, A. Chacon, M. Wagner, A. Bauer, G. Brandl, B. Pedersen, H. Berger, P. Lemmens, and C. Pfleiderer. Long-Wavelength Helimagnetic Order and Skyrmion Lattice Phase in Cu_2OSeO_3. *Phys. Rev. Lett.*, 108: 237204, 2012.

[96] X. Z. Yu, Y. Tokunaga, Y. Kaneko, W. Z. Zhang, K. Kimoto, Y. Matsui, Y. Taguchi, and Y. Tokura. Biskyrmion states and their current-driven motion in a layered manganite. *Nat Commun*, 5:–, 2014.

[97] S. Heinze, K. von Bergmann, M. Menzel, J. Brede, A. Kubetzka, R. Wiesendanger, G. Bihlmayer, and S. Blugel. Spontaneous atomic-scale magnetic skyrmion lattice in two dimensions. *Nat Phys*, 7(9):713–718, 2011.

[98] S. Mühlbauer. *Vortex Lattices in Superconducting Niobium and Skyrmion Lattices in Chiral MnSi: An Investigation by Neutron Scattering*. PhD thesis, Technische Universität München, 2009.

[99] A. Bauer. *Investigation of itinerant antiferromagnets and cubic chiral helimagnets*. PhD thesis, Technische Universität München, 2014.

[100] N. Romming, C. Hanneken, M. Menzel, J. E. Bickel, B. Wolter, K. von Bergmann, A. Kubetzka, and R. Wiesendanger. Writing and Deleting Single Magnetic Skyrmions. *Science*, 341(6146):636–639, 2013.

[101] A. Bauer and C. Pfleiderer. *Generic Aspects of Skyrmion Lattices in Chiral Magnets*, pages 1–28. Springer International Publishing, Cham, 2016.

[102] A. Bogdanov and A. Hubert. Thermodynamically stable magnetic vortex states in magnetic crystals. *Journal of Magnetism and Magnetic Materials*, 138(3):255–269, 1994.

[103] A. Furrer and J.S. Mesot, Thierry. *Neutron Scattering in Condensed Matter Physics*. World Scientific Press, April 2009.

[104] H. Rauch and S.A. Werner. *Neutron Interferometry: Lessons in Experimental Quantum Mechanics, Wave-particle Duality, and Entanglement*. Oxford University Press, 2015.

[105] H. Friedrich. *Scattering Theory*. Lecture Notes in Physics. Springer Berlin Heidelberg, 2013.

[106] D.S. Sivia. *Elementary Scattering Theory: For X-ray and Neutron Users*. OUP Oxford, 2011.

[107] B. Hammouda. Probing nanoscale structures - The SANS Toolbox. URL `https://www.ncnr.nist.gov/staff/hammouda/the_SANS_toolbox.pdf`.

[108] R. Andersson, L. F. van Heijkamp, I. M. de Schepper, and W. G. Bouwman. Analysis of spin-echo small-angle neutron scattering measurements. *Journal of Applied Crystallography*, 41(5):868–885, 2008.

[109] L.A. Feigin and D.I. Svergun. *Structure Analysis by Small-Angle X-Ray and Neutron Scattering*. Springer US, 2013.

[110] T. Krouglov, I. M. de Schepper, W. G. Bouwman, and M. T. Rekveldt. Real-space interpretation of spin-echo small-angle neutron scattering. *Journal of Applied Crystallography*, 36(1):117–124, 2003.

[111] G. Porod. Die Röntgenkleinwinkelstreuung von dichtgepackten kolloiden Systemen. *Kolloid-Zeitschrift*, 124(2):83–114, 1951.

[112] J. Šaroun. Evaluation of double-crystal SANS data influenced by multiple scattering. *Journal of Applied Crystallography*, 33(3 Part 1):824–828, 2000.

[113] M. R. Eskildsen. *Small Angle Neutron Scattering Studies of the Flux Line Lattice in the Borocarbide Superconductors*. PhD thesis, Risø National Laboratory, 1998.

[114] A. Furrer. *Neutron Scattering in Layered Copper-Oxide Superconductors*. Physics and Chemistry of Materials with Low-Dimensional Structures. Springer Netherlands, 2012.

[115] N. Kardjilov, I. Manke, A. Hilger, M. Strobl, and J. Banhart. Neutron imaging in materials science. *Materials Today*, 14(6):248 – 256, 2011.

[116] D. Mannes, E. Lehmann, A. Masalles, K. Schmidt-Ott, A. v Przychowski, K. Schaeppi, F. Schmid, S. Peetermans, and K. Hunger. The study of cultural heritage relevant objects by means of neutron imaging techniques.

Insight - Non-Destructive Testing and Condition Monitoring, 56(3):137–141, 2014.

[117] K.-U. Hess, A. Flaws, M.J. Mühlbauer, B. Schillinger, A. Franz, M. Schulz, E. Calzada, D.B. Dingwell, and K. Bente. Advances in high-resolution neutron computed tomography: Adapted to the earth sciences. *Geosphere*, 7(6):1294–1302, 2011.

[118] C. Grünzweig. Visualization of a Fired Two-Stroke Chain Saw Engine Running at Idle Speed by Dynamic Neutron Radiography. *SAE Technical Paper*, (2010-32-0013), 2010.

[119] I.S. Anderson, R. McGreevy, and H.Z. Bilheux. *Neutron Imaging and Applications: A Reference for the Imaging Community*. Neutron Scattering Applications and Techniques. Springer, 2009.

[120] C. Grünzweig, G. Frei, E. Lehmann, G. Kühne, and C. David. Highly absorbing gadolinium test device to characterize the performance of neutron imaging detector systems. *Review of Scientific Instruments*, 78(5):053708, 2007.

[121] C. Grünzweig. *Neutron Grating Interferometry for Imaging Magnetic Structures in Bulk Ferromagnetic Materials*. PhD thesis, ETH Zürich, 2009.

[122] C. Grünzweig, F. Pfeiffer, O. Bunk, T. Donath, G. Kühne, G. Frei, M. Dierolf, and C. David. Design, fabrication, and characterization of diffraction gratings for neutron phase contrast imaging. *Review of Scientific Instruments*, 79(5): 053703, 2008.

[123] E. Lau. *Ann. Phys.*, 6:417, 1948.

[124] M. Chabior. *Contributions to the characterization of grating-based x-ray phase-contrast imaging*. PhD thesis, Technische Universität Dresden, 2011.

[125] A. Hipp, M. Willner, J. Herzen, S. Auweter, M. Chabior, J. Meiser, K. Achterhold, J. Mohr, and F. Pfeiffer. Energy-resolved visibility analysis of grating interferometers operated at polychromatic X-ray sources. *Opt. Express*, 22 (25):30394–30409, 2014.

[126] F. Pfeiffer, C. Grünzweig, O. Bunk, G. Frei, E. Lehmann, and C. David. Neutron Phase Imaging and Tomography. *Phys. Rev. Lett.*, 96:215505, 2006.

[127] H. Li, B. Schillinger, E. Calzada, L. Yinong, and M. Muehlbauer. An adaptive algorithm for gamma spots removal in CCD-based neutron radiography and tomography. *Nuclear Instruments and Methods in Physics Research Section A: Accelerators, Spectrometers, Detectors and Associated Equipment*, 564(1): 405 – 413, 2006.

[128] M. Chabior, T. Donath, C. David, M. Schuster, C. Schroer, and F. Pfeiffer. Signal-to-noise ratio in x ray dark-field imaging using a grating interferometer. *Journal of Applied Physics*, 110(5):053105, 2011.

[129] S. Marathe, L. Assoufid, X. Xiao, K. Ham, W. W. Johnson, and L. G. Butler. Improved algorithm for processing grating-based phase contrast interferometry image sets. *Review of Scientific Instruments*, 85(1):013704, 2014.

[130] M. Born, E. Wolf, A.B. Bhatia, D. Gabor, A.R. Stokes, A.M. Taylor, P.A. Wayman, and W.L. Wilcock. *Principles of Optics: Electromagnetic Theory of Propagation, Interference and Diffraction of Light*. Cambridge University Press, 2000.

[131] C. Grünzweig, J. Kopecek, B. Betz, A. Kaestner, K. Jefimovs, J. Kohlbrecher, U. Gasser, O. Bunk, C. David, E. Lehmann, T. Donath, and F. Pfeiffer. Quantification of the neutron dark-field imaging signal in grating interferometry. *Phys. Rev. B*, 88:125104, 2013.

[132] C. Grünzweig, C. David, O. Bunk, M. Dierolf, G. Frei, G. Kühne, J. Kohlbrecher, R. Schäfer, P. Lejcek, H. M. R. Rønnow, and F. Pfeiffer. Neutron Decoherence Imaging for Visualizing Bulk Magnetic Domain Structures. *Phys. Rev. Lett.*, 101:025504, 2008.

[133] R. Gähler, R. Golub, and T. Keller. Neutron resonance spin echo - a new tool for high resolution spectroscopy. *Physica B: Condensed Matter*, 180:899 – 902, 1992.

[134] S. K. Lynch, V. Pai, J. Auxier, A. F. Stein, E. E. Bennett, C. K. Kemble, X. Xiao, W.-K. Lee, N. Y. Morgan, and H. H. Wen. Interpretation of dark-field contrast and particle-size selectivity in grating interferometers. *Applied optics*, 50(22):4310–4319, 2011.

[135] W. Yashiro, Y. Terui, K. Kawabata, and A. Momose. On the origin of visibility contrast in x-ray Talbot interferometry. *Opt. Express*, 18(16): 16890–16901, 2010.

[136] M. Strobl. General solution for quantitative dark-field contrast imaging with grating interferometers. *Sci. Rep.*, 4:7243, 2014.

[137] T. Donath, M. Chabior, F. Pfeiffer, O. Bunk, E. Reznikova, J. Mohr, E. Hempel, S. Popescu, M. Hoheisel, M. Schuster, J. Baumann, and C. David. Inverse geometry for grating-based x-ray phase-contrast imaging. *Journal of Applied Physics*, 106(5):054703, 2009.

[138] S. W. Lee, D. S. Hussey, D. J. Jacobson, C. M. Sim, and M. Arif. Development of the grating phase neutron interferometer at a monochromatic beam line. *Nuclear Instruments and Methods in Physics Research Section A: Accelerators, Spectrometers, Detectors and Associated Equipment*, 605(1-2), 2009. ITMNR 08 Proceedings of the sixth Topical Meeting on Neutron Radiography.

[139] A. Hilger, N. Kardjilov, T. Kandemir, I. Manke, J. Banhart, D. Penumadu, A. Manescu, and M. Strobl. Revealing microstructural inhomogeneities with dark-field neutron imaging. *Journal of Applied Physics*, 107(3):036101, 2010.

[140] J. Kim, S. W. Lee, and G. Cho. Visibility evaluation of a neutron grating interferometer operated with a polychromatic thermal neutron beam. *Nuclear Instruments and Methods in Physics Research Section A: Accelerators, Spectrometers, Detectors and Associated Equipment*, 746:26 – 32, 2014.

[141] J. Schelten and W. Schmatz. Multiple-scattering treatment for small-angle scattering problems. *Journal of Applied Crystallography*, 13(4):385–390, 1980.

[142] F. Mezei, C. Pappas, and T. Gutberlet. *Neutron Spin Echo Spectroscopy: Basics, Trends and Applications*. Lecture Notes in Physics. Springer Berlin Heidelberg, 2008.

[143] M. Strobl, C. Grünzweig, A. Hilger, I. Manke, N. Kardjilov, C. David, and F. Pfeiffer. Neutron Dark-Field Tomography. *Phys. Rev. Lett.*, 101:123902, 2008.

[144] T. H. Jensen, M. Bech, I. Zanette, T. Weitkamp, C. David, H. Deyhle, S. Rutishauser, E. Reznikova, J. Mohr, R. Feidenhans'l, and F. Pfeiffer. Directional x-ray dark-field imaging of strongly ordered systems. *Phys. Rev. B*, 82:214103, 2010.

[145] V. Revol, C. Kottler, R. Kaufmann, A. Neels, and A. Dommann. Orientation-selective X-ray dark field imaging of ordered systems. *Journal of Applied Physics*, 112(11):114903, 2012.

[146] W. Yashiro, S. Harasse, K. Kawabata, H. Kuwabara, T. Yamazaki, and A. Momose. Distribution of unresolvable anisotropic microstructures revealed in visibility-contrast images using x-ray Talbot interferometry. *Phys. Rev. B*, 84:094106, 2011.

[147] T. Reimann, S. Mühlbauer, M. Horisberger, B. Betz, P. Böni, and M. Schulz. The new neutron grating interferometer at the ANTARES beamline - Design, Principle, and Applications -. *Journal of Applied Crystallography*, 49, 2016. in press.

[148] B. Betz, R. P. Harti, M. Strobl, J. Hovind, A. Kaestner, E. Lehmann, H. Van Swygenhoven, and C. Grünzweig. Quantification of the sensitivity range in neutron dark-field imaging. *Review of Scientific Instruments*, 86 (12):123704, 2015.

[149] M. Strobl, B. Betz, R. P. Harti, A. Hilger, N. Kardjilov, I. Manke, and C. Gruenzweig. Wavelength-dispersive dark-field contrast: micrometre structure resolution in neutron imaging with gratings. *Journal of Applied Crystallography*, 49(2):569–573, 2016.

[150] V. F. Sears. Neutron scattering lengths and cross sections. *Neutron News*, 3 (3):26–37, 1992.

[151] M. Chabior, M. Schuster, M. Goldammer, C. Schroer, and F. Pfeiffer. Influence of the grating profiles on the image quality in grating-based x-ray imaging. *Nuclear Instruments and Methods in Physics Research Section A: Accelerators, Spectrometers, Detectors and Associated Equipment*, 683:71 – 77, 2012.

[152] F. Pfeiffer, O. Bunk, C. Schulze-Briese, A. Diaz, T. Weitkamp, C. David, J. F. van der Veen, I. Vartanyants, and I. K. Robinson. Shearing Interferometer for Quantifying the Coherence of Hard X-Ray Beams. *Phys. Rev. Lett.*, 94: 164801, 2005.

[153] U. Bonse and M. Hart. TAILLESS X-RAY SINGLE-CRYSTAL REFLECTION CURVES OBTAINED BY MULTIPLE REFLECTION. *Applied Physics Letters*, 7(9):238–240, 1965.

[154] W.H. Zachariasen. *Theory of X-Ray Diffraction in Crystals*. Dover phoenix editions. Dover Publications, 2004.

[155] T. Takahashi and M. Hashimoto. Neutron rocking curves in non-absorbing crystals. *Physics Letters A*, 200(1):73 – 75, 1995.

[156] P. P. Ewald. Zur Begründung der Kristalloptik. *Annalen der Physik*, 359 (24):557–597, 1917.

[157] J. G. Barker, C. J. Glinka, J. J. Moyer, M. H. Kim, A. R. Drews, and M. Agamalian. Design and performance of a thermal-neutron double-crystal diffractometer for USANS at NIST. *Journal of Applied Crystallography*, 38 (6):1004–1011, 2005.

[158] S. R. Kline. Reduction and analysis of SANS and USANS data using IGOR Pro. *Journal of Applied Crystallography*, 39(6):895–900, 2006.

[159] T. Imae, T. Kanaya, M. Furusaka, and N. Torikai. *Neutrons in Soft Matter*. Wiley, 2011.

[160] E. Calzada, F. Gruenauer, M. Mühlbauer, B. Schillinger, and M. Schulz. New design for the ANTARES-II facility for neutron imaging at FRM II. *Nuclear Instruments and Methods in Physics Research Section A: Accelerators, Spectrometers, Detectors and Associated Equipment*, 605(1-2):50 – 53, 2009. ITMNR 08 Proceedings of the sixth Topical Meeting on Neutron Radiography.

[161] A. S. Tremsin, E. H. Lehmann, J. B. McPhate, J. V. Vallerga, O. H. W. Siegmund, B. White, P. White, W. B. Feller, F. C. de Beer, and W. Kockelmann. Quantification of Cement Hydration through Neutron Radiography with Scatter Rejection. *IEEE Transactions on Nuclear Science*, 62(3):1288–1294, 2015.

[162] Micromotive. Micromotive mikrotechnik: www.micromotive.de, 2016.

[163] H. Friedrich, V. Wagner, and P. Wille. A high-performance neutron velocity selector. *Physica B: Condensed Matter*, 156:547 – 549, 1989.

[164] NIST. Neutron scattering lengths and cross sections: https://www.ncnr.nist.gov/resources/n-lengths/, 2016.

[165] A.P. Kaestner, S. Hartmann, G. Kühne, G. Frei, C. Grünzweig, L. Josic, F. Schmid, and E.H. Lehmann. The ICON beamline - A facility for cold neutron imaging at SINQ. *Nuclear Instruments and Methods in Physics Research Section A: Accelerators, Spectrometers, Detectors and Associated Equipment*, 659(1):387 – 393, 2011.

[166] R. Gilles, A. Ostermann, and W. Petry. Monte Carlo simulations of the new small-angle neutron scattering instrument SANS-1 at the Heinz Maier-Leibnitz Forschungsneutronenquelle. *Journal of Applied Crystallography*, 40 (s1):s428–s432, 2007.

[167] S. Désert, V. Thévenot, J. Oberdisse, and A. Brûlet. The new very-small-angle neutron scattering spectrometer at Laboratoire Léon Brillouin. *Journal of Applied Crystallography*, 40(s1):s471–s473, 2007.

[168] A. Heinemann and S. Mühlbauer. SANS-1: Small angle neutron scattering. *Journal of large-scale research facilities*, 2015.

[169] C. Dewhurst. Grasp.

[170] S. Seidlmayer, J. Hattendorff, I. Buchberger, L. Karge, H. A. Gasteiger, and R. Gilles. In Operando Small-Angle Neutron Scattering (SANS) on Li-Ion Batteries. *Journal of The Electrochemical Society*, 162(2):A3116–A3125, 2015.

[171] V. Pipich and Z. Fu. KWS-3: Very small angle scattering diffractometer with focusing mirror. *Journal of large-scale research facilities*, 2015.

[172] T. Reimann, M. Schulz, C. Grünzweig, A. Kaestner, A. Bauer, P. Böni, and S. Mühlbauer. Neutron dark-field imaging of the domain distribution in the intermediate state of lead. *Journal of Low Temperature Physics*, 182(3-4): 107–116, 2016. ISSN 0022-2291.

[173] J. D. Livingston and W DeSorbo. *Superconductivity*, volume 2. Marcel Dekker, 1969.

[174] D. R. Lide, editor. *CRC Handbook of Chemistry and Physics*. CRC Press, 74 edition, 1993.

[175] L. Kramer. Thermodynamic Behavior of Type-II Superconductors with Small κ near the Lower Critical Field. *Phys. Rev. B*, 3:3821–3825, 1971.

[176] D. R. Aston, L. W. Dubeck, and F. Rothwarf. "Intermediate Mixed" State of Type-II Superconductors. *Phys. Rev. B*, 3:2231–2236, 1971.

[177] C.P. Herring. The interphase surface energy of superconducting niobium. *Physics Letters A*, 47(2):103 – 104, 1974.

[178] D. K. Christen, H. R. Kerchner, S. T. Sekula, and P. Thorel. Equilibrium properties of the fluxoid lattice in single-crystal niobium. II. Small-angle neutron-diffraction measurements. *Phys. Rev. B*, 21:102–117, 1980.

[179] M. Laver, C. J. Bowell, E. M. Forgan, A. B. Abrahamsen, D. Fort, C. D. Dewhurst, S. Mühlbauer, D. K. Christen, J. Kohlbrecher, R. Cubitt, and S. Ramos. Structure and degeneracy of vortex lattice domains in pure superconducting niobium: A small-angle neutron scattering study. *Phys. Rev. B*, 79:014518, 2009.

[180] M. Benkraouda and J. R. Clem. Critical current from surface barriers in type-II superconducting strips. *Phys. Rev. B*, 58:15103–15107, 1998.

[181] E. H. Brandt. Geometric barrier and current string in type-II superconductors obtained from continuum electrodynamics. *Phys. Rev. B*, 59:3369–3372, 1999.

[182] A. Pautrat and A. Brûlet. Temperature dependence of clusters with attracting vortices in superconducting niobium studied by neutron scattering. *Journal of Physics: Condensed Matter*, 26(23):232201, 2014.

[183] URL `http://www.mateck.de/`.

[184] A. Aharoni. Demagnetizing factors for rectangular ferromagnetic prisms. *Journal of Applied Physics*, 83(6):3432–3434, 1998.

[185] D. K. Finnemore, T. F. Stromberg, and C. A. Swenson. Superconducting Properties of High-Purity Niobium. *Phys. Rev.*, 149:231–243, 1966.

[186] M. Tinkham. Effect of Fluxoid Quantization on Transitions of Superconducting Films. *Phys. Rev.*, 129:2413–2422, 1963.

[187] C. C. Koch, J. O. Scarbrough, and D. M. Kroeger. Effects of interstitial oxygen on the superconductivity of niobium. *Phys. Rev. B*, 9:888–897, 1974.

[188] J. R. Clem and Zh. Hao. Theory for the hysteretic properties of the low-field dc magnetization in type-II superconductors. *Phys. Rev. B*, 48:13774–13783, 1993.

[189] S. L. Li, H. H. Wen, and Z. X. Zhao. Modeling and simulation on the magnetization in field-cooling and zero-field-cooling processes. *Physica C: Superconductivity*, 316(3-4):293 – 299, 1999.

[190] H.W. Weber, E. Seidl, M. Botlo, C. Laa, E. Mayerhofer, F.M. Sauerzopf, R.M. Schalk, H.P. Wiesinger, and J. Rammer. Magnetization of low-κ superconductors I the phase transition at H_{c1}. *Physica C: Superconductivity*, 161(3):272 – 286, 1989.

[191] S. Mühlbauer, C. Pfleiderer, P. Böni, E. M. Forgan, E. H. Brandt, A. Wiedenmann, U. Keiderling, and G. Behr. Time-resolved stroboscopic neutron scattering of vortex lattice dynamics in superconducting niobium. *Phys. Rev. B*, 83:184502, 2011.

[192] J. Kohlbrecher. Sasfit: A program for fitting simple structural mmodel to small angle scattering data. online, https://kur.web.psi.ch/sans1/SANSSoft/sasfit.html, 2012.

[193] H. Furukawa. Dynamics-scaling theory for phase-separating unmixing mixtures: Growth rates of droplets and scaling properties of autocorrelation functions. *Physica A: Statistical Mechanics and its Applications*, 123(2):497 – 515, 1984. ISSN 0378-4371.

[194] H. Furukawa. A dynamic scaling assumption for phase separation. *Advances in Physics*, 34(6):703–750, 1985.

[195] L. Embon, Y. Anahory, A. Suhov, D. Halbertal, J. Cuppens, A. Yakovenko, A. Uri, Y. Myasoedov, M. L. Rappaport, M. E. Huber, A. Gurevich, and E. Zeldov. Probing dynamics and pinning of single vortices in superconductors at nanometer scales. *Scientific Reports*, 5:7598–, 2015.

[196] F. Gömöry. Characterization of high-temperature superconductors by AC susceptibility measurements. *Superconductor Science and Technology*, 10(8): 523, 1997.

[197] M. R. Koblischka and R. J. Wijngaarden. Magneto-optical investigations of superconductors. *Superconductor Science and Technology*, 8(4):199, 1995.

[198] Ch. Jooss, J. Albrecht, H. Kuhn, S. Leonhardt, and H. Kronmüller. Magneto-optical studies of current distributions in high - T_c superconductors. *Reports on Progress in Physics*, 65(5):651, 2002.

[199] W. Treimer, O. Ebrahimi, N. Karakas, and R. Prozorov. Polarized neutron imaging and three-dimensional calculation of magnetic flux trapping in bulk of superconductors. *Phys. Rev. B*, 85:184522, 2012.

[200] N. Kardjilov, I. Manke, M. Strobl, A. Hilger, W. Treimer, M. Meissner, T. Krist, and J. Banhart. Three-dimensional imaging of magnetic fields with polarized neutrons. *Nat Phys*, 4(5):399–403, 2008.

[201] Z. X. Ye, Qiang Li, M. Suenaga, and V. F. Solovyov. *Magneto-Optical Studies of Ybco Thick Films in the Critical State*, pages 175–182. Springer Netherlands, Dordrecht, 2004.

[202] E. H. Brandt. Superconductor disks and cylinders in an axial magnetic field. I. Flux penetration and magnetization curves. *Phys. Rev. B*, 58:6506–6522, 1998.

[203] A. Forkl. Magnetic flux distribution in single crystalline, ceramic and thin film high- $T_mathrmc$ -superconductors. *Physica Scripta*, 1993(T49A):148, 1993.

[204] P.N. Mikheenko and Yu.E. Kuzovlev. Inductance measurements of HTSC films with high critical currents. *Physica C: Superconductivity*, 204(3):229 – 236, 1993.

[205] C. S. Tedmon, R. M. Rose, and J. Wulff. Resistive Measurements of Structural Effects in Superconducting Niobium. *Journal of Applied Physics*, 36(3):829–835, 1965.

[206] P. Milde, D. Köhler, J. Seidel, L. M. Eng, A. Bauer, A. Chacon, J. Kindervater, S. Mühlbauer, C. Pfleiderer, S. Buhrandt, C. Schütte, and A. Rosch. Unwinding of a Skyrmion Lattice by Magnetic Monopoles. *Science*, 340 (6136):1076–1080, 2013.

[207] Y. Onose, Y. Okamura, S. Seki, S. Ishiwata, and Y. Tokura. Observation of Magnetic Excitations of Skyrmion Crystal in a Helimagnetic Insulator Cu_2OSeO_3. *Phys. Rev. Lett.*, 109:037603, 2012.

[208] T. Schwarze, J. Waizner, M. Garst, A. Bauer, I. Stasinopoulos, H. Berger, C. Pfleiderer, and D. Grundler. Universal helimagnon and skyrmion excitations in metallic, semiconducting and insulating chiral magnets. *Nat Mater*, 14(5):478–483, 2015.

[209] Y. Nii, A. Kikkawa, Y. Taguchi, Y. Tokura, and Y. Iwasa. Elastic Stiffness of a Skyrmion Crystal. *Phys. Rev. Lett.*, 113:267203, 2014.

[210] A. Neubauer, C. Pfleiderer, B. Binz, A. Rosch, R. Ritz, P. G. Niklowitz, and P. Böni. Topological Hall Effect in the A-Phase of MnSi. *Phys. Rev. Lett.*, 102:186602, 2009.

[211] F. Jonietz, S. Mühlbauer, C. Pfleiderer, A. Neubauer, W. Münzer, A. Bauer, T. Adams, R. Georgii, P. Böni, R. A. Duine, K. Everschor, M. Garst, and A. Rosch. Spin Transfer Torques in MnSi at Ultralow Current Densities. *Science*, 330(6011):1648–1651, 2010.

[212] A. Bauer and C. Pfleiderer. Magnetic phase diagram of MnSi inferred from magnetization and ac susceptibility. *Phys. Rev. B*, 85:214418, 2012.

[213] A. S. Tremsin and W. B. Feller. The theory of compact and efficient circular-pore MCP neutron collimators. *Nuclear Instruments and Methods in Physics Research Section A: Accelerators, Spectrometers, Detectors and Associated Equipment*, 556(2):556 – 564, 2006.

[214] S. W. Wilkins, A. W. Stevenson, K. A. Nugent, H. Chapman, and S. Steenstrup. On the concentration, focusing, and collimation of x-rays and neutrons using microchannel plates and configurations of holes. *Review of Scientific Instruments*, 60(6):1026–1036, 1989.

[215] A.S. Tremsin, J.V. Vallerga, J.B. McPhate, O.H.W. Siegmund, W.B. Feller, L. Crow, and R.G. Cooper. On the possibility to image thermal and cold neutron with sub-15 μm spatial resolution. *Nuclear Instruments and Methods in Physics Research Section A: Accelerators, Spectrometers, Detectors and Associated Equipment*, 592(3):374 – 384, 2008.

[216] A.S. Tremsin, J.B. McPhate, J.V. Vallerga, O.H.W. Siegmund, J.S. Hull, W.B. Feller, and E. Lehmann. High-resolution neutron radiography with microchannel plates: Proof-of-principle experiments at PSI. *Nuclear Instruments and Methods in Physics Research Section A: Accelerators, Spectrometers, Detectors and Associated Equipment*, 605(1-2):103–106, 2009. ITMNR 08 Proceedings of the sixth Topical Meeting on Neutron Radiography.

[217] S. Peetermans, A. King, W. Ludwig, P. Reischig, and E. H. Lehmann. Cold neutron diffraction contrast tomography of polycrystalline material. *Analyst*, 139:5765–5771, 2014.

[218] A. S. Tremsin, D. F. R. Mildner, W. B. Feller, and R. G. Downing. Very compact high performance microchannel plate thermal neutron collimators. *IEEE Transactions on Nuclear Science*, 51(3):1020–1024, June 2004.

[219] T. Adams. *Neutronenstreuung an Skyrmionengittern in chiral Magneten.* PhD thesis, Technische Universität München, 2015.

[220] S. V. Grigoriev, S. V. Maleyev, A. I. Okorokov, Yu. O. Chetverikov, and H. Eckerlebe. Field-induced reorientation of the spin helix in MnSi near T_c. *Phys. Rev. B*, 73:224440, 2006.

[221] E. Zeidler, W. Hackbusch, J. Hromkovič, B. Luderer, H.R. Schwarz, J. Blath, A. Schied, S. Dempe, G. Wanka, and S. Gottwald. *Springer-Taschenbuch der Mathematik: Begründet von I.N. Bronstein und K.A. Semendjaew Weitergeführt von G. Grosche, V. Ziegler und D. Ziegler Herausgegeben von E. Zeidler.* SpringerLink : Bücher. Springer Fachmedien Wiesbaden, 2012.